Plans for

TEVATRON Run IIB

December 2, 2001

Contributors

T. Berenc
B. Chase
P. Derwent
J. Dey
K. Gollwitzer
P. Hurh
K. Koba
V. Lebedev
A. Leveling
J. MacLachlan
J. Marriner
K. Meisner
S. Nagaitsev
J. Morgan
J. Ried,
V. Shiltsev
J. Steimel
S. Werkema

Editors

D. McGinnis
H. Montgomery

1 Introduction

It is recognized that an experimental program, in the course of which greater than 15 fb^{-1} of integrated luminosity is delivered by the Tevatron complex to each of the two collider experiments, CDF and D0, has considerable discovery potential.[1] Achieving this integrated luminosity requires an increase in the instantaneous luminosity of a factor of 2-3 beyond that anticipated during Run IIa (the current run). The robustness of the physics program would be enhanced if more integrated luminosity could be achieved. The window of opportunity is bounded in time by the start of operation of the Large Hadron Collider for physics, which is anticipated towards the end of the decade.

Considerable work was done to examine the potential of the Tevatron complex to achieve such a goal. An extensive report[2] was prepared by April 1997 but not completed nor published. The plan described in this report includes a subset of the possibilities suggested in that report.

We concentrate on justifying the approach currently proposed, and describe a plan of execution, which we feel is responsive to the imperatives of the physics. In Chapter 2, we outline the overall strategy and scope. The components of the project are distributed throughout the accelerator complex. The priorities and schedules have been developed by balancing the difficulty and cost of each sub-component versus its potential to enhance the performance of the overall complex as a function of time. In Chapter 3, we describe the scope and current status of each of the sub-projects. In Chapter 4, we provide a summary of the needed resources, the cost and schedule. Finally in Chapter 5, we summarize.

2 Project Strategy, Scope & Goal

2.1 Collider Luminosity

The luminosity of the Tevatron collider may be written as

$$L = \frac{3\gamma_r f_0}{\beta^*}\left(BN_{\bar{p}}\right)\left(\frac{N_p}{\varepsilon_p}\right)\frac{F\left(\beta^*,\theta_x,\theta_y,\varepsilon_p,\varepsilon_{\bar{p}},\sigma_z\right)}{\left(1+\varepsilon_{\bar{p}}/\varepsilon_p\right)} \qquad (2.1.1)$$

where $\gamma_r=E/mc^2$ is the relativistic energy factor, f_0 is the revolution frequency, and β^* is the beta function at s=0 (where it is assumed to attain the same minimum in each plane). The proton (antiproton) beam transverse emittance $\varepsilon_p(\varepsilon_{\bar{p}})$ is defined to be $\varepsilon = 6\pi\gamma_r\sigma^2/\beta$ for a bunch with a gaussian distribution and assumed to be the same in both transverse planes (throughout this document we use the 95% normalized emittance), B is the number of bunches, $N_p\,(N_{\bar{p}})$ is the number of protons (antiprotons) per bunch, θ_y and θ_y are the crossing half-angles, σ_z is obtained from the rms proton and antiproton bunch lengths $\sigma_z^2 = \left(\sigma_{zp}^2+\sigma_{z\bar{p}}^2\right)/2$ and $F\leq 1$ is a form-factor that accounts for the depth of focus (hourglass) and crossing angle effects on the luminosity caused by non-zero bunch lengths. The bunch lengths depend on the longitudinal emittance and the rf voltage, but the luminosity depends only on the bunch lengths. In Run IIa, the form-factor is dominated by the hourglass effect (the design crossing-angle is 0). For gaussian beams the hourglass effect may be written as:

$$F = \frac{\sqrt{\pi}\beta}{\sigma_z}e^{\frac{\beta^2}{\sigma_z^2}}\operatorname{erfc}\left[\frac{\beta}{\sigma_z}\right] \qquad (2.1.2)$$

where the complementary error function is related to the error function by $\operatorname{erfc}(z)=1-\operatorname{erf}(z)$. For Run IIb the crossing angle effect is large and the luminosity comes mainly from the z=0 region where the hourglass effect is small. In this case the form-factor F may be written as

$$F = \frac{1}{\sqrt{1+\sigma_z^2\left(\theta_x^2/\sigma_x^2+\theta_y^2/\sigma_y^2\right)}} \qquad (2.1.3)$$

where $\sigma_x^2 = \left(\sigma_{xp}^2+\sigma_{x\bar{p}}^2\right)/2$ and similarly for y.

The luminosity formula Eq. (2.1.1) is written so as to emphasize the major issues in achieving high luminosity. The first quantity in parentheses is the total number of antiprotons. Under current and probably future operating conditions, the most important factor contributing to the achievable luminosity is the total number of antiprotons in the ring, $BN_{\bar{p}}$. The second most important factor is the proton phase space density, N_p/ε_p, which is constrained by the need to limit the beam-beam tune shift. The form-factor (F) and the emittance ratio $\varepsilon_p/\left(\varepsilon_p+\varepsilon_{\bar{p}}\right)$ are important, but they cannot exceed unity and the amount of luminosity that can be gained using these factors is limited.

2.1.1 Beam-Beam effect

The formula for the (linear) antiproton beam-beam tune shift with no crossing angle is:

$$\Delta\nu = 6\frac{r_p}{4\pi} n_c \frac{N_p}{\varepsilon_p}$$
$$= 0.0073\ (\pi\,\text{mm-mrad}/10^{10})\ n_c \frac{N_p}{\varepsilon_p} \qquad (2.1.4)$$

where r_p is the classical proton radius ($1.535\text{x}10^{-18}$ m) and n_c is the number of interaction points. Operating experience in the Tevatron suggests that the maximum tolerable beam-beam tune shift lies in the range 0.02 to 0.025.

When the beam-beam tune shift is caused primarily by head-on interactions at zero crossing-angle, the beam-beam tune shift determines the maximum value of the factor N_p/ε_p, which appears in Eq. (2.1.1). For Run IIb, the formula Eq. (2.1.4) does not apply. In Run IIb, the beams cross at an angle to avoid unwanted beam-beam interactions near the interaction region. The crossing angle at the interaction region dramatically reduces the beam-beam tune shift (some higher order effects increase), and the sum of the long range interactions cause tune shifts comparable to those at the interaction points. These crossing angle and long range effects depend on both N_p and ε_p separately, and may partially cancel depending on the detailed geometry of the beams and their orbits. These issues are discussed in considerably more detail elsewhere[3]. With a naive application of Eq. (2.1.4) as a guide and considering the complicated nature of the beam-beam interaction, increasing N_p/ε_p in order to increase the collider luminosity is probably severely limited.

2.1.2 Antiproton Production

Of the many technical issues involved with high luminosity proton-antiproton colliders, there is probably no more fundamental limitation than the requirement that antiprotons must be produced at least as rapidly as they are consumed in beam-beam collisions. The minimum production rate is

$$\Phi_{\bar{p}}^{(\min)} = n_c \sigma_a L \qquad (2.1.5)$$

where n_c is the number of collision points and L is the luminosity. The cross-section is the cross-section for scattering outside the acceptance of the Tevatron. This cross-section is only slightly less than the total cross-section. We assume that σ_a is 70 mb at 1000 GeV. With 2 collision points a luminosity of $4.0\text{x}10^{32}$ $\text{cm}^{-2}\text{-sec}^{-1}$ is sustained with a minimum antiproton production rate of 20×10^{10} hr^{-1}.

A more realistic estimate of the antiproton flux must take into account the fact that antiprotons beam-beam collisions are not the only mechanism for antiproton loss. We define the antiproton utilization efficiency as the number of antiprotons lost through

beam-beam collisions divided by the total number of antiprotons produced. During the latter part of Run Ib the antiproton utilization efficiency was about 7%.[i]

The second consideration in determining the antiproton flux required is that neither the luminosity nor the stacking rate is constant. For example, during the Run Ib period referred to above the Tevatron was producing beam-beam collisions for the experiments 51%[ii] of the time. The average initial luminosity of these stores was 1.25×10^{31} cm^{-2}-sec^{-1}, but the average rate of accumulating luminosity during a store (29 nb^{-1}/hr) corresponds to a luminosity 35%[iii] lower. Thus, the Run Ib experience is consistent with the "Snowmass Criterion": that the integrated luminosity obtained is equal to the peak luminosity times the length of the run divided by 3. The peak stacking rate during Run Ib was $7.2x10^{10}$ hr-1. During the same Run Ib running period the antiproton source was stacking 62% of the time at an average rate of $4.3x10^{10}$ hr-1 (60% of the peak value[iv]). Thus, the total number of antiprotons accumulated was 37% (also roughly 1/3) of the peak rate times the length of the run. It should be noted that the percentages of time given for both the Tevatron and the Antiproton Source have no corrections for effects such as scheduled and unscheduled maintenance; they represent actual operating experience during an extended run.

The antiproton utilization efficiency must increase dramatically for Run IIa when the luminosity is expected to increase to 2×10^{32} $cm^{-2}sec^{-1}$ from the Run Ib value of 2×10^{31} $cm^{-2}sec^{-1}$ while the stacking rate increases from 7×10^{10} hr^{-1} to 20×10^{10} hr^{-1}. If the duty factors and efficiencies experienced in Run Ib were to remain the same, then the antiproton utilization efficiency would have to increase to 42%. However, the use of the Recycler as post-Accumulator should side-step the problem of reduced stacking rate when the Accumulator stack size increases above about 50×10^{10}. Accounting for the increase in average stacking rate and assuming a negligible inefficiency in the process of transferring beam to the Recycler, an antiproton utilization of perhaps 25% would be sufficient to achieve the Run IIa goals. The increase in antiproton utilization efficiency is expected to arise from improved transmission through the Main Injector, from avoiding the inefficiency of coalescing the antiproton bunches, and from the recovery of unspent antiprotons by the Recycler at the conclusion of a Tevatron store.

For the purposes of the Run IIb design, we assume that the Run IIa goals will be met but that there will be no further increases in the antiproton utilization efficiency (see Table 2.1). Under these assumptions, the increase in luminosity is directly proportional to the increase in stacking rate, and we conclude that peak stacking rates of about $6x10^{11}$ antiprotons per hour are required to support two interaction regions at $4x10^{32}$ cm^{-2}-sec^{-1}. This rate is a 5-fold increase in stacking rate over the Tevatron I design, a 6-fold increase over the best stacking rate achieved, and a 3-fold increase over the projected Run II stacking rate. Clearly, dramatic increases in the antiproton production rate are an essential element of any plan to achieve a luminosity of $4x10^{32}$ cm^{-2}-sec^{-1} in the Tevatron proton-antiproton collider.

---

[i] During the period October 1, 1994 to July 23, 1995 100.5 pb-1 of integrated luminosity was delivered to each of the two experiments and $1.91x10^{14}$ antiprotons were produced.

[ii] Reliability row in Table 2.1

[iii] Store Efficiency Factor row in Table 2.1

[iv] Pbar Production Efficiency row in Table 2.1.

Run	Ib	IIa (without Recycler)	IIa (with Recycler)	IIb	
Typical Luminosity	1.6	8.6	11.9	41.0	$x10^{31}cm^{-2}sec^{-1}$
Integrated Luminosity	3.1	17.1	23.4	80.9	pb^{-1}/wk
Interactions/crossing	2.5	2.2	1.1	3.7	
Pbar Bunches	6	36	103	103	
Store efficiency factor	0.65	0.65	0.65	0.65	
Form Factor	0.59	0.74	0.40	0.40	
Protons/bunch	23.0	27.0	27.0	27.0	$x10^{10}$
Pbars/bunch	5.6	3.1	2.7	9.4	$x10^{10}$
Pbars lost in collisions	8.4	34.1	46.8	161.7	$x10^{10}$
Total pbars	33.6	110.2	278.8	963.4	$x10^{10}$
Peak Pbar Prod. Rate	7.0	17.0	19.0	62.0	$x10^{10}$/hr
Avg. Pbar Prod.Rate	4.2	10.2	16.2	55.8	$x10^{10}$/hr
Pbar Prod. Eff.	60	60	85	90	%
Reliability	50	50	50	50	%
Pbar Transmission Eff.	50	90	90	90	%
Recycling efficiency	0	0	50	50	%
Pbar Utilization	12	28	24	24	%
β*	35	35	35	35	cm
Bunch Length (rms)	0.6	0.37	0.37	0.37	m
Energy	900	980	980	980	GeV
Bunch Spacing	3500	396	132	132	nS
Crossing 1/2 Angle	0	0	136	136	μrad per plane
Proton Emittance	23	20	20	20	π-mm-mrad
Pbar Emittance	13	15	15	15	π-mm-mrad
Luminosity lifetime	17	13	13	13	hr
Store Length	16	12	12	12	hr

Table 2.1 *Run II parameter table.*[i]

2.2 Run IIa Expectations

Table 2.1 is a working parameter table for Run IIa. It illustrates the changes required to achieve the Run IIa luminosity goals and also the benefits of antiproton recycling. Run IIa requires a modest improvement in proton intensity and about 8 times more antiprotons (spread over 6 times more bunches). The peak antiproton stacking rate is required to increase substantially (about a factor of 3) to produce the necessary antiprotons.

[i] The Run Ib column represents average of 32 stores over the period March 8-April 21, 1995

2.2.1 The Main Injector

The Main Injector project without the Recycler ring should provide initial luminosities up to 8.6×10^{31} $cm^{-2}sec^{-1}$. The Main Injector project goals are shown in Table 2.*2*. The major components of the Main Injector project are:

1. more protons on the antiproton production target (1.7x)
2. faster cycle time for antiproton production (1.6x)
3. increased antiproton transmission through the accelerator complex (1.8x)
4. shorter bunch lengths in the Tevatron because of improvements in RF coalescing efficiency (1.25x)
5. more protons per bunch in the Tevatron (1.17x)

Parameter	Goal	
Intensity per bunch	6×10^{10}	
Total Pbar production intensity	5×10^{12}	(84 bunches)
Proton beam transverse emittance	18π	mm-mrad
Proton beam longitudinal emittance	0.2	eV-sec
Main Injector transverse admittance (@8.9 GeV)	$40\ \pi$	mm-mrad
Main Injector longitudinal admittance (@8.9 GeV)	0.5	eV-sec
Coalesced bunch intensity	3×10^{11}	(per bunch)
Coalesced bunch transverse emittance	$18\ \pi$	mm-mrad
Coalesced bunch longitudinal emittance	2.0	eV-sec

Table 2.*2 Main Injector Project Goals*

2.2.2 The Recycler Ring

The Recycler ring will further increase the initial luminosity to a level of 2×10^{32} $cm^{-2}sec^{-1}$ by:

1. recovering antiprotons from the Tevatron (1.6x)
2. raising the average antiproton production rate. (1.4x)

The Recycler is described elsewhere.[4] The most important design goal is to recover, on average, 50% of the antiprotons that could potentially be recovered. This goal could be met, for example, if 75% of the antiprotons are recovered from 75% of the stores that end normally[i]. We assume that we will continue to achieve the 50% antiproton recovery efficiency for Run IIb despite the increased number of bunches, the higher intensities, and (possibly) somewhat larger emittances.

The average antiproton production rate will be increased by the Recycler ring because the antiproton stack in the Accumulator will be transferred to the Recycler before the stochastic cooling systems in the Accumulator saturate. Antiproton transfers from the Accumulator to the Recycler must be done relatively quickly, with good efficiency, and minimal phase space dilution. Since antiproton transfers from the Accumulator to the Recycler will be done much more frequently in Run IIb, this transfer process will be revisited in Run IIb.

[i] In Run Ib 71% of the stores were intentionally terminated. The others typically ended because of the failure of some critical component.

2.2.3 The Tevatron

Initial operation in Run IIa will be with 36 proton bunches and 36 antiproton bunches. As the luminosity approaches 2×10^{32} $cm^{-2}sec^{-1}$, the number of interactions per crossing will rise to a level that may be unacceptable to the detectors. At this point, the number of bunches will be increased by a factor of about three. The bunch spacing would shrink from 396 nS to 132 nS. At 132 nS bunch spacing, a crossing angle will have to be introduced at the detectors in the Tevatron to eliminate unwanted parasitic crossings. This crossing angle (136 μrad ½ angle per plane) will unfortunately reduce the luminosity by ~40% to 1.2×10^{32} $cm^{-2}sec^{-1}$.

In order to recycle the antiprotons, they must be separated from the protons. We plan to eliminate the protons at the end of a Tevatron store, before deceleration. This plan has the advantage of making the deceleration process much easier because of the absence of beam-beam interaction effects. In addition, this scheme allows the deceleration of the antiprotons on the central orbit which has better field quality and more aperture than the helical orbit used for acceleration. However, the plan does require removal of the protons from the Tevatron at high field, when the Tevatron magnets have the least margin against quenches induced by beam loss. While we have substantial experience with removing the protons with scrapers for special experiments (the proton and antiproton beams are spatially separated), it typically takes half an hour to complete the process. Improvements both in technique and speed would be highly desirable. At the moment, it is uncertain how this goal will be accomplished in Run II.

The Run IIb parameters require the removal of about 3 times the number of proton bunches. The techniques established for Run II may require modification. We assume that an adequate solution will be found based on Run II experience.

2.3 Run IIb Strategy

The key feature in the Run IIb parameter list is to increase the antiproton production rate by a factor of three over Run IIa. The major components of the plan are:

1. Increase the number of protons on the antiproton production target
2. Increase the antiproton collection efficiency by:
   a. Increasing the gradient of the antiproton collection lens
   b. Increasing the aperture of the antiproton collection transfer line and Debuncher ring
3. Increase the antiproton flux capability of the Accumulator Stacktail momentum stochastic cooling system
4. Implement electron cooling in the Recycler Ring
5. Streamline and improve antiproton transfers between the Accumulator and the Recycler.

In addition to increasing the number of antiprotons in the collider, we are pursuing an ambitious research program aimed at reducing beam-beam effects in the Tevatron collider with an electron lens.

The following sections will give a brief overview of each of the Run IIb projects.

2.3.1 Protons on the Antiproton Production Target

Studies[5] have shown that in order to achieve very high performance of the proton source (Linac and Booster) there are many issues that would need to be addressed. In turn this results in a rather expensive project to make big improvements in the intensity of protons out of the Main Injector. We therefore have concentrated on a project called slip-stacking that takes advantage of the large momentum acceptance of the Main Injector and the fast cycle rate of the Booster.

With slip-stacking, two successive Booster batches are injected into Main Injector and coalesced into a single batch via RF manipulations. This project has the potential of doubling the amount of protons on the antiproton production target for a single Main Injector acceleration cycle. However, the minimum size of the longitudinal phase space of the combined batch must be at least double the size of a single Booster batch. This larger longitudinal phase space would result in larger bunch lengths of the protons on target but because of inherent non-linearities in the antiproton debunching process, the larger proton bunch lengths do not translate into larger final momentum spread of the antiprotons after debunching. The length of time it takes to accelerate the second Booster batch plus the time it takes to coalesce both batches will add about 10% to the length of the Main Injector acceleration cycle. Assuming negligible loss during the coalescing and acceleration process, we are expecting an effective increase by a factor of 1.8 in the number of protons on target per unit time.

The advantage of this project is that it requires relatively simple electronics to be installed into the Main Injector low-level RF system, which can be done parasitically during Run IIa operations. The main disadvantage of this project is that it involves RF manipulations of intense beams at very low RF voltages resulting in a severe beam-loading situation. We plan on correcting the beam-loading with direct RF feedback around the RF cavities in the Main Injector. Simulations show that very large loop gains are needed to remove the beam loading to a sufficient level. The large loop gains are associated with a number of stability issues.

When the Main Injector starts providing beam for the NUMI project sometime in 2004-2005, the Main Injector acceleration cycle time will have to be increased by about 20% to accommodate the injection of five extra Booster batches destined for the NUMI target. The effective increase in the number of protons on target from Run IIa to Run IIb will then be reduced from a factor of 1.8 to a factor of 1.5.

2.3.2 Antiproton Collection

The phase space of the antiprotons produced from the production target is much larger than the collection aperture of the transfer line (AP2) connecting the target to the Debuncher ring and the Debuncher ring itself. The production efficiency of 15 antiprotons per 10^6 protons on target achieved in late Run Ib was a result of an effective 150 π-mm-mrad (normalized) collection aperture. By increasing the collection aperture to 300-400 π-mm-mrad, we can expect an increase in antiproton production efficiency to $29\text{-}35 \times 10^{-6}$ antiprotons/proton. There are only a few physical apertures in the collection system that are smaller than 400π-mm-mrad. Most of the aperture limitations are a result of misalignment. A large fraction of this project will be to align the apertures of

collection components using beam-based alignment techniques. The small number of components that do not have the 400 π-mm-mrad physical aperture will be upgraded or replaced.

A pulsed Lithium Lens is used to focus the antiprotons into the AP2 beamline. If the lens gradient can be increased from the present 750 T/m to 1000 T/m (the TEV I design goal), the antiproton production efficiency would increase to 32×10^{-6} for a 300 π-mm-mrad aperture and 40×10^{-6} for a 400 π-mm-mrad aperture. The Lithium lenses exhibit a finite lifetime, which is lower for higher gradients. Although the understanding of lens failure is not complete, the current design has certain identifiable weaknesses. Two approaches are being pursued. On the one hand, a new solid-Lithium lens design is well advanced. On the other, an R&D project, involving the use of liquid Lithium, is underway in collaboration with the Budker Institute, Novosibirsk. Since the handling of liquid Lithium is very difficult, the liquid lens is treated as more speculative than the solid lens work.

By increasing the lens gradient and the collection aperture, the combined increase in production efficiency could be a factor of 2.0 – 2.7 over Run Ib.

2.3.3 Antiproton Source Stochastic Cooling

The 4-8 GHz Debuncher stochastic cooling upgrade that was completed before the start of Run IIa was designed to accommodate the antiproton fluxes that were anticipated for Run IIb[6]. The Stacktail momentum stochastic cooling system in the Accumulator was designed to cool relatively large stacks for Run IIa. Large stacks in the Accumulator place severe constraints on how much antiproton flux the Stacktail system can accommodate because of the limited dynamic range of the system.

In Run IIb, the antiprotons will be transferred to the Recycler before the Accumulator stack size becomes too big. With the constraint of large stacks removed, the Stacktail system can be reconfigured so as to accommodate the large increase in antiproton flux. We feel that this reconfiguration can be done with the present 2-4 GHz bandwidth system so that very little (if any) new hardware would have to be built. The downside of this approach is that the stacktail system will do less cooling and place a larger burden of cooling on the Debuncher and Recycler momentum cooling systems. An alternative approach is to upgrade the Stacktail momentum system to 4-8 GHz as was suggested in the TEV33 draft Report.[2] However, building stochastic cooling electrodes that function at 8 GHz in the high dispersion sections of the Accumulator is thought to be exceeding difficult.

2.3.4 Recycler Electron Cooling

As mentioned in the preceding section, the brunt of momentum cooling large antiproton stacks will be placed on the Recycler ring. At present, stochastic cooling is installed in the Recycler Ring. Because the cooling rate of stochastic cooling systems is inversely proportional to the number of particles, the antiproton accumulation rate will deteriorate as the stack grows bigger.

Electron cooling can reduce the spread in all three components of beam momentum simultaneously. Its primary advantage over stochastic cooling is that the

cooling effect is practically independent of antiproton beam intensity up to the Recycler stack sizes of about 2×10^{13} antiprotons. Its greatest disadvantage is that the effect is very weak until the antiproton emittances are already close to the values wanted in the collider. Thus, the two processes can be seen as complementary rather than competitive. Electron cooling will prove very powerful in the Recycler as an add-on to the stochastic pre-cooling in the Antiproton Source and Recycler.

For electron cooling to work, the particle velocity of the electron beam must match the velocity of the antiproton beam. Since we are going to use electron cooling to cool 8 GeV antiprotons, the energy of the electron beam must be 4.3 MV. To obtain sufficient cooling rates for Run IIb, the electron beam current will be about 300 mA resulting in electron beam power of 1.3 MW. Since present high voltage sources for cold electron beams can only provide power in the range of tens of kilowatts, extremely high re-circulation efficiency of the electron beam must be obtained.

A major R&D program has been underway for some years to develop an electron cooling capability at Fermilab. The practice and principles of electron cooling are well established for ions with kinetic energy of less than 500 MeV/nucleon. For antiprotons at 8 GeV, the fundamentals are the same, but hardware development is required and the technical problems differ. To date, electron cooling at relativistic energies remains an unproven technology, and thus constitutes a high-risk segment of the Run2b upgrades plan. Fermilab is currently the only laboratory pursuing the high-energy electron cooling R&D at full scale

2.3.5 Rapid Antiproton Transfers

One of the key improvements of the Main Injector project was improved antiproton transfer efficiency though the accelerator complex. For Run IIb, the same transfer efficiency is needed. Presently, at each 8 GeV antiproton transfer between the Accumulator to the Main Injector, we spend well over one hour preparing the transfer line. The long setup time is the result of many undesirable features of operating this line at low energies where hystersis effects and tight physical apertures have serious consequences.

During Run IIb, transfers between the Accumulator and Recycler will occur every fifteen minutes. Clearly, the setup time for the transfer line should be a small fraction of this interval. One approach would be to replace the 8 GeV operation of this line with the construction of a single dedicated 8 GeV transfer line. However, this option would be extremely expensive and installation would require significant interruption to integrating luminosity during Run IIa .

The approach that we have decided for Run IIb is a careful analysis and redesign of the optics at 8 GeV and to develop a rigorous set of protocols for handing hysterisis effects. In addition, operational aspects of the 8 GeV will be streamlined with more diagnostics and software. With a more forgiving optics design and frequent transfers, we expect the effects of pulse-to-pulse variations on the performance of the line should be greatly diminished.

2.3.6 Antiproton Tuneshift in the TEVATRON

In the Tevatron, the antiproton bunches suffer a tuneshift due to their interactions with the more intense proton bunches. In multibunch operation, the tuneshifts vary from antiproton bunch to antiproton bunch, leading to an effective spread in tune. An electron lens, consisting of a short, low energy, electron beam propagating along the axis of a solenoidal field, can induce a tuneshift on the antiproton bunches, which has the opposite sign to that, which they experience, from the protons. With appropriate choice of parameters two such lenses could provide effective beam-beam tuneshift compensation. An R&D program has resulted in the construction and, recently, the successful testing of a single such device. If results continue to be positive the use of such devices could lead to a longer luminosity lifetime in the Tevatron and hence to a large integrated luminosity. Because of the R&D nature of this project, we have not explicitly assigned any luminosity gains for Run IIb from this project. As mentioned earlier, operations with up to 6 bunches each of protons and antiprotons appear possible for antiproton tune shift parameters up to 0.02-0.025. Although there is no experience as yet with larger numbers of bunches, controlling the tune spread of the antiprotons whether bunch-to-bunch or within a bunch will be an important aspect. We therefore see the Tevatron electron lens as a potentially important new tool. As this project matures, we will evaluate its role in Run IIb.

3 Sub-Project Description

The goal of Run IIb accelerator upgrades is to triple the antiproton production rate over the anticipated Run IIa target. In this chapter, we describe the scope and current status of each of the sub-projects. Before these projects are described in detail, a brief overview of the Fermilab accelerator complex will be given.

The Fermilab Collider Accelerator Complex

The Fermilab accelerator complex is shown in Figure 3.1. Antiproton production at Fermilab begins with the production of H- ions that are accelerated to 750 keV in the Crockoft-Walton pre-accelerator. The ions are injected into the Linac were they are accelerated to a kinetic energy of 400 MeV. The H- ions are stripped of their electrons at injection into the Booster. The stripping of H- ions allows the production of high intensity proton beams by multi-turn injection. Typically ten to eleven turns are injected into the Booster. The Booster RF systems bunches the proton beam into 84 bunches. The train of 84 bunches is called a Booster "batch". The Booster accelerates the protons to 8 GeV. The Booster can support an acceleration cycle rate of 15 Hz. At 8 GeV, the batch of protons is extracted from the Booster into the MI-8 transfer line and injected into the Main Injector. The Main Injector accelerates the beam to 120 GeV. The beam at 120 GeV is kicked out of the Main Injector into the P1 transfer line.

The P1 transfer line extends from the Main Injector to the Tevatron. At the end of the P1 line the beam flows into the P2 line. The P2 line is actually a remnant of the old Main Ring Accelerator. The P2 line connects to the AP1 transfer line. At the end of the AP1 transfer line is the antiproton target station. The 120 GeV protons hit a nickel target and the resulting secondary beam is transferred into the AP2 transfer line. The first magnetic element of the AP2 line is the lithium lens. The AP2 line accepts only 8 GeV secondaries (with a 5% momentum spread) and funnels the beam into the Debuncher ring. The Debuncher ring has a slightly larger circumference than the Booster Ring. The primary purpose of the Debuncher ring is to reduce the large momentum spread of the antiproton beam by bunch rotation. The debunching process lasts about 60 mS. Since the Main Injector requires a minimum acceleration period of 1.5 S, the antiproton beam is stochasticly pre-cooled in the Debuncher for the remaining time.

Just prior to the extraction of another 120 GeV proton batch from the Main Injector to the target station, the pre-cooled antiproton beam is transferred from the Debuncher to the injection orbit of the Accumulator storage ring. The longitudinal phase space density of the antiproton beam is compressed by a factor of 10,000 by the Accumulator Stacktail momentum stochastic cooling system. After enough antiprotons have been accumulated in the core orbit of the Accumulator, the antiproton production process is halted. The beam is bunched with the Accumulator RF systems and extracted out of the Accumulator into the AP3 transfer line. The AP3 line connects back up to the AP1 line. For antiproton transfers, the energy of the AP1, P2, P1 and Main Injector is set to 8 GeV. The antiprotons follow the reverse route to Main Injector and during the latter part of Run IIa will be injected into the 8 GeV Recycler Ring were the beam will be cooled with previously injected stacks from the Accumulator.

When the Tevatron is ready for another collider store, the proton beam will be preferentially scraped away at 980 GeV. The remaining antiprotons will be decelerated to 150 GeV in the Tevatron and transferred back to the Main Injector via the P1 line. The antiprotons are decelerated to 8 GeV in the Main Injector and transferred to the Recycler for assimilation into the stored core of antiprotons.

With the Tevatron energy set at 150 GeV, a batch of protons is accelerated to 8 GeV in the Booster. However, only seven of the 84 bunches are extracted out of the Booster and transferred into the Main Injector. The seven bunches are accelerated to 150 GeV in the Main Injector. At 150 GeV the seven bunches are coalesced into a single bunch by a series of longitudinal bunch rotations using RF systems of several different harmonics. The single proton bunch is injected into the Tevatron. This process is repeated for the desired number of bunches in the Tevatron (36 in Run IIa. The switch to 132 nS operation will require multi-bunch coalescing.) Once the Tevatron is filled with protons, antiprotons are extracted out of the Recycler and coalesced into high intensity bunches in a similar process. The antiprotons are transferred from the Main Injector to the Tevatron via the A1 line. Once the Tevatron is filled with protons and antiprotons, the Tevatron is ramped to an energy of 980 GeV and the proton and antiproton beams are brought into collision.

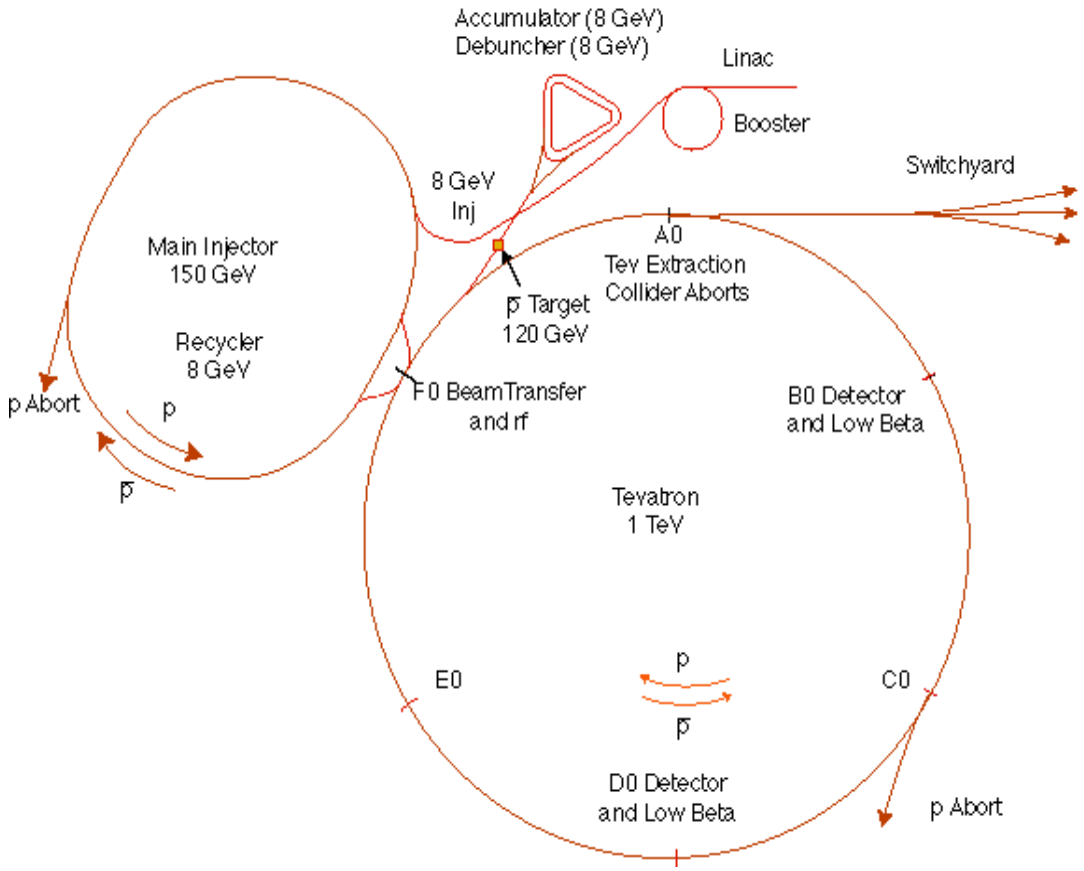

Figure 3.1 *The Fermilab Accelerator complex.*

3.1 Protons on the Antiproton Target

3.1.1 Introduction

3.1.1.1 Justification

The goal of the Run IIb upgrades is to increase total antiproton yield to collisions. This should lead directly to the necessary luminosity required to reach the 15 fb^{-1} goal for Run II. Increasing the antiproton yield will involve increasing the proton flux on the antiproton target, improving the collection efficiency, and increasing the antiproton cooling rate. This project deals with increasing the proton flux on the antiproton target.

The machines responsible for providing protons to the antiproton target are the Linac, Booster, and Main Injector. The Linac provides about 50 mA of beam current to the Booster at 400 MeV. The Booster then accepts Linac beam for nine or ten revolutions to provide the Main Injector with about $5x10^{12}$ protons at 8 GeV. The Main Injector accelerates the beam to 120 GeV for the antiproton production target. The antiproton Debuncher ring and the Booster have the same circumference, so only a single Booster batch can be applied to the target before the Debuncher ring is full. The Main Injector has a circumference seven times the Booster's, so it can provide the target with beam and still have five batches of space for other uses (ie NuMI).

The most straight-forward method of increasing flux on target would be to increase the current in the Linac, or inject more rotations of Linac beam in the Booster. This would lead to higher current in the Main Injector. Unfortunately, space charge effects limit the amount of beam that can be injected into the Booster[7]. Injecting more than 500 mA into the Booster reduces its efficiency to the point where no more beam reaches the Main Injector. In order to increase beam intensity, we need to reduce the effect of space charge in the Booster, or we need to take advantage of the extra space in the Main Injector.

Slip stacking takes advantage of the extra longitudinal phase space in the Main Injector. It is a method of injecting two batches of Booster beam into the Main Injector and combining the two batches into one double charged batch before extracting to the antiproton target. Two batches of beam are injected consecutively into the Main Injector with slightly different momenta. The different momentum batches have slightly different velocities, and one batch eventually overtakes the other batch. When the two batches completely overlap, the RF voltage is increased to provide a bucket big enough to contain the entire momentum space of the two batches. There are two critical and conflicting parameters that determine the efficiency of slip stacking. First, the momentum separation between the batches must be large enough, compared to the bucket size, to minimize the interference between the two batches. Second, the momentum separation should be minimized at capture time in order to keep the longitudinal emittance of the final batch low.

Of course the momentum separation between the batches must not be larger than the momentum acceptance of the Main Injector. If the longitudinal emittance of the Booster beam is maintained at about 0.1 eV-s, the bucket height required to contain the beam in the absence of beam loading is about 9 MeV. The Main Injector has a measured momentum acceptance of about 1.4% (See Figure 3.1.1). This corresponds to about 124

MeV of acceptance or about fourteen Booster batches stacked end to end in energy space. This is more than enough aperture for successful slip stacking. Because of the large momentum aperture in the Main Injector, simplifying operational issues can take precedence over minimizing the momentum aperture required by the slip stacking process.

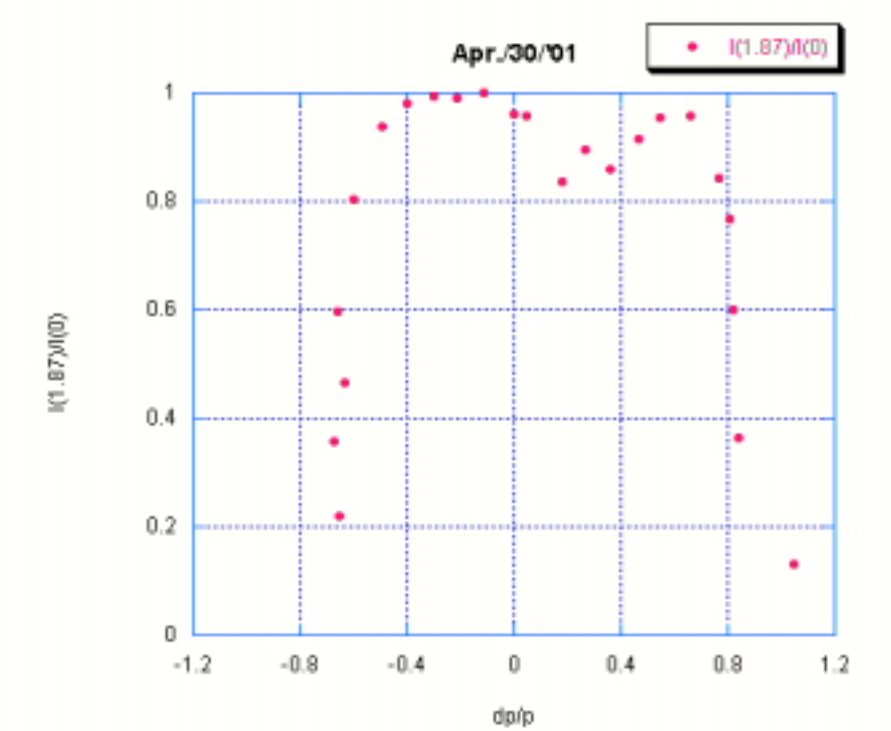

Figure 3.1.1 *Main Injector momentum aperture. This plot measures main injection efficiency as a function of momentum offset. The momentum offset is created with a three bump at the radial position feedback pickup*.

3.1.1.2 Slip Stacking Process

The slip stacking process in the Main Injector can be described in four phases: first batch injection, second batch injection, slipping, and capture. The first batch injection is essentially the same as any injection from Booster to Main Injector. If momentum aperture were a premium in the Main Injector, the first batch would be injected off momentum to the upper edge of the aperture. Because there is so much momentum aperture in the Main Injector, there is no need to inject the first batch off momentum. Therefore, the first batch is injected on the Main Injector's central orbit (Figure 3.1.2), just like all other Main Injector cycles. The only difference between first batch injection and standard injection is the capture voltage is about a factor of ten less for slip stacking. Since the Booster cannot match to such a low voltage, the Booster executes bunch rotation before extraction. Between the time that the first batch is injected and the second batch is injected, the first batch is decelerated off the central orbit sufficiently to make room for the second batch in longitudinal phase space (Figure 3.1.3).

After the first batch has been injected and decelerated, the RF voltage that is to be synchronous with the second batch is activated. (It is deactivated during first batch injection to minimize emittance growth caused by interference between the two RF

voltages.) The second batch is also injected on the central orbit of the Main Injector, just behind the first batch (Figure 3.1.4). Since the first batch was decelerated off the central orbit, it now has a lower velocity than the second batch, and the particles from the second batch will overtake the first batch (Figure 3.1.5). The total RF voltage in the cavities and the total RF component of the beam current see 100% amplitude modulation as the batches slip past each other. Damage to the longitudinal emittance of the two batches is minimized because the frequency separation is significantly greater than the synchrotron frequency.

Once the two batches are completely aligned the capture process begins. The two RF voltage waveforms used for each batch jump in frequency to the same value. This value is the average frequency between the two slipping frequencies. Simultaneously, the total RF voltage is increased to create a bucket that encloses the entire momentum spread created by both batches. Presently, there is no good way to preserve the longitudinal emittance of the combined batch, and it is assumed that the beam will eventually filament to some emittance higher than twice the single batch emittance. After the beam is captured (Figure 3.1.6), it is accelerated to 120 GeV with the standard stacking ramp. It is important that the emittance is kept low enough to be accelerated through transition in the Main Injector. It also must be low enough to fit within the momentum aperture specifications of the accumulator.

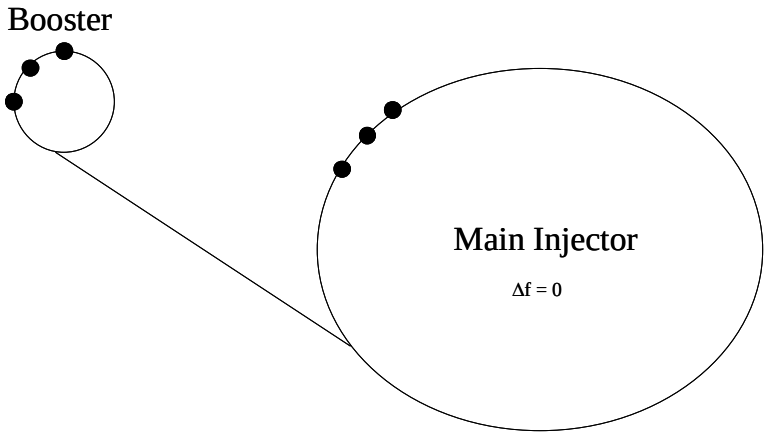

Figure 3.1.2 *First batch injection: First batch injected on Main Injector's central orbit.*

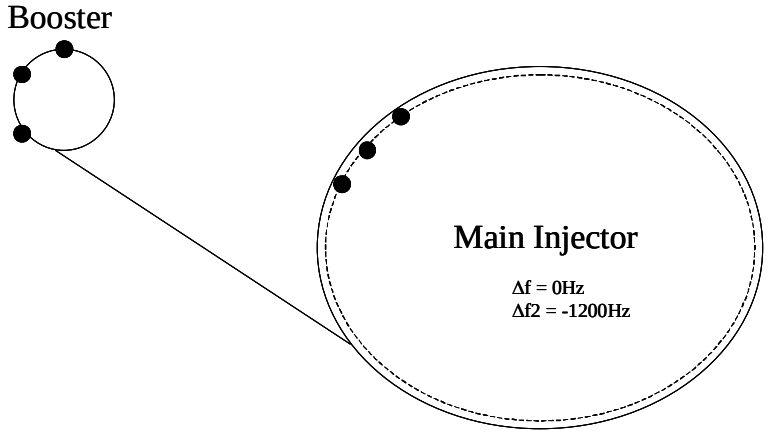

Figure 3.1.3 *First batch decelerated to make room for second batch.*

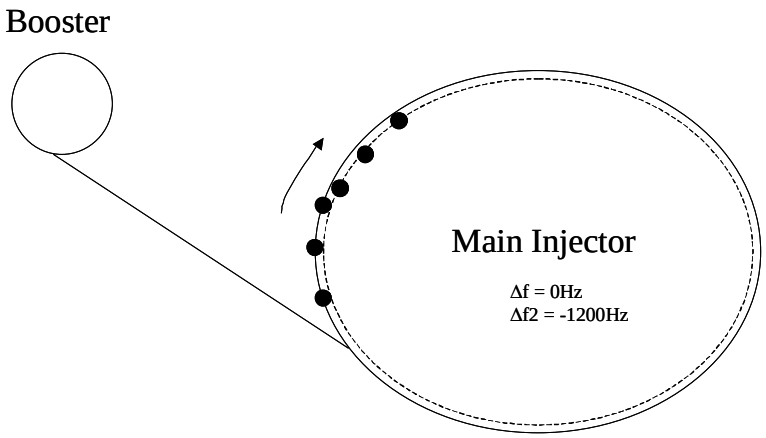

Figure 3.1.4 *Second batch injection on the Main Injector central orbit, just behind the first batch.*

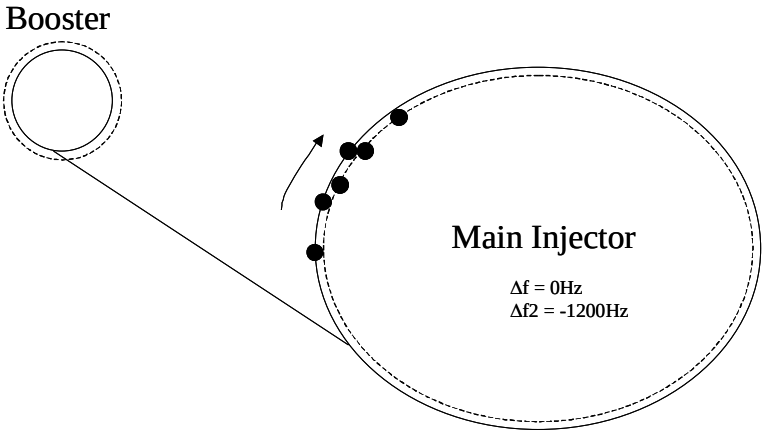

Figure 3.1.5 *Batches slipping. The second batch begins to overtake the first batch because of the differences in velocity.*

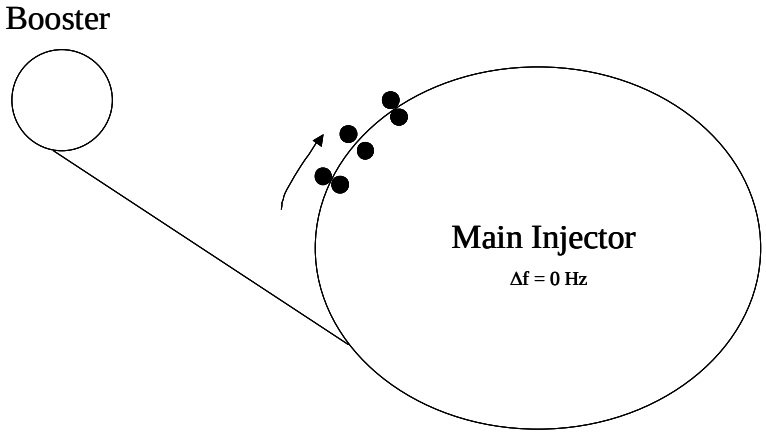

Figure 3.1.6 *Batch profile immediately after capture*

3.1.1.3 Slip Stacking Efficiency

Slip stacking will nearly double the overall flux on the antiproton target. There losses in efficiency due to the larger longitudinal emittance and extra cycle time is required to inject two batches and slip together. One Booster cycle occurs every 15Hz. Two batches can slip together in approximately one Booster batch time. This time becomes critical when NuMI operation is considered. For NuMI operation, after the two batches for stacking have been combined and the frequency offsets zeroed, five more batches will be injected. If the slipping time is even slightly greater than a Booster cycle, an entire Booster cycle will be wasted until NuMI injection can begin (the Booster magnet power supply is a resonant circuit and can't be held off). The following table illustrates the improvement over standard stacking given different slip stacking scenarios.

Because of the small buckets sizes and large beam currents involved in slip stacking, beam loading becomes the dominant barrier to a reliable slip stacking process. Beam will fall out of the buckets at the currents and voltages specified without proper beam loading compensation. These effects have been simulated, and some beam loading compensation systems have already been tested on the Main Injector. The operation systems, however, are not sufficient for slip stacking at high intensity. The most challenging aspect of the project is the design of a state of the art beam loading compensation system.

Slip stacking studies have already begun in the Main Injector. Many modifications to the RF system were required to facilitate the basic mechanics of slip stacking. The rest of the paper discusses the details of these modifications. It will also cover slip stacking simulation work, and it will cover the details of the beam loading issues and possible cures.

Operation Mode	Booster Cycles	Cycle Time	Relative Intensity Of Stacking Pulse	Stacking Improvement
Stacking	1	1.466s	1	1
Slip Stacking	3	1.6s	1	1.8
Slip Stacking w/ NuMI	8	1.93s	1	1.5

Table 3.1.1 *Relative Improvement in Proton Flux for Different Operating Scenarios*

3.1.2 Basic Hardware

Slip stacking is a predominantly longitudinal process, and the control for longitudinal processes lies in the RF system of the accelerator. The only hardware changes needed to facilitate slip stacking are in the RF control systems. The actual changes can be easily supported by the existing cavities and power supplies

3.1.2.1 LLRF

Many changes were made to the LLRF system when the Main Injector replaced the main ring. The system is now primarily digital. The voltage-controlled oscillator (VCO) was replaced with a numerically controlled oscillator (NCO) controlled by a DSP (Figure 3.1.7). Each NCO drives the IF ports of an I-Q modulator with its local oscillator input at 50 MHz. The NCOs have a 32 bit frequency register, making the frequency setting precise to about 2mHz. The DSP can update the NCO frequency value at about a 10 kHz rate, which is more than sufficient for the acceleration ramps in the Main Injector.

The new LLRF system also performs most of its feedback control digitally. It is equipped with a number of digitizers that look at error signals generated by the instrumentation. The instrumentation includes a phase detector for phase feedback and a beam position monitor for radial position feedback. The signals are sampled and stored in the DSP. The DSP then performs the appropriate filtering and gain control for the loops. The DSP will then update the frequency value of the NCO based on a combination of the frequency program and the feedback values.

Another task that the LLRF system must perform is the generation of the revolution marker. This marker remains synchronous with the beam revolution frequency, and it is used to define bucket enumeration. A marker that is synchronized with the first bunch in a batch of beam at injection will be synchronized with the same bunch for every injection. The marker is used to trigger kickers and instrumentation. Keeping the marker synchronized to the revolution frequency is straightforward. Since the RF output of the LLRF system must be synchronized with the beam, it can be used as a clock for a divide-by-N counter, where N is set to the harmonic number of the machine. To maintain consistent enumeration, either the marker must be reset by the same signal that triggers Booster extraction, or the marker itself must trigger Booster extraction. The Main Injector LLRF system uses both techniques. When the Main Injector is empty, the Booster resets the marker, and when there is beam already in the Main Injector, the Main Injector revolution marker triggers Booster extraction.

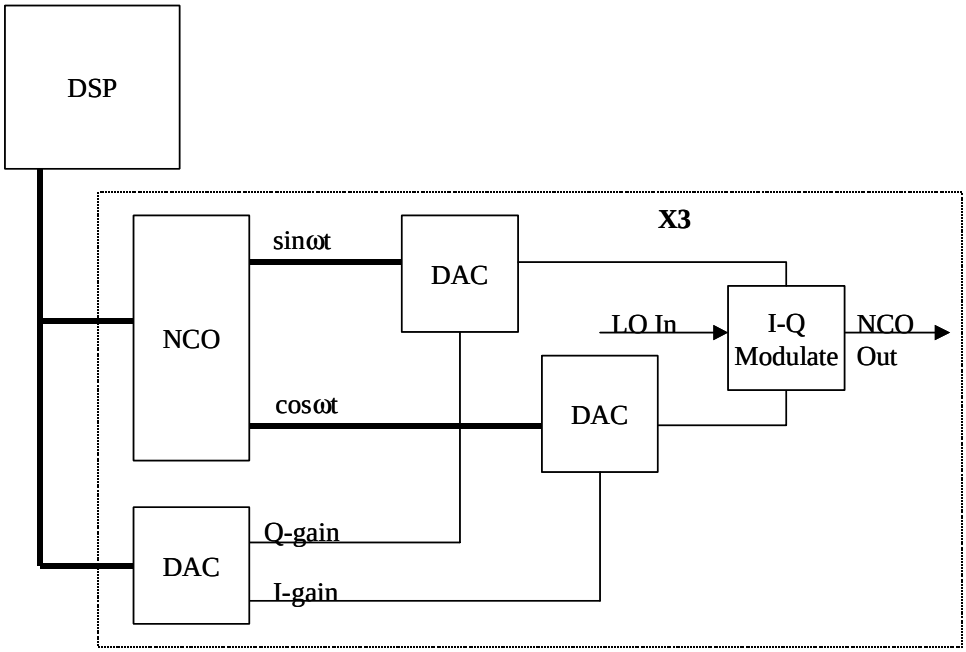

Figure 3.1.7 *Block diagram of NCO module. The DSP controls the NCO frequency setting, and the DAC that controls the phase shift prior to the I-Q modulator. The LO phase is matched on all three modulators, and the three NCOs are set to run the same frequency ramps. This makes the phase shift between outputs independent and precise.*

During some Main Injector cycles, the total RF voltage seen by the beam must be dropped to a very low value, sometimes zero. Coalescing is one application where the voltage must be varied. The RF voltage is dropped to a low level to rotate the 53 MHz

buckets for minimum energy spread. Then, the 53 MHz voltage is turned off, and a 2.5 MHz RF system is enabled to rotate multiple 53 MHz bunches into one "superbunch". The 53 MHz system is then re-enabled to recapture the bunch into a single bucket. There is a lower limit to the anode bias voltage, and it is not low enough for coalescing. Paraphasing is one solution to the problem, and it was incorporated into the LLRF system.

Paraphasing is a process in which the RF cavities are divided into two groups, and each group is driven by a LLRF signal with a different synchronous phase. If the difference in synchronous phase between the two groups is 180° and if the total amplitude of the two groups is balanced, then the beam will see a zero net RF voltage. Paraphasing can develop arbitrary RF voltage levels without varying the anode bias if the difference between synchronous phase angles can be controlled arbitrarily (Figure 3.1.8).

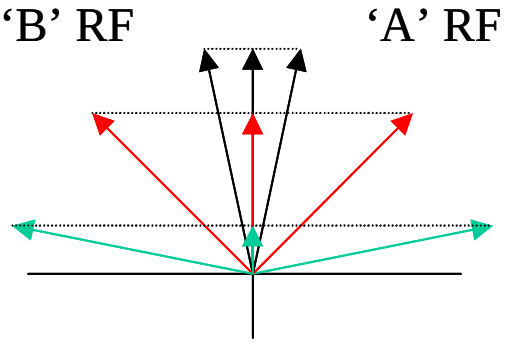

Figure 3.1.8 *Paraphase illustration. Arbitrary voltage levels, along the vertical axis, are generated by varying the phase difference between the 'A' and 'B' RF outputs.*

The LLRF system generates three independent RF outputs. Two of the outputs are used as the RF drive for the cavities, and each output drives a different group of cavities in the paraphase process (Figure 3.1.9). The third output is used as a beam synchronous signal for instrumentation and for generating the revolution marker. Independent NCO I-Q systems generate each output. Each NCO system has bipolar amplitude control on each I-Q leg, controlled by a DAC. This DAC is controlled by the DSP, and this gives the DSP the ability to place an arbitrary phase shift on any output.

For slip stacking, the Main Injector LLRF system must generate two RF signals with independent frequency controls. The distribution of the outputs to the cavities is already in place because of the paraphase system. Since each output has its own NCO system, one could program different frequency ramps to each output through the NCO. However, the NCOs have no means of communicating their relative phase offsets. The relative phase between the RF outputs becomes very important at the end of the slip stacking cycle. If the phase between the outputs is not adequately controlled, the RF seen by the beam could be paraphased at some arbitrary angle, causing large variations in capture voltage amplitude.

Instead of having independent frequency ramps for each NCO, it is better to use the independent paraphase control for each output. The paraphase system controls the phase shift on each output through an I-Q (In-phase-Quadrature phase) modulator. The phase shifter can generate a frequency offset on its output if the phase control is a ramped input (Figure 3.1.10). The DSP stores independent frequency offset tables for each output and converts the tables into phase ramps. It updates the I-Q DACs every time

there is a phase step. This technique provides a significant advantage over changing the NCO frequency. The DSP maintains a very precise phase control between the two outputs, and it can dictate the exact paraphase angle at the end of the slip stacking cycle. Its greatest limitation is the DAC update rate, which limits the maximum offset frequency and the timing precision of the capture process.

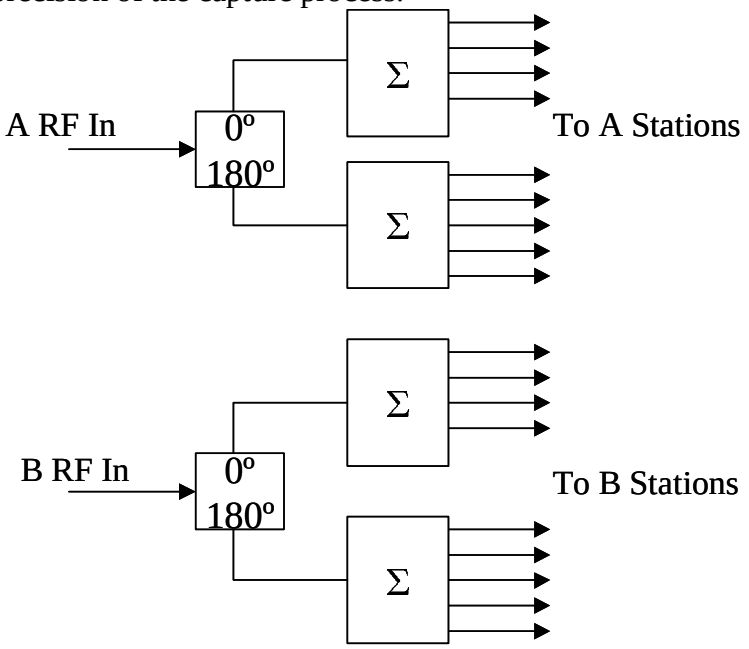

Figure 3.1.9 *Paraphase fanout. Two outputs of NCO module each drive half the RF stations. The hybrid is needed because the cavities are physically separated by half an RF wavelength.*

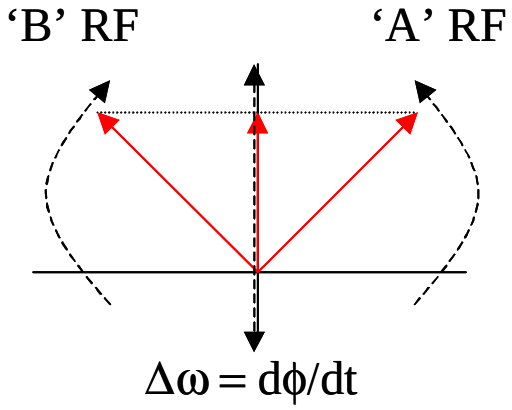

Figure 3.1.10 *Vector diagram showing paraphase control generating offset frequencies. The offset frequency is equal to the time derivative of the phase shift ramp.*

A preliminary slip stacking routine for the LLRF system has been tested on the Main Injector. First, both outputs are set to the nominal injection frequency before injection (Figure 3.1.11). This is used by the high level system to sample control loop errors for a smooth turn on at the end of the slip stacking cycle. The second RF output is given a positive offset frequency (1200 Hz) before injection to minimize destructive interference on the first batch of injected beam. The first batch of beam is injected

synchronous with the first RF output. Both RF outputs are then decelerated until the second RF output has zero offset frequency, and the first output has a negative frequency offset (-1200 Hz). The second batch of beam is injected, and both outputs are accelerated until the frequency offsets on the two outputs are equal and opposite (+-600 Hz) (Figure 3.1.12). This is done so that the two batches are captured by a frequency with a net zero offset. Otherwise, the system must maintain the offset frequency after capture and into acceleration. Just before the batches are aligned, the frequencies are brought closer together in order to reduce the total bucked separation at capture time. Once the two batches are aligned, the frequency offsets are set to zero.

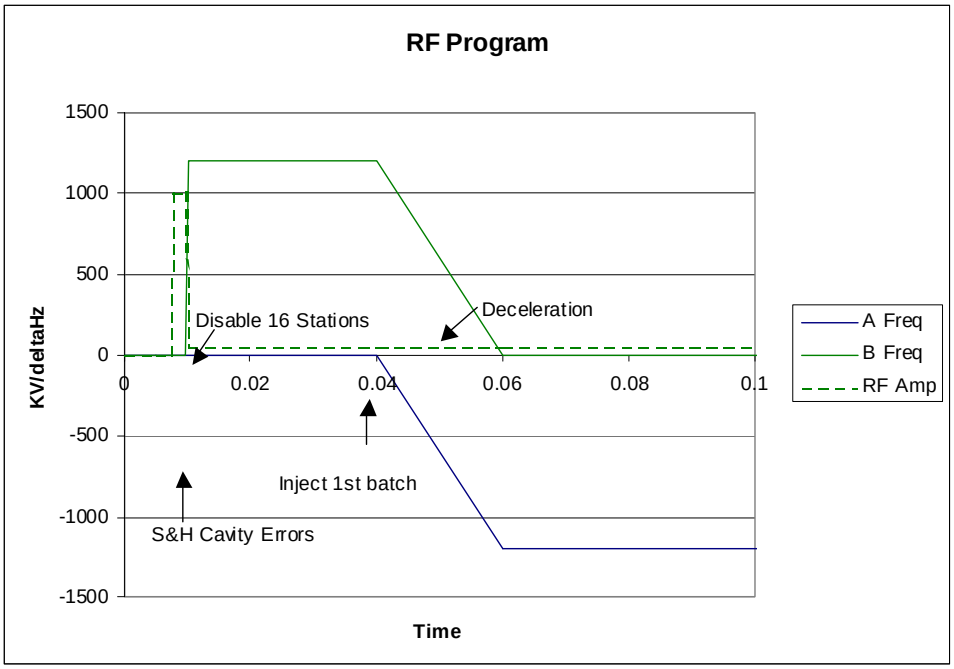

Figure 3.1.11 *Frequency offset program and RF drive level program for slip stacking. The error signals on the cavity feedback loops are sampled before the cavities are gated off. The first batch is injected and decelerated. The frequency difference between 'A' and 'B' outputs is kept constant.*

The next step in the process involves enabling the LLRF feedback loops and beginning the normal single batch acceleration process to 120 GeV. This has not been tried yet in preliminary tests. It appears to be possible to re-enable the loops after capture. The coalescing process already disables and enables feedback loops without noticeable effects on the beam quality.

Once the offset frequency signals are generated, it is relatively straight forward to generate the signals in the proper RF cavities. There are still some minor modifications to the high level system necessary to facilitate slip stacking in the Main Injector.

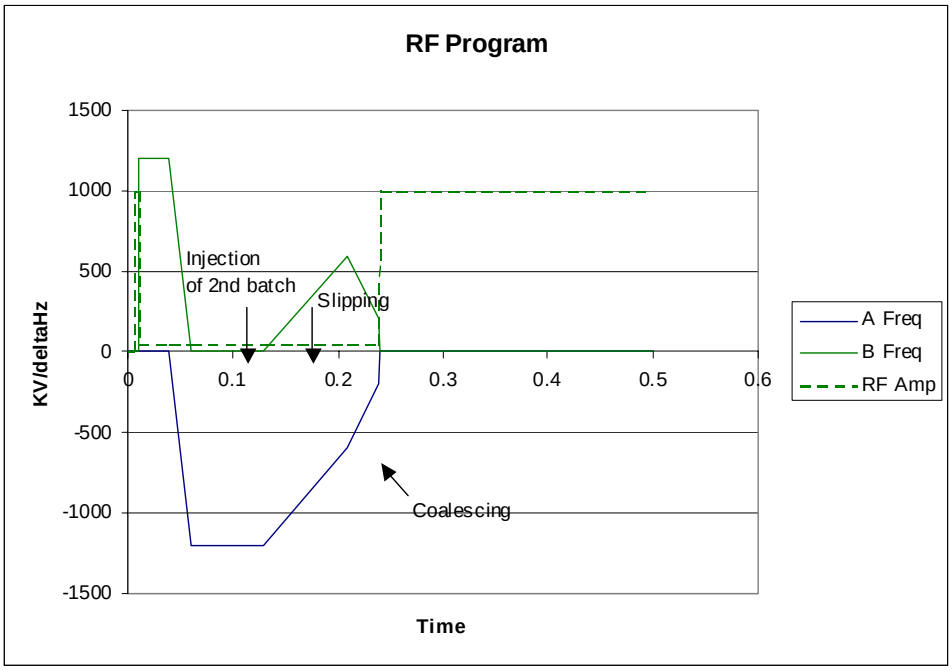

Figure 3.1.12 *Frequency offset program and RF drive level program for slip stacking. After the second batch is injected, the beam is accelerated so that the energy offsets are symmetric about the nominal orbit. Just before the batches are combined, the energy difference is reduced. The frequency offsets are set to zero, and the RF drive is increased simultaneously to hold both batches at capture.*

3.1.2.2 HLRF

The high level RF system is defined as all of the hardware used to get the signal from the LLRF distribution to the cavity gap. This includes the cavity itself and all RF power amplifiers downstream of the LLRF system (Figure 3.1.13)[8]. The cavity is a ferrite bias tuned resonant structure. The resonant frequency of the cavity varies from 52.8 MHz to 53.1 MHz from low to high ferrite bias current. The Q of the resonant cavity varies from 3500 to 5000, and the shunt impedance varies from 250 kOhms to 520 kOhms. The cavity has a 12:1 step up ratio from the RF power input to the gap. The primary power limit to the cavity comes from the ferrite tuners. The tuners cannot hold off a voltage greater than 9 kV without sparking.[9]

The cavity is driven by a Y567 tetrode power tube. This tube is capable of delivering about 75 kW of CW RF power. The plate of the power tube is biased by another Y567 tube in series, and this tube holds off the 30 kV DC bias from the power supply. The grid of the series tube controls the amount of bias on the plate of the power tube. A solid state power amplifier drives the cathode of the power tube with about 4 kW of power capability. The power tube also has a fixed screen voltage supply, and a programmable grid bias supply.[8]

There are four feedback loops around each cavity. One loop maintains the proper resonant frequency of the cavity through control of the ferrite bias current. The loop keeps the anode and cathode voltages in phase for maximum power efficiency and fundamental beam loading compensation. Another loop maintains the proper RF voltage on the cavity by measuring the DC screen current. If the screen current gets too large, the

low level RF drive to the cavity is reduced. Likewise, if the screen current gets too low, the drive is increased so that the RF waveform fills the entire anode bias. This means that during normal operation, the anode bias dictates the RF voltage in the cavity. The signal from the cavity gap monitor is also fed back into the cavity drive, reducing the fundamental cavity impedance seen by the beam by a factor of 10. Finally, there is a fanout/fanback phase lock loop that compares the gap monitor voltage phase with the LLRF drive. This loop helps maintain a very precise phase relationship between different cavities for better paraphase operations.

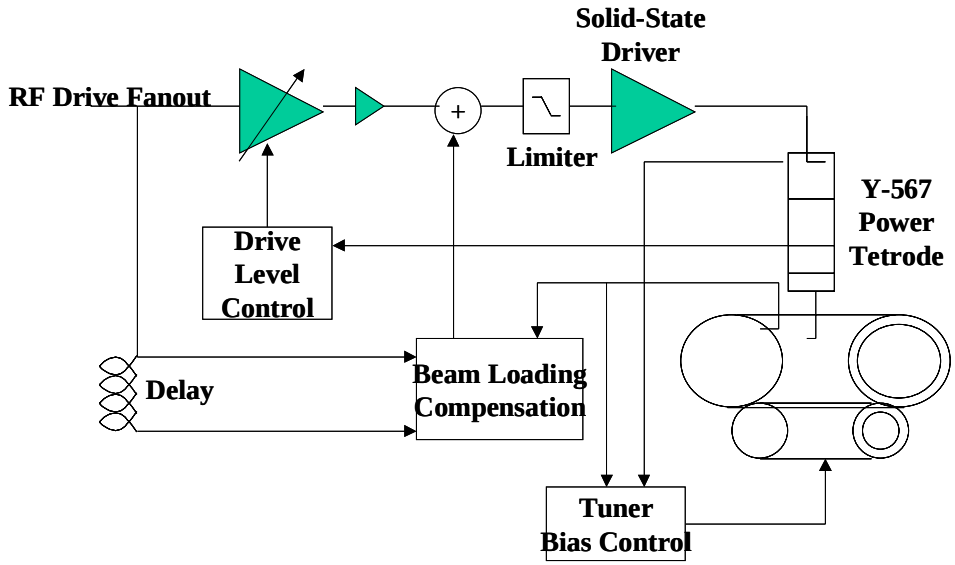

Figure 3.1.13 *Block diagram of Main Injector high level RF system. The drive level control receives its error signal from the DC screen current. Not pictured, the fanout-fanback phase loop.*

The modifications to the high level RF system necessary to facilitate slip stacking are a product of having to operate at a low voltage and still maintain beam loading compensation systems. Because of the way the power tube is biased, there is a limit to how low the plate can be biased. Therefore, the plate bias is kept high and only two stations are activated during the slip stacking process. Even though only two stations are active, the other sixteen stations must keep their RF feedback loops active. Instead of turning off the tubes completely, only the RF drive is disabled on the sixteen cavities. This keeps the tube biased and the feedback loop active during slip stacking. Special gates were added to the RF drive input to the amplifiers, so that single cavity drives could be activated without disabling the tube bias.

Because there is no RF voltage in most of the cavities during slip stacking, many of the feedback loops around the stations will not regulate properly. These feedback loops have relatively large settling times, and if the errors are allowed to float to a rail, the beam will be adversely affected while the loop tries to settle again. In order to insure that the cavities regulate quickly after they're turned on, the errors from the feedback loops are sampled before the cavities are shut down. The errors are held during the slip stacking process and allowed to track again after the stations have been reenergized.

A preliminary RF voltage program has been tested on the Main Injector. First, all of the RF stations are active, and their feedback loop errors are sampled and held. Before

the first batch is injected, all but one RF station is gated off. Just before the second batch is injected, the station with the RF synchronous with the second batch is turned on. All of the stations are activated precisely at capture time.

3.1.3 Low Intensity Slip Stacking

In order to better understand the basic mechanics of slip stacking, studies have been performed at intensities below the level where beam loading effects begin to dominate. These studies were performed in simulation and in the Main Injector itself.

3.1.3.1 Simulations

The simulations provide valuable information about idealized operating conditions for optimal slip stacking. These operating parameters would be difficult to determine empirically, because the operating conditions of the Main Injector change frequently during the course of studies. Without the aid of the simulation results, problems with slip stacking due to Main Injector setup errors would be much more difficult to diagnose.

"ESME is the program used to simulate longitudinal manipulations. The program ESME has been developed to model those aspects of beam behavior in a proton synchrotron that are governed by the radio frequency systems. It follows the evolution of a distribution in energy-azimuth coordinates turn-by-turn by iterating a map corresponding to the single-particle equations of motion. The map parameters may be updated each turn to reflect the action of the beam current on the individual particles through feedback loops, space charge, coupling impedance, etc. Over eighteen years of development it has been applied to a significant range of problems in rf capture, transition crossing dynamics, bunch coalescing, longitudinal single bunch and multi bunch stability. The standard output includes practically all of the information available from single particle dynamics like, for example, bucket area, bunch emittance, synchrotron frequency, slip factor, etc. Both input and output for collective motion calculations may generally be represented in frequency domain or time domain, as convenient in a particular application." [10]

There has been no need to modify the distribution version of ESME to do the slip stacking simulations; however, this does not mean that it has been unnecessary to write code. ESME is written with ten dummy entries for attaching application specific code. For the slip stacking application, three of these entry points are used. One subroutine, which has been around for a long time and more or less taken for granted by regular users, is used to make 166 copies of a 0.1 eVs bunch and place them at the desired bunch centers for the two batches (Figure 3.1.14). A second very short routine is used to test the location of marker particles located at the stable fixed points of the center bunches of each batch and to stop tracking when they are aligned in phase. These two routines are all that is required to find the emittance dilution and optimum frequency curves including performance degradation by beam loading. However only simplistic conclusions with respect to compensation techniques can be established without additional code.[11]

One of the first results derived from the simulation is the importance of energy separation between the batches while they are slipping (Figure 3.1.15) (Figure 3.1.16). Both bunch trains experience the full effect of both RF systems. At sufficient frequency

separation, the extra frequency excitation averages to zero in a small fraction of a synchrotron oscillation period. At some energy separation, the phase motion of the two batches will be practically independent. For example, if the buckets overlap 50% in energy, the single particle motion is chaotic everywhere within the buckets. Tangential buckets define a lower limit for stable motion, but the simulations show rapid emittance growth. Emittance growth is not entirely absent at much larger separations, but simulations show an acceptably small amount of growth when the buckets are separated by four bucket-heights in energy. This corresponds to a space for a completely empty bucket between the upper and lower buckets.[11]

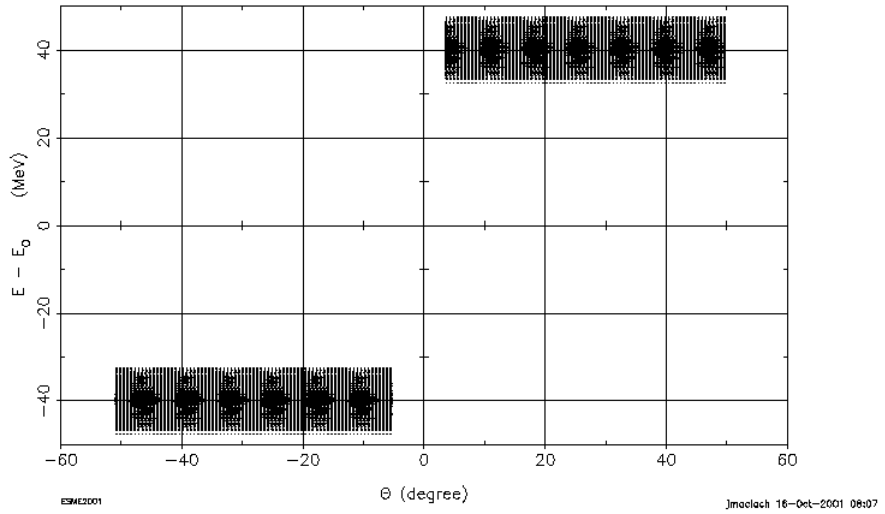

Figure 3.1.14 *Initial condition setup for slip stacking simulation. Two batches of 83 bunches each are injected with offset energies. Q represents the azimuthal position of the beam in the Main Injector.*

Parameter	Symbol	Value	Units
Mean reference orbit radius	R_O	528.30	M
Synchronous Energy	E_s	8938.28	MeV
Transition energy/m_oc^2	γ_T	18.6	
RF peak voltage, each system	V_o	150	kV
RF peak voltage at closest approach	V_o	85	kV
RF harmonic	h	588	
Shunt resistance of 20 RF cavities	R_{shunt}	2	MΩ
Loaded Q of cavities	Q	2000	
Synchrotron tune (150 kV)	ν_s	0.003	
Bucket height	H_B	12.9	MeV
Stationary bucket area	S_B		eV-s
Phase space area occupied by simulated particles	S_b		eV-s

Table 3.1.2 *Accelerator and beam parameters used in slip stacking simulation*[11]

The capture of two bunches into a single bucket will produce gross emittance dilution unless the bunches can be brought much closer together than four bucket-heights on center. It is possible to accelerate the two batches into each other just before capture. Although chaos does develop, it does take time. If the batches are accelerated quickly

enough, there will be a net gain in overall captured emittance. Simulations show a better final emittance when the bunches are captured closer together in energy with an acceleration angle and slightly off angle with respect to RF phase alignment (Figure 3.1.17).

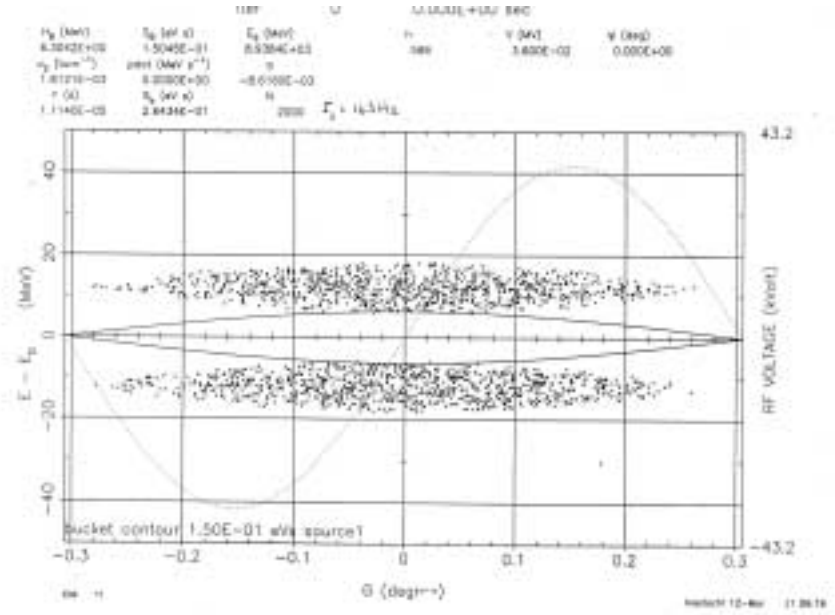

Figure 3.1.15 *This initial condition shows the two batches have already started to slip. Longitudinal emittance of each bunch is 0.1 eV-s.*

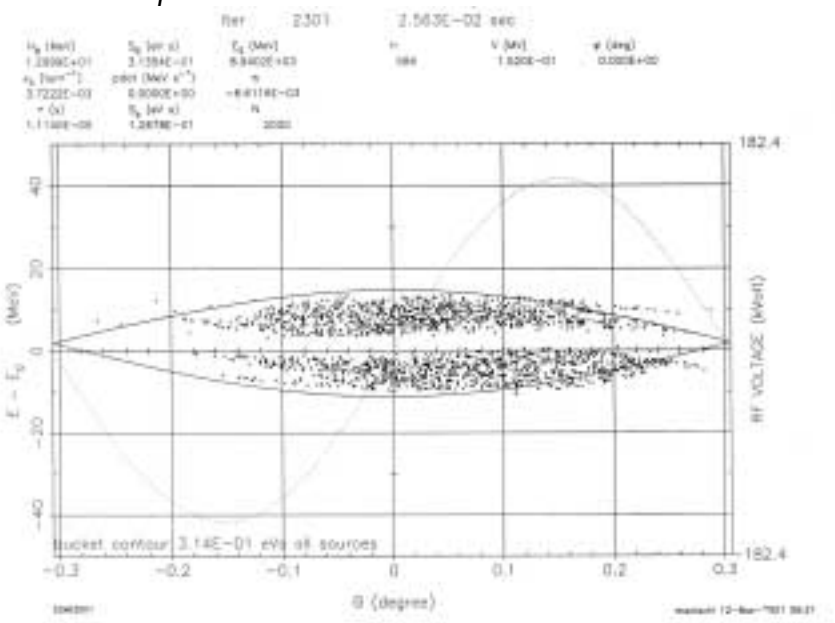

Figure 3.1.16 *This shows the beam profile at capture time. The longitudinal emittance of each bunch has not diluted significantly, and the final emittance is about three times the initial bunch emittance. These results do not include beam loading.*

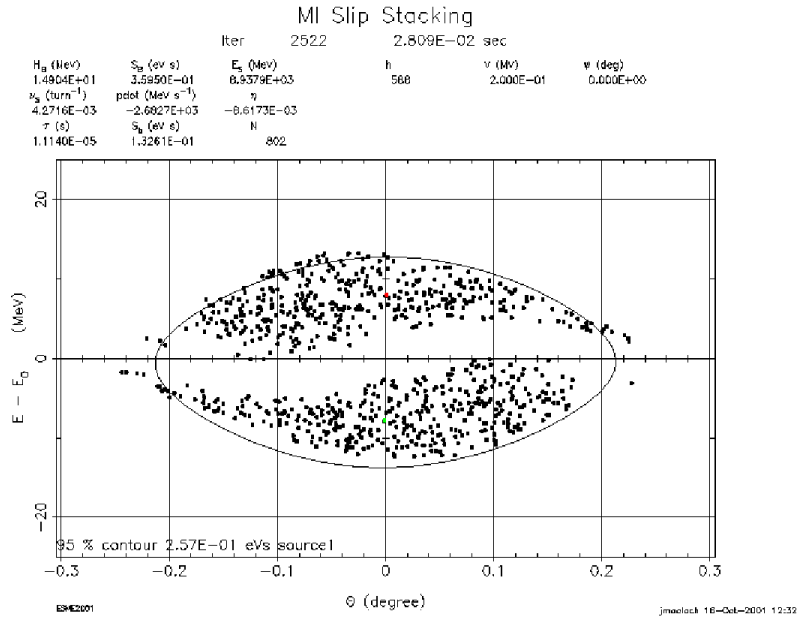

Figure 3.1.17 *Simulation of capture including reducing energy offset before capture. This improves final emittance by about 17%. Does not include effects of beam loading.*

3.1.3.2 Beam Studies

With many of the necessary hardware changes in place, it is possible to test most of the slip stacking process. In order to compare real beam emittance growth with simulations, it is important to eliminate injection mismatches. Because the slip stacking bucket height is so much smaller than the normal stacking bucket height, the Booster must rotate its bunches prior to extraction for proper bucket matching into the Main Injector (Figure 3.1.18, Figure 3.1.19).

Parameter	Symbol	Value	Units
RF voltage, each system	V_o	62.5	kV
Synchrotron frequency	f_s	219	Hz
Frequency separation	Δf	1200	Hz
Bucket area, each system	A_o	0.2	eV*s
Initial longitudinal emittance, 0.7e12 intensity	S_o	~0.1	eV*s

Table 3.1.3 *RF parameters for Main Injector slip stacking tests*

The Booster is also equipped with a paraphasing system for the purpose of eliminating the fundamental RF voltage during multi-turn injection from the Linac. The system is also utilized for bunch rotation just before extraction. The trigger time and paraphase angle are adjusted so that the beam performs a quarter synchrotron rotation prior to extraction. This technique works well at lower Booster intensities. At the present time, instabilities in the Booster are increasing the longitudinal emittance beyond the acceptance of a slip stacking bucket. These instabilities must be remedied in order to perform high intensity slip stacking (Figure 3.1.20).

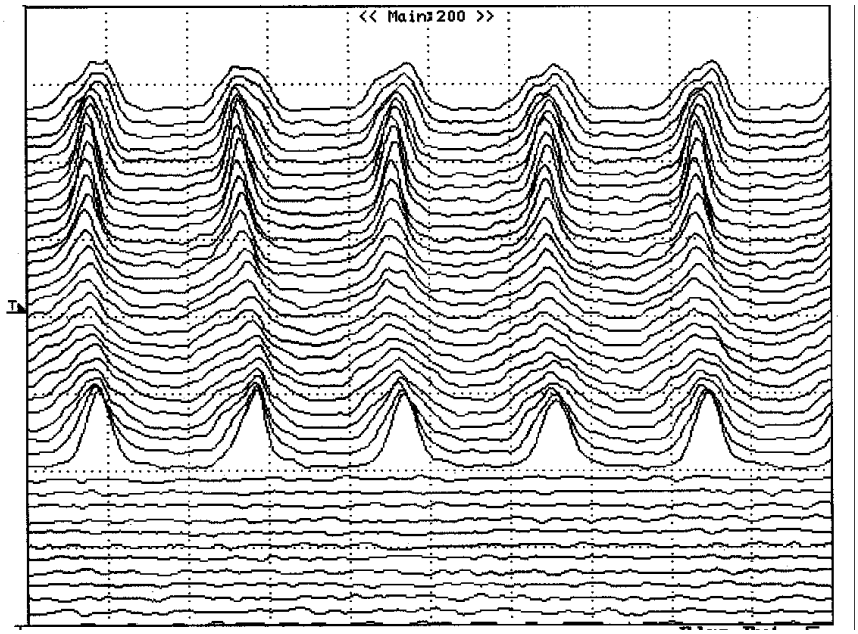

Figure 3.1.18 *Longitudinal pickup response of injection into the Main Injector slip stacking bucket without Booster bunch rotation as a function of time. Successive traces show the signal developing through the injection process (mountain range plot). There is a large quadrupole oscillation present. Intensity is 0.7e12 protons/batch.*

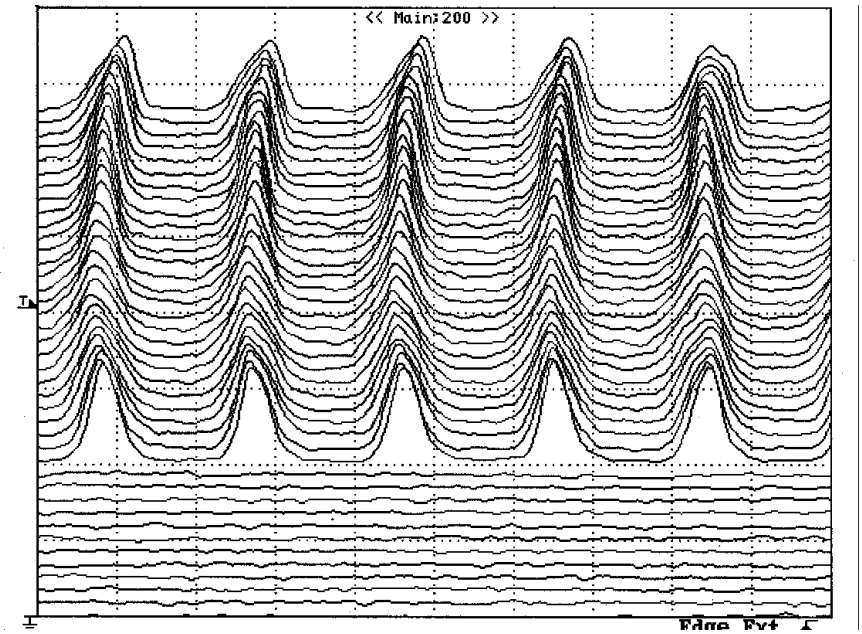

Figure 3.1.19 *Injection into Main Injector slip stacking bucket with bunch rotation in Booster tuned up. Intensity is 0.7e12 protons/batch.*

Once bunch rotation is tuned up in the Booster, the injection parameters for the first batch are tuned in the Main Injector. For this tuning, only the RF station that is synchronous with the first batch is enabled. There is a significant amount of RF leakage through all of the stations even when their drives are disabled, a mountain range plot

shows the effect of the offset frequency leakage (Figure 3.1.21). To tune the injection parameters, all stations are set to the same frequency, making it easier to diagnose injection mismatch. By enabling a second batch synchronous RF station, one can test the bucket separation effects on beam emittance without the effect of beam loading (Figure 3.1.22) (Figure 3.1.23) (Figure 3.1.24).

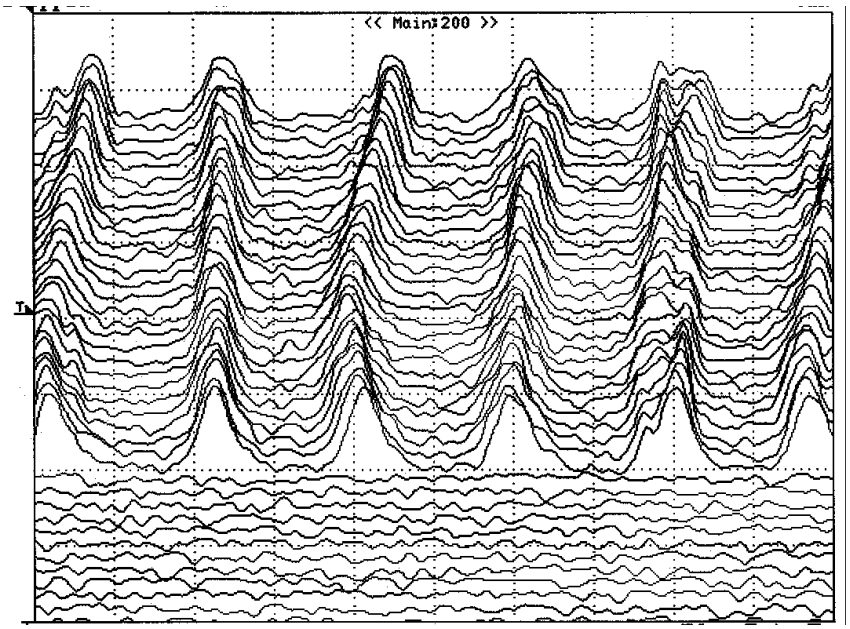

Figure 3.1.20 *Injection into Main Injector slip stacking bucket with bunch rotation in Booster tuned up. Intensity is 1.5e12 protons/batch. Problems with bunch energy errors are already evident.*

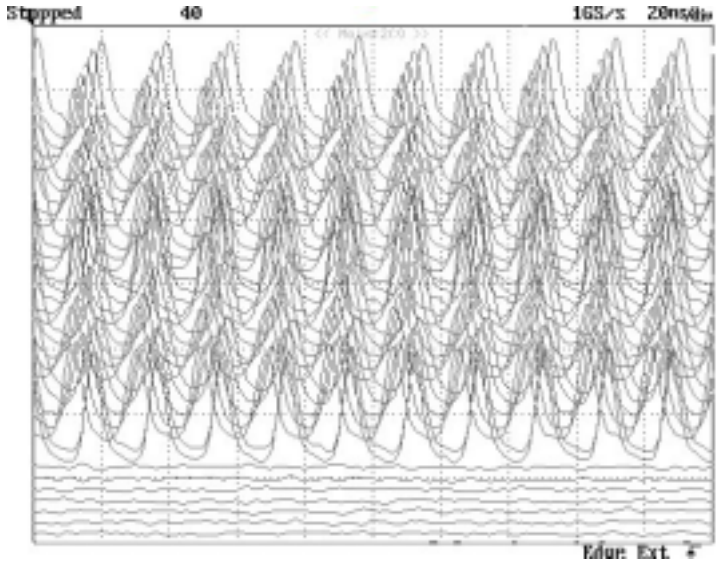

Figure 3.1.21 *Injection into Main Injector slip stacking bucket with offset frequency output from LLRF but offset stations gated off. The effect of RF leakage is apparent.*

Tuning the second batch is a bit more complicated than tuning the first batch. The bucket offset and phase offset are dictated by the integral of the frequency offset curve

for the second batch. Both offset frequency ramps are programmed to follow the second batch ramp, and only the second batch RF station is enabled. The second batch is injected at the time in the cycle when it would normally be injected, and the injection phase and bucket offset are tuned for minimal injection mismatch and batch separation respectively.

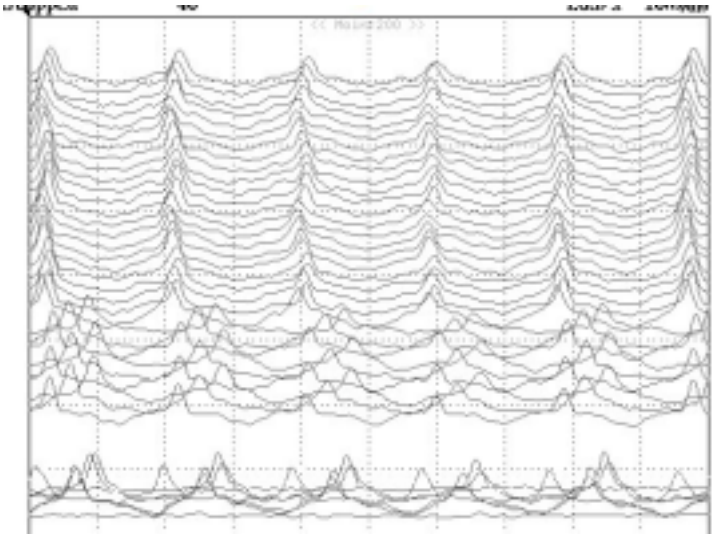

Figure 3.1.22 *Emittance preservation of first batch with 600Hz frequency separation. This separation is not enough to keep the buckets from overlapping.*

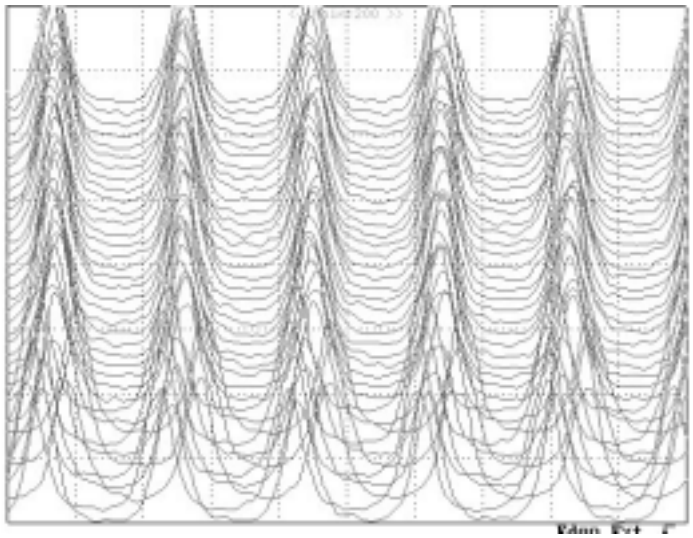

Figure 3.1.23 *Emittance preservation of first batch with 1200Hz frequency separation. The energy separation between slipping buckets is slightly greater than four times the RF bucket height.*

After the second batch injection is tuned, it is straight-forward to test the entire low energy process. In the first attempt with the Main Injector, the frequencies were kept at a constant separation during the slipping process. Some time slightly before capture, the frequencies were ramped to a smaller separation to reduce the total emittance occupied by the two batches prior to capture. At capture time, the frequency offsets were

set to zero, and all of the RF cavities were enabled (Figure 3.1.25) (Figure 3.1.*26*) (Figure 3.1.*27*) (Figure 3.1.28) (Figure 3.1.29).

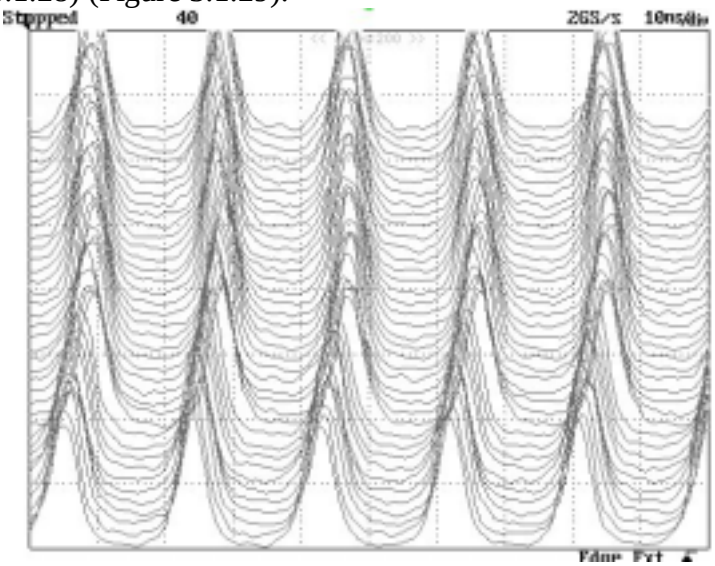

Figure 3.1.24 *Emittance preservation of first batch with 1800Hz frequency separation. This separation is well above having a whole bucket separation in energy between the slipping batches, although not much improvement over 1200Hz separation.*

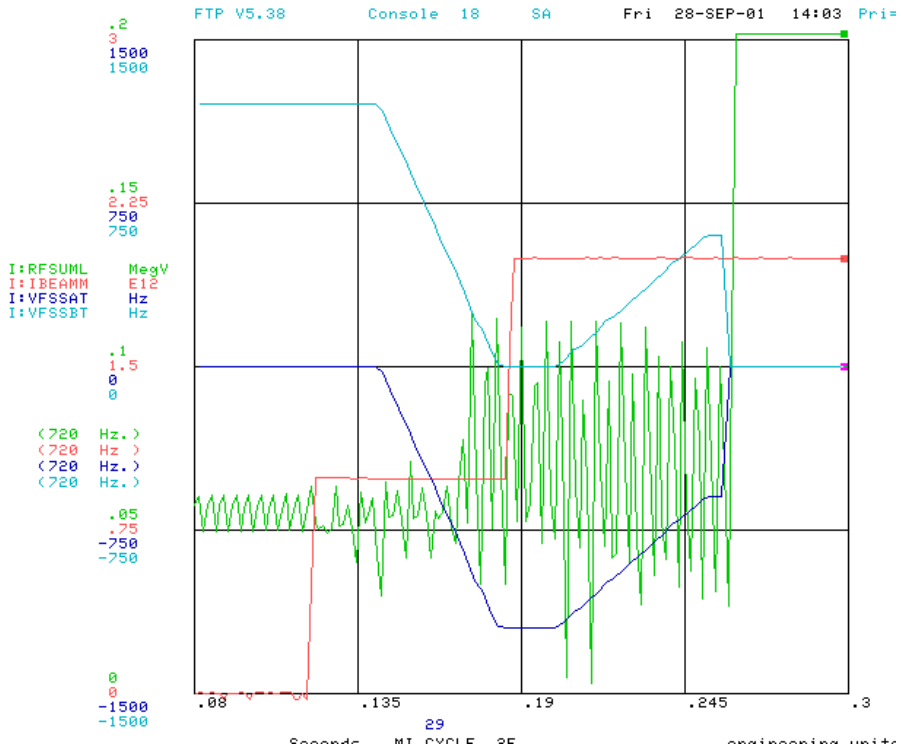

Figure 3.1.25 *Plot of Main Injector slip stacking cycle. I:RFSUML is the total RF voltage seen by the beam. Notice the large modulation when the 'B' RF is activated. I:IBEAMM is the total beam intensity in the Main Injector. I:VFSSAT and I:VFSSBT are the offset frequencies of the 'A' RF and 'B' RF respectively.*

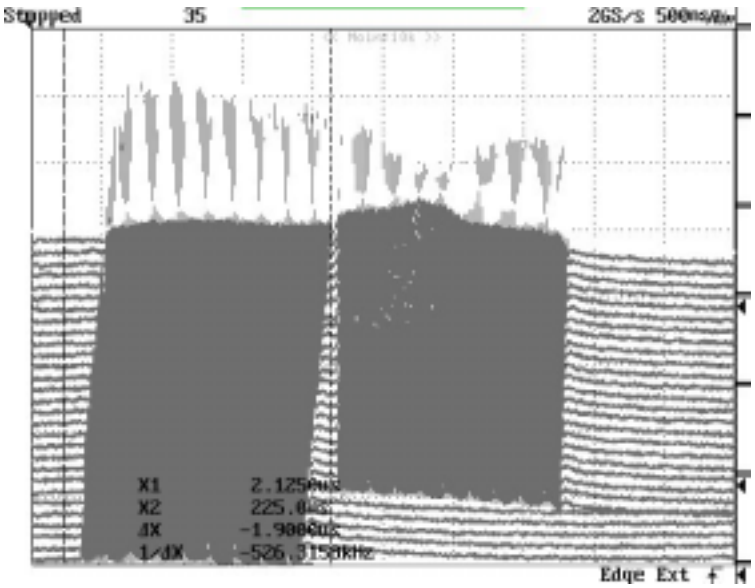

Figure 3.1.*26 Mountain range plot showing Main Injector slip stacking just after the second batch is injected*

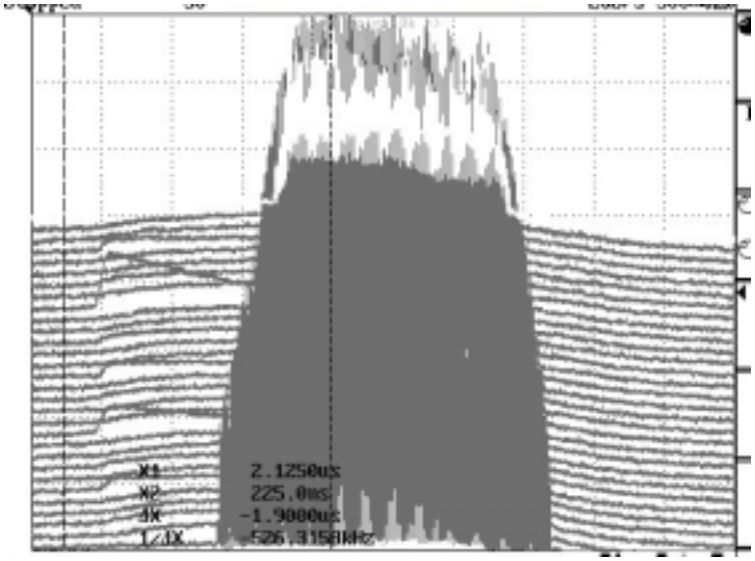

Figure 3.1.*27 Mountain range plot showing Main Injector slip stacking when the two batches are captured into a single batch*

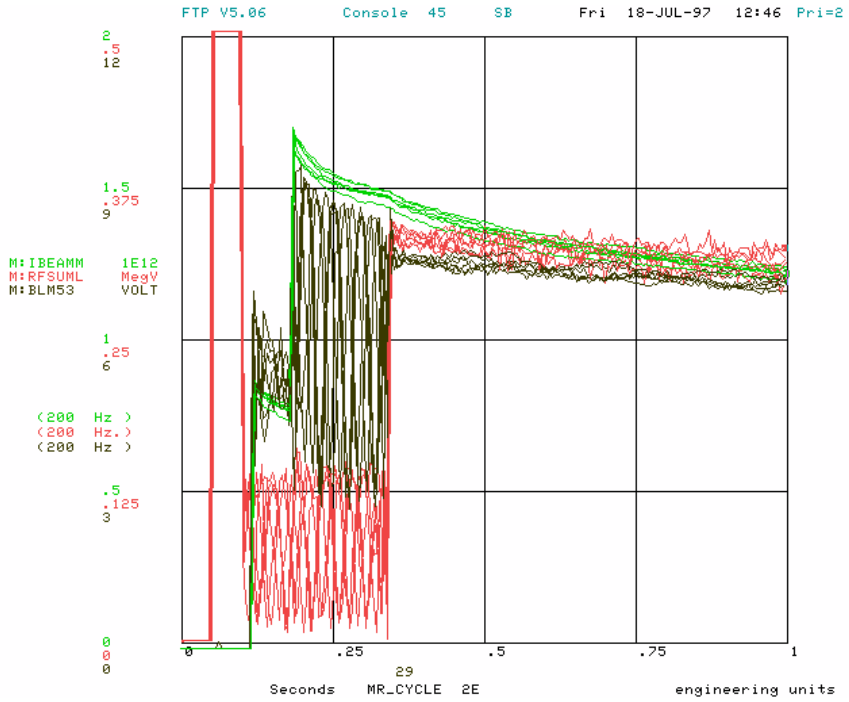

Figure 3.1.28 *Plot of main ring slip stacking cycle. M:RFSUML is the total RF voltage seen by the beam. M:IBEAMM is the total beam intensity in the main ring. M:BLM53 represents the 53 MHz component of beam current. This gives a measure of the amount of beam still left in the bucket.*

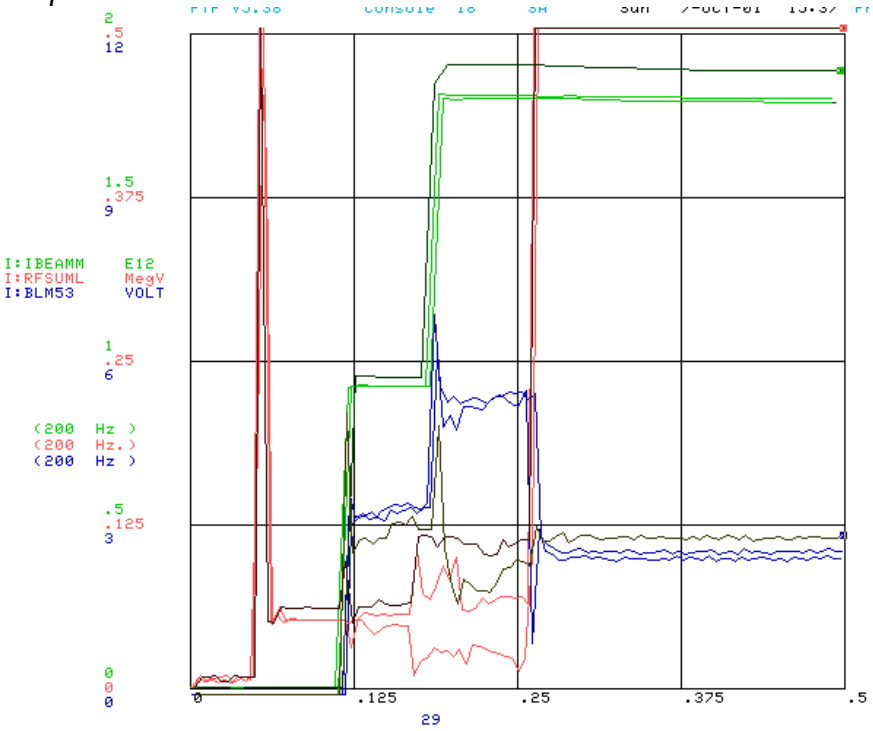

Figure 3.1.29 *Plot of Main Injector slip stacking cycle.*

3.1.4 Beam Loading

3.1.4.1 Beam Loading Theory

The greatest limitation to practical slip staking intensities is beam loading in the RF cavities. There are many aspects of beam loading that must be addressed in order to satisfactorily accelerate high intensity beam with low voltages. First, the RF cavities must provide enough average power to contain the beam in the bucket. This not only includes maintaining the proper bucket height, it also includes maintaining enough extra voltage for focusing in the presence of beam loading. In the absence of any feedback on the beam or cavity, this aspect is referred to as a Robinson criterion.[12] In general, this criterion states that the total power delivered to the cavity by the beam current must be about equal to or less than the power delivered to the cavity by the power amplifiers.

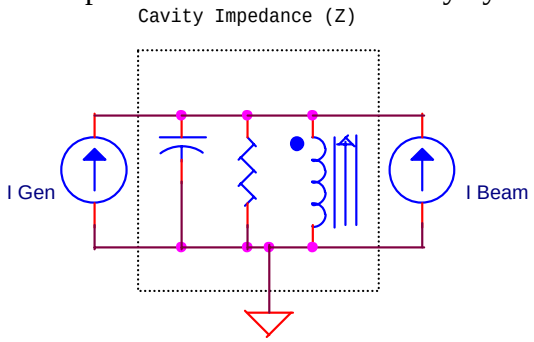

Figure 3.1.30 *Cavity block diagram. Total current (It) is IGen + IBeam.*

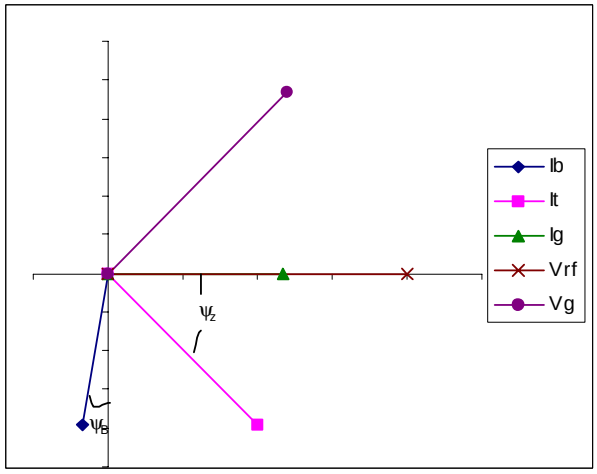

Figure 3.1.31 Vector sum of IGen and IBeam with cavity detuned such that IGen and Vrf are in phase. ψ_z is the detuning angle

To understand this, one can view the cavity as a resonant circuit that is driven by two current sources (Figure 3.1.30).[12] The two current sources represent the drive from the power amplifier (Ig) and the beam itself (Ib). These sources are out of phase by 90° for a stationary bucket, and they are out of phase by 90° plus the synchronous phase angle for an accelerating bucket. For optimum power efficiency, the amplifiers should see a purely resistive load. Thus, the resonant frequency of the cavity is detuned until the

total voltage is in phase with the current generated by the power amplifier (*Figure 3.1.31*).

A Robinson instability occurs when the phase of the generator voltage (Vg), which is defined as the voltage in the cavity without beam, is 180° out of phase with the beam current (Figure 3.1.32). At this point, beam with a small synchronous phase error will not receive the necessary focusing power needed to bring it back into the bucket. The exact definition of the threshold for this instability is given in Eq. (3.1.1), where ψ_L is the load angle between Vrf and Ig. The condition for $\sin(2\psi_L)>0$ is discussed later in the introduction.

$$0 < \sin(2\psi_Z) < 2Y\cos(\psi_B)$$

$$Y = \frac{I_B}{\mathrm{Re}(I_T)} \qquad (3.1.1)$$

The threshold defined above assumes that no other feedback loops act on the beam and cavity voltage. Usually, feedback loops will control the load angle, the synchronous phase, and the cavity voltage amplitude. Instabilities develop in these systems at large beam intensities because the different loops begin to couple.[13] For example, a change in synchronous phase for an intense beam will also cause a change in the load angle, and a change in the voltage amplitude. These problems have been analyzed, and the conditions for stability are more complex. However, in most cases, the loops still remain stable as long as the power generated in the cavity by the beam does not exceed the power generated by the power amplifier.[13]

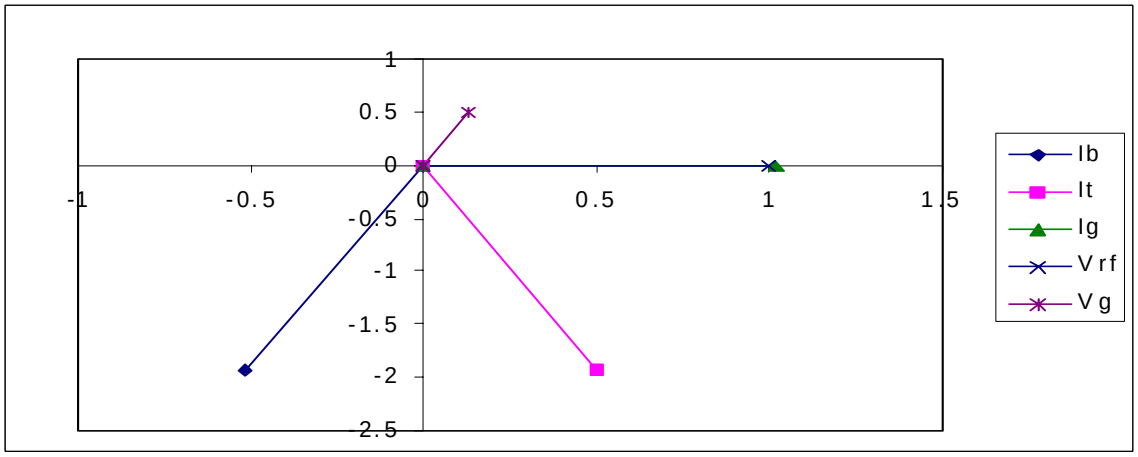

Figure 3.1.32 *Vector diagram of a cavity at the limit of the Robinson instability. Vg and Ib are at opposite phases.*

Of course situations arise in which the amount of beam in an accelerator is far beyond the stability limits explained above. It may not be possible for the power amplifiers to provide enough voltage to maintain the stability, and it may not be desirable to have such a large bucket size.

Another aspect of beam loading is referred to as transient beam loading. As a bunch of beam first passes through the RF cavity, it loads the cavity down by an amount proportional to the intensity of the bunch. The next bunch through sees a smaller RF voltage than the first bunch, and the last bunch of the batch sees the smallest voltage of

all. Such a distribution in amplitudes could lead to large differences in synchronous phase and cause emittance blowup. For slip stacking, the transient voltage in the cavity varies by as much as 40 kV.[14] This is 40% of the total voltage on a batch and will certainly cause adverse effects, as the simulations will show. Also, during slip stacking, as the two batches of beam are slipping past each other, the fundamental component of the beam current is 100% AM modulated with the difference in frequencies. This implies that there are components of transient beam loading within the fundamental resonance of the cavity.

3.1.4.2 **Beam Loading Simulation**

Simulations reveal the adverse affects of beam loading in the slip stacking process. The simulations use the cavity parameters such as Q, shunt impedance, and resonant frequency to generate the appropriate wake fields generated by the beam. (Figure 3.1.33) (Figure 3.1.34) (Figure 3.1.35) (Figure 3.1.36)

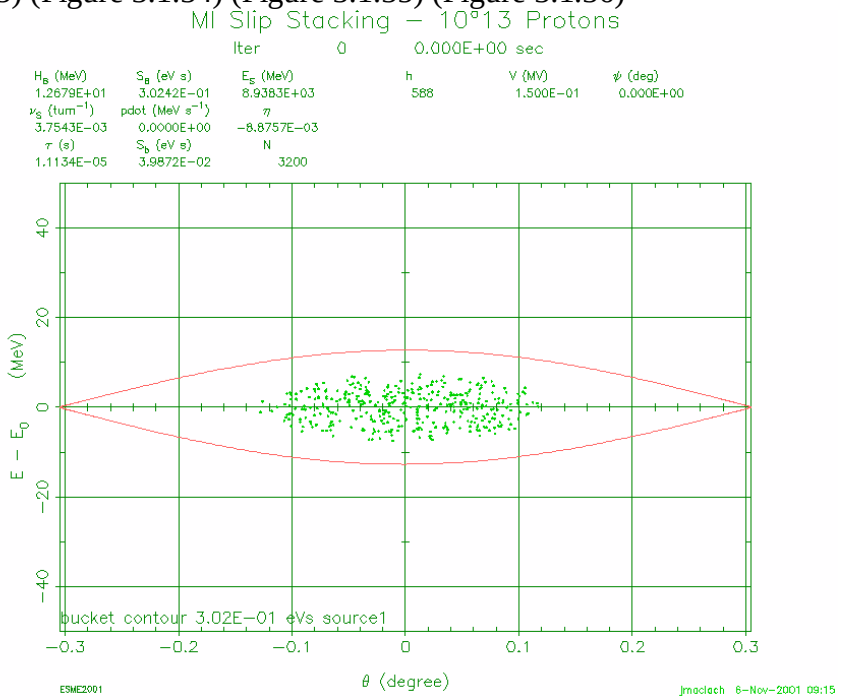

Figure 3.1.33 *Initial condition setup for a single bunch in a batch for slip stacking including beam loading. Initial longitudinal emittance is 0.1 eV-s.*

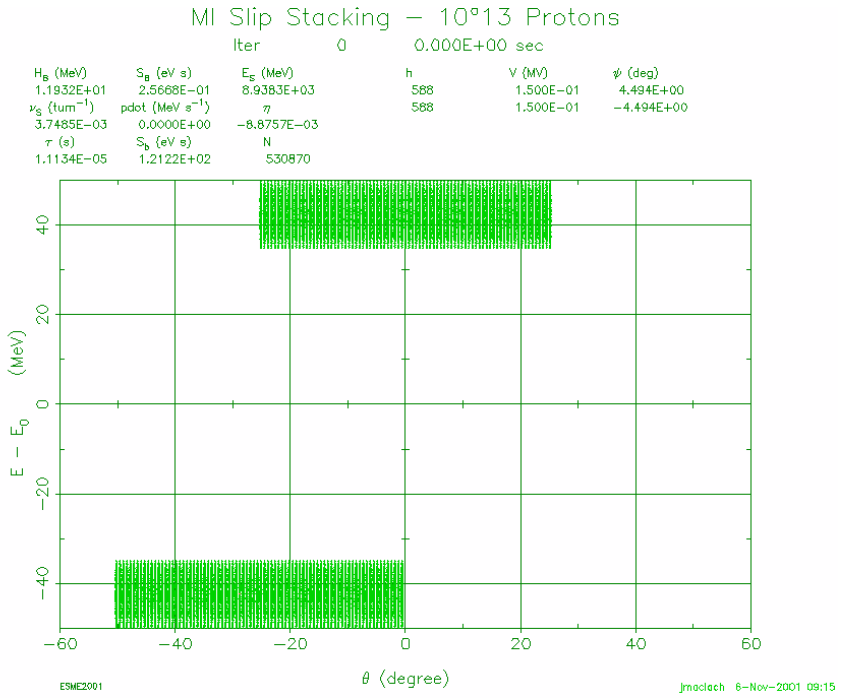

Figure 3.1.34 *Initial condition setup for both batches of beam for slip stacking including beam loading. Intensity is 5e12 protons/batch. θ represents azimuthal position around the Main Injector.*

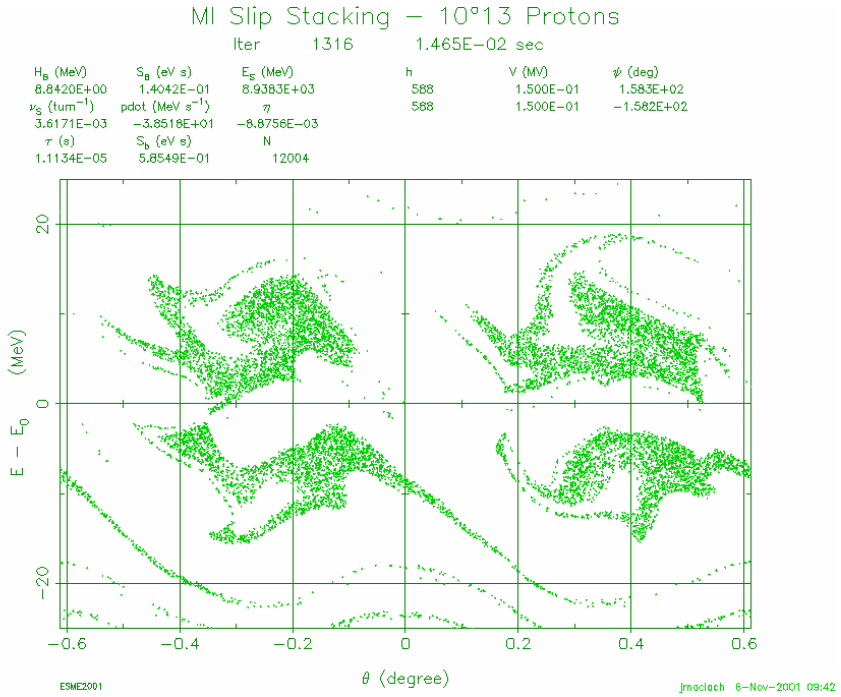

Figure 3.1.35 *Final profile for captured beam for two bunches in a batch for slip stacking including beam loading with no compensation.*

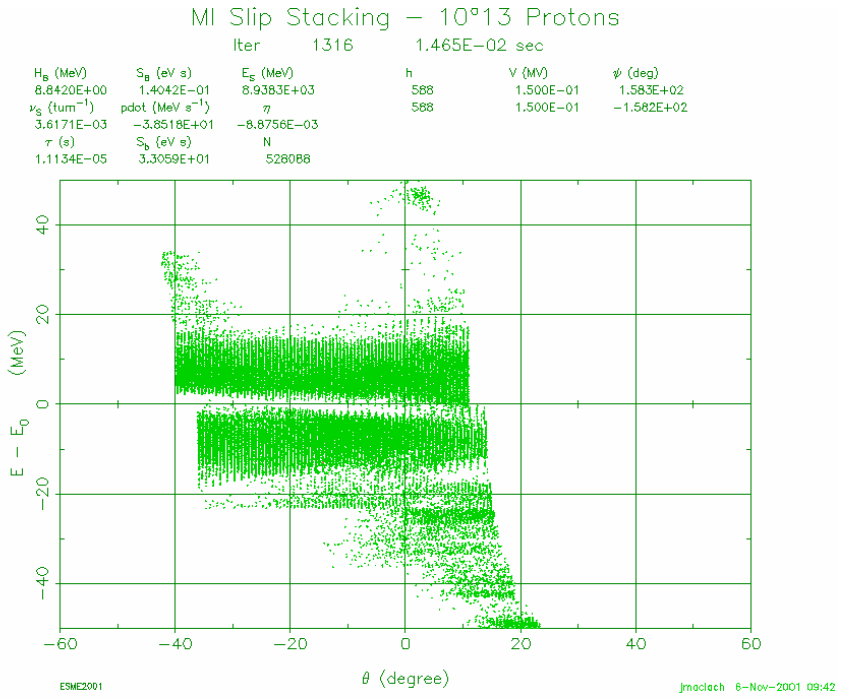

Figure 3.1.36 *Final profile for captured beam for both batches for slip stacking including beam loading with no compensation.*

3.1.5 Beam Loading Compensation

In order to overcome the limitations on slip stacking imposed by beam loading, some method of reducing the effect beam loading must be applied to the cavities. One possibility for reducing the effect of the beam in the cavity is by decreasing the cavity impedance. This will also require more power from the RF power amplifier, negating the benefit of the low acceleration power required. Another possibility is to virtually reduce the cavity impedance through feedback. By applying the beam generated voltage to the input of the power amplifiers, the cavity impedance seen by the beam is reduced without requiring more power from the amplifiers. However, implementation of a feedback system requires careful design to ensure there is enough stability margin in the loop itself.

3.1.5.1 Beam Loading Compensation Theory

One of the most common methods of beam loading compensation is direct RF feedback. In this method, a signal derived from the actual cavity voltage is fed back into the cavity drive (Figure 3.1.37). This reduces the effective impedance seen by the beam and the fanout drive as show in Equation (3.1.2). For stability purposes, the beam reacts dynamically as if it was under the influence of a much higher voltage. This new, effective voltage is proportionally greater than the actual drive voltage by the open loop gain of the feedback loop (Figure 3.1.38) (Figure 3.1.39). If the feedback loop has an ideal response with no delay, the effective shunt impedance and Q of the cavity are reduced by the open loop gain.

$$Z^* = \frac{Z}{1 + ZGS} \qquad (3.1.2)$$

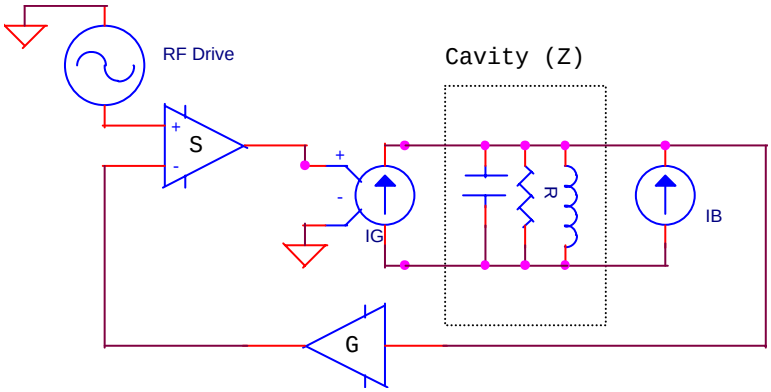

Figure 3.1.37 *Block diagram of direct RF feedback. The feedback gain is G, and the transconductance is S.*

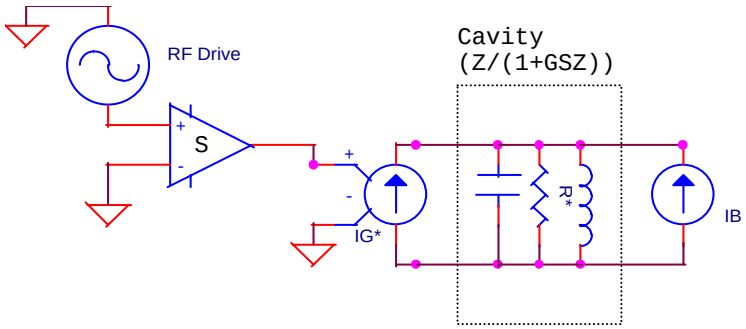

Figure 3.1.38 *Block diagram of equivalent circuit as seen by the beam and the RF drive.*[14]

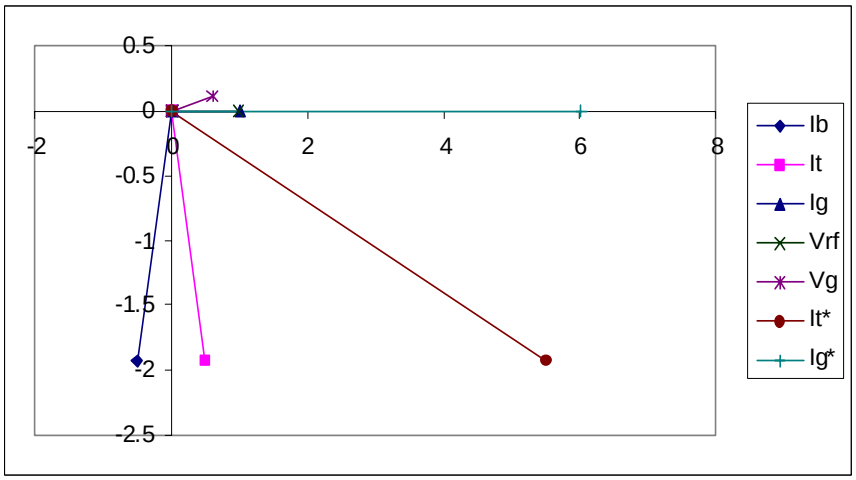

Figure 3.1.39 *Vector diagram of cavity with feedback compensation. The loop gain (GS) is 20dB. Ig* and It* are the virtual currents seen in the equivalent circuit.*

Of course it is impossible to physically construct a zero delay system, especially when the summing point and output are separated by 100 feet of cable. All physical feedback systems have stability limits on the amount of open loop gain. The Nyquist stability criterion states that a system will be stable as long as the complex mapping of its open loop response does not encircle the (1,0) point. For most of the feedback systems in

the Main Injector, this criterion is over specified. The open loop response of the system is not allowed to have the real part of its response exceed one. This limits the amount of gain that the direct RF feedback system can achieve without driving the cavity unstable as shown in Equation (3.1.3).

$$G\max = \frac{\pi Q}{2\omega_r \tau}$$

$$R\min = \frac{R}{G\max} \qquad (3.1.3)$$

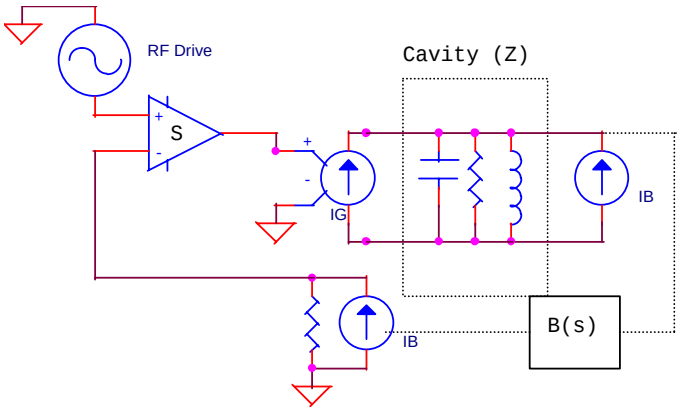

Figure 3.1.40 *Feedforward block diagram where S is the transconductance of the amplifier and B(s) is the beam response*

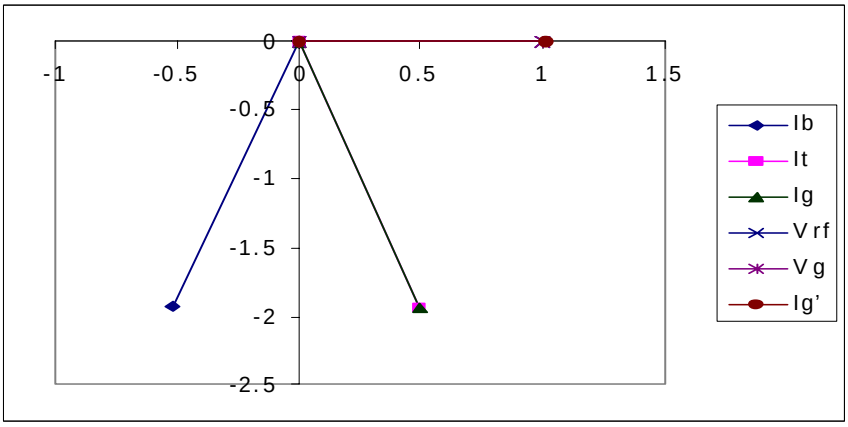

Figure 3.1.41 *Vector diagram of a cavity with ideal feedforward compensation. The generator current and total current are always the same. This puts the generator voltage always in phase with the RF voltage and no Robinson instability can occur.*

Another method of beam loading compensation is called feedforward compensation. In this method, a low impedance beam current detector creates the signal that is applied to the RF drive. The amplification of the signal from the detector to the cavity is set so that the power amplifier in the cavity produces a current that exactly opposes the beam current (Figure 3.1.40). If the match is perfect, the cavity voltage becomes completely decoupled from the beam current (Figure 3.1.41).[15] Because matching is so critical in this system, it is essential that the signal corresponding to a

particular bunch from the detector be applied to the same bunch as it comes around in the cavity. In a highly relativistic system, it is impossible to outrun the beam with signal propagation. Therefore, the signal must be fed back on the bunch after approximately one revolution.

In the feedforward system, the amount of compensation achieved is not limited by Nyquist stability limits like the direct RF feedback system. The limits of the feedforward system are determined by the ability to match the beam current with the power amplifier. Many factors can affect this matching, the worst being changes in the gain of the power amplifier chain and the non-linearity of the power tube transconductance. This greatly limits the robustness of the feedforward system and makes it more difficult to engineer than the direct RF feedback system.[16] Also, there is still a weak feedback loop involving the beam response to changes in the cavity voltage. The beam could be driven unstable longitudinally without proper design of the feedforward response.

3.1.5.2 Beam Loading Compensation Simulation

Some simulations have been performed which describe the effect of beam loading compensation on slip stacking. These simulations show the effect of an ideal direct RF feedback system. They show how the slip stacking would respond to a cavity with reduced shunt impedance and Q, which implies a zero delay system (Figure 3.1.42) (Figure 3.1.*43*) (Figure 3.1.44) (Figure 3.1.45). Some work still needs to be done in order to simulate more physical systems.

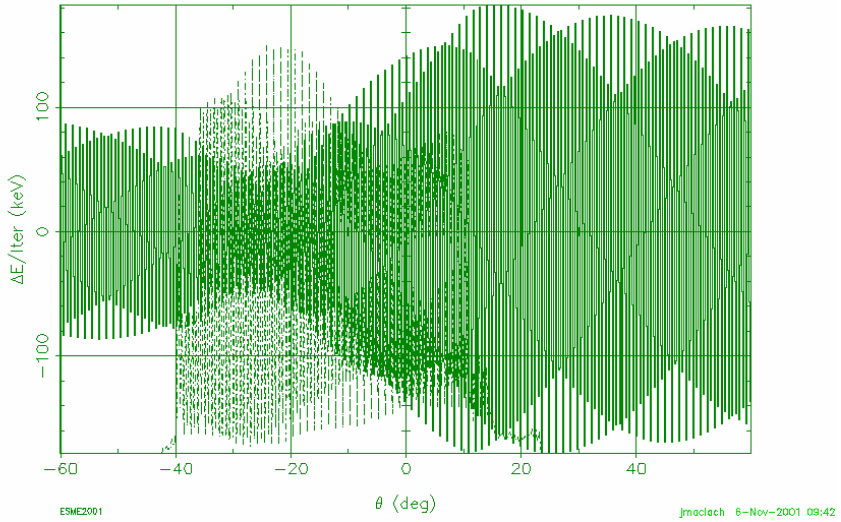

Figure 3.1.42 *Inverse FFT of beam current and cavity voltage in slip stacking simulation with no beam loading compensation. Intensity is 10^{13} protons. Time in cycle is close to capture time.*

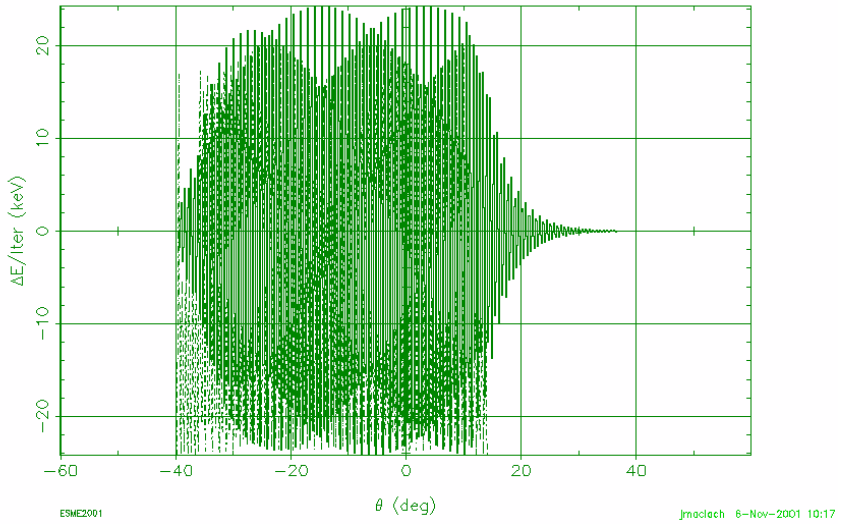

Figure 3.1.*43 Inverse FFT of beam current and cavity voltage in slip stacking simulation with ideal direct RF feedback with 40dB of loop gain. Intensity is 10^{13} protons. Time in cycle is close to capture time.*

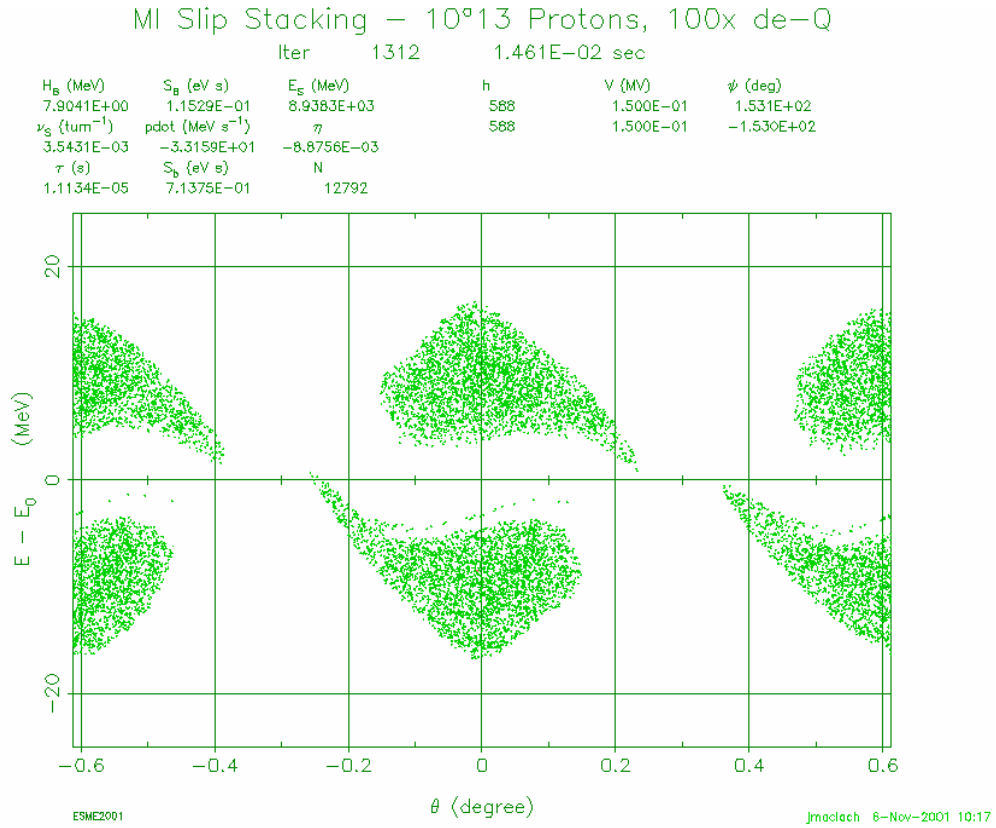

Figure 3.1.44 *Final profile for captured beam for two bunches in a batch for slip stacking including an ideal direct RF feedback system with 40dB of loop gain. Intensity is 10^{13} protons*

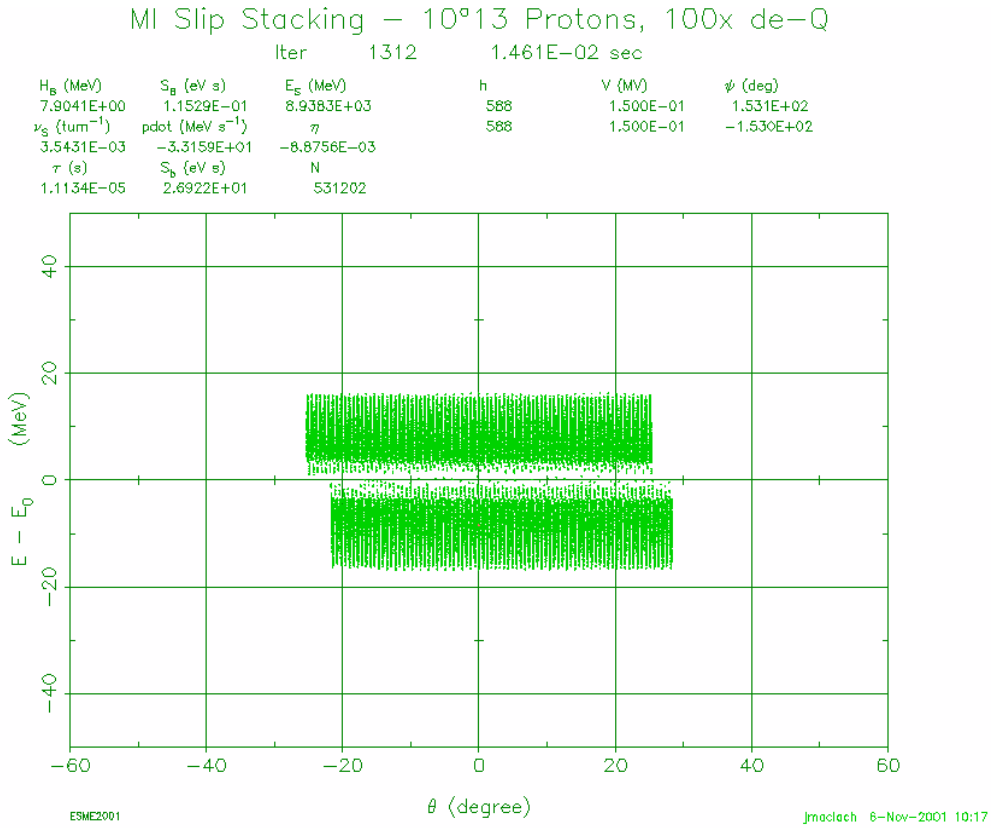

Figure 3.1.45 *Resulting profile for captured beam for both batches for slip stacking including beam loading with an ideal direct RF feedback system with 40dB of loop gain. Intensity is 10^{13} protons*

3.1.5.3 **Direct RF Feedback**

The Main Injector is equipped with a direct RF feedback system (Figure 3.1.46).[8] Each cavity has an independent feedback system. The system consists of a module that converts the signal from the cavity gap monitor to baseband (Figure 3.1.47). The signal is low-pass filtered, up-converted, and combined with the fundamental amplifier drive signal. It is important that the phase of the open loop response remain 180° at the fundamental frequency for maximum stability margin. Because the system works through the entire Main Injector ramp, the feedback system must maintain the proper phase intercept as the fundamental frequency changes. There is enough fixed delay in the loop to cause a 60° error in the phase intercept over the frequency ramp without compensation. The system maintains the proper phase by using different delays for the up-convert and down-convert RF references in the feedback module. The up-convert reference delay is matched to the LLRF fanout delay to the cavity, and the down-convert delay is matched to the cavity gap signal from the tunnel. With the proper delays on the references, the feedback module will adjust its delay to maintain the proper phase intercept for the system.

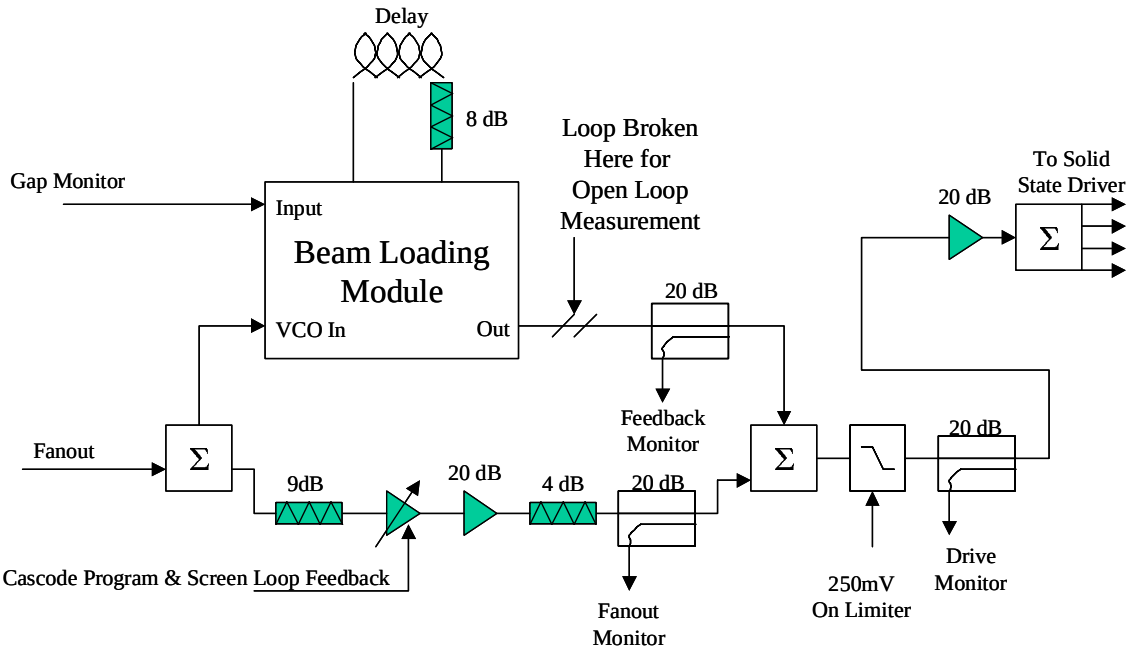

Figure 3.1.46 *Direct RF feedback system in the Main Injector*

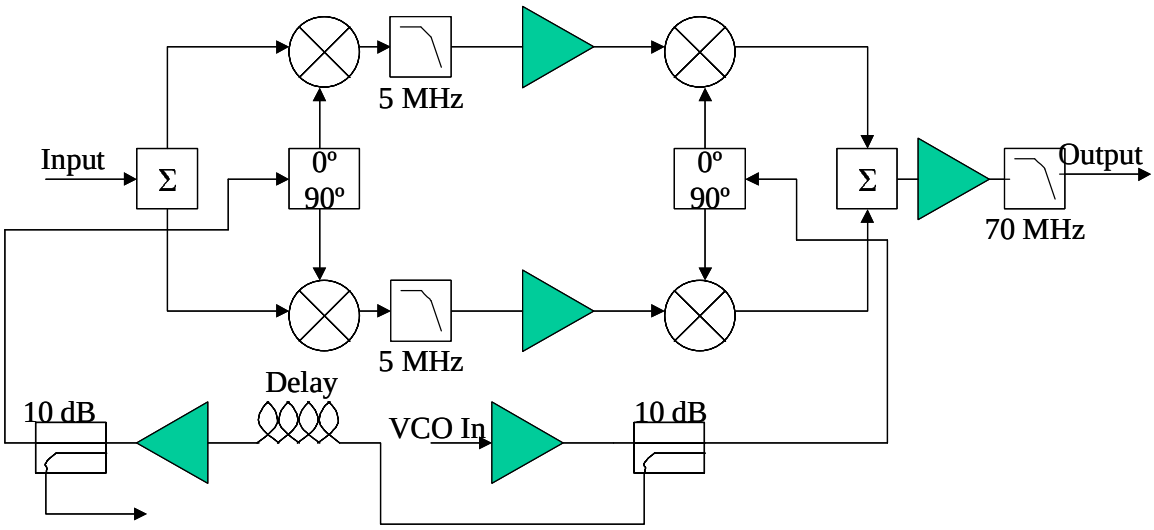

Figure 3.1.47 *Block diagram of the beam loading module. The superheterodyne structure is designed to track the phase response with the changing VCO frequency. The downconvert reference is synchronized with the cavity gap signal, and the upconvert reference in synchronized with the fanout.*

Maintaining proper phase intercept improves the stability margin, but there is still a stability limit on the allowable open loop gain on the system. The current Main Injector system will only allow an open loop gain of about 26 dB with a reasonable gain margin (Figure 3.1.48) (Figure 3.1.49). The feedback module has a fixed gain profile, in frequency, over many revolution harmonics, so the cavity response dictates the open loop bandwidth. Because of the high Q of the cavity, the open loop gain of the system rolls

off quickly. Thus, the system performs insignificant beam loading compensation at any revolution harmonics other than the fundamental.

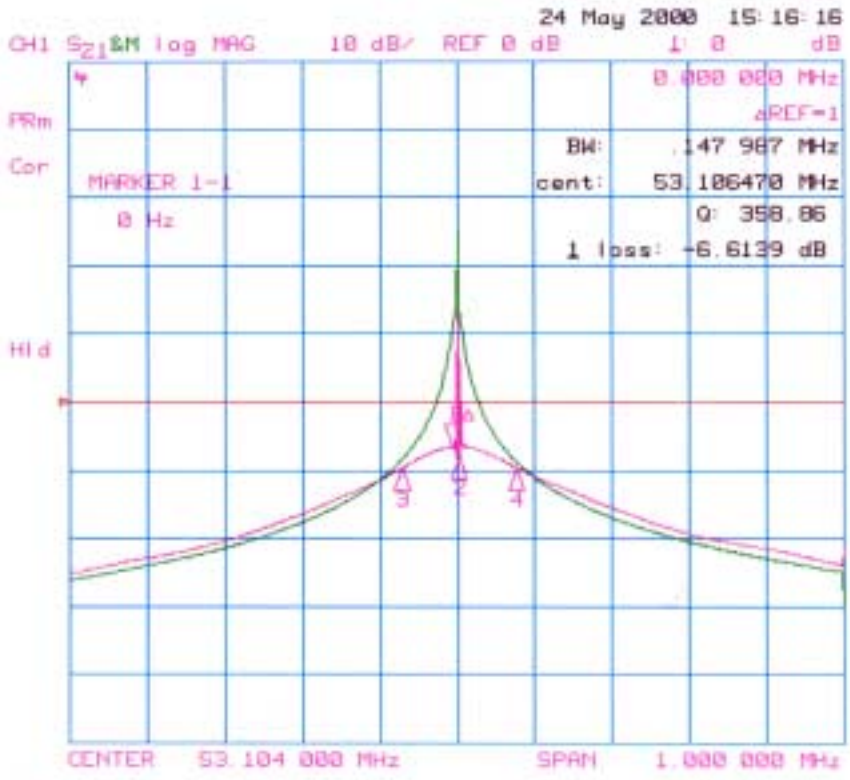

Figure 3.1.48 *Cavity response with 20dB of direct RF feedback beam loading compensation (pink) and without (green).*

In order to provide beam loading compensation at the revolution harmonics, the feedback module must be modified. First, to ensure the proper open loop phase intercept for multiple revolution harmonics, the system must have a delay equal to some multiple of the revolution period. Second, the bandwidth of the filter should not be dictated by the cavity, since this is not optimal for stability. The bandwidth of the system could be reduced to the point of just containing the frequency difference between the two batches in a slip stacking cycle. Of course the filter would necessarily have the same shape around the fundamental frequency as well as multiple revolution lines. This implies some kind of digital filter sampling at the fundamental frequency with taps at multiples of the revolution frequency.[17]

A digital filter for beam loading compensation is already being designed. The current design uses a DSP with a highly parallel architecture, clocked at a multiple of the fundamental frequency (Figure 3.1.50). The down-converted signal from the cavity gap is digitized and stored in FIFO memory blocks. Data from the memory blocks are burst into the DSP, and the DSP performs the filtering calculations. Output data from the DSP is burst into another set of FIFO memory blocks which drive a DAC. The FIFO memory blocks maintain the system delay at one revolution period. The output of the DAC is up-converted and combined with the cavity fanout drive. Calculations done for an IIR filter in the DSP show that open loop gains on the order of 40dB are achievable (Figure 3.1.51) (Figure 3.1.52). To maximize the gain margin for the revolution harmonics, the signals

for the revolution harmonics will follow a different path than the fundamental, so that they can receive a 90° phase shift. This is to compensate for the cavity response, which is reactive at the revolution harmonics.

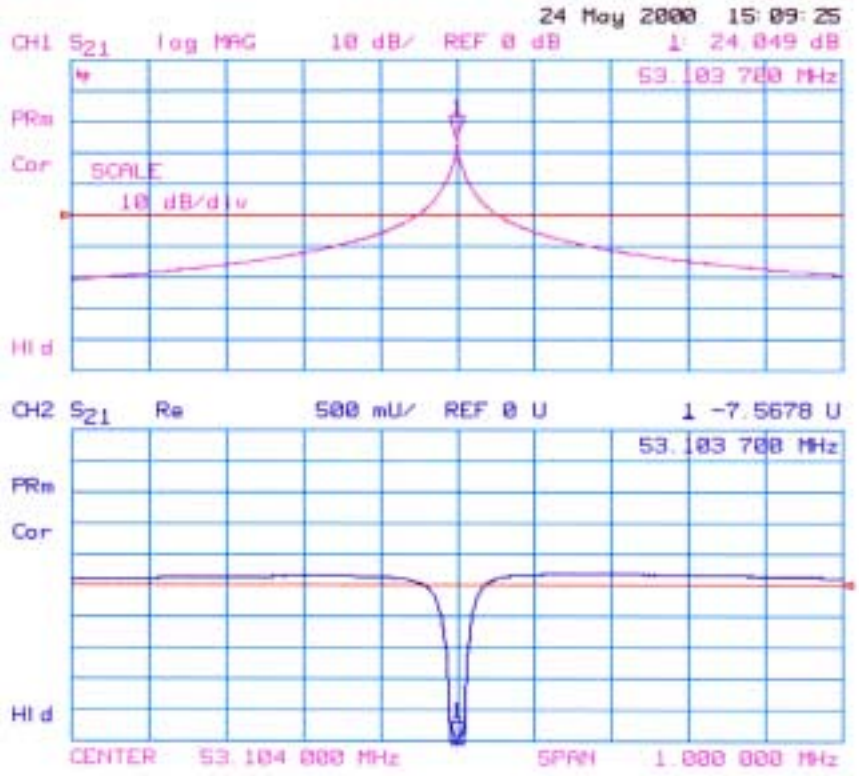

Figure 3.1.49 *Cavity response with 20dB of direct RF feedback beam loading compensation. Notice that the real part of the response is well below +1.*

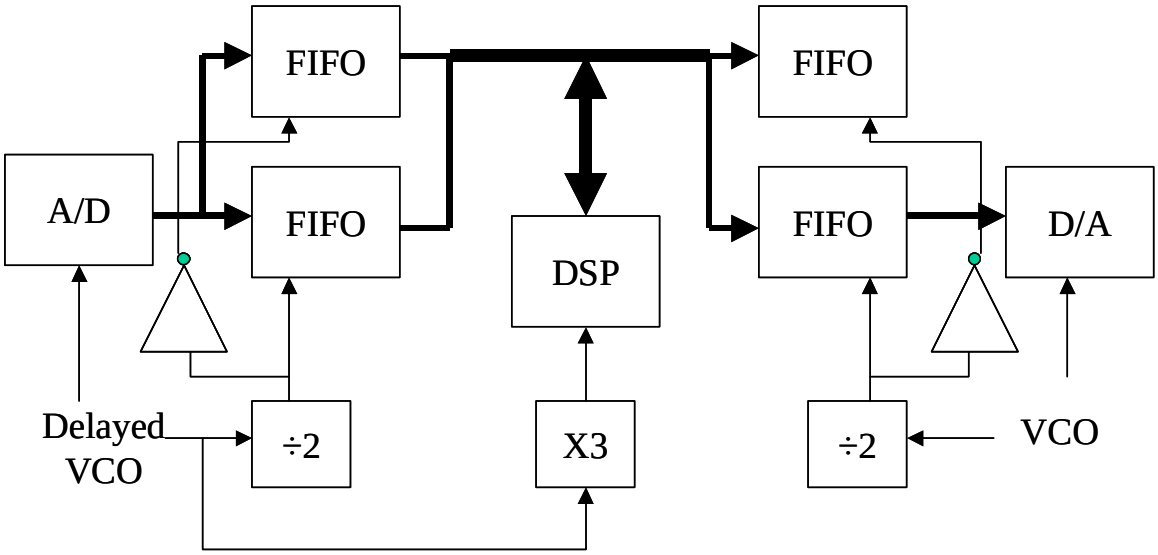

Figure 3.1.50 *Block diagram of digital direct RF feedback system. The DSP calculates the filter response and bursts data to and from the FIFOs. The digitizer and DAC are clocked with references at differing delays to track the changing revolution period of the Main Injector.*

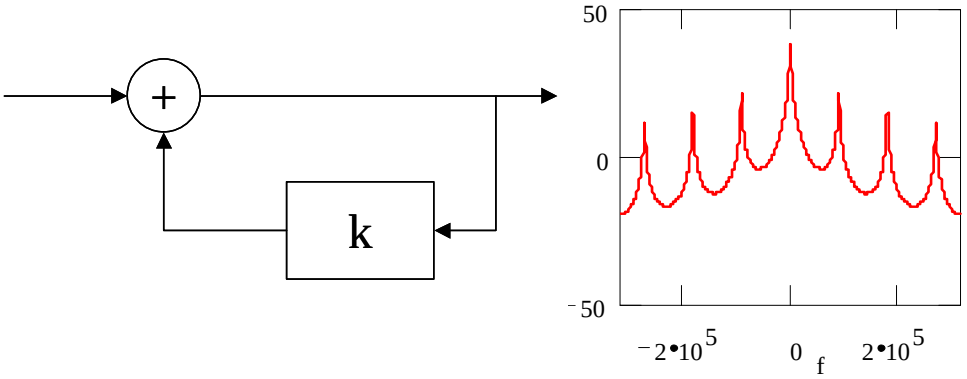

Figure 3.1.51 *Program for IIR comb filter in the DSP and simulated open loop response of system through cavity when* $k = 1 - 2^4$

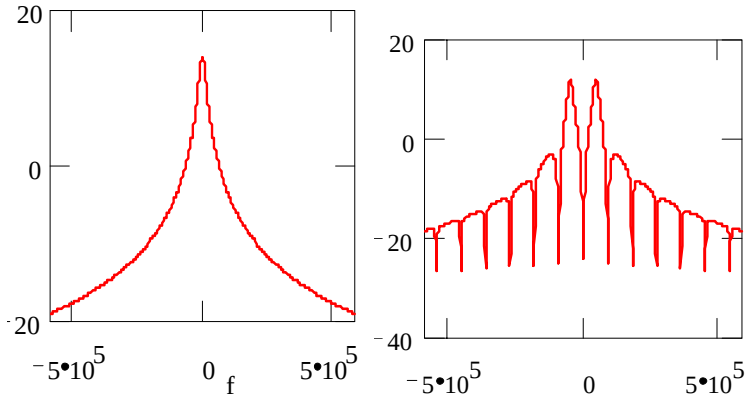

Figure 3.1.52 *Sample of cavity response without beamloading compensation and sample of cavity response with digital direct RF feedback.*

There are three operating conditions that could stress the RF power limitations of the high level system with beam loading compensation. First, fast changes in the RF fanout drive will cause the feedback system to overdrive the power amplifier. A RF fundamental feedback system forces more current into the cavity when there are transients in the drive. This is how the feedback system makes the impedance and Q of the cavity appear lower to the fanout. Unfortunately, transients that occur at moderately high RF voltage levels will attempt to drive the power amplifiers well beyond there power limits (i.e. transition crossing). To compensate for this, a limiter is placed downstream of the feedback summing junction. Although the limiter does prohibit effective beam loading compensation at transition crossing, the RF voltage is very high at this point in the cycle, minimizing beam loading effects.

The second RF power limitation of the fundamental feedback system is the drive power required at the summing junction. The gain from the fanout drive to the cavity is reduced by the feedback gain. If the loop gain is high enough, high power RF amplifiers would be necessary to drive the low level summing junction of the cavity. This is very costly when multiplied by 18 stations, and it limits the loop gain in the current Main Injector direct RF feedback system. Currently, the loop gain in the feedback system is not time variable, and the amount of power required to drive the summing junction at

peak RF power output pushes the limits of the medium power drive amplifiers upstream of the summing junction. The 20dB limit on the loop gain could be improved with higher power RF amplifiers or variable gain feedback loops that can increase the loop gain when less (or zero) cavity voltage is required.

The third and most prohibitive RF power limitation observed on the direct RF feedback system is the current drive required for effective compensation. When the fundamental frequency is the only component compensated by the feedback system (and the cavity is allowed to tune itself for beam loading), the power amplifiers are not required to supply more power, except for dynamic changes to the fundamental component of the beam or the fanout drive. Compensation of frequency components other than the fundamental (or even the fundamental if the cavities are not tuned to compensate for beam loading), such as revolution harmonics, will require that the power amplifier have enough available power to match the current in the other frequency components. There is very little power dissipated in the cavity at these frequency components, because the impedance of the cavity is usually very low at these frequencies, and the feedback causes the impedance to look even smaller. The critical factor is the available current in the power amplifier circuit.

As mentioned earlier, the Main Injector RF power amplifiers utilize a cathode follower circuit on the power tube. This means that the solid state drivers must provide all of the current required by the power tube. The two specifications that determine the power amplifier's ability to provide effective compensation are the power tube's maximum current capacity and the solid state drivers maximum power output. The current capacity of the tube should be enough to handle the slip stacking load. Although the peak current of the beam during slip stacking exceeds the tube's maximum average current rating, this rating is a thermal rating and can be scaled with duty factor. The solid state driver also has enough power to handle the slip stacking current.[9]

3.1.5.4 Feedforward

Some tests of the power amplifier chain's ability to handle the current requirements of beam loading compensation have already begun. To test the amplifier's response to transient beam loading, a feedforward system is used instead of a digital feedback system. Constructing a compensation system that is stable and operates on revolution harmonics is easier with feedforward. The feedforward system currently being tested in the Main Injector uses a wall current monitor for its beam current source. The signal from the wall current monitor is down-converted, filtered, and delayed digitally (Figure 3.1.53). The output of the digital delay drives a special cavity fanout system. Instead of having a system of equal length cables, this fanout system is designed to have delays different by the beam transit time between cavities. At each of the cavities, the signal is upconverted and combined with the drive (Figure 3.1.54).

The disadvantage of the feedforward system is the beam signal and power amplifier current must match very closely. There is no inherent correction mechanism like there is in a feedback system. Therefore, the system can only operate in very well defined conditions. It cannot track energy changes or changes in RF amplitude or operating conditions. Also, it is extremely important that the signal path be completely linear, otherwise the feedforward signal will be too distorted to cancel out the beam signal when the two meet in the cavity. The power tube is a major source of nonlinearity

in the signal path. It is so bad that, without compensation, only very specific beam profiles will work with the feedforward system. Regular stacking cycles are the only cycles where significant feedforward compensation is observed in the cavities (Figure 3.1.55).

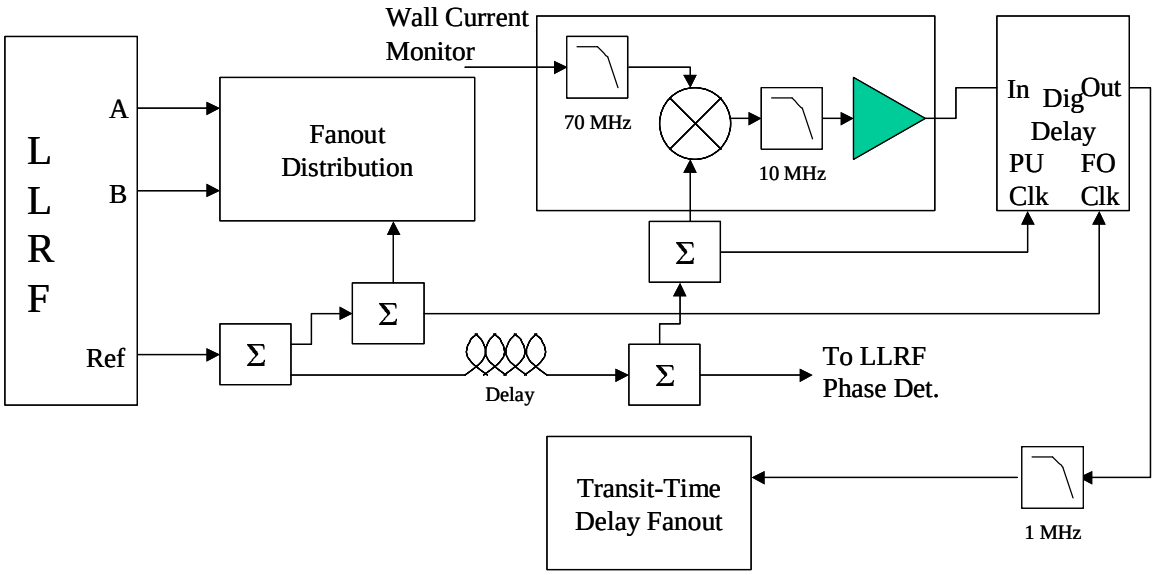

Figure 3.1.53 *Feedforward beam signal processing. Signal from the wall current monitor is downconveted, filtered, and delayed digitally. The output from the delay enters the transit-time delay fanout.*

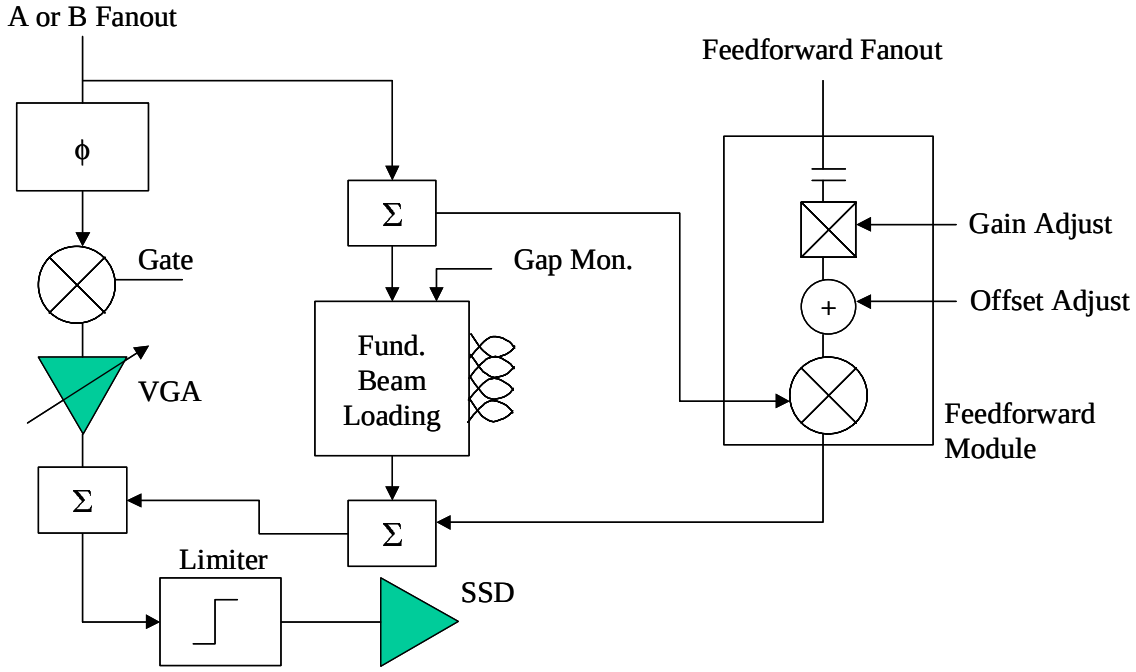

Figure 3.1.54 *The signal from the feedforward processing is upconverted and combined with the fanout and direct RF feedback signals.*

It would be desirable to have a feedforward system working in conjunction with a feedback system for slip stacking. Both systems would help each other and may ease some of the specifications on each system for reaching the beam loading compensation goals. Beam loading compensation is most important during the slipping process when the RF buckets are very small. This process has the advantage that it occurs at a single energy, and the cavities are fixed at a certain voltage level. The challenge is to deal with the multiple fundamental components of beam.

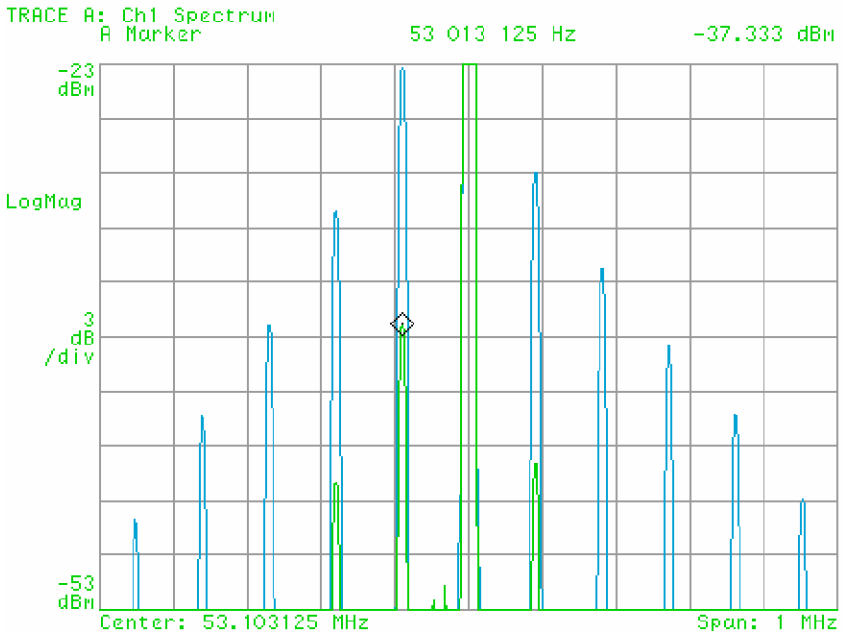

Figure 3.1.55 *Results of feedforward compensation on a single cavity during a normal stacking cycle at high field. The blue trace is the spectrum of the cavity gap without compensation, and the green trace is with compensation.*

3.1.6 Other Slip Stacking Issues

There are some other miscellaneous issues that need to be addressed to make slip stacking a reliable means of increasing antiproton flux. Once the two batches are captured into a single batch, the main ring cycle must continue, as it does for a standard stacking cycle, and accelerate beam to 120 GeV. The difference between this and a standard stacking cycle is that the beam now has twice the intensity and three times the emittance.

Before beam can be accelerated, the main ring LLRF system must reestablish lock to the beam, and the high level feedback loops must be re-enabled. As was mentioned previously, the high level loops have been modified to allow for smooth turn on after capture. The LLRF system should not have a problem reestablishing lock to the beam. It already successfully reestablishes lock to beam after a coalescing cycle where synchronization is transferred from the 53 MHz system to the 2.5 MHz system and back again.

Another issue in the acceleration process is transition crossing. The Main Injector was designed to handle as much as 0.5 eV-s of longitudinal emittance at transition

without significant emittance dilution.[18] This should be tested as part of the slip stacking operational commissioning. If there is significant emittance dilution at 0.3 eV-s, then some kind of gamma-t jump may need to be implemented.

Finally, coupled bunch instabilities may develop at the new, high intensities. For slip stacking only, there should not be a serious problem. The design goal for slip stacking is 1e13 protons per pulse, and the Main Injector has already achieved its commissioning goal of 2e13 protons for fixed target with only simple coupled bunch feedback loops that are still available for use. When NuMI begins its operation, however, the intensity goal of the Main Injector will get to 3e13 protons per pulse. This may lead to faster growing instabilities.

The digital beam loading compensation system can be modified easily to become a synchrotron motion damper as well. By changing the dsp program, the digital filter can have a response at the revolution frequency and the synchrotron sidebands. It may even be possible to automatically track the frequencies of the synchrotron sidebands. The digital compensation system can also be modified to act as a transverse damper. It will not be the case of just changing the dsp software as it is for the longitudinal case, but once the dsp, its clocks, and memory interfaces all work together, adding extra channels for processing stripline pickups is relatively straight forward.

3.1.7 Conclusions

There are four distinct paths of effort required to successfully commission slip stacking. First, low intensity operational studies one the Main Injector must continue. These studies include tuning the capture process, finding the optimal frequency separation, accelerating to 120 GeV, and documenting beam emittance for different beam loading compensation conditions. Second, the simulations must prove their reliability against the beam studies. The simulations must model beam loading accurately, and they must have a reliable model for physical beam loading compensation, not just zero delay feedback. Third, studies on beam loading compensation systems must continue. A simple feedforward system must be commissioned in the Main Injector to insure that the high level system has the available power to compensate beam loading during slip stacking. Finally, work should continue on a digital beam loading compensation system. Although there is not enough data to prove that we need a digital system yet, it is highly likely that we will, given the beam loading parameters slip stacking necessitates. Since a complicated digital feedback system requires a significant amount of lead time, work should continue in parallel with the other studies.

The goal of the project is to have high intensity slip stacking commissioned by the middle of FY03. Achieving this goal will require the following budget and full time equivalents:

Budget:

Digital feedback system x 18 cavities + spares	$190,000
High level RF system upgrades	$70,000

This budget assumes that no major upgrades of the RF power amplifiers or cavities are necessary. As it stands, no calculations have revealed any short comings in the high level system to handle beam loading compensation with slip stacking.

FY02 Full time equivalents:

2 Engineers – Design and commissioning of beam loading compensation hardware, modification of high level systems as necessary, modification of low level RF system as necessary.

2 Physicists – Study slip stacking operation, commission slip stacking, simulate slip stacking in the presence of beam loading and beam loading compensation.

2 Technicians – Construction of beam loading compensation hardware, modifications of high level systems as necessary.

FY03 Full time equivalents:

1 Engineers, 1 Physicists 1 Technicians

	Total	M&S	Labor	Phys.	Eng.	Draft	Tech	CP
FY02	770	170	600	2	2	0	2	0
FY03	390	90	300	1	1	0	1	0
FY04	0	0	0	0	0	0	0	0
FY05	0	0	0	0	0	0	0	0
Project	1160	260	900	3	3	0	3	0

Table 3.1.4 *Funding profile for slip stacking project.*

3.2 Antiproton Collection

3.2.1 Machine physics and potential

Potentially, antiproton collection and beam transport efficiency can be greatly improved between the antiproton production target and the Debuncher. An increase in the effective aperture due to better beam steering, an improved optics match and the removal of aperture restrictions would provide the largest contribution to increasing antiproton yield. These improvements should almost double the antiproton yield as compared with the historical best. A more modest gain of 10 to 20% is expected due to modifications to the lithium lens. Reducing the beam spot from its current size will also result in a 5 to 10% increase in antiproton yield. To accommodate increased beam power on the production target from slip stacking, a sweeping system will be installed. With the sweeping system, the beam spot size can remain small, even after slip stacking brings twice the proton beam intensity. Overall, the antiproton yield is expected to grow from the present level of 15×10^{-6} to about 40×10^{-6} antiprotons per proton after the collection and beam transport upgrades have been implemented.

We will start our consideration with the basic physics principles that determine antiproton production and collection. Then, we will consider practical limitations and formulate the upgrade path.

3.2.1.1 Optimization of production and collection for antiprotons created in the target

Currently, a nickel target is used for antiproton production. Nickel can sustain an unusually large energy deposition of up to 1000 Joules/g and is therefore considered to be the best material for the target.[19] Simulations of antiproton production in a nickel target were performed by with MARS code developed by N. Mokhov.[20] Figure 3.2.1 presents the total yield of antiprotons produced by a 120 GeV proton beam into a momentum acceptance of ±2.25% about an 8 GeV kinetic energy as a function of the target length. One can see that the total yield grows rapidly with target length, but unfortunately the phase space density is saturated well before the total antiproton yield is maximized. In reality, only a small fraction of antiprotons are accepted into the debuncher and one needs to find an optimum set of conditions to fit the maximum number of antiprotons into the finite phase space of the ring. Figure 3.2.2 shows the coordinates of antiprotons in the $x - x'$ phase space produced by a proton beam with rms beam size of 100 μm and an 8 cm long nickel target. Particle *x*-coordinates were translated to the longitudinal coordinate at which the second order moments $\langle x\theta_x \rangle$ and $\langle y\theta_y \rangle$ are equal to zero. If there were no scattering or absorption of antiprotons in the target, this coordinate (waist position) would be in the center of the target. In reality, it is shifted downstream of the target center. We denote this position by δs. For an 8 cm target, it is approximately 2.1 mm. The circle on the plot presents the boundary of phase space with acceptance ε=25 mm mrad and β function β^* = 1.5 cm.

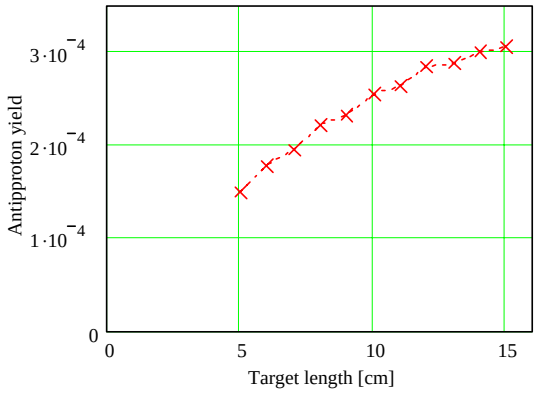

Figure 3.2.1 Dependence of total antiproton yield on the length of the nickel target for a 120 GeV proton beam, momentum acceptance is ±2.25%.

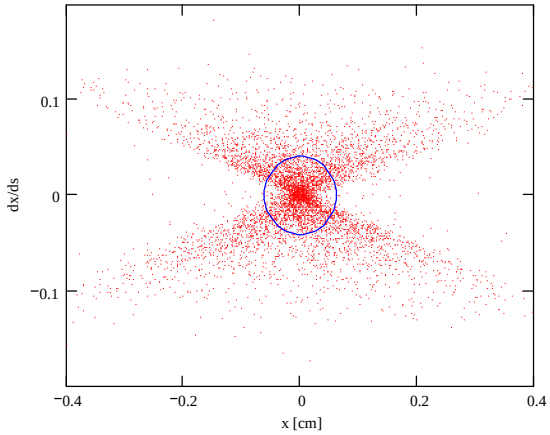

Figure 3.2.2 *Coordinates of antiprotons in x - x' phase space simulated with MARS code for a proton beam of 120 GeV and an rms beam size of 100 μm. The circle inscribes a phase space with ε = 25 mm mrad and β^* = 1.5 cm.*

Figure 3.2.3 shows the angular distribution function for antiprotons exiting the target. As one can see from the figure, it can be described by a gaussian distribution[21]

$$f(\theta) \propto \exp\left(-\frac{\theta^2}{2\sigma_\theta^{\,2}}\right)$$

$$\sigma_\theta \approx \frac{1.1}{\gamma}\sqrt{\frac{m_\pi}{m_p}} \qquad (3.2.1)$$

where m_p and m_π are the proton and pion masses, σ_θ=45 mrad.

Figure 3.2.4 shows the antiproton yield as function of β^* for different target lengths and machine acceptances. Horizontal and vertical acceptances are considered to be equal; and the momentum acceptance is ±2.25%, so that the phase space of the accepted antiprotons is determined by the following equations,

$$\left(\frac{x_i^{\,2}}{\beta^*} + x_i'^{2}\beta^*\right) + \left(\frac{y_i^{\,2}}{\beta^*} + y_i'^{2}\beta^*\right) \le \varepsilon$$

$$\left|\frac{\Delta p_i}{p_0}\right| \le 0.0225$$

(3.2.2)

The β functions are related to the waist position, δs, whose dependence on target length is presented in Figure 3.2.5. The waist is displaced from the target center due to scattering and absorption of antiprotons in the target.

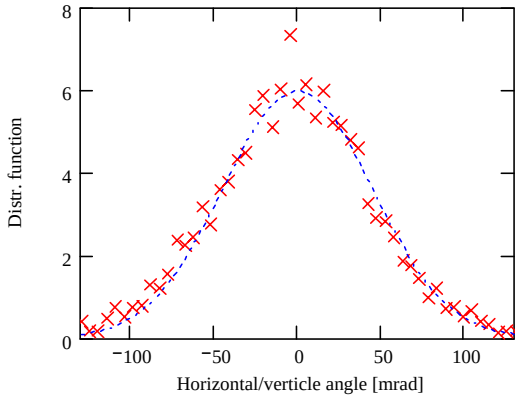

Figure 3.2.3 *Angular distribution function of 8 GeV antiprotons coming out of an 8 cm nickel target; proton beam energy is 120 GeV. The dashed line represents a gaussian distribution with* σ_θ *= 45 mrad*

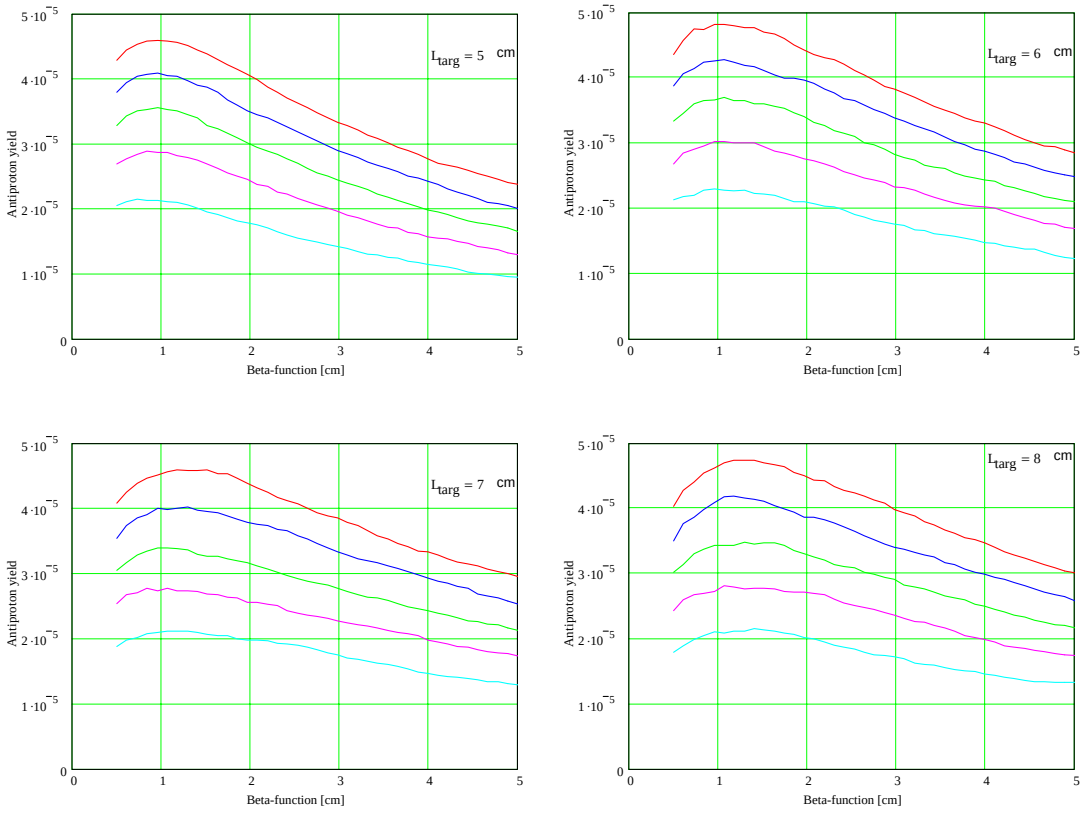

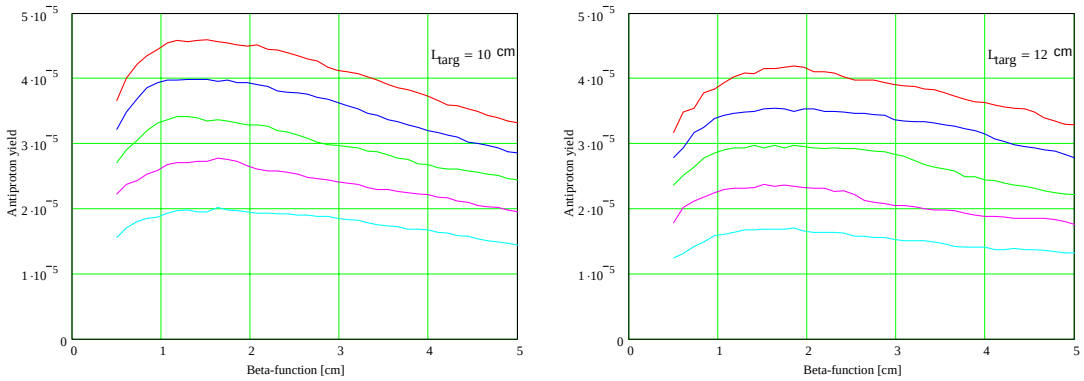

Figure 3.2.4 *Dependence of antiproton yield into ±2.25% momentum spread on the β function at the target for the beam acceptances of 15, 20, 25, 30 and 35 mm mrad, and target lengths from 5 to 12 cm. Corresponding waist positions are shown in* Figure 3.2.5. *The proton beam energy is 120 GeV, and the rms beam size at the target is 100 μm. The kinetic energy of antiprotons is 8 GeV.*

As one can see from Figure 3.2.4, for every given target length, the maximum yield is achieved at an optimal β function which is almost independent of acceptance. Figure 3.2.6 shows the maximum antiproton yield as function of the target length for different machine acceptances and for the optimal β function. Figure 3.2.7 shows the dependence of this optimal β function on the target length. The optimal β function is approximately 1/6 of the target length, which is significantly different from the $1/2\sqrt{3}$ dependence predicted in reference [21]. Taking this into account, we can introduce the effective emittance of antiprotons exiting the target to be equal to

$$\varepsilon_{eff} \equiv \beta^*_{opt}\sigma_\theta^{\,2} \approx \frac{1}{5}\frac{m_\pi}{m_p}\frac{L_{t\,\mathrm{arg}}}{\gamma^2} \qquad (3.2.3)$$

where $\beta^*_{opt} = L_{t\,\mathrm{arg}}/6$ is the optimal β function, and L_{targ} is the target length. For a target length of 8 cm, that yields $\varepsilon_{eff} \approx 26$ mm mrad.

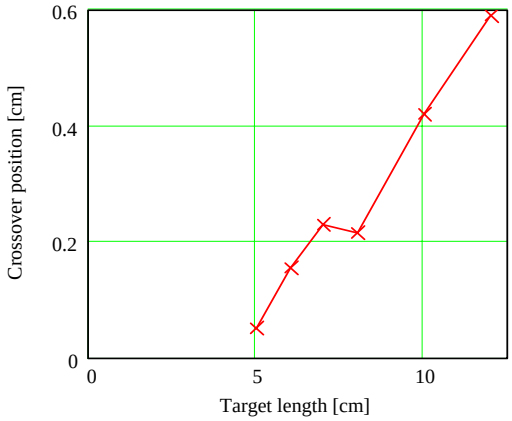

Figure 3.2.5 *Dependence of the waist position on the target length for data presented in Figure 3.2.4; proton beam energy is 120 GeV, and rms beam size at the target is 100 μm.*

In the above discussion, the antiproton yield was calculated for an ideal but unfortunately non-realistic collection scheme. Large antiproton angles require a short focusing lens for their collection. The lithium lens is the most appropriate focusing element for the Fermilab antiproton source parameters, but scattering and absorption in the lens as well as its non-linearity cause a reduction in antiproton yield. There are also practical limitations on the achievable lithium lens focusing strength, which further complicate the optimization. We consider this in detail in the following sections.

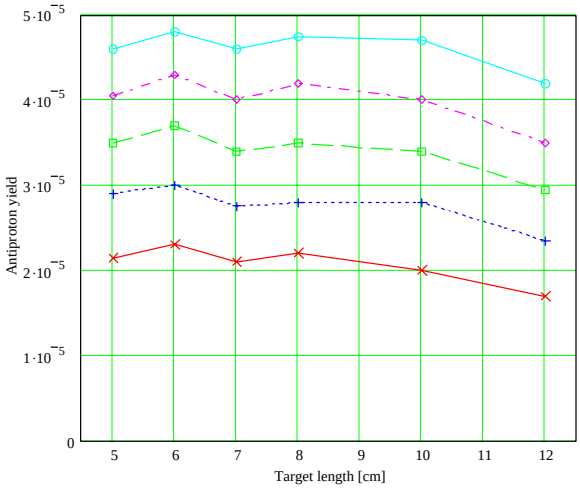

Figure 3.2.6 *Dependence of maximum antiproton yield into ±2.25% momentum spread on the target length for the beam acceptances of 15, 20, 25, 30 and 35 mm mrad. Proton beam energy is 120 GeV, and rms beam size at the target is 100 μm. Kinetic energy of antiprotons is 8 GeV.*

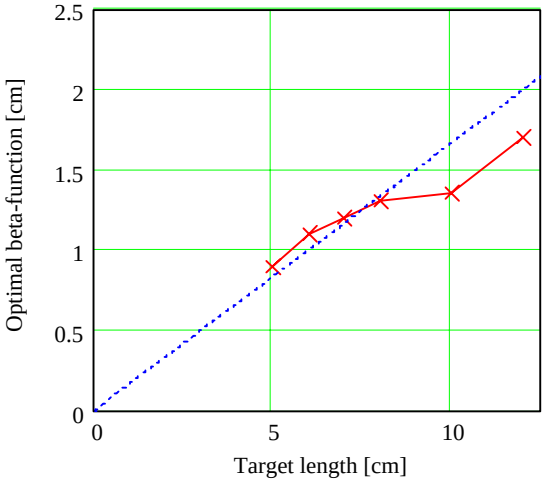

Figure 3.2.7 *Dependence of the optimal β function on the target length for data presented in Figure 3.2.6.*

3.2.1.2 Scattering and absorption of antiprotons in the lithium lens

Nuclear scattering and absorption of the antiprotons in the lithium lens are the major mechanisms for antiproton loss in the lens. The loss of antiprotons due to their strong interactions with lens material can be estimated by the following expression,

$$\kappa_{lens} = \exp\left(-\frac{L_{Li}}{L_{Abs_{Li}}} - \frac{L_{Be}}{L_{Abs_{Be}}}\right) \approx 0.82$$

(3.2.4)

where L_{Li} =15.5 cm and L_{Be}=1.2 cm are total lengths of lithium and beryllium traversed by the beam, and $L_{Abs_{Li}}$ =102 cm and $L_{Abs_{Be}}$ =30.2 cm are nuclear collision lengths for lithium and beryllium. This estimate is in remarkable agreement with the results from MARS simulations.

Multiple scattering in the lens can be estimated by the following formula,

$$\sqrt{\overline{\theta^2}} = \frac{13.6\,\mathrm{MeV}}{\beta \mathrm{P c}} \sqrt{\frac{\mathrm{L_{Li}}}{\mathrm{X_{Li}}} + \frac{\mathrm{L_{Be}}}{\mathrm{X_{Be}}}} = 0.635\,\mathrm{mrad}$$

(3.2.5)

where X_{Li}=155 cm and X_{Be}=35.3 cm are the radiation lengths for lithium and beryllium. Figure 3.2.8 presents a comparison of results obtained with Eq.(3.2.5) and the results from MARS simulations. There is good agreement between simulation and Eq.(3.2.5) for angles below 2 mrad. For large angles, as is expected, MARS produces long non-gaussian tails. Only a small fraction of the particles are located in the tails, therefore we can neglect them with a negligible penalty in the accuracy of the calculations. The scattering in the lens causes emittance growth, which can be estimated by the following formula:

$$\Delta\varepsilon = R_{lens}\sqrt{\overline{\theta^2}}$$

(3.2.6)

For a lens with radius 1 cm, that yields $\Delta\varepsilon$ = 6.3 mm mrad. Figure 3.2.9 shows the decrease in antiproton yield due to multiple scattering in the lens for a fixed β function at the target of 1.5 cm. One can see that for acceptances above 20 mm mrad, the loss is sufficiently small so that nuclear absorption is the major mechanism for particle loss. For smaller acceptances, multiple scattering causes a significant loss in yield. This can be partially compensated for by reducing the β function on the target as shown in Figure 3.2.10.

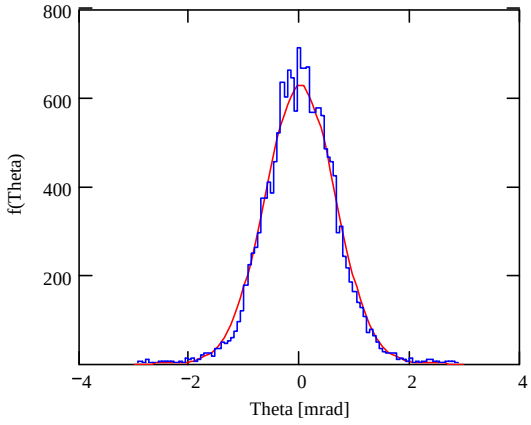

Figure 3.2.8 *Distribution functions of a point like beam after passing through the lithium lens, simulated by MARS and computed with use of the multiple scattering formula of Eq. (3.2.5).*

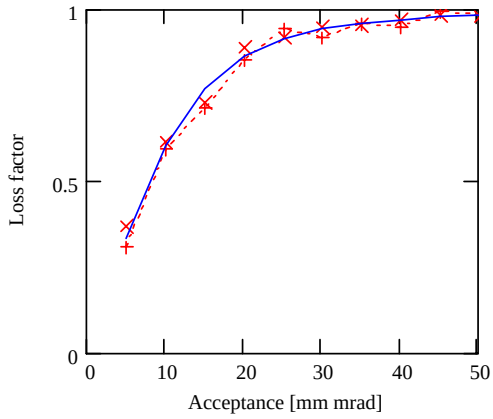

Figure 3.2.9 *Loss of antiproton yield due to multiple scattering as a function of machine acceptance for the current lithium lens. The β function at the target is 1.5 cm.*

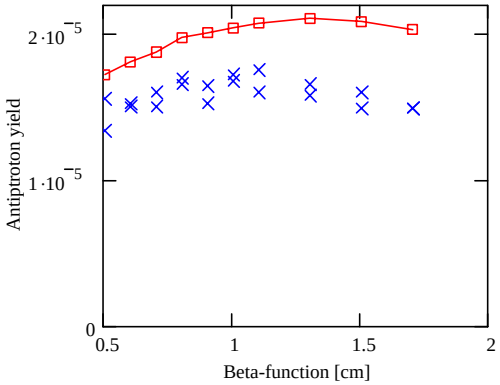

Figure 3.2.10 *Dependence of antiproton yield on the beta function at the target for an acceptance of 15 mm mrad. Solid line – no scattering and absorption in the lens, × – only multiple scattering is taken into account.*

To optimize the antiproton yield with multiple scattering taken into account, we assume that the phase space of antiprotons accepted into the ring is described by the following expression,

$$\frac{x_i^2 + y_i^2}{R_{lens}^2} + \frac{x_i'^2 + y_i'^2}{\varepsilon^2} R_{lens}^2 \le 1$$

$$\left|\frac{\Delta p_i}{p_0}\right| \le 0.0225 \qquad (3.2.7)$$

That means that the accepted antiprotons take up the entire lens cross-section and the β function at the exit of the lens has zero derivative. Figure 3.2.11 presents the antiproton yield as function of lens gradient for different lens lengths and radii. Multiple scattering is taken into account, but the lens is still considered to be linear. As will be shown below the non-linearity does not affect the yield for current lens parameters. For every given lens gradient, the distance between the lens and the target was adjusted to achieve the maximum yield.

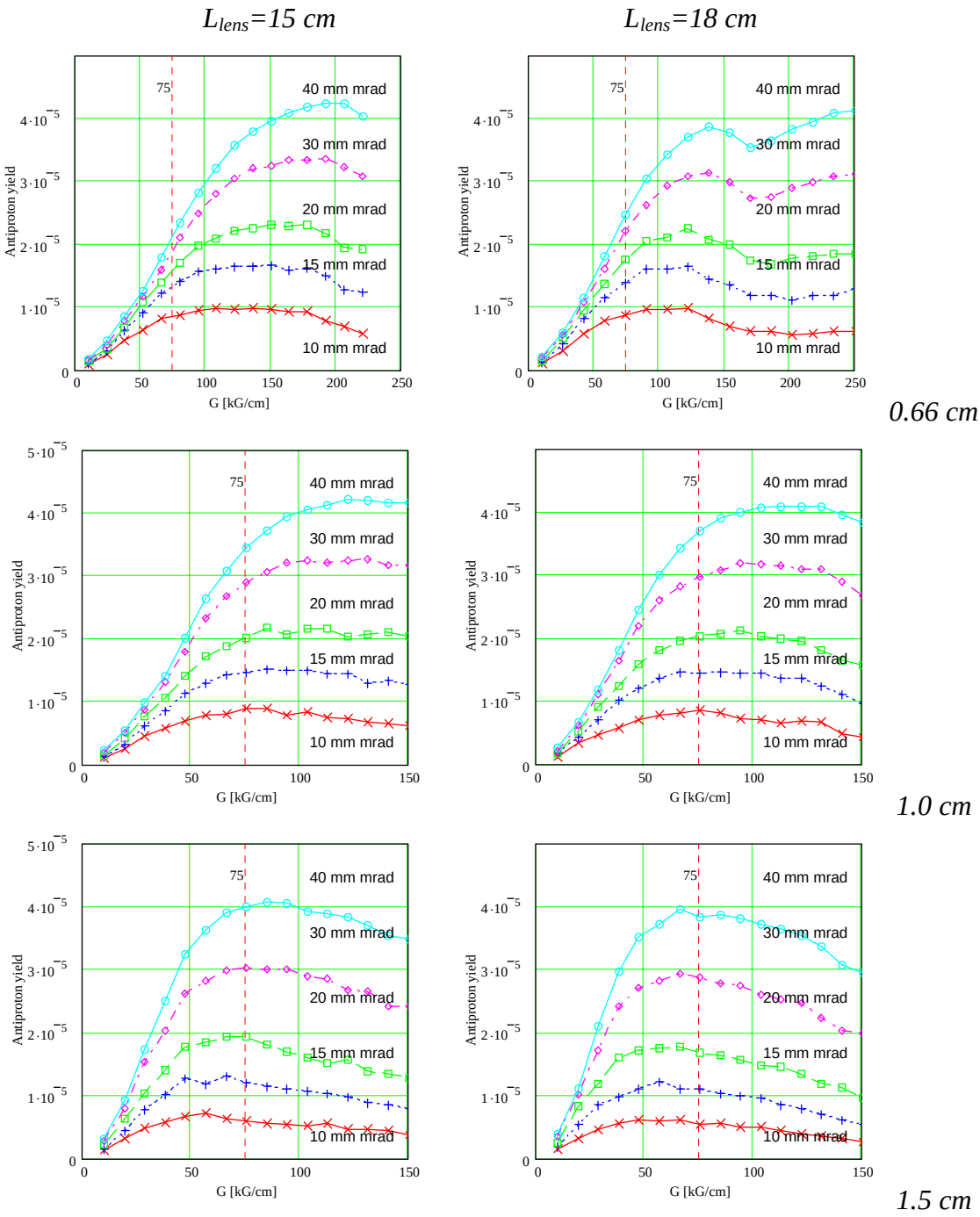

Figure 3.2.11 *The dependence of antiproton yield on the lithium lens gradient for different lens lengths and radii; top - R_{lens}=0.66 cm, middle - R_{lens}=1.0 cm, bottom - R_{lens}=1.5 cm. Rms proton beam size at the target is 130 μm. Energy acceptance is ±2.25%.*

One can see that the peak yield is decreasing with increased radius and length of the lens. The former occurs due to a larger contribution of multiple scattering (see Eq.(3.2.6)), while the latter is related to increased antiproton absorption. The current design of the lithium lens limits its gradient to about 75 kG/cm. Up to this maximum gradient, all

measurements of antiproton collection have exhibited an antiproton yield growth with increasing lens strength. That agrees with simulations, but one should not expect that a further increase of the focusing would bring a significant improvement for acceptances below 20 mm mrad. There can be a moderate increase for larger acceptances, but even in the case of 40 mm mrad acceptance, a yield increase of about 20% would require a 50% increase in lens gradient. That is not possible with a lens of the current design. Note that although reducing the lens radius looks like a reasonable alternative based on Figure 3.2.11, it is limited by rapid growth of the beam size downstream of the lithium lens. A lens radius around 1 cm is about the minimum that can be used to match the lens to the downstream optics (see section 3.2.1.5 for a description of the AP2/Debuncher aperture improvements).

3.2.1.3 Target energy deposition and beam sweeping

Antiprotons are produced from the interaction between a 120 GeV proton beam from the Main Injector and a nickel target. Quadrupole magnets focus the incident beam on the target, a smaller beam spot increases the antiproton collection efficiency, but also increases the peak energy deposition on the target. Early targets made of Tungsten were damaged at only modest intensities, so a switch to copper targets was made in the late 1980's. When intensities in the old Main Ring reached their peak at around 3.25×10^{12} protons per pulse (ppp), measurements indicated that melting occurred during the beam pulse and adversely affected the yield. Though the reduction in yield from melting was only a few percent, it became clear that a change in target material, spot size or beam position would be required for running at intensities expected in the Main Injector era without a significant reduction in yield. The penalty for increasing the energy deposition beyond the melting point would not only be reduced yield, but possible damage due to the shock waves developed in the target during the beam pulse.

During the latter part of Collider Run I, nickel targets began to be used in place of the copper targets. Nickel is similar in atomic structure to copper, so the optimum target length and yield characteristics of the two materials are nearly identical. Nickel has the advantage that the onset of melting requires nearly twice the energy deposition as copper. In addition, nickel is more tolerant of the shock waves that will develop during the beam pulse. However, without a beam sweeping mechanism in place, the spot size on the target would still need to be increased to prevent damage.

Figure 3.2.12 illustrates the dependence of antiproton yield on the targeted rms proton beam size for different acceptances and a lens gradient of 75 kG/cm. One can see that the antiproton yield begins to decrease for beam sizes greater than 100 μm and that the rate of decrease is faster for smaller acceptances. To maximize antiproton yield, it would be desirable to keep the proton beam size at or below 100 μm. The transport line leading to the target is capable of delivering a beam spot size that is this small. However, reducing the beam to this size with a proton intensity of 5×10^{12} ppp would result in a peak energy deposition in the target beyond the melting point of nickel. Figure 3.2.13 shows the relationship between beam spot size, antiproton yield and peak energy deposition with 5×10^{12} protons on target. Melting in the nickel target would be expected with spot sizes below about 0.2 mm. Under these conditions, the ideal spot size to produce maximum yield would most likely cause damage to the target. Slip stacking in

the Main Injector could bring as much as $1x10^{13}$ protons on target, further aggravating the problem.

Note that over the range of possible antiproton source parameters, the following empirical formula can be used to closely approximate the results of numerical calculations[22]

$$E_D \approx 890[\mathrm{J/g}]\left(\frac{200\,\mu\mathrm{m}}{\sigma_{pb}}\right)^2 \frac{N_p}{5\cdot 10^{12}} \qquad (3.2.8)$$

The formula determines the peak energy deposition as a function of the rms size of the proton beam, σ_{pb}, and the number of protons on target, N_p. Note also that the development of the particle shower causes the peak energy deposition to be about twice the energy deposition due to ionization losses of the primary proton beam.

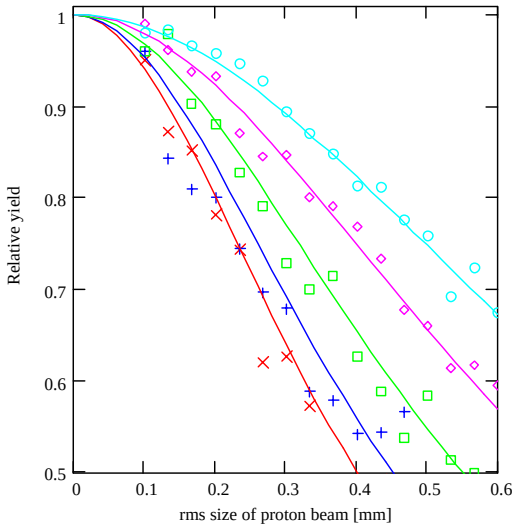

Figure 3.2.12 *Dependence of relative antiproton yield on rms size of the proton beam for acceptances of 10, 15, 20, 30 and 40 mm mrad (curves follow from bottom to top); target length of 8 cm, antiproton absorption and scattering in the lens are taken into account, lens gradient is 75 kG/cm.*

The idea of sweeping the proton beam across the target to reduce peak heating is not a new one, the Tevatron I design report included beam sweeping as a future upgrade. The design phase of the sweeping project began in 1993 and included several years of research and development. Early sweeping designs made use of kicker style magnets similar to those used to transfer beam between the accelerators. In the final design, the sweeping magnets have four two-phase conductor windings rotated about the beam axis to correct magnetic field non-linearities. The proton beam traces a circular trajectory about the target during the beam pulse as illustrated in Figure 3.2.14. The power supply required to provide the bipolar magnet current pulse involves two-stage compression with saturated reactors.

The targeted beam needs to be moved about 0.3 mm during the 1.6 μs beam pulse, resulting in about a factor of five decrease in the peak energy deposition. This reduction is enough so that the spot size can be reduced almost to the point that maximum

yield can be attained, even after slip stacking is commissioned. Sweeping magnets are required both upstream and downstream of the target to preserve the proper trajectory of the antiprotons entering the AP-2 line. There is a small loss of aperture due to the larger beam size passing through the lithium lens. The sweep magnets are of a single design, there are two upstream sweep magnets and a single downstream sweep magnet because the proton beam has an energy of 120 GeV and the antiproton beam is only 8 GeV. There are differences in the striplines and other external details of the downstream magnet in the vault as compared to the upstream magnets located in the AP-1 line.

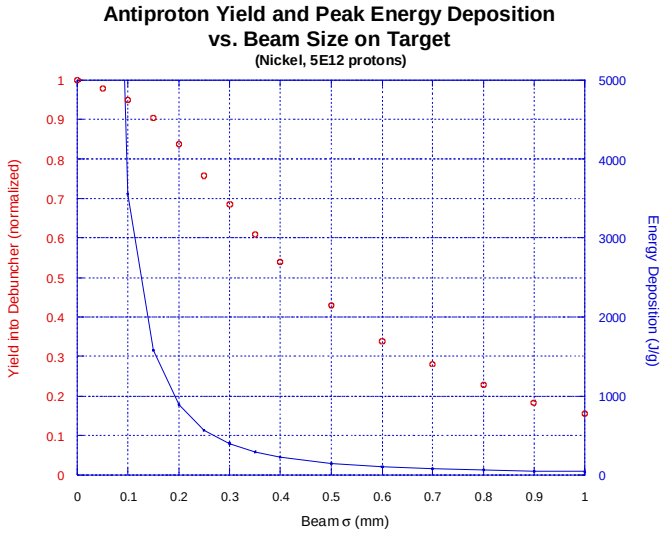

Figure 3.2.13 *Beam spot size vs. Debuncher yield and peak energy deposition in the target (15 mm mr).*

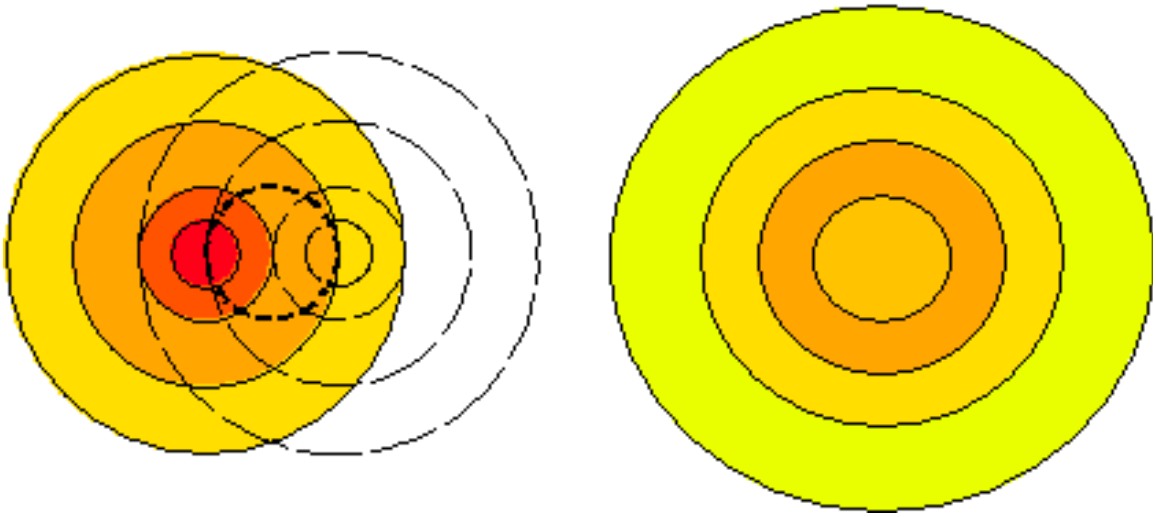

Figure 3.2.14 *Reduction in peak energy deposition with beam sweeping*

3.2.1.4 Effects of lithium lens focusing non-linearity on the antiproton yield

A major non-linearity in the lithium lens focusing is related to the skin effect. At present, the lens current represents a 350 μs long half-period sinusoidal pulse. The skin depth at the characteristic frequency 1/(2*0.00035)≈1400 Hz is 4.5 mm. That is half the size of the lens radius and implies that there is a significant delay in the penetration of magnetic field in to the lens. Figure 3.2.15 shows the results of calculations of the magnetic field penetration into a lithium cylinder with 1 cm radius. It was obtained by expanding the pulse into a Fourier series, finding the solution for the harmonics and performing an inverse Fourier transform numerically. One can see that the maximum gradient is achieved at an RF phases between 30 and 60 deg. There is also a solution for a continuous sinusoidal wave shown in the figure. Although this solution is quite different at the beginning of the pulse, it converges later and there is a negligible difference for the 30 to 60 deg. phases of interest. Therefore we will use this solution,

$$B(r,t)=\frac{2I_0}{cr_0}\,\mathrm{Re}\left(\frac{\mathrm{ber}_1\left(\sqrt{2}\,r/\delta\right)+i\,\mathrm{bei}_1\left(\sqrt{2}\,r/\delta\right)}{\mathrm{ber}_1\left(\sqrt{2}\,r_0/\delta\right)+i\,\mathrm{bei}_1\left(\sqrt{2}\,r_0/\delta\right)}e^{i\omega t}\right) \qquad (3.2.9)$$

for further calculations. Here δ is the skin-depth for frequency $f=1/(2T)$, T is the duration of the pulse, I_0 is the current amplitude, r_0 is the radius of the lithium cylinder, and ber(x) and bei(x) are the modified Bessel functions. Expanding the Bessel functions into a Fourier series:

$$\mathrm{ber}_1(\mathrm{x})\approx \mathrm{f_r}(\mathrm{x})\equiv\frac{1}{\sqrt{2}}\left(-\frac{\mathrm{x}}{2}-\frac{\mathrm{x}^3}{16}+\frac{\mathrm{x}^5}{384}+\frac{\mathrm{x}^7}{18432}-\frac{\mathrm{x}^9}{1474560}\right)$$

$$\mathrm{bei}_1(\mathrm{x})\approx \mathrm{f_i}(\mathrm{x})\equiv\frac{1}{\sqrt{2}}\left(\frac{\mathrm{x}}{2}-\frac{\mathrm{x}^3}{16}-\frac{\mathrm{x}^5}{384}+\frac{\mathrm{x}^7}{18432}+\frac{\mathrm{x}^9}{1474560}\right) \qquad (3.2.10)$$

we obtain an expression which has been used in the tracking simulations presented in Section 3.2.1.5,

$$B(r,t)=\frac{2I_0}{cr_0}\,\frac{\left(\frac{x}{2}-\frac{x^5}{384}+\frac{x^9}{147456}\right)\cos\tilde{\psi}-\left(\frac{x^3}{16}-\frac{x^7}{18432}\right)\sin\tilde{\psi}}{\sqrt{{f_r}^2(x_0)+{f_r}^2(x_0)}} \qquad (3.2.11)$$

where

$$\tilde{\psi}=\omega t-\psi \quad , \quad \psi=\mathrm{atan}\left(\frac{f_i(x_0)}{f_r(x_0)}\right)+\frac{\pi}{4} \quad , \quad x=\sqrt{2}\,\frac{r}{\delta} \quad , \quad x_0=\sqrt{2}\,\frac{r_0}{\delta} \qquad (3.2.12)$$

Operationally, the present Fermilab lithium lens has a phase of ψ = 30°, a time when the magnetic field is still very nonlinear. Maximum linearity of the gradient is achieved at about 45° and the maximum magnetic field gradient is developed in the

center of the lens is at about 67° as shown in Figure 3.2.16. Gradient variations across the lens cross-section are ±7% at the phase of maximum linearity. The mean value of the gradient is about 77% of the gradient calculated without the skin-effect taken into account.

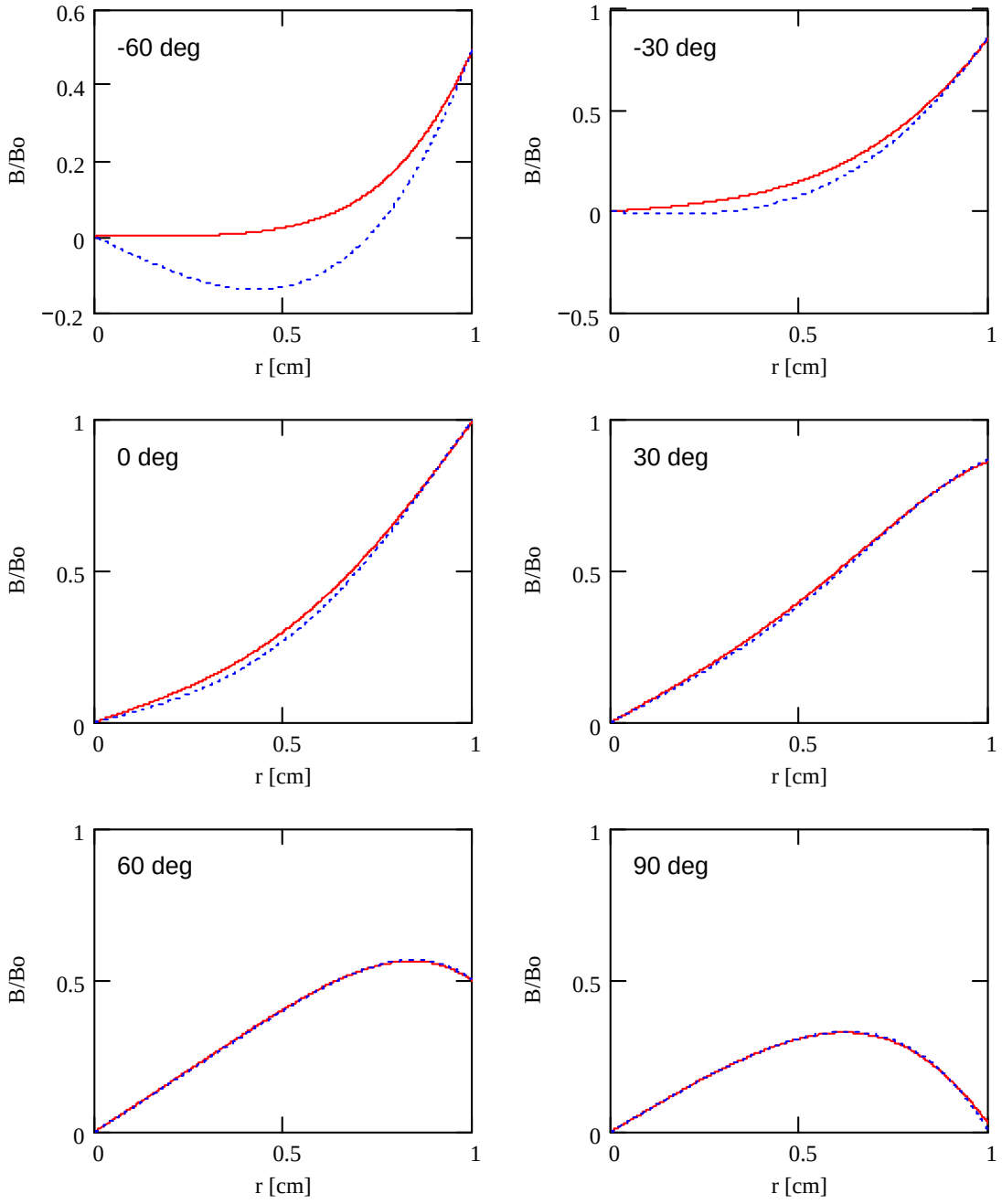

Figure 3.2.15 *Calculated dependence of the lens magnetic field on radius for different times during the 350 μs half period sinusoidal pulse. Time is expressed in phase so that the end and the beginning of the pulse correspond to ±90 deg. The dotted line represents the solution for a continuous sinusoidal wave.*

The temperature gradient across the lithium cylinder causes an additional non-linearity in the lens focusing. The gradient is related to the heating of the lens by the amplitude of the current pulse. For a 1.5 s repetition time, the average power left in the lens is about 100 W/cm. It produces a temperature gradient across the lens so that the exterior has a lower temperature and, consequently, lower resistivity. It produces higher current density in the exterior, which partially compensates for the magnetic field non-linearity due to the skin effect.

A worst-case estimate can be done for a stationary case. Then, the temperature dependence on radius is:

$$T(r) = T(0) + \frac{P}{4\pi\kappa}\frac{r^2}{r_0^{\,2}} \qquad (3.2.13)$$

where $\kappa = 0.82$ W/cm/K is the thermal conductivity of lithium, and P is power per unit length. For P = 110 W/cm one obtain the temperature difference of 10 K and the corresponding current density change, $\Delta j/j$, of about 4%. That yields 2% correction for magnetic field with dependence on radius described by the following formula:

$$B(r) = B_0\frac{r}{r_0}\left(1 + \frac{1}{2}\frac{\Delta j}{j}\frac{r^2}{r_0^{\,2}}\right) \qquad (3.2.14)$$

In reality the time between pulses is longer than the decay time of the temperature wave,

$$\tau_Q = \frac{C r_0^{\,2}}{2\kappa} \approx 1.2\,\mathrm{s} \qquad (3.2.15)$$

where C = 1.95 J/K/cm^3 is the heat capacity of lithium. That determines that the actual temperature difference is well below the above estimate.

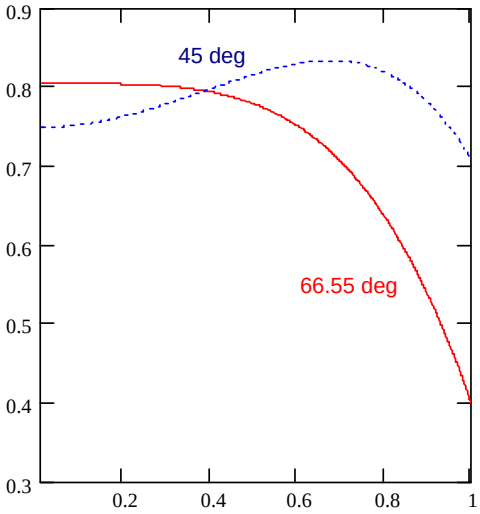

Figure 3.2.16 *Calculated dependence of lens magnetic field on radius at the time when the maximum linearity of focusing (45 deg) and the maximum gradient (66.55 deg) in the lens center are achieved. The result is normalized by the constant determined by the following equation:* $G_{\max} = 2I_0 / cr_0^{\,2}$.

Non-linearities due to the lens edges are even smaller than those due to temperature gradient. For the stationary case in the lens body we can expand the current density from the lens axis,

$$j_z(r,z) = j_z(z)\big|_{r=0} - \frac{r^2}{4}\frac{d^2}{dz^2}\left(j_z(z)\big|_{r=0}\right) + \frac{r^4}{64}\frac{d^4}{dz^4}\left(j_z(z)\big|_{r=0}\right) + \ldots \qquad (3.2.16)$$

That yields the following expansion for magnetic field,

$$B_\theta(r,z) = \frac{2\pi}{c}\left[rj_z(z)\big|_{r=0} - \frac{r^3}{8}\frac{d^2}{dz^2}\left(j_z(z)\big|_{r=0}\right) + \frac{r^5}{192}\frac{d^4}{dz^4}\left(j_z(z)\big|_{r=0}\right)\right] + \ldots \qquad (3.2.17)$$

Integrating it with the equation of motion, one obtains the first non-linear correction for the lens focusing:

$$\frac{\Delta\Phi}{\Phi} = \frac{3}{8}\frac{rr'}{L_{lens}} \qquad (3.2.18)$$

For r = 1 cm, L_{lens}=15 cm and r'= 1/15 we obtain $\Delta\Phi/\Phi \sim 10^{-3}$. There is an additional correction related to sphericity of beryllium windows. Numerical solution for the stationary current contribution yields that this correction is about 3×10^{-3}.

Summarizing, we can conclude that the non-linearity due to the skin effect makes the largest contribution. We will neglect other non-linearities in further calculations. As was already mentioned, maximum lens linearity is achieved at 45 deg and this phase should be used for estimates in approximating linear focusing. Then for the lens gradient we can write

$$G \approx \frac{2I_0}{cr_0^2}\frac{\rho_{Ti}}{\rho_{Ti} + 2\rho_{Li}\dfrac{d_{Ti}}{r_0}}0.78 \approx \frac{2I_0}{cr_0^2}0.74 \qquad (3.2.19)$$

where ρ_{Li} = $11.4\cdot10^{-6}$ Ω·cm and ρ_{Ti} = $42\cdot10^{-6}$ Ω·cm are the resistivities for lithium and titanium, d_{Ti} is the thickness of titanium cylinder containing lithium, and the coefficient 0.78 is determined by the field decrease due to skin effect as was presented in Figure 3.2.16. Thus, the lens current of 500 kA corresponds to about 74 kG/cm lens gradient.

Simulations of the antiproton yield with the lithium lens non-linearity taken into account did not exhibit any significant drop in yield in comparison with the linear lens simulations. Figure 3.2.17 shows the change in yield as a function of the change of lithium lens strength and the proton beam arrival time expressed in the phase of the lens pulse for two different pulse lengths. One can see that shortening the lens pulse from 360 to 200 μs reduced the yield by only about 2% while the non-linearity, $B(r)/r$, grew from ±7% to (+10 – -50)%. Figure 3.2.17 also depicts that due to the stronger skin effect for a shorter pulse, one needs to change the arrival time from 40 to 75 deg. and to increase the lens current by 1.8/1.3~1.4 times to compensate the gradient loss. Thus, a decrease of the lens power consumption due to shorter pulse is overcompensated by increased lens current and the total power consumption ends up being higher for a shorter pulse. Similarly, the power consumption grows for a pulse longer than 360 μs because in this

case the lens current is not changed significantly and power grows proportionally with pulse length. Thus, the choice of a 360 μs pulse length looks to be well optimized.

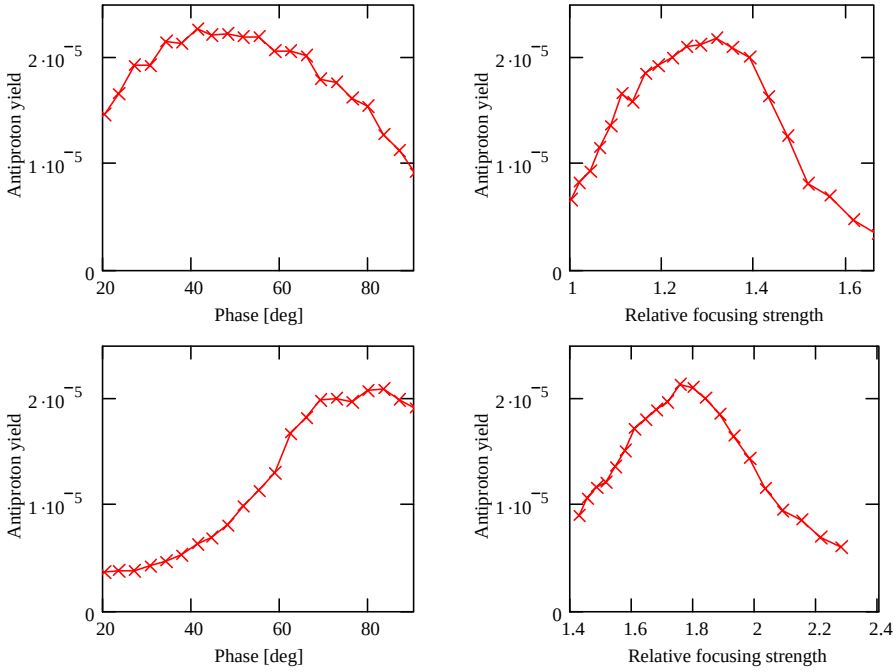

Figure 3.2.17 *Dependence of antiproton yield on the arrival time (left) and the lithium lens current (right) for a pulse lengths of 360 μs (top) and 200 μs (bottom). Arrival time is expressed in degrees of pulse phase. The focussing strength is given relative to the strength without the skin effect. Transverse acceptance is 20 mm mrad; the momentum acceptance is ±2.25%.*

3.2.1.5 Effects of the Debuncher acceptance on AP-2 line optics

In optimum conditions, the β function at the exit of the lens is determined by its radius and the acceptance of antiprotons captured in the Debuncher, $\beta_{lens} = r_0^{\,2} / \varepsilon$. That means that if the Debuncher acceptance is increased, the optics of the transport line has to be modified so that the target assembly optics will be matched with the Debuncher optics. Figure 3.2.18 presents β functions and dispersion functions optimized for Debuncher acceptances of 25 and 40 mm mrad. One can see that an increase in Debuncher acceptance decreases the β function in the lithium lens. Consequently, that leads to a β function increase in the first triplet, so that the beam size in the triplet grows proportionally with the acceptance of the Debuncher. There is plenty of free aperture in the first triplet for a 25 mm mrad acceptance, but it begins to get tight for a 40 mm mrad acceptance. Figure 3.2.19 presents the beam envelopes and aperture limitations for 25 and 40 mm mrad acceptances.

Another concern for the AP2 beam optics is the effects of energy spread on beam transport. The energy spread of protons accepted into the Debuncher is more than ±2% and one needs to identify how much it compromises beam transport quality. Figure 3.2.20 presents the results of particle tracking through the line. One can see that rms emittances decrease rapidly at the beginning of the line. That is related to scraping particles at the beam exterior and is accompanied by a reduction in beam intensity as can be seen from

the bottom portion of Figure 3.2.20. Note also that the scraping also causes step decreases in the beam envelopes (determined as the maximum particle transverse coordinate for a given longitudinal position). Through most of the line, the beam emittances do not grow. However, at the end of the line, there is a significant vertical emittance increase which is accompanied by an intensity decrease due to scraping at the very end. This emittance growth is related to chromatic effects, which are most pronounced at the end of the line due to the very strong focusing from the vertical dispersion suppressor quadrupoles.

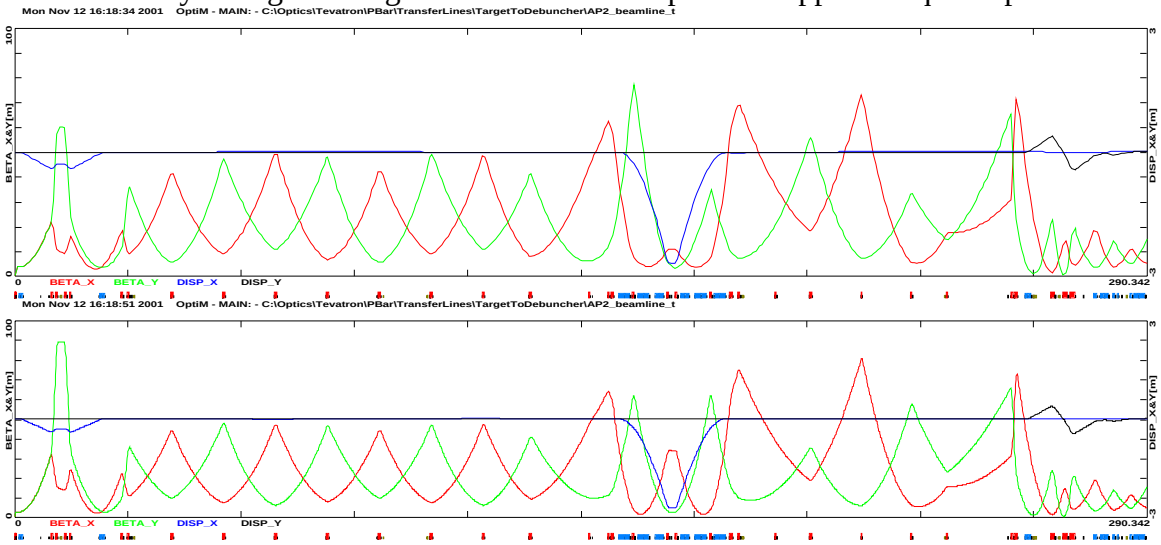

Figure 3.2.18 *β functions and dispersion in the AP2 line for Debuncher acceptance of 25 mm mrad (top) and 40 mm mrad (bottom).*

Figure 3.2.21 presents the dependence of antiproton yield on the acceptance at three different locations along the line and for two different optics solutions optimized for 25 and 40 mm mrad and a lithium lens gradient of 75 kG/cm. The chosen locations are (1) the target exit where the phase density is not disturbed by any optics effects, (2) the middle of the transport line before the main horizontal bends where the optics effects do not cause a phase space dilution, and (3) the end of the line. The dependence of yield on acceptance was obtained by particle tracking from the target to the chosen locations with all optics effects (including lens non-linearity and scattering) taken into account. To compute the yield, we counted the antiprotons that were able to pass through the AP-2 line and fell inside the Debuncher acceptance. As one can see, the transport through the first half of the line causes about a 30% decrease in the antiproton yield. It is related to the scattering and absorption of antiprotons in the lens. This is verified by good agreement between yields calculated by particle tracking through the first half of the line and computations presented in Figure 3.2.11 which takes into account only scattering and absorption in the lithium lens (shown by crosses in Figure 3.2.21). The tracking exhibited about 10% dilution in the second half of the line, which is related to chromaticity at the end of the line. One can also see that both optics exhibit approximately the same antiproton yield in the acceptance range of 10 to 40 mm mrad, which illustrates the relative insignificance of a "perfect" optics match in the AP-2 line. This occurs if the beamline acceptance is larger than the Debuncher acceptance.

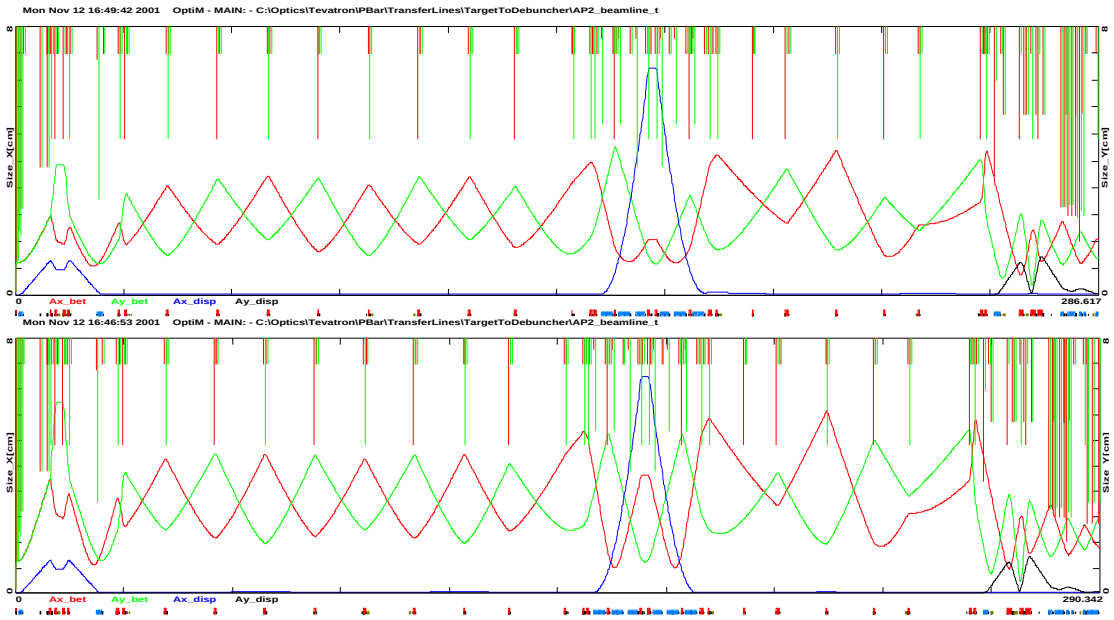

Figure 3.2.19 *Beam envelopes in AP2 line for a Debuncher acceptance of 25 mm mrad (top) and 40 mm mrad (bottom). Aperture limitations are shown by the vertical lines with the colors corresponding to the color of the same plane. Synchrotron size is shown for an energy spread of 2.5%.*

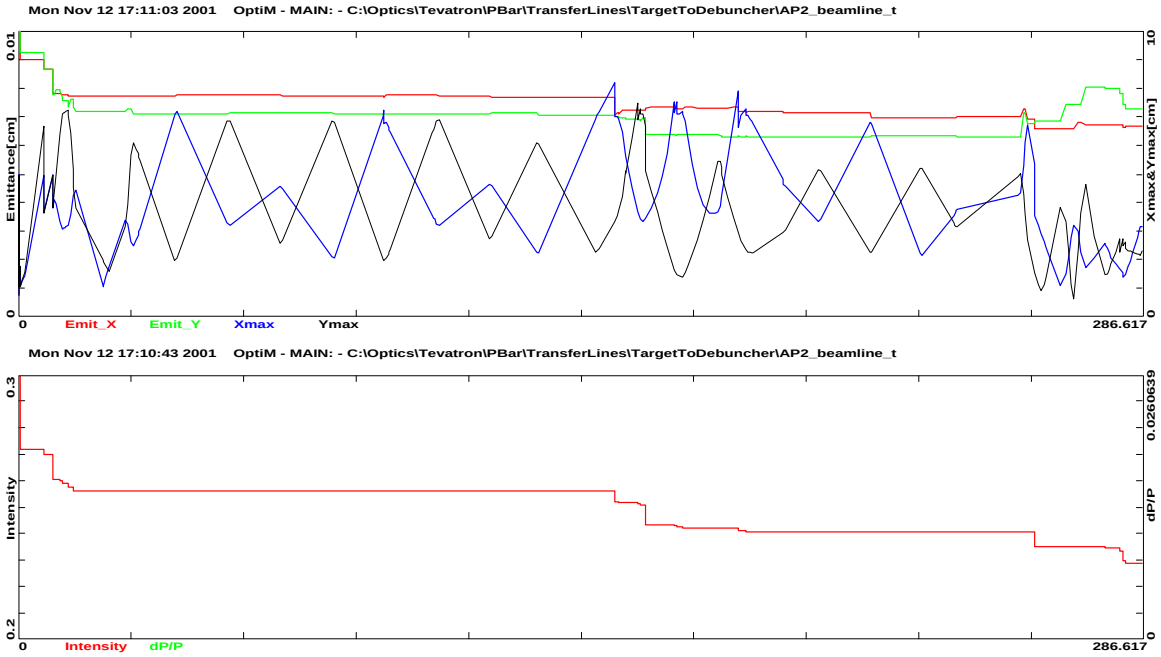

Figure 3.2.20 *Tracking results for optics optimized for 25 mm mrad acceptance. The top picture presents horizontal and vertical rms emittances for surviving particles and horizontal and vertical beam envelopes in the AP-2 line. The bottom picture depicts the antiproton intensity relative to the total antiproton yield from the target (fraction of surviving antiprotons).*

There are two types of chromaticity affecting the performance of the beamline. They are the chromaticity of the beam envelope and the chromaticity of dispersion. The major contribution for this emittance growth comes from the chromatic behavior of the vertical beam envelope. Figure 3.2.22 presents the ratio of the vertical β function for particles with a momentum offset to the vertical β function for particles at the nominal energy as a function of the vertical betatron phase advance. With these variables, the perturbation of the β function oscillates at double the betatron frequency. The initial β function oscillation is excited by the lithium lens with amplitude

$$\frac{\Delta\beta}{\beta} \approx \frac{F}{\beta^*}\frac{\Delta p}{p} \qquad (3.2.20)$$

where β^* is the β function at the target, and F is the lithium lens focusing distance. That corresponds with $\Delta\beta/\beta \approx 0.2$ for a 2% momentum deviation. Then the β function is also excited in the first triplet and oscillates with approximately the same amplitude to the end of the line, where it is strongly excited by the strong quads of the vertical dispersion suppressor. The real problem is actually related to the second order correction for the beta function perturbation. To demonstrate it, the maximum β function oscillations are plotted as a function of momentum in Figure 3.2.23. To take into account that the phase of the perturbation is altered by 180° with a change of sign of the momentum deviation, the sign of $(\beta/\beta_0 - 1)_{max}$ was chosen to be negative for a negative momentum deviation. One can see that for a small momentum deviation, both horizontal and vertical degrees of freedom exhibit approximately the same chromaticity and are linear with momentum. For large negative momentum changes, the vertical envelope chromaticity is greatly amplified which leads to the above mentioned emittance dilution.

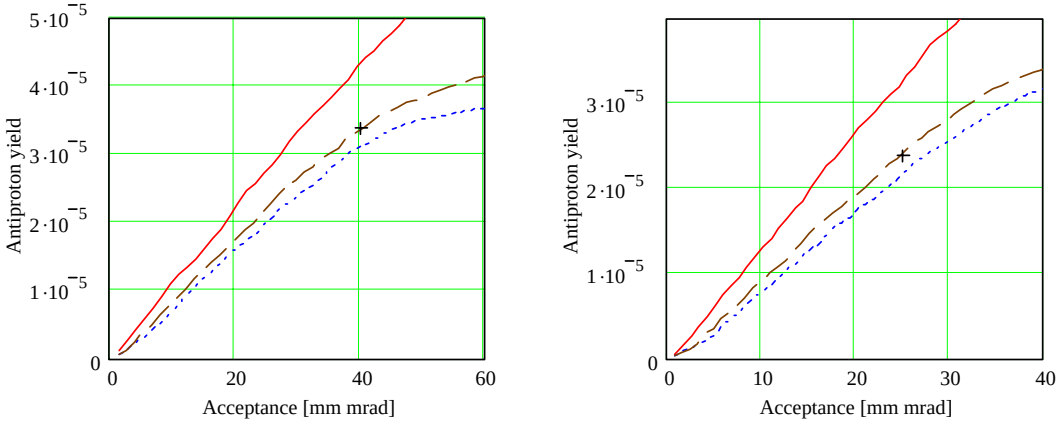

Figure 3.2.21 *Dependence of antiproton yield on acceptance for optics solutions optimized for acceptances of 25 and 40 mm mrad; solid curve – yield at the target, dashed curve – yield in the center of the transport line (Q717), dotted curve – yield at the end of the line, cross – the yield corresponding to the results presented in Figure 3.2.11.*

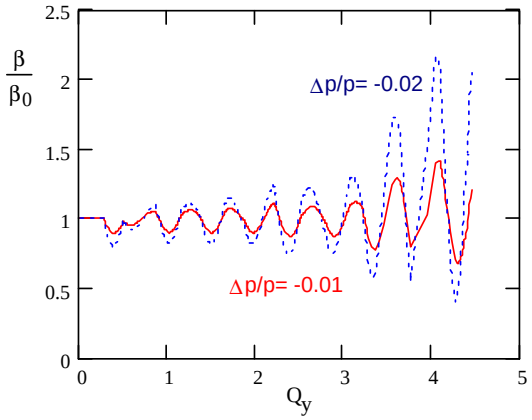

Figure 3.2.22 *Relative variations of the vertical* β *function as function of the vertical betatron phase advance for Δp/p = -0.01 (solid curve) and Δp/p = -0.02 (dotted curve).*

Although less visible in the tracking, the chromaticity of dispersion can also lead to emittance dilution. In the tracking previously described, we considered that the beam is perfectly steered through the line, resulting in the acceptance of the AP-2 line being larger than the Debuncher acceptance. In this case, there are particles on the fringe of the Debuncher acceptance. These particles are oscillating in and out due to dispersion imperfections, leaving the antiproton yield unchanged. If the acceptance of the line is the same or smaller than the Debuncher acceptance, the chromaticity of dispersion leads to an additional decrease in yield. To demonstrate the contribution of the higher order dispersion effects into beam emittance growth, Figure 3.2.24 presents the dependence of Courant-Snyder invariants excited by a momentum change for particles having zero initial betatron amplitudes. As one can see, a momentum deviation of 2% can excite the betatron motion with an effective emittance up to 2 mm mrad, corresponding to a betatron oscillation of about 25% of the machine aperture.

All of the effects described in this section can be significantly improved with a modest upgrade of the beam line optics. The change in optics may require relocating quadrupole magnets and changing power supply configurations. Additional study time will be required to formulate the upgrade path.

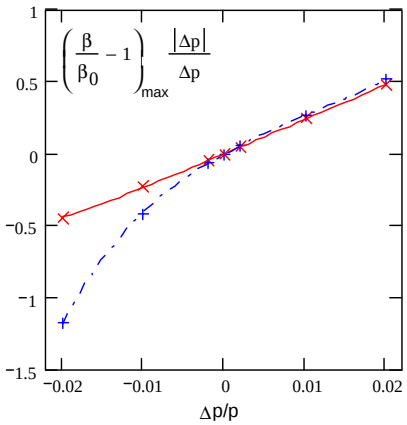

Figure 3.2.23 *Dependence of the maximum* β *function variation on momentum; solid curve – horizontal plane, dash-dotted curve – vertical plane.*

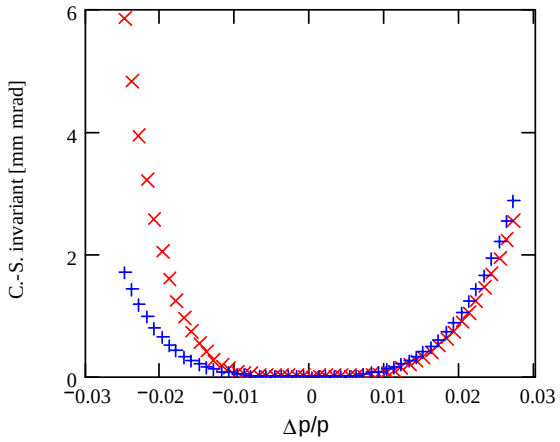

Figure 3.2.24 *Effective amplitude of betatron motion (Courant-Snyder invariant) excited in the Debuncher due to higher order dispersion; × - horizontal motion, + - vertical motion.*

3.2.2 Solid lithium lens

Efforts to create a reliable, high gradient (greater than 1000 Tesla/m with a 1 cm. lens), solid lithium conductor collection lens for Run IIb are being concentrated in three areas. First, the current lens design is being investigated to discover the nature of past failures and any predictable shortcomings of the structural design. Second, design and analysis of new lens design possibilities are being conducted with the end goal of producing and testing prototype high gradient lenses. Finally, since there are indications that the lithium pre-load pressure is important to lens survival, research and development of an improved lens filling process is underway.

3.2.2.1 Technical description

3.2.2.1.1 Current Lens Design Investigation

The existing collection lens design is being investigated in order to identify areas of improvement for future lens development. Activity is occurring on two fronts: autopsy of failed lenses and finite element analysis (FEA) of the actual design.

3.2.2.1.1.1 Autopsy of Failed Lenses

In the past, autopsy of failed lenses has been avoided due to the hazardous nature of radioactive lithium. However, with careful planning and controls in place (and since failed lenses have had appreciable time to radioactively decay), it is now safely achievable. The autopsy of the lenses will be performed by melting and removing the lithium conductor core, and then rinsing with water in order to react away any residual lithium. The work will be performed in an inert atmosphere with byproducts carefully collected and measured. After the emptied lens is disassembled, the various lens components may be visually inspected to identify locations and mechanisms of failure. Since failures have primarily consisted of breaches of the titanium cooling jacket

(septum) allowing lithium into the cooling water medium, it is hoped that inspection might indicate areas of the septum that require improvement.

3.2.2.1.1.2 Finite Element Analysis of Current Lens Design

FEA of the current lens design is being conducted to provide a complete visualization of the structural stresses in lens components during a pulse. The current level of FEA technology enables geometrical details and cyclic loading to be modeled that have not been included in previous analyses. The FEA of the current lens design starts with a thermal diffusion simulation of the current pulse, includes thermal and structural stress effects, and results in stress and deflection of lens components at time points of interest. All of this is done within the ANSYS FEA package. A Fermilab PPD ANSYS expert, Z. Tang, is developing this analysis method. It is hoped that results will indicate any weak points of the current lens design that can be correlated with actual lens failure autopsy results. This will greatly aid in the future design of high gradient solid lenses.

3.2.2.1.2 New High Gradient Solid Lens Design

Design efforts for a new high gradient lens are concentrated in four areas. First, a method of simulating how lens geometry changes (radius, length, end regions, etc.) affect anti-proton yield is being developed. Second, the same FEA tools described above will be utilized to evaluate new lens designs. Third, a new bonding technology (namely diffusion bonding) is being investigated for high gradient lens application. Fourth, the results of the above three areas are being applied in a prototype program that will allow real-world testing of lens design improvements.

3.2.2.1.2.1 Lens/Beam Physics Modeling

The existing design of the solid collection lens is similar to that originally conceived in the early 1980s. The lens was designed to operate with a gradient of 1000 Tesla/meter, but rather early in the target station history, it was determined that extended operation for millions of pulses is not possible above about 750 Tesla/meter. As a consequence, the collection efficiency has been less than desirable. Pbar collection is a complex, multivariable problem. Late in the 1990s, A program called MCLENS based upon the shielding code CASIM was written to model antiproton production, collection and transport. One perceived shortcoming in the MCLENS program is that the magnetic field is modeled as an infinite cylinder and does not consider end effects. This results in the overestimation of both the actual collection lens length and efficiency.

A new collection lens modeling effort based upon the MARS code was undertaken. The new model was used to generate the figures presented earlier in this section. In the MARS version of the collection lens model, non-linear, magnetic field end effects are considered. Based on the updated model, most lens parameters appear to be well optimized. One exception is the lens length. There appears to be the potential for a modest increase in antiproton yield for a lens that is approximately 20% longer. In general, though, the ideal lithium lens would be extremely short and run with a surface magnetic field far greater than present technology allows.

3.2.2.1.2.2 FEA of New Lens Designs

Using the same FEA tools developed by Z. Tang of PPD to analyze the current lens design, design improvements for the new high gradient lens will be analyzed. Effects of various materials for different components, geometrical changes, cooling parameter changes and component stresses will be investigated. As previously described, the model will simulate several cycles of loading (several hundred pulses) to achieve quasi-static status. Then stress results will be looked at from a fatigue perspective to evaluate proposed design changes.

3.2.2.1.2.3 Diffusion Bonded Septum Joints

The current method for joining individual septum components is electron beam welding. Although this method can be highly successful, it has its drawbacks in terms of fatigue, weld to weld consistency, and costs. Another method of joining (diffusion bonding) has been identified and will be investigated for applicability to septum construction. This new method of joining uses high temperature and moderate pressure to achieve complete bonding (crystal growth across joint) with more uniform microstructure, less residual stress, and for less cost than electron beam welding. Use of diffusion bonding, however, is untried for this application and requires major geometrical changes for maximum benefit. These geometrical changes can be included in the FEA mentioned earlier.

3.2.2.1.2.4 Fatigue Testing

A fatigue testing program has been undertaken in collaboration with Argonne National Laboratory's Corrosion Section. The emphasis of the testing will be to determine the endurance limit for the most critical diffusion bonded joint, located in the center of the inner conductor tube. There will also be fatigue testing of the parent material and unbonded (solid) material for comparison. To mimic actual operating loads and joint geometries, it will be necessary to utilize cylindrical joint samples and stress them in tension in the same direction as the joint line. Failed specimens will be analyzed, including microscopic evaluation, to confirm failure modes. Specimens that survive the endurance limit of $2x10^7$ cycles will be examined for cracking or other signs of imminent failure.

3.2.2.1.2.5 Prototype Program

Results of the physics modeling and FEA will be used to produce design improvements that will be tested in a series of prototype high gradient lenses. The prototypes will be constructed on an aggressive schedule in order to meet Run IIb needs. The prototypes will allow us to test pulse the new designs in a real-world operating environment. It is expected that at least two prototypes will be required before succeeding at the goal of a robust (10 million + pulses), high gradient (10+ Tesla surface field) solid collection lens.

3.2.2.1.3 Lens Filling Research and Development

Past experience and preliminary simulation results have strongly indicated that lithium pre-load pressure is linked to long term success of a solid lithium collection lens. Pre-load pressure is necessary to oppose the magnetic pinching effect during a current

pulse and keep the lithium conductor material from separating from the septum wall. Currently this pressure is provided during the initial fill of the lens with lithium. Unfortunately, because of the difficulty with volume contractions of the lithium and problems with instrumentation of the lens itself, confidence that proper pre-load pressure has been attained is not high. Research and development is currently underway to improve the fill process in terms of equipment, instrumentation, and data acquisition so that future fills of both current lenses and prototype lenses will be successful. In addition research and testing is planned to explore the possibility of adjusting the pre-load after the actual fill using, as of yet, mechanisms that are yet to be designed.

3.2.2.2 Plan and status

3.2.2.2.1 Current Lens Design Investigation

3.2.2.2.1.1 Autopsy of Failed Lenses

Five solid lenses, which have failed in service, are to be dissembled to determine the failure modes. The removal of lithium from the lenses occurs in two phases. In the first phase, a lens body is heated to the lithium melting temperature and then low-pressure argon gas is applied to aid in lithium removal. In the second phase, water is circulated through the room temperature lens body to react with and remove remaining lithium from surfaces of the steel and titanium structures. A third phase involves the recombination of hydrogen released from the second phase by controlled combustion. The collection and analysis of the resulting water vapor may shed some light on the production of gases such as helium, and hydrogen resulting from the interaction of the particle shower with lithium.

Two lenses (#20 and #21) were unfilled during the summer of 2001. Both lenses had a short service life and had failures of the inner septum. Both lenses exhibited an axial crack on the inner septum, consistent with fatigue failure. Cross-sections made at the fracture location indicate a brittle fracture propagating from the inside surface with a ductile fracture occurring over the last 1/3 of the wall thickness at the outer diameter surface. Two more lenses (#17 and #18) are being unfilled during the fall of 2001 and should have their failure analysis complete in early 2002. These lenses had a relatively long service life. The remaining lens that is scheduled for unfilling (#22) failed in September 2001 and is still very radioactive. The plan is to allow several months of cool-down time before attempting any work on this lens. Lens #22 had the longest lifetime of any lens, more than $9x10^6$ pulses, and is of particular interest to us.

3.2.2.2.1.2 FEA of Current Lens Design

FEA of the current lens design is now complete. Stress and deflection results were generated for several load cases. The results have been summarized in P-Bar Note #663 "FEA Analysis of AP-0 Target Hall Collection Lens (Current Design)". In summary, stress cycles seem to be within the endurance limits of the materials. However, the analysis indicates signs of separation of lithium from the septum inner conductor tube (Ti 6Al-4V) during the magnetic pinch at the design gradient (1,000 T/m). This separation could not be modeled accurately by the ANSYS model and must be investigated further.

There is also some indication that the center body to septum seal area undergoes large deformation and/or stresses which could results in lithium leakage at the seal.

3.2.2.2.2 New High Gradient Solid Lens Design

3.2.2.2.2.1 Lens/Beam Physics Modeling

Significant progress has been made in producing the new collection lens model. Most of the programming work required for the MARS modeling work has been completed. Magnetic field calculations have been made using the program ANSYS and the results of those calculations have been incorporated in the MARS model so that end effects are now considered. Quantitative comparisons of production efficiency of the existing and future lens designs can be presently made. Since experimental data is not in complete agreement with preliminary MARS calculations, accelerator studies are planned to compare measurements with output from the model.

3.2.2.2.2.2 FEA of New Lens Designs

The ANSYS analysis of the high gradient prototype lens has been completed, although a full report has not been written. In summary, stress cycles seem to be much lower for a higher gradient (1,300 T/m). However indication of lithium/titanium separation is also apparent. Future investigations are planned to include exploration of material property temperature dependencies and the lithium/titanium separation phenomenon. However, these analyses will require careful investigations into the material properties of lithium in the plastic state (including strain rate dependencies). Projected dates for the completion of these further analyses are not easily determined. But it is hoped that a more complete understanding of the mechanical behavior of the lens during a pulse via ANSYS analyses will be achieved by spring 2002.

3.2.2.2.2.3 Diffusion Bonded Septum Joints

Diffusion bonding technology has been used to manufacture several sample joints for metallurgical analysis. From this work a joint design has been chosen as being optimal for the most critically stressed joint in the septum (inner conductor tube joint). This joint design exhibits good grain growth across the bond line, good microstructure for strength, and minimal stress concentration features (crack initiation sites) at the surface. Manufacture of the samples also resulted in the realization that, if the lens body is also made out of titanium alloy, both the body and the septum can be joined as one diffusion-bonded component. This should result in a much faster and cost effective joining process, not to mention that it eliminates a critical lithium seal. Currently 30 joint samples are being prepared for fatigue testing to determine the joint's endurance limit for fatigue.

3.2.2.2.2.4 Fatigue Testing

The diffusion bond fatigue testing program is continuing at a slow pace. All sample raw material has been prepared (bonded) and initial tensile testing of the first samples is currently underway at Argonne National Laboratory (ANL). Once sample geometry has been confirmed by these initial tests, the fatigue test samples will be final machined and sent to ANL for endurance limit determination. Past delays have been largely due to lack of test technician manpower at ANL. Future delays may involve

sample material inconsistency (more samples may need to be fabricated). Projected date for completion of the diffusion bond fatigue testing program is now spring 2002 although information regarding the endurance limit of the material may be available earlier.

3.2.2.2.2.5 Prototype Program

Time constraints have required the design of a prototype high gradient lens before all the design data have been determined (it will take several months for fatigue testing joints for instance). However, using the preliminary data currently available a reasonable first prototype can be designed and constructed that will yield valuable experience with the diffusion bonding process and indicate if identified design improvements are beneficial. This prototype is in the final stages of design. It uses a 1.5 mm titanium alloy septum wall, 1 mm was used previously. It will be constructed via diffusion bonding, which results in a water-cooled titanium alloy body. The body and septum are one piece, which eliminates the troublesome lithium seal between body and septum. It is also interesting to note that the diffusion-bonded design precludes the inclusion of lithium 'buffer' volumes that were part of the previous design.

3.2.2.2.3 Lens Filling Research and Development

The entire lens filling instrumentation system has been re-engineered to achieve better signal to noise ratio and increase sensitivity. Several tests have been run with the instrumentation system to ensure its robustness during a fill. A 'dummy' lens was assembled that made use of an actual lens assembly to mimic the fill process using hydraulic oil. Thus the fill process can be simulated many times and calibration of instrumentation at various pressures and temperatures can be performed. Compression testing of lithium has also been conducted to aid in the understanding of lithium behavior during the fill process. This information also came in useful for the lens FEA described earlier. A number of calibration runs have been performed using the dummy lens. Work on pre-load adjustment schemes has not progressed beyond the conceptual design stage.

3.2.2.2.4 Budget and manpower requirements

During FY 2002, completion of the first prototype solid lithium lens is estimated to cost 28k$ of M&S. The second prototype lens will require approximately 43k$ of M&S. Fatigue testing is estimated to incur another 45k$ of M&S. Simulation studies will require little or no outlay for M&S. Due to the research and development nature of the project, it is recommended to use a higher contingency on these projections of about 20%. Thus, the total (including contingency) M&S budget projection for FY '02 is 130 k$.

The total manpower requirement for FY '02 is 3.0 full time equivalents. The breakdown is as follows:

Physicist	@0.5 FTE
Engineer	@1.0 FTE
Technician	@0.8 FTE
Drafting	@0.7 FTE

The solid lens upgrade effort should gradually ramp down after FY '02. M&S requirements will remain about the same for FY '03 at 120 k$. For FY '04 M&S will drop

to 60k$ and then 0 k$ in FY '05. Similarly, manpower requirements will be 1.7 FTE in FY '03, dropping to 0.5 FTE in FY '04 with 0 FTE requested for FY '05.

	Total	M&S	Labor	Phys.	Eng.	Draft	Tech	CP
FY02	430	130	300	0.5	1	0.7	0.8	0
FY03	290	120	170	0.2	0.5	0.2	0.8	0
FY04	110	60	50	0.1	0.1	0	0.3	0
FY05	0	0	0	0	0	0	0	0
Project	830	310	520	0.8	1.6	0.9	1.9	0

Table 3.2.1 *Funding profile for the Solid Lithium Lens Upgrade*

3.2.3 Liquid lithium lens

3.2.3.1 Technical description

Collaboration between Fermilab and the Budker Institute of Nuclear Physics in the form of an Accord was begun in July 1997. The purpose of the Accord is to explore the feasibility of producing and operating a collection lens containing a liquid lithium conductor. It is believed that the current solid lithium collection lens operation is mainly limited due to complications arising from the rapid heating and expansion of the lithium conductor. Significant heating of the lithium conductor occurs during the electrical current pulse. In the solid lens design, large stresses develop on the titanium inner septum tube that can lead to failure. In the liquid lithium lens design, the stresses are reduced due the fluid characteristics of the liquid lithium and the use of buffer volumes. Heat deposited by the current pulse is removed by continuous pumping of the liquid lithium from the lens body to an external heat exchanger.

It is also believed that in the solid lens running at high gradient, the lithium conductor becomes separated from the inner titanium conduction tube due to a magnetic pinch, which occurs at or below design gradient. The separation of lithium from the inner conductor wall could lead to arcing in the lithium conductor, poor heat transfer, and high level cyclic stresses. In both cases, adequate pre-load pressure must be provided to prevent separation from occurring. In the liquid lithium lens, it is believed that the pressure of the lithium piping system can be controlled to prevent the separation of lithium from the inner conducting tube. The liquid lithium project as currently conceived, requires of a number of auxiliary external support systems to pump liquid lithium, control system pressure, lithium flow and lithium temperature. These systems would bring significant complications to target station operation.

3.2.3.2 Plan and status

The work outlined in the Accord is divided into four phases. Phase 1 included the performance of engineering calculations and conceptual design work. Additional design work and construction of components including a lens power supply were to be completed in Phase 2. In Phase 3, the goal is to operate a lens for 1 million pulses at a surface field of 13 Tesla. The purpose of testing a lens at such high gradient is to ensure that operation at a surface field of 10 Tesla would be reliable for many millions of pulses. In addition, the tested lens, power supply, lithium pumping and pressure systems and lens

control systems are to be delivered to Fermilab. Finally in Phase 4, a second untested lens of the same design is to be built and shipped to Fermilab.

Phases 1 and 2 are considered to be more or less complete. Phase 3 is currently ongoing. To date, two lens designs have been attempted and have failed well below the design gradient. In a review held at Fermilab during the week beginning April 9, 2001, it was learned that testing of a 3rd generation lens was scheduled to begin at BINP in May/June 2001. The testing has been delayed until at the end of 2001. It is planned to ship a lithium pumping system equipped with locking valves, pressure system, and system controls to Fermilab in the winter of 2001/2002. At the same time, a power supply designed for operation of either a solid lens or a liquid lithium lens will be shipped to Fermilab. The delivery of the tested lens will depend on completion of successful testing. The purpose of shipping the lithium contour and associated controls, perhaps in advance of delivery of a successful lens, is to get Fermilab involved in the operation of a liquid lithium system so that experience with system operation can begin to accrue.

The original Accord, which was signed in July 1997, was scheduled at that time to be completed during the year 2000. Unforeseen difficulties in this work have delayed its timely completion. At this time, an amendment is being prepared to provide additional funds to BINP to allow continued work for tasks outlined in Phase 3. Given sufficient time and resources, there is no reason to believe a liquid lithium lens can not be produced. At this time however, it is not clear that sufficient time is available to complete the liquid lens project in time for RUN IIb. If testing of a liquid lithium lens is eventually successful, significant resources will be required to configure a liquid lithium lens system into the modular form required for target vault operation.

3.2.3.3 Budget and manpower requirements

Most of the effort on the liquid lithium lens will continue to take place at BINP in FY '02. It is difficult to project the successful completion of a prototype lens, particularly in view of the lengthy delays and complications that have occurred to date. When success has been achieved, the effort will shift to Fermilab where an extensive effort will be required to adapt the liquid lithium lens to use in the pbar target vault. M&S outlay for FY '02 will be primarily for a final payment to BINP after a successful high gradient test and shipping costs associated with the lens contour and power supply.

	Total	M&S	Labor	Phys.	Eng.	Draft	Tech	CP
FY02	230	200	30	0.2	0	0	0.1	0
FY03	850	330	520	0.4	1.5	1	1.8	0.5
FY04	600	200	400	0.5	1	0.3	2	0.2
FY05	200	100	100	0.4	0.2	0	0.4	0
Project	1880	830	1050	1.5	2.7	1.3	4.3	0.7

Table 3.2.2 *Funding profile for the Liquid Lithium Lens Project*

The total manpower requirement for FY '02 is only a total of 0.3 FTE. 0.2 FTE of physicist time will be needed to monitor progress at BINP and 0.1 FTE of technician time to begin to make preparations for the arrival of the lens contour and power supply.

Anticipating a successful test in late FY '02 or early FY '03, a significant increase in M&S and labor will be required to continue the project. For instance, M&S

requirements jump to 300 k$ in FY '03 with 5.2 FTE of labor. At this point, existing target station personnel will not be adequate to cover the three Run IIb projects and operational demands. Additional engineering and technician support would be required for FY '03 and '04. Both M&S and labor are expected to drop substantially in FY '05 as the system shifts to operational use.

3.2.4 Beam sweeping

3.2.4.1 Technical description

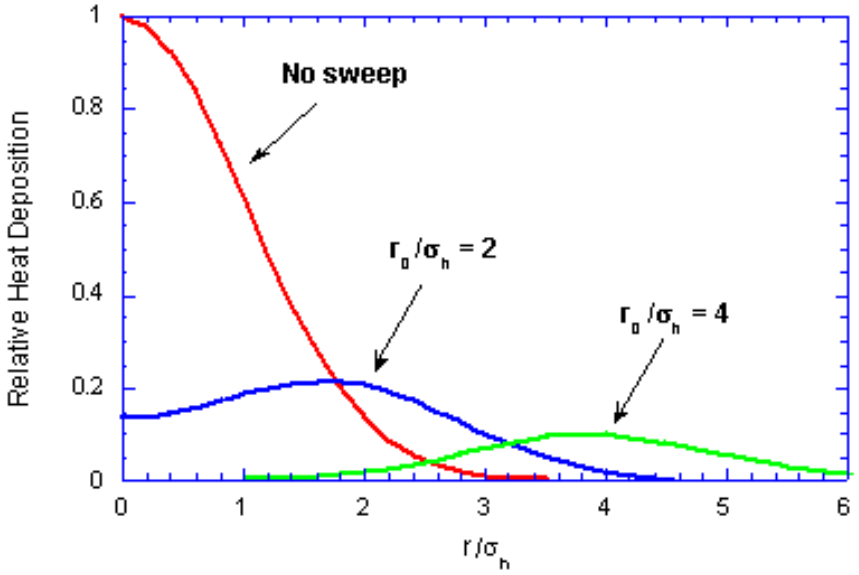

Figure 3.2.25 *Energy deposition as a function of sweep radius.*

The beam sweeping system is designed to trace a 0.33 mm radius circular pattern on the target during the beam pulse. The magnet and power supply designs evolved from this requirement and the need to provide adequate aperture for both the primary and secondary beam. Sweeping the beam 0.33 mm results in a factor of five reduction in peak energy deposition for beam with a spot size of 0.16 mm, and a factor of eight reduction with a spot size of 0.1 mm (Figure 3.2.25). This would allow targeting beam at $1x10^{13}$ per pulse with a spot size of 0.1 mm without damage or melting to the nickel target. As described earlier, antiproton yield is nearly maximized with a spot size of 0.1 mm.

There are two upstream magnets to sweep the beam on the target, and one magnet located immediately downstream of the collection lens to unsweep the beam. The upstream and downstream magnets are identical in design with a 2.8 cm aperture and a 56 cm length (Figure 3.2.26). Although the magnets themselves are interchangeable, the support structures and power striplines are very different. The magnets have a 2-phase, 4-conductor winding excited by two power supplies that deliver sinusoidal current waveforms in quadrature to generate a 625-kHz rotating dipole field. The field uniformity would not have been adequate without twisting the conductors by 180° over the length of the magnet. With this arrangement, the field along the beam path is uniform and rotating.

Approximately 6 kA will be required in the windings to provide a 900 G deflecting field. The peak inductive voltage drop is only 5 kV (2.5 kV to ground), reducing the risk of breakdown in the ionized environment created by the secondary beam shower. Mo-Permalloy pressed-powder cores were used because of the ease of construction and the relatively high thermal conductivity and Curie temperature of this material.

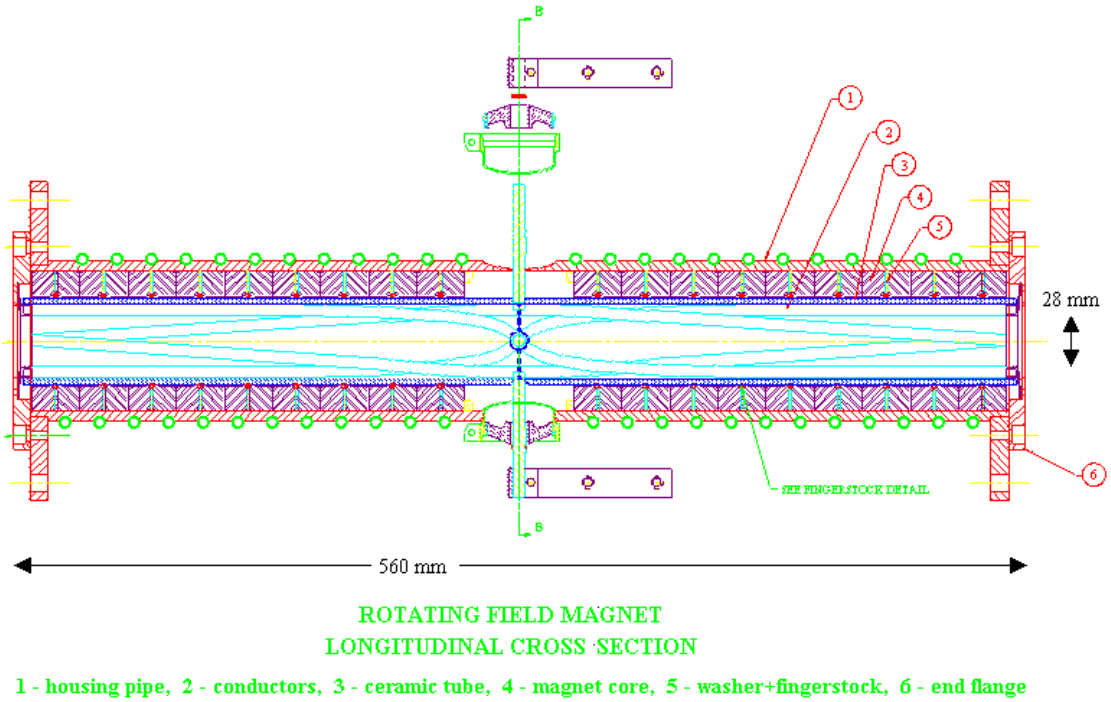

Figure 3.2.26 *Beam sweeping magnet.*

The power supplies are located on the floor of the AP-0 service building, about 15 m from \the sweeping magnets. The power supplies use pulse compression to excite a ringing circuit. Two-stage compression with saturated reactors were chosen to facilitate the transfer of the current pulse to the ringing circuit and to provide the capability to utilize a SCR switch for resonant charging of the first stage. The power supply has been somewhat over-designed and may be able to deliver up to 80% more current if a larger sweeping radius is needed in the future. The timing of the current pulse is very sensitive to component temperature, so a computer driven feedback control is required to compensate. The sweeping and unsweeping magnets also need to be precisely timed with respect to each other.

3.2.4.2 Plan and status

When the beam sweeping project was begun, it was scheduled to be completed in parallel with the construction of the Main Injector. The project is behind schedule at this point, although most of the major fabrication has been done. The sweeping magnet power supplies are essentially a custom design and many of the components were not available commercially. All of the personnel originally involved in the project have left Fermilab so there have been inefficiencies due to lack of experience.

Presently, one of the bipolar power supplies has been test pulsed approximately 2 million times. This power supply is being tested with the downstream module, stripline and magnet assembly at AP0. The two upstream sweeping power supplies have also been completed and are being tested and matched. If there aren't any major component failures during the testing phase, the power supplies will be deemed operational and tunnel installation will begin. There is also a rather complex stand-alone controls system that keeps the upstream and downstream magnet synchronized. It will be tested at AP0 with the existing test setup.

The magnets and stripline assemblies have had several design flaws that have required attention. In some cases, a total redesign has been required to make the components functional. A request was made to keep the upstream sweeping magnets under vacuum, requiring the design and fabrication of a ceramic beam pipe. A realistic goal would be to have them ready for installation in the tunnel during the winter of 2001/2002.

Despite the delays in implementing the sweeping system, it hasn't caused a serious reduction in antiproton yield yet. As the Main Injector intensity increased to $5x10^{12}$ ppp, there was no obvious loss of antiproton yield. The spot size on target was somewhat larger than optimal, planned lattice changes will allow a reduction in spot size. When the spot size is reduced, there will likely be local melting in the target and some loss in yield. After an initial testing program is completed with the sweeping components out of the tunnel, testing with beam will commence. Prior to installing the downstream sweeping magnet in the vault, the upstream sweeping magnets will be installed and tested with beam. The secondary emission monitor located just upstream of the target and beam position monitors in AP-2 can be used to detect beam motion. After confidence is gained in the upstream magnets, the downstream magnet can be installed and the testing phase completed. The downstream magnet will be located in an extremely radioactive environment. Once it is in place, it will be difficult to do any significant mechanical modifications due to residual radiation. The goal would be to enter the beam-testing phase in the spring 2002, with the system operational in summer 2002.

3.2.4.3 Budget and manpower requirements

The beam sweeping system is expected to be commissioned in FY '02 after lingering design problems are resolved and a testing program is completed. 50 k$ of M&S will be required to complete these tasks with 1.1 FTE of labor. The majority of the labor will be technician time for correcting design flaws and testing the equipment. The system should shift to operational use in FY '03.

	Total	M&S	Labor	Phys.	Eng.	Draft	Tech	CP
FY02	160	50	110	0.2	0.2	0	0.6	0.1
FY03	0	0	0	0	0	0	0	0
FY04	0	0	0	0	0	0	0	0
FY05	0	0	0	0	0	0	0	0
Project	160	50	110	0.2	0.2	0	0.6	0.1

Table 3.2.3 *Funding profile for beam sweeping*.

3.2.5 AP-2 and Debuncher aperture improvements

3.2.5.1 Technical description

3.2.5.1.1 Alignment

Alignment of many components is done via surveys. Beam studies can also be used to align accelerator components.

3.2.5.1.1.1 Survey

The AP-2 beamline and Debuncher ring will be surveyed as needed and when manpower is available. In particular, the sections of the accelerator that have moved due to the tunnel moving: the region where the MI-8 beamline crosses underneath the AP-2 beamline. Survey work will be done to guarantee the overall alignment of AP-1, target station and AP-2. Results of the surveys may lead us to move some elements of the accelerator.

3.2.5.1.1.2 Movable Stands

Beam studies involving the stand of a single accelerator component can be done to center the beam within the component. For some of the Debuncher elements there are stands with remotely controlled motors. A remotely controlled motor can be used to center the element while beam is circulating.

The general procedure is to heat the beam and then move an element until beam loss is observed. By finding the stand positions where beam losses begin, the component can then be centered between the loss making positions.

3.2.5.1.1.3 Portable Quadrupole Alignment Fixture

For components without motorized stands, the procedure will be to study the aperture with local bumps, make an access to move the component, and then repeat the aperture studies to see if an improvement has been made. However, moving such components requires the support of surveyors to determine the amount of the move. Due to the amount of manpower and time needed, this procedure will not be performed often.

A portable quadrupole alignment fixture has been developed. With this fixture, it is believed that the time and manpower needed would be reduced significantly for moving a quadrupole. Using this fixture, the above studies procedure could be performed quickly using only a few people (both studies and access). It is estimated that the fixture can be used on 90% of the Debuncher quadrupoles; the rest of the quadrupoles reside in areas with interfering transfer or cryogenic lines.

3.2.5.1.2 Physical Apertures

The expected beam size and aperture of components are being compared to see if there will be future restrictions as the acceptance of AP-2 and Debuncher increase. Below are the areas/elements that are currently being investigated.

3.2.5.1.2.1 Debuncher Injection Region

The AP-2 beamline injects vertically into the Debuncher ring. The injection channel has been modified recently with the replacement of the injection septum and

reorientation of a few Debuncher quadrupoles. After the injection septum, there is a BPM-quadrupole combination. The BPM and star-chamber beam pipe through the quadrupole are special larger aperture versions of these types of components and have been offset vertically during the recent work. A picture looking down the vacuum chamber (taken during the installation of the new injection septum) shows that the top of the BPM appears to be lower than the wall of the upper part of the star-chamber. The vertically injected beam may be hitting the top of the BPM. Even with moving the BPM, the quadrupole could still be an aperture for greater than 35 mm-mrad injected beam.

The current SQC quadrupole can be replaced with a LQD quadrupole. The LQD pole-to-pole distance is nearly the same diameter of the extended star-chamber inside of the SQC; a large star-chamber made to fit within a LQD will have plenty of aperture. The Debuncher dipole bus and a 200A power supply could power the LQD to achieve the same field strength as the current SQC. The BPM can be placed on the downstream side of the quadrupole.

3.2.5.1.2.2 RF Cavities

Three RF cavities are located in regions of high dispersion in the Debuncher. With larger acceptance, the increased beam size combined with dispersion may cause DRF1-1, DRF2 and DRF3 to become aperture restrictions. DRF1-1 and DRF2 are located in the same lattice locations (D=1m) while DRF3 resides where the dispersion is 1.6m. The smaller DRF2 and DRF3 cavities are located in the first region of dispersion after injection. Relocating the cavities to low dispersion regions (~0m) would remove the dispersion contribution to the beam size through these cavities.

3.2.5.1.2.3 Debuncher Cooling Band 4

The separation of the arrays in the band 4 tanks of the Debuncher cooling system is 38.1 mm. For the upstream ends of the horizontal band 4 tanks, β_h is 9.2 m. β_v is 11.2 m at the upstream end of the vertical band 4 tank. With the current arrays, the β functions would have to be less than 9.1 m to achieve 40 mm mrad. The current tanks provide horizontal and vertical apertures of 38.4 mm mrad and 32.4 mm mrad, respectively.

3.2.5.1.2.4 Dipole Beam Pipes

The beam pipe within the dipoles of AP-2 and the Debuncher are not curved. In some cases, the dipoles themselves are not curved: modified wide-gap B1 magnets and four 6-4-120 magnets in AP-2. A straight magnet is oriented to be parallel to the orbit in the middle of the magnet and offset so that the beam's curved orbit does not hit the vacuum chamber wall. The other dipoles, two wide-gap SDE magnets in the AP-2 and all of the Debuncher SDD magnets, are curved but the vacuum chamber is made up of two straight rectangular pipes welded at an angle.

3.2.5.1.3 Orbit Correction

Improved orbit control will make it easier to avoid aperture obstructions. Due to the Debuncher cooling upgrades, many trim dipoles were removed and there is not much real estate to apply trims in new locations.

3.2.5.1.3.1 AP-2

Currently, AP-2 steering is done with a total of nine trim dipoles spread throughout the beamline. Changes in any of the trim dipoles affect the entire orbit; additional steering is required. The decommissioned Debuncher trim dipoles and power supplies can be applied to the AP-2 beamline. The only new items will be stands for the trim dipoles (the AP2 beamline hangs from the enclosure ceiling) and cable runs. Also individual shunts on the major left bend (six dipoles) will be installed to provide steering.

3.2.5.1.3.2 Debuncher

There are few places in the Debuncher where trim dipoles can be inserted. Due to this space limitation, remotely controlled Debuncher quadrupole stands will be used to induce dipole kicks. One advantage of movable stands is that kicks in both planes can be implemented.

3.2.5.1.4 BPM Systems

The BPM systems of AP-2 and the Debuncher are based upon a Z80 processor data acquisition. The knowledge to keep these electronics functioning is limited and the Debuncher BPM system with its multiplexer switch and gain system make the BPM systems not very reliable and hard to maintain. Parts of the BPM electronics and data acquisition system will be replaced.

3.2.5.1.4.1 AP-2

The AM/PM RF modules of the AP-2 BPM system will be retained while new sample-hold electronics and a commercial data acquisition will be implemented. The data acquisition will communicate with an ACNET front end via Ethernet. All changes are done upstairs in the service building; no accesses will be necessary for implementation.

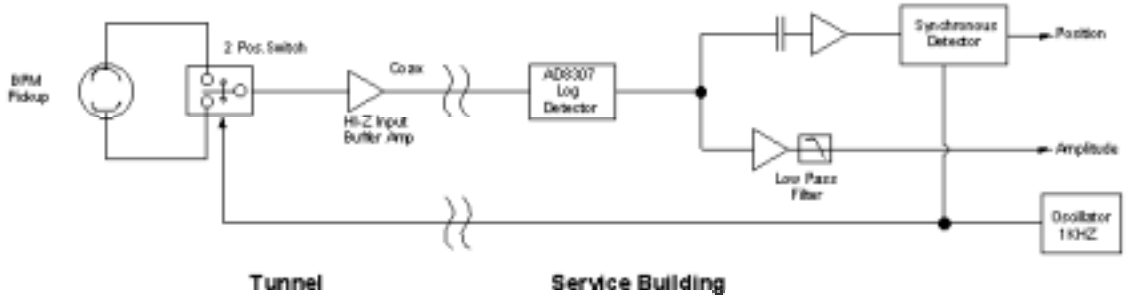

Figure 3.2.27 *BPM system*

During reverse proton studies of the AP-2 line, it is desirable to have the beam position measured between quadrupoles IQ1-4 and the lithium lens. A BPM assembly could be installed in an available slot in the target vault to provide beam positions in both planes.

3.2.5.1.4.2 Debuncher

The current Debuncher BPM system was designed to be used in a closed orbit mode (2.5MHz) and a turn-by-turn mode (53MHz). Historically, the latter mode has not been used much. The new BPM systems will be specialized to perform closed orbit

measurements. The Debuncher BPM system consists of 120 beam pickups. The signals are routed to six "houses". Each house handles 20 channels of BPM data.

Generally signals from each of the pickups, here referred to as A and B, are combined in hardware to give sum and difference signals or are brought individually to the electronics for further processing. Matching the signal paths and calibrating out the differences can be costly. This design attempts to alleviate some of the problems by using only one RF signal path and switching between A and B signals.

A solid state RF switch is positioned as close to A and B pickup outputs as practical. This minimizes the length of the connecting line and allows for easier gain matching. The output of the RF switch is routed up to the service building where the rest of the electronics are located. The RF signal is received by a logarithmic amplifier whose output is proportional to the log of the amplitude of the received signal. Rapidly alternating the RF switch between A and B channels produces an amplitude modulated signal. This amplitude modulation is proportional to the amplitude difference between A and B pickups and appears at the output of the log amp as square wave modulation riding on the average signal level. A synchronous detector, implemented either by an op-amp circuit whose gain is switched between +1 and -1 or by subtracting alternating samples from an A/D converter, is used to recover the amplitude of the modulated signal. Synchronous detection is a very powerful method of signal recovery.

The tunnel electronics consisting of protection diodes, solid state switch, buffer amplifiers, calibration coupler and regulators are contained in a connectorized box similar to the one used in the Accumulator BPM's. The switch is operated by a buffered TTL signal from the service building electronics. The beam is bunched by an existing 2.5 MHz RF system. An Analog Devices AD8307 Log Detector receives the amplitude modulated 2.5 MHz signal. The dynamic range is -60 dBm to +12 dBm. The output of the log detector can either be synchronously demodulated by an Analog Devices AD630 or sent to an A/D converter and demodulated in software. Hardware demodulation has the disadvantage of requiring individual alignment of each channel. A test unit uses a standard 200 MHz Pentium desktop computer with a National Instruments PCI-6032E 16 channel, 16 bit, 100 ksample/sec converter card. A PC104 format processor and A/D card will be tested soon. Approximately 80,000 floating point operations per second are required to digitally process the data for each house. Once processed, the intensity and position data will probably only need to be updated at 15 Hz or slower. The house processors will communicate with an ACNET front-end processor via Ethernet. The front end will format the data streams for presentation to the standard ACNET Console and provide for further data processing and presentation. A simple TCP/IP protocol has been demonstrated to work between the house processor and the front end.

3.2.5.1.5 Debuncher Lattice

Improved AP-2 and Debuncher apertures will allow beam to be spread out over a greater phase space than what has been handled by the Debuncher before. It is not apparent that the Debuncher is capable of performing all the necessary functions to the beam in additional phase space. Studies of the Debuncher will be done to determine if there is any need for lattice upgrades.Three possible lattice improvements are being considered to ensure that the dynamic aperture exceeds the physical aperture and optimizing the lattice for both RF bunch rotation and stochastic cooling. There is no

provision in the Debuncher for skew-quadrupole errors, which could further increase the beam size and cause the beam to be scraped; skew-quad correctors may be needed. The Debuncher operates with a tune near 9.75 in both planes; it is not known if beam in the additional phase space will interact with either fourth order resonance and require octupole correctors. A γ_t ramp may be desirable to provide a sufficiently large RF bucket for bunch rotation (small value of η increasing the momentum aperture at injection) and sufficient mixing for stochastic cooling (large value of η).

3.2.5.2 Plan and status

3.2.5.2.1 Alignment

3.2.5.2.1.1 Survey

The Antiproton Source has a standing request to perform surveys when the resources are available. Hopefully over the next year, the surveying requirements for the rest of Fermilab will allow the surveying of AP-1, target station, AP-2 and Debuncher.

On occasion, quick surveys of suspect single components have been. During the Fall 2001 shutdown, the DRF2 and DRF3 cavity tanks showed elevated levels of radioactive activation to the inside (of the Debuncher ring). Mis-alignment was considered with other possibilities for the explanation of the activation (decay products after the first dipole in the Debuncher, mis-steering of the beam and first aperture restriction in the Debuncher). Surveyors found both ends of each tanks off the centerline defined by the surrounding quadrupoles; the tanks have been aligned. As studies and measurements indicate, surveys and alignment of specific components will be done.

3.2.5.2.1.2 Movable Stands

Most of the Debuncher pick-ups and kickers are movable. These stands have been, and will continued to be, exercised to center the component on the beam. At this time, the only plans for adding new movable stands is for quadrupoles to be used for beam steering (see below).

3.2.5.2.1.3 Portable Quadrupole Alignment Fixture

An early prototype for the alignment stand is currently being worked on. Some engineering work still needs to be done to mount the necessary measurement calipers to the device. High accuracy digital calipers have already been procured. The fixture should be completed and ready for lab testing early 2002. To use the fixture in the tunnel will require frequent access interspersed with beam studies to position the quadrupole; this procedure is expected to take 1-2 shifts per quadrupole. .

3.2.5.2.2 Physical Apertures

3.2.5.2.2.1 Debuncher Injection Region

The LQD magnets are used in one place of the Accumulator lattice (6 total). Currently, there is only one spare LQD. The option to build another LQD is being investigated. If the existing LQD is inserted, the SQC with the modified star-chamber will be left in the tunnel ready for easy re-insertion if the LQD is needed in the

Accumulator. A special beam pipe for the LQD needs to be made and new bellow-flange units will have to be designed and fabricated.

3.2.5.2.2.2 RF Cavities

Three DRF3 options that have been proposed:

Option 1) Move DRF3 upstream by 34". It will require no cabling work, just vacuum. Since D' between D5Q10 and D5Q11 is non-zero, the closer to D5Q10, the better. This move reduces dispersion from 1.6 M to ~1.4 M.

Option 2) Move DRF3 from its present position between D5Q10 and D5Q11 to the upstream end of D5Q10. This will require IP510 (ion pump) be moved to the downstream end of D5Q10, and DRF2 moved upstream to make enough room. Again, no cabling work is necessary, but vacuum work and welding will be. A bellows will need to be added between the cavities. The dispersion at DRF3 then goes from 1.6 M down to 1.05 M. This looks like a best first thing to try.

Option 3) DRF3 can be relocated to the downstream end of the adiabatic cavity DRF1-8 (between D5Q6 and D5Q7). Dispersion here is –0.002 M. To make this work, DRF1-8 will need to be moved upstream by 18" and have 3" of beam pipe trimmed off each end. IP506 will need to be moved to the upstream end of D5Q6. Also, the RF phase for DRF1-8 would need to be changed (cabling upstairs) and the fan-back cable shortened to compensate for the reduced time of flight between cavities. Bellows between cavities and a spool piece to replace DRF3 at its old location will be needed. This move is nice because if we do decide to move any other RF in the Debuncher, the DRF3 cavity will not need to be relocated again.

Unfortunately, moving DRF2 or DRF1-1 is considerably more involved. However, it is possible to put every one of the RF cavities in a region of low dispersion.

1) Remove both DRF2 and DRF3 from their present positions and replace the sections with large aperture spool pieces. Install both cavities between D5Q6 and D5Q7 where DRF1-8 presently is. This will not require any upstairs changes, just re-routing DRF2 and DRF3 cables.

2) For the adiabatic cavities, remove DRF1-1 and DRF1-8 from the beamline and move them both over to D20. At present, there is room between D2Q7 and D2Q6 for DRF1-1 if the horizontal and vertical trim dipoles are removed and a movable quad stand is placed under either of these two quads. DRF1-8 could be installed between D2Q6 and D2Q5 if the pump-out port and ion pump are moved to one end of the straight.

3) The issues concerning controls for the adiabatic cavities are much more involved. Presently, there is enough room in AP30 to house all of the amplifiers and low level equipment. There is also the matter of bringing the necessary RF signals in for system drive and phase lock.

3.2.5.2.2.3 Debuncher Cooling Band 4

The Debuncher cooling band 4 arrays would have to be redesigned so that the separation of the arrays is at least 42.3 mm to achieve 40 mm mrad aperture. Other choices include decreasing the beta functions through the tanks or removing band 4 cooling. Studies will be performed to determine the effect of removing band 4 from the overall cooling system.

3.2.5.2.2.4 Dipole Beam Pipes

Simulations will be performed to determine if any of the dipole vacuum chambers need to be replaced. New beam pipes will have to be designed and installation will require significant downtime. This is work that would not be done in the next few years.

3.2.5.2.3 Orbit Correction

3.2.5.2.3.1 AP-2

The elements of AP-2 are well separated with the exception of components at the upstream end (prior to quadrupole Q704), in the major left bend (between Q716 and Q721) and at the downstream end (Q730 to the injection septum).

Forward proton studies (requiring the polarity to the AP-2 beamline and Debuncher to be switched) done in February 2001 showed a *bouncing* horizontal orbit during the first long straight section. The horizontal bend elements at the upstream end of AP-2 are the momentum selecting magnet (PMAG) within the target station and a short left bend dipole H704; the first horizontal trim dipole is after Q711: HT711. The phase advance between PMAG and H704 is nearly 180^o. The distance between Q704 and H704 is 6m. A horizontal trim dipole (proposed HT704) placed directly downstream of quad 704 would be 90^o from both PMAG and H704.

Vertical orbit correction at the upstream end of the AP-2 beamline is done by two trim dipoles: VT702 and VT706. These trims are not optimally situated since the phase advance between them is 135^o. If a new trim dipole (proposed VT704) is added near H704, then the phase advance from VT702 will be 90^o. Unfortunately, the current vertical beta function passes through a minimum (4 meters) at H704.

At the down stream end of AP-2, one needs to be concerned about the position and angle to the entrance of the injection septum. In the horizontal plane, HT730 and HT731 are ideally situated at respectively 180^o and 90^o in phase advance from the injection septum. Vertically, the only control is the downward bend dipole V730, which is phase advance 360^o prior to the entrance to the injection septum. Another vertical correction device is desired. At 90^o prior to the injection septum is Q732 in a well-packed region. Further upstream, VT730 could be inserted directly after HT730 and would be nearly at the correct phase advance. Otherwise, one would need to go to 450^o in phase: just prior to Q727 and 48m from the injection septum. Proposed VT727 is desirable anyway for position control at V730. The difficulty with inserting VT730 is that the beam line is headed downward and essentially above the Debuncher. Whereas the other correction dipoles will be a relatively straightforward installation, VT730 will be more difficult due to its location and orientation.

During the Fall 2001 shutdown, shunts have been added to six dipole magnets providing horizontal control through the major left bend. If vertical control is deemed necessary through the bending section, then there is plenty of room to insert dipole trims.

Due to limited manpower, none of the dipole trims have been installed. It will probably take two shutdown days to install a stand, dipole trim and cables per location; the exception is the proposed VT730.

3.2.5.2.3.2 Debuncher

For the last year, five motorized stands have been used in the Debuncher. In both planes, local bumps have been successfully implemented by using a combination of these movable quads and existing trim dipoles. Ten more of these stands (9 SQC and 1 SQD style) were constructed this last summer and the flexible bellows have been ordered. These will be installed in the first half of 2002 when manpower and shutdowns permits (several days). The injection, extraction and cooling system pickup regions are the priority. To have a complete set of local orbit bumps, an additional twenty motorized quadrupole stands will be needed. Beam studies will help define where further motorized stands will be needed for orbit control.

3.2.5.2.4 BPM Systems

3.2.5.2.4.1 AP-2

CDF collaborator Alexei Semenov designed a new sample-hold unit during 2001. Five prototype boards have been fabricated; final assembly of the board and testing need to be done. A few commercial available WebDAQ units have been purchased. Brian Winer and Richard Hughes of Ohio State University (CDF) along with Beams Division Controls Department have shown that java programs can communicate with the WebDAQ within the ACNET environment. Clock-trigger cables will have to be pulled to each house location. In 2002, testing will be done by installing a house in parallel with the existing system in AP50. To implement along the entire AP-2 beamline, the F27 service building needs to have Ethernet installed.

There are presently no BPM's located in the target vault. It would be desirable to have at least one BPM in each plane in the vault to improve orbit measurements of AP-2 made with reverse protons. A new BPM assembly will need to be fabricated and adapted for use in the target vault. Support electronics will also be required as there are presently none in the AP-0 service building.

3.2.5.2.4.2 Debuncher

Using a Stanford Research model DS345 Function Generator as a modulated signal source and a Tektronix TDS3012 oscilloscope as the synchronous detector, modulation of 0.02 dB can be clearly detected. A signal with no modulation results in an equivalent noise floor of 0.002 dB. Figure 3.2.28 shows the test setup used to characterize the performance of the log amp and data acquisition system. With a 3 dB difference between A and B signals, the worst-case (when not calibrated) error was 0.16 dB. Calibration reduced the worst-case error to 0.05 dB. The average deviation was 0.0095 dB. On a test stand, an Accumulator style split sleeve BPM pickup has been investigated. Scaling to the larger Debuncher BPM pickup, the central sensitivity between 2.5 MHz and 53 MHz is 0.373 dB/mm. Plate to plate isolation is 40 dB at 2.5 MHz.

In FY2001, Fermilab Record of Invention FAA-783 was submitted. Demonstration of performance of synchronous detection has been shown. Printed circuit

cards have been fabricated for the pickup switching and buffer electronics as well as for the log detector and synchronous demodulator electronics. Data acquisition using a 16 channel 16 bit PCI A/D converter card was shown to work in a modest desktop PC. A java based Open Access Client (OAC) was demonstrated for transferring measurement data from a PC to ACNET.

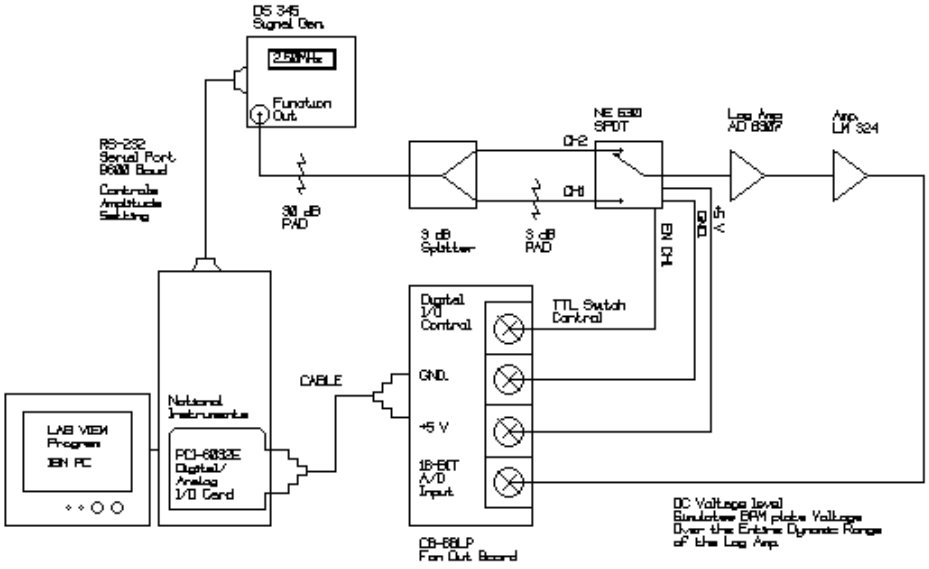

Figure 3.2.28 *BPM system*

Bench testing of the switching preamp will be conducted at the beginning of FY2002. Additional measurements of the full aperture response of a split plate BPM pickup will be done to fully characterize the non-linearities. A PC-104 industrial computer will be tested for data acquisition and demodulation. Additional work will begin be done on the OAC to communicate with small processors using standard TCP/IP requests.

A beam test using the synchronous demodulation scheme on a single BPM will be done early in 2002. It is expected that a full (20 BPM) house will be ready for testing in the spring of 2002; installation will depend upon the availability of tunnel time. Installation of all 120 preamps in the tunnel could be completed by fall 2002. Early in FY2003, the installation of service building electronics and commissioning of the system and application software will be done.

3.2.5.2.5 Debuncher Lattice

The Debuncher lattice model is being upgraded and studies will be performed to verify the lattice model. Further studies and modeling will be done to investigate possible problems with the larger beam phase space in the Debuncher. The results of the studies and modeling will determine if any upgrades are needed.

3.2.5.3 Budget and manpower requirements

Most of the projections are “top-down” due to the nature of not knowing the results of studies or simulations. The estimates assume that all projects are necessary. The

projections given below present labor in the following format: Phys./ Eng./ Tech./ Draft./ Comp. Prof. FTEs.

3.2.5.3.1 Alignment

Alignment will be ongoing project. In FY02, the portable quadrupole alignment fixture will be finished. The FY02 cost is 50 k$ and labor is 0.2/0.0/0.2/0.0/0.0. The estimates for FY03-FY05 are 25 k$ and 0.2/0.0/0.1/0.0/0.0.

	Total	M&S	Labor	Phys.	Eng.	Draft	Tech	CP
FY02	90	50	40	0.2	0	0	0.2	0
FY03	55	25	30	0.2	0	0	0.1	0
FY04	55	25	30	0.2	0	0	0.1	0
FY05	55	25	30	0.2	0	0	0.1	0
Project	255	125	130	0.8	0	0	0.5	0

Table 3.2.4 *Funding profile for aperture alignment.*

3.2.5.3.2 Physical Apertures

Studies in FY02 will define the path for the following years. Projects will start in FY02 with costs and labor of 200 k$ and 0.3/0.2/0.2/0.2/0.0. The main project years will be FY03 and FY04; each will incur costs and labor requirements of 600 k$ and 0.3/0.5/2.0/1.0/0.0. The projects will be finish in FY05: 250 k$ and 0.3/0.2/1.0/0.2/0.0.

	Total	M&S	Labor	Phys.	Eng.	Draft	Tech	CP
FY02	290	200	90	0.3	0.2	0.2	0.2	0
FY03	980	600	380	0.3	0.5	1	2	0
FY04	980	600	380	0.3	0.5	1	2	0
FY05	330	250	80	0.3	0.2	0.2	0.1	0
Project	2580	1650	930	1.2	1.4	2.4	4.3	0

Table 3.2.5 *Funding profile for physical aperture project*.

3.2.5.3.3 Orbit Control

Most of the orbit control will be done during the FY02 and FY03; each will be 200 k$ and 0.5/0.1/0.2/0.2/0.2. The final two years, FY04 and FY05, will be to do fine tuning of the orbit control: each 75 k$ and 0.2/0.0/0.1/0.1/0.0.

	Total	M&S	Labor	Phys.	Eng.	Draft	Tech	CP
FY02	320	200	120	0.5	0.1	0.2	0.2	0.2
FY03	320	200	120	0.5	0.1	0.2	0.2	0.2
FY04	115	75	40	0.2	0	0.1	0.1	0
FY05	115	75	40	0.2	0	0.1	0.1	0
Project	870	550	320	1.4	0.2	0.6	0.6	0.4

Table 3.2.6 *Funding profile for orbit control project*

3.2.5.3.4 BPM Systems

The goal is to get both systems operational as soon as possible to help with the studies. It is expected that the work can be completed in FY02 and FY03; each will cost 100 k$ and the labor will be 0.2/1.5/2.0/0.0/1.0.

	Total	M&S	Labor	Phys.	Eng.	Draft	Tech	CP
FY02	570	100	470	0.2	1.5	0	2	1
FY03	570	100	470	0.2	1.5	0	2	1
FY04	0	0	0	0	0	0	0	0
FY05	0	0	0	0	0	0	0	0
Project	1140	200	940	0.4	3	0	4	2

Table 3.2.7 *Funding profile for BPM systems project*

3.2.5.3.5 Debuncher Lattice

In FY02, studies and initial designs will be done incurring no cost, 0 k$; labor will be 1.0/0.2/0.1/0.1/0.0. The projects will mainly be done in FY03 and FY04 each incurring cost of 500 k$ and using labor of 1.0/1.0/2.0/0.8/0.5. The projects should finish in FY05: 200 k$ and 0.5/0.2/1.0/0.2/0.5.

	Total	M&S	Labor	Phys.	Eng.	Draft	Tech	CP
FY02	140	0	140	1	0.2	0.1	0.1	0
FY03	1030	500	530	1	1	0.8	2	0.5
FY04	1030	500	530	1	1	0.8	2	0.5
FY05	440	200	240	0.5	0.2	0.2	1	0.5
Project	2640	1200	1440	3.5	2.4	1.9	5.1	1.5

Table 3.2.8 *Funding Profile for Debuncher lattice upgrade*.

3.2.6 Conclusion

By implementing the upgrades suggested in this section, antiproton yield in the Debuncher could approach 40×10^{-6} antiprotons per proton. After examining the physics principles involved in targeting and collecting beam, it is clear that increasing the aperture of AP-2 and the Debuncher is the surest way to increase antiproton production efficiency into the Debuncher. Increasing the number of protons on the production target with Main Injector slip-stacking is described in another section, it will bring a nearly linear increase in antiproton flux into the Debuncher. The challenge with slip-stacking from the perspective of the antiproton source is to maintain the same production efficiency from the target station with increased heating of the target. The beam sweeping system should be able to accomplish this goal and should be operational before the Main Injector intensity is increased.

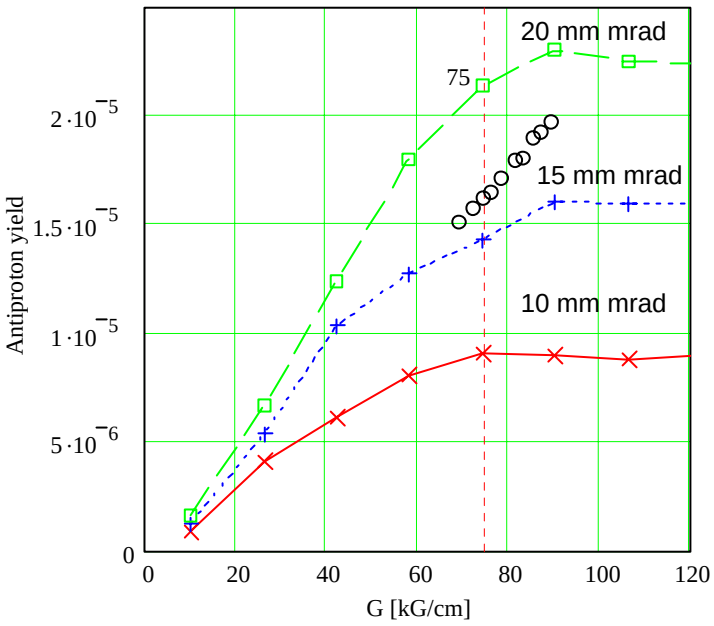

Figure 3.2.29 *Modeled lens gradient vs. yield with experimental data.*

Considerable effort has been put into increasing the gradient of the lithium lens while preserving a reasonable operational lifetime. The motivation for increasing the lens gradient has been based on measurements made during Collider Run I. The measurements suggested that a nearly linear relationship existed between antiproton production efficiency into the Debuncher and lithium lens gradient. Figure 3.2.29 has data from one of these studies overlaying data generated from the beam model. As our understanding of the antiproton production and collection process improves, so too does the realization that beam spot size, target length, lithium lens strength, the AP-2 lattice and AP-2 and Debuncher apertures are all intertwined in a complex fashion. It is difficult to only change one or two of these parameters in a beam study and generate meaningful results.

Carefully planned and executed beam studies will be crucial in improving our understanding of the present state of the antiproton source and accurately identifying improvements. Measurements of the AP-2 lattice are particularly important for understanding the dynamic aperture of that line and confirming that beam entering the Debuncher is properly matched. Measurements of the relationship between beam spot size on the production target and AP-2 and Debuncher yield can be compared to the model to estimate apertures at various points. For the proposed upgrades to succeed, adequate study time must be provided during Run IIa.

3.3 Antiproton Source Stochastic Cooling

Cooling the large fluxes coming off the target and into the Debuncher and Accumulator is a difficult project. The performance of both systems is a function of the longitudinal density of the incoming beam. We will describe a model and our approach to calculating the longitudinal density delivered from the Debuncher to the Accumulator.

The design choices for the Accumulator stochastic cooling systems were made under the assumption that the Recycler is the final repository for the antiprotons. Since electron cooling performance improves as density increases while stochastic cooling performance declines, we can make some tradeoffs in the system design that optimize it for the maximum flux through the Accumulator rather than maximizing both flux and the momentum density of the accumulated beam.

We will need to upgrade the longitudinal stochastic cooling systems in the Accumulator. The current 2-4 GHz stacktail cooling system, which moves the injected beam from the deposition orbit to the core, was designed to have a maximum flux of ~35 mA/hour. Changes in the system design will be necessary to handle a flux of 60 mA/hour or greater. We use a numerical simulation of the Fokker-Planck equation[23], which includes beam feedback, to predict the performance of the upgrade design.

3.3.1 Antiproton Longitudinal Phase Space

3.3.1.1 Introduction

In this section, the longitudinal phase space of the beam during $\bar{p}$ stacking is traced from the beginning of proton bunch rotation at 120 GeV in the Main Injector to the point at which pre-cooled antiprotons are ready for extraction to the Accumulator. The purpose of this examination is to determine what, if any, performance upgrades are required to achieve a sufficiently narrow $\bar{p}$ momentum spread for stochastic momentum stacking in the Accumulator at the required rate. The processes affecting longitudinal phase space during this part of the stacking cycle are: Main Injector bunch rotation, targeting and collection, Debuncher bunch rotation, and Debuncher momentum cooling. The impact of each of these processes on the longitudinal phase space of the beam will be considered in sequence.

The starting point of the calculations that follow is an estimate of the longitudinal emittance (s_p) of the proton beam at 120 GeV in the Main Injector prior to bunch rotation. This estimate is derived from an ESME[24] model of slip stacking at 8.9 GeV/c in the Main Injector[25]. The phase space distribution of two combined Booster batches prior to acceleration in the Main Injector is shown in Figure 3.3.1. The phase space volume occupied by the beam in this figure is not matched to the RF bucket. Consequently, filamentation will cause the beam to fill up the unoccupied phase space within the bucket and the longitudinal emittance of the beam will approach the RF bucket area. Assuming an additional dilution of 10 to 15% during acceleration and transition crossing, the final proton longitudinal emittance at 120 GeV prior to bunch rotation is estimated to be: s_p = 0.35 eV-sec.

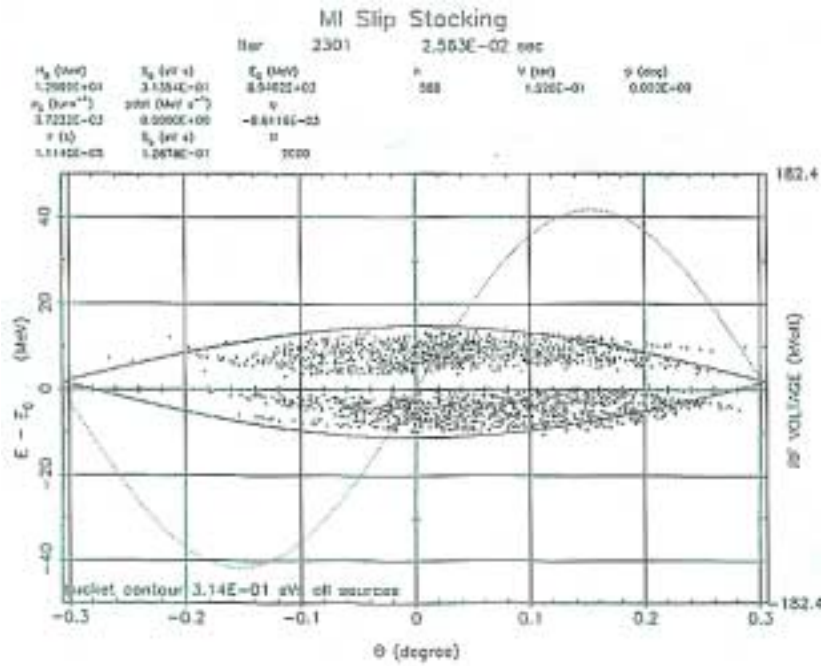

Figure 3.3.1 *Longitudinal phase space distribution of two combined Booster batches at 8.9 GeV/c in the Main Injector. The RF bucket area is 0.31 eV-sec.*

3.3.1.2 Main Injector Bunch Rotation

Main Injector bunch rotation consists to two 90° rotations in longitudinal phase space that function to minimize the bunch length of the proton beam prior to extraction onto the $\bar{p}$ production target. The sequence of RF manipulations that accomplish this is illustrated in Figure 3.3.2. Table 3.3.1 summarizes the Main Injector parameters used in the Run IIb bunch rotation model[i].

Beam Energy	E	120	
GeV Longitudinal Emittance	s_p	0.35	eV-sec
Maximum RF Voltage	V_{max}	4.0	MV
Low voltage value	V_{low}	500	kV
Final Bunch Length (95% Full Width)	Δt	**809**	**psec**
Final Energy Spread (95% ½ Width)	$\Delta E/E$	**0.185**	**%**

Table 3.3.1 *Main Injector Bunch Rotation Parameters*

The increased proton longitudinal emittance from slip stacking causes a slower rotation velocity for high amplitude protons during the final rotation at high voltage. This has the effect of adding beam to the tails of the final bunch length distribution. Figure 3.3.3 compares the nearly linear rotation of 0.10 eV-sec bunches with that of the

[i] The Main Injector bunch rotation model is an ESME model that was originally constructed by Ioanis Kourbanis.

0.35 eV-sec bunches expected during slip stacking. The final slip stacking bunch length and energy distributions are shown in Figure 3.3.4.

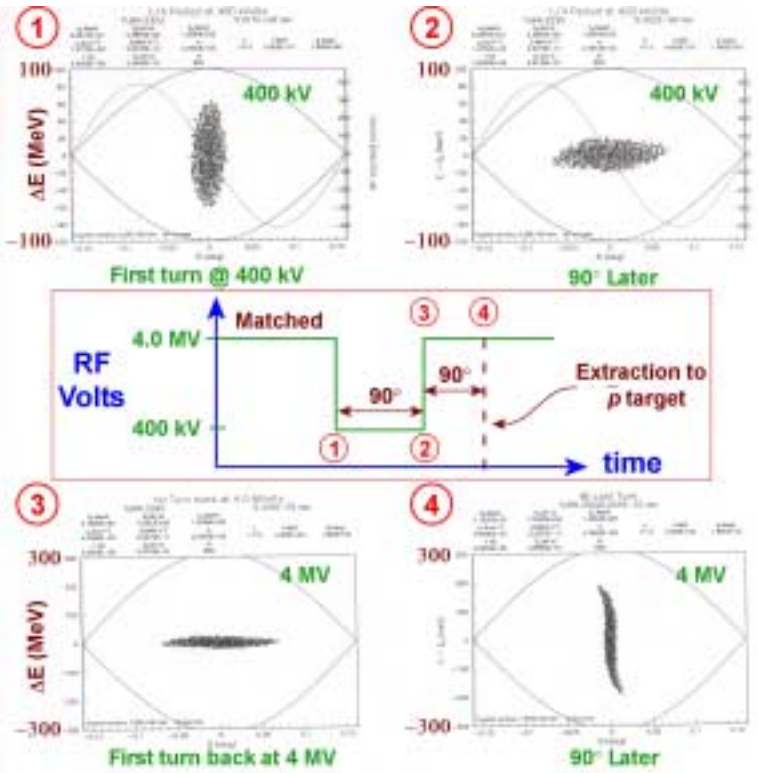

Figure 3.3.2 *The sequence of Main Injector RF manipulations during bunch rotation. The shape of the longitudinal phase space volume occupied by the beam at the various points shown is typical of near linear bunch rotation. Prior to bunch rotation, the phase space occupied by the beam is matched in 4.0 MV buckets. The sequence is initiated by para-phasing the RF cavities down to a few hundred kV (the exact value of the low voltage setting is determined by the longitudinal emittance of the beam). The beam, which is no longer matched to the RF bucket, begins to tumble in phase space (points ① to ②). After a quarter of a synchrotron period, the voltage is rapidly brought back to 4.0 MV (point ③). Since the beam is still unmatched, it will continue to rotate in phase space. The beam is extracted to the* $\bar{p}$ *production target after another quarter period rotation at 4.0 MV (point ④). At this point, the bunch length of the beam is at its minimum.*

It is interesting to note that the bunch length of protons on the $\bar{p}$ production target expected from the Main Injector during slip stacking is very nearly the same as the bunch length that was realized in Run Ib[i] ($s_p \approx 0.25$ eV-sec) from the Main Ring. This coincidence is entirely accounted for in terms of the difference between the Main Ring and the Main Injector. For linear bunch rotation, the following relationship between Main Injector and Main Ring bunch lengths is true:

[i] Run Ib parameters – Longitudinal emittance: $s_p \approx 0.25$ eV-sec, measured bunch length: $\Delta t_{MR} = 800$ psec.

$$\Delta t_{MI} = \sqrt{\frac{s_{MI}}{s_{MR}}}\left(\frac{\eta_{MI}}{\eta_{MR}}\frac{h_{MI}}{h_{MR}}\right)^{1/4}\Delta t_{MR}$$

$$; \quad \sqrt{\frac{0.35}{0.25}}\left(\frac{0.0020}{0.0028}\frac{588}{1113}\right)^{1/4}\Delta t_{MR}$$

$$; \quad (0.774)\sqrt{\frac{0.35}{0.25}}\Delta t_{MR}$$

(3.3.1)

The actual bunch length is slightly larger than that predicted by Eq. (3.3.1) since the rotation for the longitudinal emittance produced by slip stacking is not completely linear.

The large momentum spread of the proton beam after bunch rotation in the Main Injector gives rise to two issues. First, the momentum aperture of the P1, P2, and AP1 beam lines must be large enough to accept the large momentum spread of the proton beam after bunch rotation. This is in fact the case. Secondly, the dispersion function at the target must be small to avoid an increase in the proton spot size with increasing $\Delta p/p$ and the resulting reduction in $\overline{p}$ yield. This also is accomplished in the present AP1 beamline lattice.

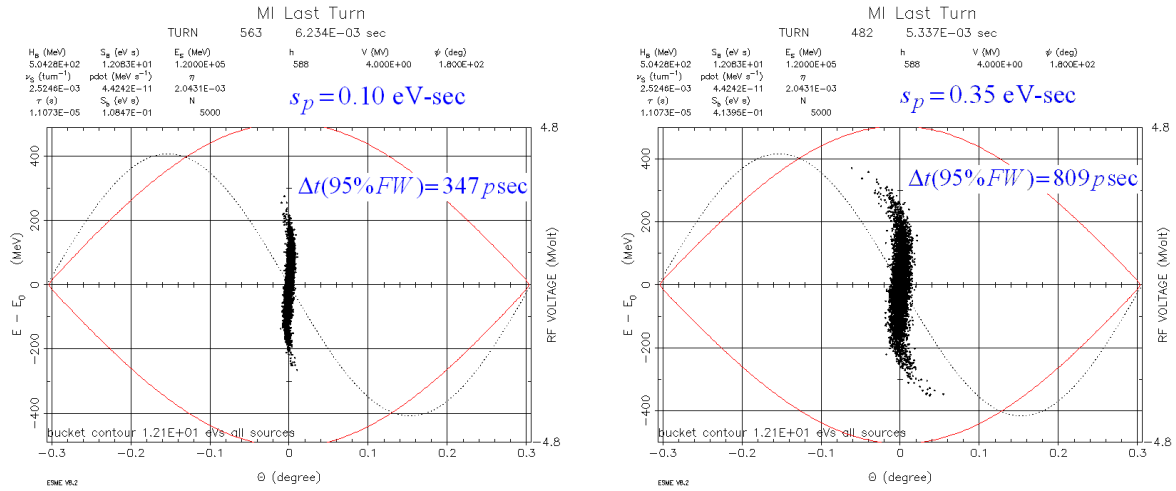

Figure 3.3.3 *Linear and non-linear bunch rotation. Each graph shows the final phase space distribution of the 120 GeV proton beam just prior to extraction. The graph on the left shows the final distribution for protons with an initial longitudinal emittance of 0.1 eV-sec. The graph on the right shows the final distribution for protons with the initial longitudinal emittance expected during slip stacking (0.35 eV-sec). The rotation of high amplitude particles is slower than that of small amplitude particles resulting in tails in the azimuthal distribution.*

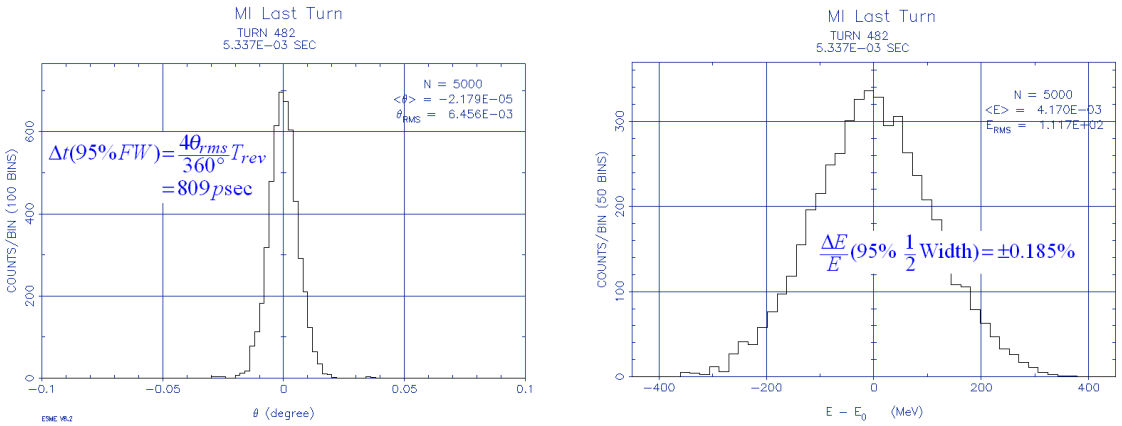

Figure 3.3.4 *Final θ (= $2\pi f_{rev}\Delta t$) and ΔE distributions for Main Injector bunch rotation during slip stacking. The θ distribution on the left shows a final proton bunch length of 809 psec (95% full width). The ΔE distribution on the right shows a final $\Delta E/E$ of 0.185% (95% half width).*

3.3.1.3 Targeting and Collection

The momentum acceptance of the AP2 beam line and the Debuncher is ±2% (±180 MeV/c at 8.9 GeV/c). The $\bar{p}$ production cross-section is essentially constant over this range of energies. Thus, the energy distribution of antiprotons with energies that fall within the momentum aperture of the AP2 line and Debuncher is uniform in energy. Furthermore, since the time scale of the $\bar{p}$ producing proton-nucleon interactions in the target is negligible in comparison to the bunch length of the incident protons, the time structure of the beam from the Main Injector is preserved.

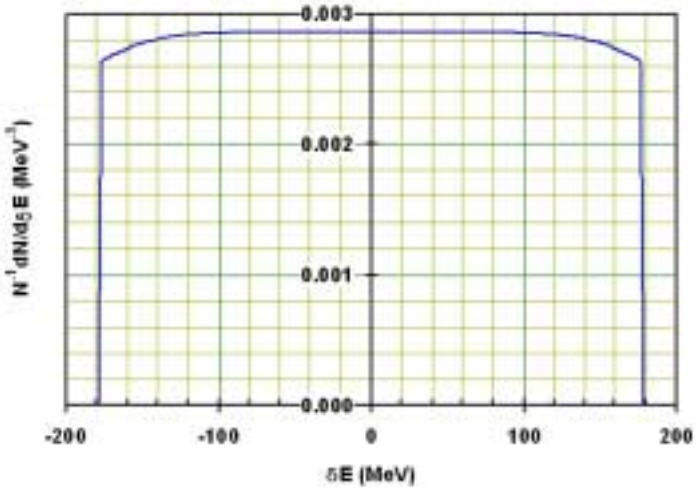

Figure 3.3.5 *Calculated energy distribution of the $\bar{p}$ beam collected from the target into a ±2.0% momentum aperture with a central momentum of 8886.3 MeV/c. The transverse emittances are: $\varepsilon_x = \varepsilon_y = 40\ \pi$ mm-mrad. The momentum aperture limit is assumed to be located at the DRF3 RF cavity in the Debuncher.*

The finite transverse emittances of the $\bar{p}$ beam will modify the momentum distribution at the edges of the aperture. Figure 3.3.5 shows the expected $\bar{p}$ energy distribution just after injection into the Debuncher. This distribution is used as the initial energy distribution for the Debuncher bunch rotation calculation.

3.3.1.4 Debuncher Bunch Rotation

A second RF bunch rotation is performed in the Debuncher. This time the rotation converts the narrow time structure of the beam from the target into DC beam with a narrow energy distribution. The sequence of RF manipulations in Debuncher bunch rotation is illustrated in Figure 3.3.6. The parameters that determine the Run IIb Debuncher bunch rotation model are summarized in Table 3.3.2. The expected $\bar{p}$ energy distribution after bunch rotation is shown in Figure 3.3.7.

Beam Energy	E	8935.7	
Slip factor	η	0.00607	
Momentum Acceptance (95% ½ width)	$\Delta p/p$	±2.0	%
Initial Bunch Length (95% full width)	Δt	809	psec
Rotator Cavity Sum Voltage	V_{rot}	5.0	MV
Bunch Rotation Time	t_{rot}	60	msec
Final Energy Spread (95% ½ Width)	$\Delta E/E$	**±0.134**	**%**
Final Energy Spread (95% ½ Width)	ΔE	**±12**	**MeV**

Table 3.3.2 *Debuncher Bunch Rotation Parameters*

The relationship between the proton bunch length and Debuncher $\Delta p/p$ after bunch rotation was calculated for the TeV33 Report[2]. The results of this calculation are shown in Figure 3.3.8. This analysis indicates that very little is gained by reducing the proton bunch length below 800 psec. Furthermore, the minimum $\Delta p/p$ achievable with the present Debuncher RF bunch rotation is approximately 0.25%. The cause of this performance limit is the finite amount of time that is required to drive the rotator cavity voltage down to 90 kV from 5 MV. During this time the beam is still rotating in phase space with the rotation becoming increasingly non-linear as the voltage is lowered. The resulting S-shaped phase space volume will always have a larger energy spread than the flat line that would be obtained if the rotation were linear.

Two remedies to this non-linear rotation in the Debuncher have been considered: (1) second harmonic (106 MHz) correction, and (2) a reduction in the value of η in the Debuncher. Neither of these remedies, when implemented without the other, gives any appreciable improvement in bunch rotation for initial bunch lengths below 1 nsec. If, however, both are implemented together, the model suggests that the reduction of $\Delta p/p$ would continue well below an initial bunch length of 1 nsec (see Figure 3.3.8). Implementation of these bunch rotation improvements is likely to be difficult and costly. Moreover, the improvement indicated for the initial bunch length expected during slip stacking is small. Therefore, they are not presently included in the scope of the upgrades proposed for Run IIb.

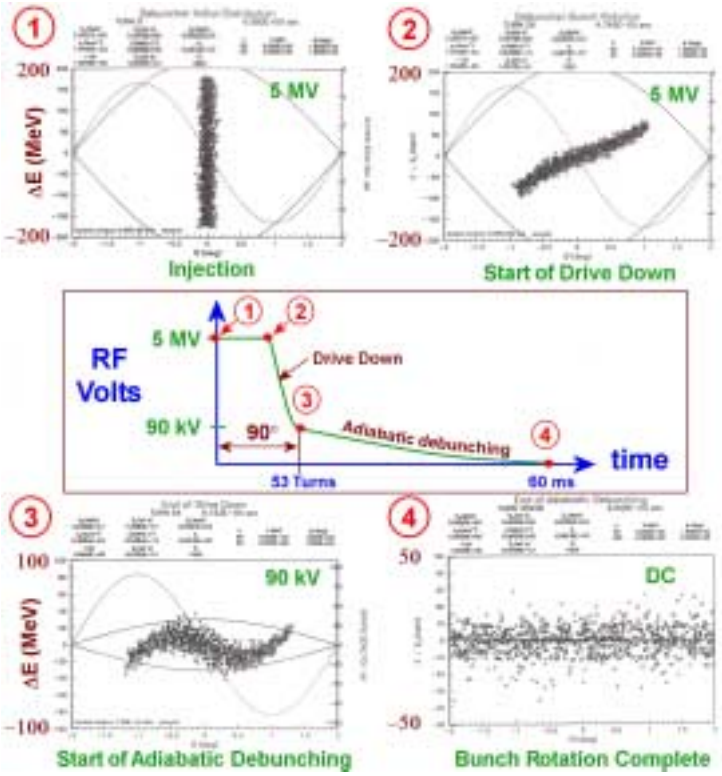

Figure 3.3.6 *The sequence of RF manipulations during bunch rotation in the Debuncher. The $\bar{p}$ beam is injected into the Debuncher into 5.0 MV RF buckets that are synchronized in phase to the Main Injector RF system. The beam, which is not matched to the RF bucket, begins to rotate in phase space (points ① to ②). After a time that is somewhat less than quarter of a synchrotron period, the voltage is rapidly driven down to about 90 kV (point ③). The beam is then adiabatically debunched (point ④).*

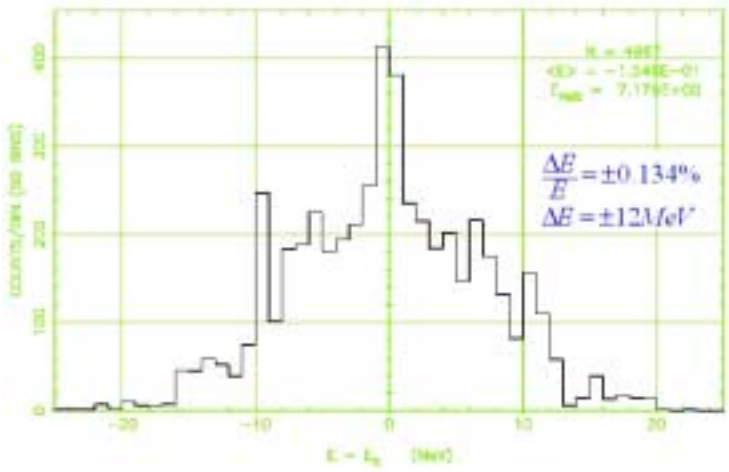

Figure 3.3.7 *ESME model calculation of the $\bar{p}$ energy distribution immediately after bunch rotation in the Debuncher. The widths indicated here are 95% half widths.*

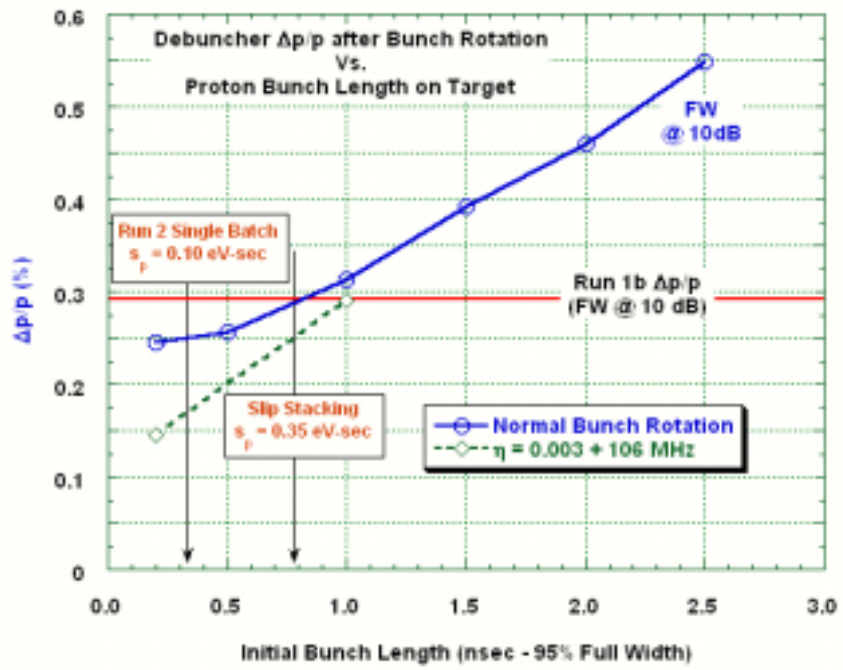

Figure 3.3.8 *$\overline{p}$ momentum spread ($\Delta p/p$) versus the bunch length of protons on the $\overline{p}$ production target. The dashed green line is the model prediction of bunch rotation performance if the value of η was reduced by a factor of two and second harmonic correction added to the Debuncher bunch rotation RF system.*

3.3.1.5 Debuncher Momentum Cooling

After bunch rotation, the $\overline{p}$ beam remains in the Debuncher for the remainder of the stacking cycle. The beam is extracted to the Accumulator immediately prior to the arrival of a new batch of antiprotons. The time between bunch rotation and extraction is used to cool the beam in all three dimensions.

Momentum cooling in the Debuncher is accomplished by a recently installed 4-8 GHz filter cooling system. A simple model of Debuncher momentum cooling has been constructed. The model is based on the design parameters of the system rather than on measured quantities[i]. Moreover, this model does not solve the Fokker-Planck equation for the time evolution of the energy distribution of the beam. Rather, the cooling rate of the system is determined by taking the second moment of each term and solving for the time dependence of $\langle E^2 \rangle$.

The model was "tested" by using the parameters of the Debuncher momentum cooling system envisioned in the TeV33 report[2]. The present model gives the same cooling rate and predicts the same thermal and schottky noise power as the model used for the TeV33 study. An upgraded model is being developed, which will be calibrated by measurements of the installed equipment. The present model, however, should be adequate to provide an estimate of the ideal performance of the Debuncher momentum

[i] Presently the measurement data available are insufficient to characterize the system.

cooling system. Table 3.3.3 summarizes the parameters used in the Debuncher momentum cooling model.

Beam Parameters:			
Intensity[i]	N	3.5×10^{8}	p s
Initial Momentum Spread (95% ½ Width)	$\Delta p/p$	±0.134	%
Machine Parameters:			
Cooling time[ii]	Δt	1.94	sec
Revolution frequency	f_{rev}	590035	Hz
η		0.00607	
Cooling Hardware Parameters:			
Pickup and Preamp effective temperature	T_{pu}	35	°K
Number of slotted waveguide pickups[iii]	N_{pu}	16	
Number of slotted waveguide kickers[iv]	N_k	32	
Average pickup impedance	Z_{pu}	12.5	kΩ
Average kicker impedance	Z_k	16.2	kΩ
Electronic gain	g_e	145	dB
Initial Noise Power:			
Thermal noise power		293	W
Schottky noise power		4507	W
Maximum power[v]		4800	W
Cooling time	τ	**0.26**	**sec**

Table 3.3.3 *Debuncher Momentum Cooling Parameters*

The 4-8 GHz bandwidth of the Debuncher momentum cooling is divided up into eight pickup and four kicker bands.[26] The variation of pickup and kicker impedance is shown in Figure 3.3.9 and Figure 3.3.10. The momentum cooling model uses an inverted parabola approximation to represent the variation of pickup and kicker impedance with frequency in each microwave band.

The electronic gain of the system includes a notch filter response. The model implements this as an ideal notch filter with a transfer function given by:

$$G_{fil}(f) = \frac{i}{2}\left(1 - e^{-2\pi i f T_{rev}}\right) \qquad (3.3.2)$$

where T_{rev} is the central orbit revolution period. The notch filter provides the energy discrimination required for the coherent part of the signal while simultaneously rejecting the noise signals at frequencies near harmonics of the revolution frequency.

[i] This is based on a stacking rate of 60 mA/hr.
[ii] This number is the stacking cycle time (2.0 sec) minus the time required for Debuncher bunch rotation (60 msec).
[iii] 8 bands in both planes.
[iv] 4 bands in both planes.
[v] The power limit is determined by a 150 W limitation for each TWT. There are 32 TWTs in the system.

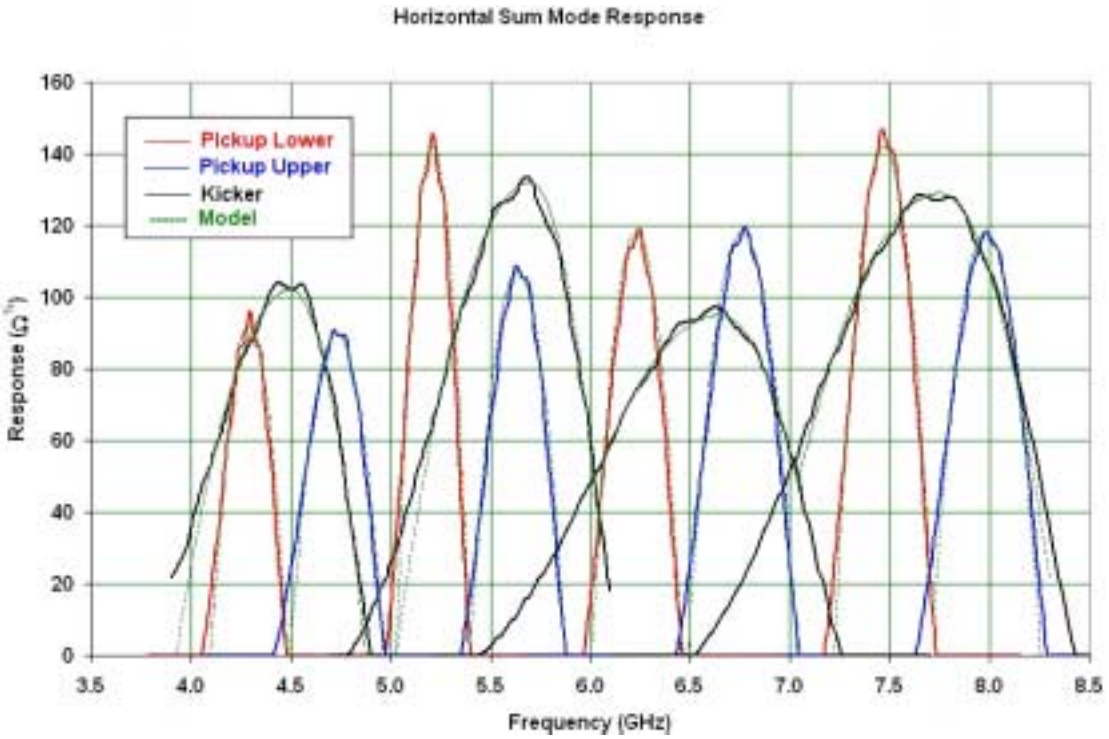

Figure 3.3.9 *Horizontal pickup and kicker impedances. The variation of the impedance for each band is represented by an inverted parabola in the momentum cooling model. The modeled Z(f) is shown by the dashed green line.*

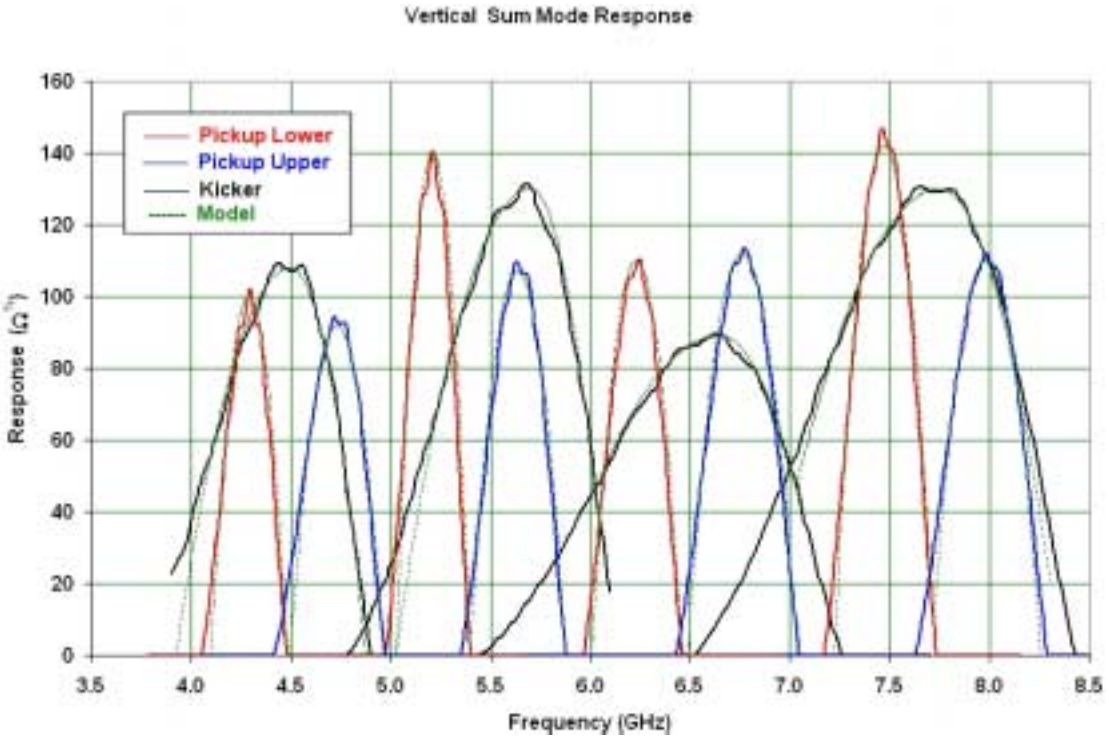

Figure 3.3.10 *Vertical pickup and kicker impedances. The variation of the impedance for each band is represented by an inverted parabola in the momentum cooling model. The modeled Z(f) is shown by the dashed green line.*

The overall system gain of the system, g_e, is limited by the maximum allowed power output to the kickers. The power output is primarily due to pickup and amplification of the schottky noise of the beam. In this regime, the maximum allowed gain decreases approximately as the inverse square root of the beam intensity[i]. Accordingly, the contribution of pickup and amplifier noise to the total noise power decreases with increasing beam intensity.

The present Debuncher momentum cooling model predicts a cooling time of 0.26 sec under Run IIb stacking conditions. This cooling time is at least a factor of five better than what has been observed with the system to date. While it is likely that the predicted cooling time will be adjusted upward as the model is refined; it is also likely that substantial increases in the performance of the installed hardware will be realized as the system is tuned-up. It seems reasonable to assume therefore, that Debuncher momentum cooling will accomplish the reduction in momentum spread required for stochastic stacking in the Accumulator.

3.3.2 Description of stochastic stacking

Stochastic stacking with a constant flux is achieved by designing a system with gain as a function of energy that falls exponentially, with characteristic energy E_d. The resulting density distribution then rises exponentially with the same characteristic energy[27]. The resulting maximum flux Φ can be expressed as:

$$\Phi = \frac{W^2 \eta E_d}{f_0 p \ln(F_{\min}/F_{\max})} \qquad (3.3.3)$$

where W is the bandwidth of the system, η is the phase slip factor, f_0 is the beam revolution frequency, p is the beam momentum, and F_{min} and F_{max} are the minimum and maximum frequencies in the system bandwidth. Planar pickups have a response which goes like $exp(-\pi x/d)$, where x is the transverse distance from the center of the pickup and d is the vertical aperture. If the pickups are located in a region of high momentum dispersion, we can design a system where the gain response falls off exponentially with energy. The region of exponential density increase is called the 'stacktail' and the region where beam accumulates is called the 'core'. Since the revolution frequency changes with energy and hence the flight time between pickup and kicker is a function of energy but the delay time through the electronics is a constant, it is necessary to use multiple sets of pickups with different gains and delays to build the gain slope across the aperture. Correlator notch filters are used to null out the signal at the core.

The present Accumulator provides a good example of the basic principles. Figure 3.3.11 shows the antiproton density distribution as a function of beam revolution frequency overlaid in the stacktail region with an exponential fit. The maximum flux for

[i] The noise power is primarily due to the schottky noise of the beam, which is in turn proportional to the square of the rms beam current: $4800W = P \propto i_{rms}^2 g_e^2 \propto N g_e^2$.

this particular stack is calculated from the results of the fit. Figure 3.3.12 shows the maximum flux from these fits versus stack size for two different stacking periods (in July and Oct 2000). Note that the fitted maximum flux, based on the slope, is of order 30 mA/hour even though the stack rate was about 10% of that number.

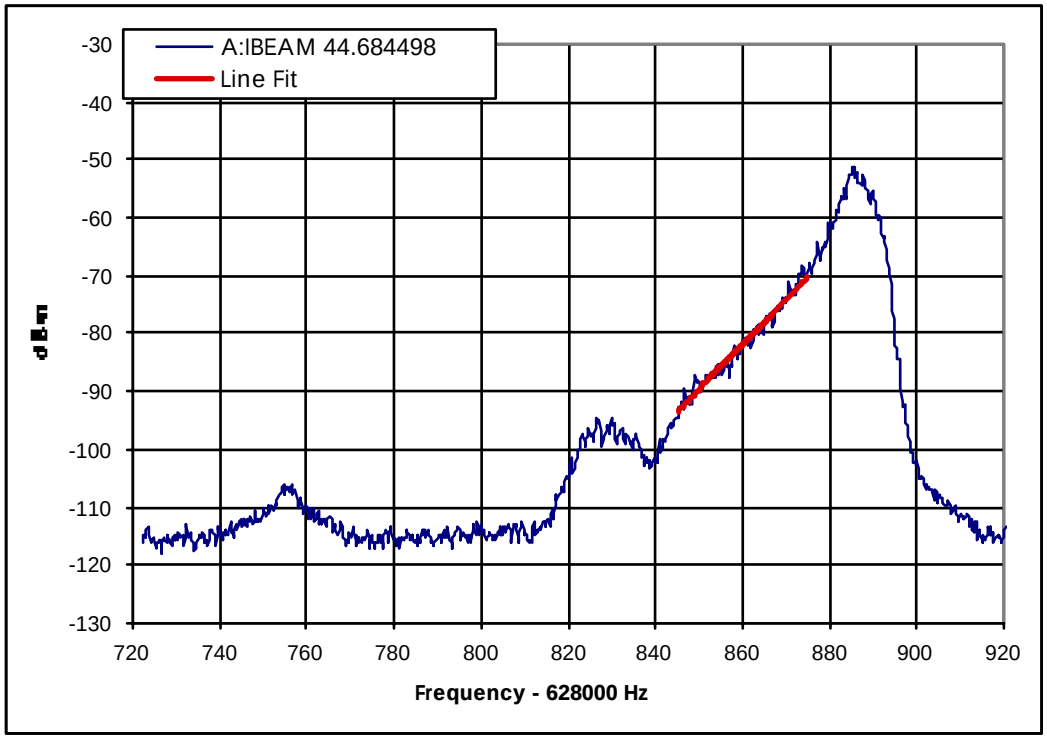

Figure 3.3.11 *Stacking density distribution overlaid with exponential fit in the stacktail region.*

Of the parameters appearing in Eq. (3.3.3) E_d, W, and η are the only ones that can reasonably be considered as changeable. The simplest approach to maximize the flux is to increase E_d. This approach sacrifices the amount of density compaction achievable, since the density grows as $exp(E/E_d)$, but has fewer implications for other systems in the Accumulator. Increasing the bandwidth clearly increases the maximum flux. However, changing the system bandwidth also requires changing the Accumulator lattice parameter η to avoid Schottky band overlap at high frequencies. The design shape of the voltage gain depends on the one-to-one map between position and momentum due to dispersion at the pickups and the corresponding many-to-one map between frequency and momentum. The Accumulator stacktail cooling creates an approximately 100 MeV/c wide "stacktail" in the longitudinal distribution of the stack in order to accommodate the incoming $\bar{p}$ flux. For the present value of η, the longitudinal Schottky bands of the 100 MeV wide stacktail distribution begin to overlap at frequencies above ~4.3 GHz. Therefore, changing the system bandwidth in a way that precludes Schottky band overlap requires changes in the Accumulator lattice.

Changing the system bandwidth was the approach taken in the upgrade that was installed between Collider Run I and Run II. The system bandwidth was doubled (from 1-2 GHz to 2-4 GHz) and η was halved (from 0.023 to 0.013) while maintaining the same E_d. This upgrade is ultimately expected to double the maximum flux. There have been

some drawbacks to this approach. The change in η has impacted the performance of the core stochastic cooling systems due to the concomitant factor of two increase in the mixing factor. Moreover, the change in γ_t that was required to lower η changed the circumference of the Accumulator injection orbit so that the harmonic relationship between it and the circumferences of the other accelerators in the Fermilab complex is now only approximate. Consequently, additional RF manipulations are now required to handle the transfers of antiprotons from the Accumulator to the Main Injector and Recycler. Given these difficulties, a further reduction in η to accommodate another bandwidth increase is very hard to justify.

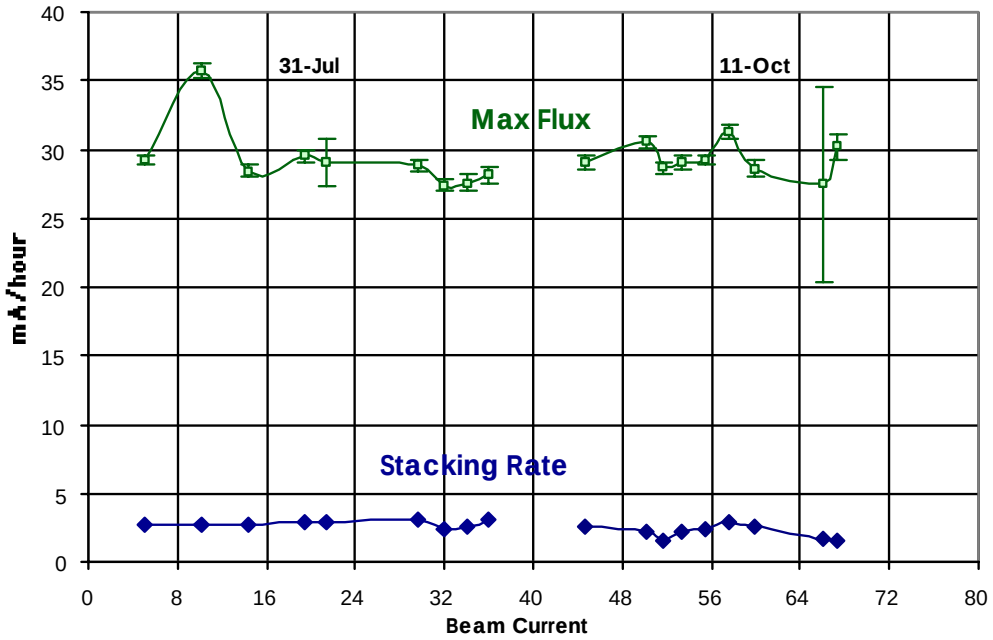

Figure 3.3.12 *Flux results (mA/hour) vs. stack size*

There are also drawbacks to the approach proposed here – increasing E_d. The Accumulator has a finite momentum aperture. It is therefore necessary to stop the flux at some point and accumulate it. In so doing, the gain function deviates from the pure exponential and other considerations come to the fore. It is necessary to match the stacktail system gain to the core system gain to have a smooth transition in the gain profile. As the density increases, diffusive beam heating from other particles (through the cooling systems) eventually dominates the cooling term and the system is no longer able to effectively increase the density. It is generally true that as the density of the core increases it becomes necessary to decrease the system gain to maintain some margin between the cooling and diffusive terms of the Fokker-Planck equation.

Another limitation is the assumption of constant input flux. The input flux is a transient, with large pulses of beam coming every 2 seconds. It is necessary for the input pulse to move completely into the stacktail region before the next pulse arrives. Any beam that remains will be phase displaced by the RF bucket moving the new pulse onto the deposition orbit. The fraction of the input pulse that moves across the aperture is a function of the gain of the system and the momentum distribution of the input pulse. The larger the gain, the more efficiently the input pulse moves off the deposition orbit. The

large gain necessary for the effective stacking of the input pulse is also detrimental, for the reasons given above) to accumulating large amounts of beam in the core. With some simplifying assumptions[28], the fraction of the beam that moves off the deposition orbit as a function of the time between input pulses can be calculated. Figure 3.3.13 shows this calculated fraction for a system that is representative of the Run IIb design. Note that for a 2 second cycle time the system fails to move 100% of the beam off the deposition orbit (the 100% mark is reached at 2.5 seconds). Increasing the gain by 3 dB moves the 100% mark down to 1.8 seconds.

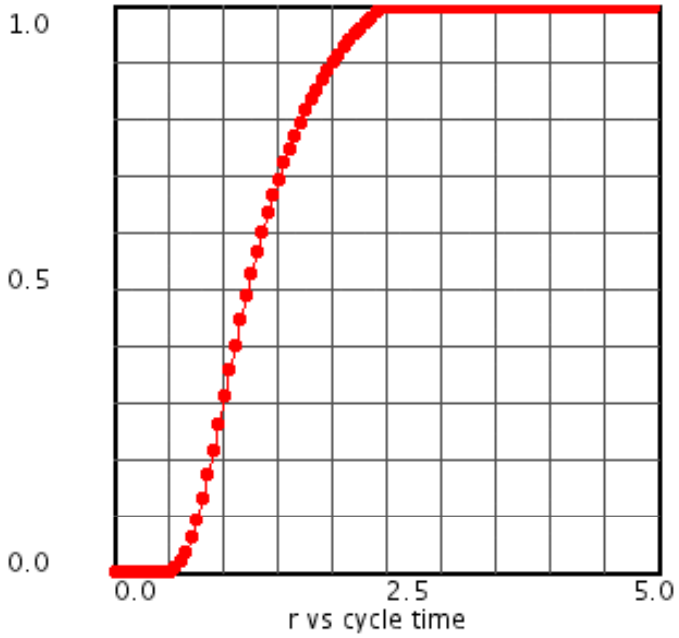

Figure 3.3.13 *Fraction of beam that moves into the stacktail region as a function of cycle time. This model is for 80 mA/hour injected and reasonable selections of the gain.*

3.3.3 System parameters

The system is being designed with the goals of handling an input flux of 80 mA/hour, a 2 second cycle time, an injection bucket height of 6 MeV at h=84, efficiencies greater than 95% for 30 minutes of stacking time, using a bandwidth of 2-4 GHz in the stacktail and 4-8 GHz in the core. To reach this goal a gain slope of 18 MeV is required. This gain slope can be achieved and the above design goals met with modifications to the current stacktail system (described below). The modifications include changing the central energy of the pickup tanks (by moving the tanks several millimeters) and adjusting the electronics gain and phase settings.

Figure 3.3.14 shows an example calculation of the gain as a function of energy. With 2 pickups, an 18 MeV gain slope can be designed. The required gain for the core system is large; therefore, as the density grows, it becomes necessary to lower the gain.

Figure 3.3.15 shows 30 minutes of stacking with the system gain from the previous figure. Several adjustments to the gain were made during the simulation because of the diffusive heating problems. An average stacking rate of 75.34 mA/hour was achieved.

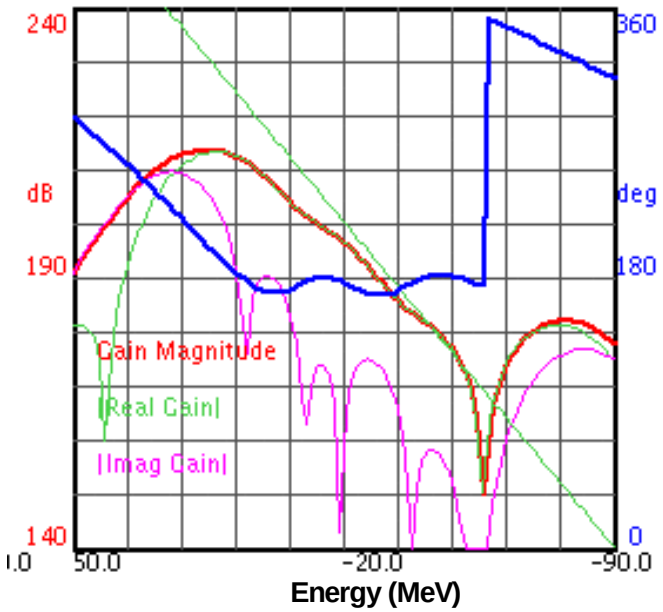

Figure 3.3.14 *Example gain slope calculation for two pickups in the stacktail and a 2-4 GHz core cooling system. Red is the magnitude, green is the real part (which does the cooling), purple is the imaginary part (which heats the beam), and blue is the overall system phase. The straight green line is a gain slope of 10 MeV for comparison.*

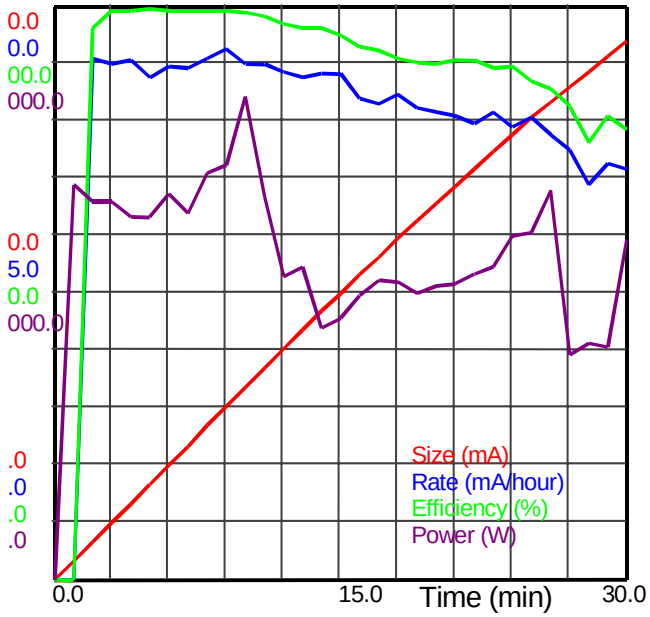

Figure 3.3.15 *Stack size, rate, efficiency, and power for 30 minutes of stacking with above configuration. The large changes in power occur when the gain is turned down because of diffusive heating problems. After 30 minutes, 37.67 mA are accumulated.*

The stacktail system consists of two sets of pickups (see Figure 3.3.16 for schematic), with independent gain and delay control. The pickups are kept at liquid nitrogen temperature to minimize electronic noise. There are 128 pickup loops at 15

MeV (with respect to the central energy of the Accumulator) and 48 pickup loops at -8 MeV. There are 128 kicker loops in 8 tanks, with 4 TWTs per tank. There is approximately 150 dB of gain from pickup to kicker. The system also makes provision for combining the signals from the 2 sets of pickup loops (and a 3rd set, not included in the figure) to fine tune the gain shape (called "compensation legs").

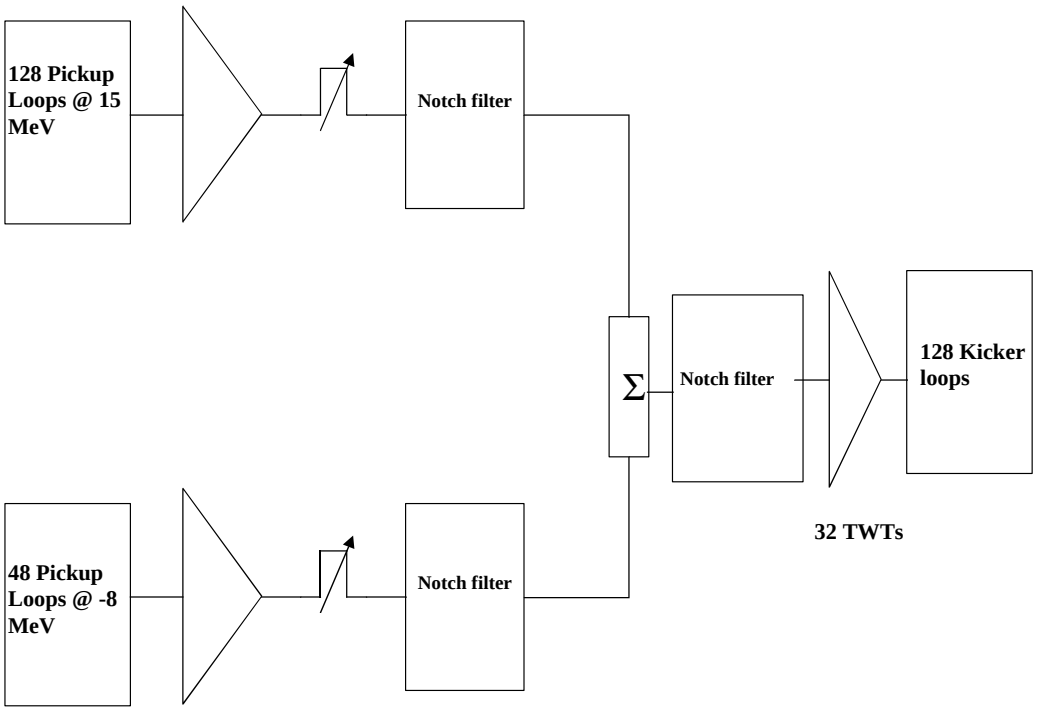

Figure 3.3.16 *Schematic diagram of the Run IIb stacktail cooling system. There are two sets of pickups at different energies, with independent gain and delay control. The system electronics has a total gain of 150 dB.*

3.3.4 Performance of the current system

The current stacktail system is functionally identical to that described above, with the exception of the pickup positions (energies) and the relative gain and delay settings. Currently, there are 128 pickup loops at 16 MeV (with respect to the central energy of the Accumulator), 48 pickup loops at the central energy, and an additional 16 pickups at -23 MeV (as a compensation leg). The pickups are kept at liquid nitrogen temperature, with a calculated effective system noise temperature of 125 K.

The current maximum stacking rate that has been achieved to date is 10 mA/hour with a 2-second cycle time, while the maximum flux (based on exponential slope) approaches 30 mA/hour. Detailed simulations of the current stacktail system have been performed. The simulated peak performance agrees well with the 30 mA/hour maximum flux from beam measurements. Figure 3.3.17 shows the simulated performance. The input flux in the simulation was adjusted until the maximum efficient stacking rate with a

2-second cycle time was achieved. After a short time period, the system reached a stable stacking rate of ~37 mA/hour. Fits to the density profile similar to those discussed in section 3.3.2 correspond to a flux of 38 mA/hour.

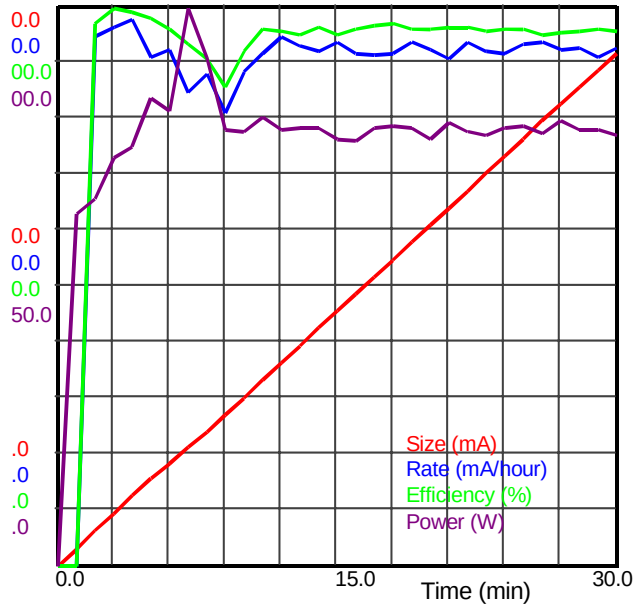

Figure 3.3.17 *Simulated performance of current Run II stacktail cooling system.*

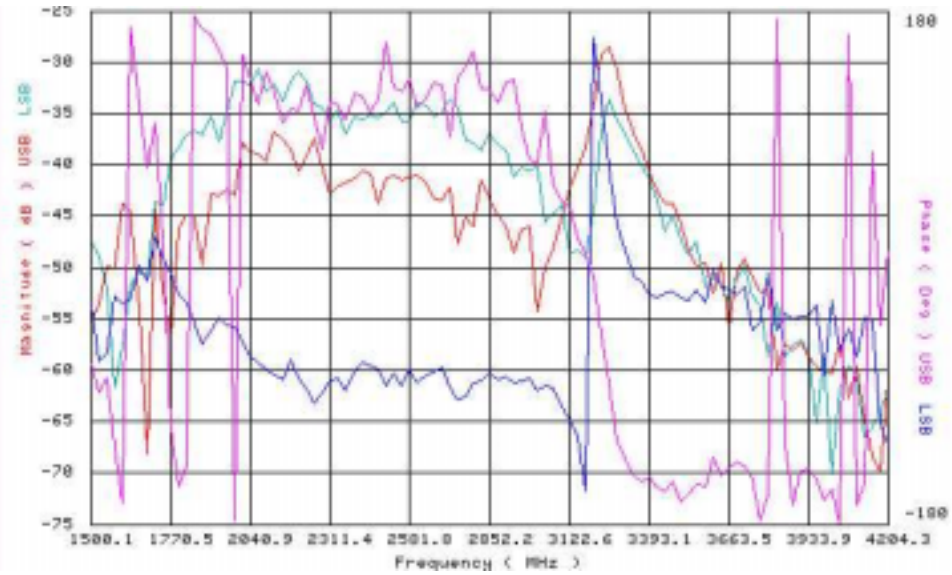

Figure 3.3.18 *Response on the Core Horizontal ßtron pickup to excitation by the stacktail kickers. Note the large response near 3.2 GHz (blue is the upper sideband, red is the lower sideband).*

Presently the stacking rate is limited by the input flux into the Accumulator. This is partly because stacking cycle times shorter than 2 sec have not been utilized. There have been two problems identified with running high power in the current stacktail cooling system.

The first problem involves a correction system, known as the 'delta kickers'. The delta kickers are a set of 4 TWTs connected to the stacktail kicker tanks in delta mode, phased to null out any transverse kicks from imperfections in the mechanical construction or alignment of the stacktail kicker tanks. Figure 3.3.18 shows the response of the core horizontal betatron pickup when the stacktail kickers are excited. There is a large response near 3.2 GHz, which has been associated with a difference mode launched in the kicker tank. The magnitude of this response is too large for the delta kickers to compensate for, as they do not have a similar spike in response around 3.2 GHz (see Figure 3.3.19). As a result, operation of the stacktail at high power causes transverse heating of the core.

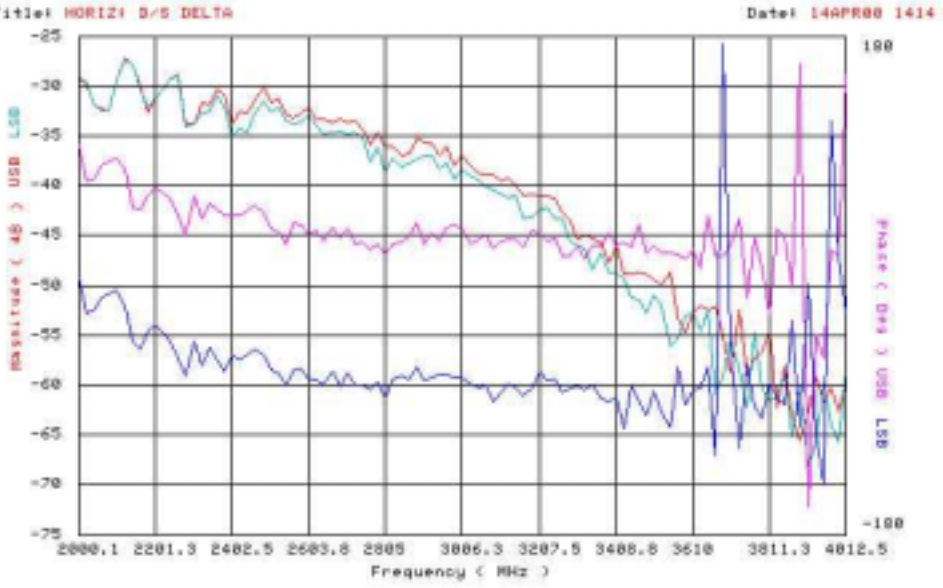

Figure 3.3.19 *Delta kicker response versus frequency*.

The second limitation to the power in the stacktail is that the system goes unstable at high power and large stacks. This instability occurs because the high density beam at the core responds coherently to the stacktail kicks, oscillating at the frequency where the kick is the largest and the gain the highest. Since the stacktail compensation legs, designed to null out the pickup response of near the core, have not yet been phased in properly, this signal shows up on the stacktail pickups. Eventually, the system goes into positive feedback mode somewhere in the 2-4 GHz frequency band. The compensation legs will be commissioned in the near term future.

3.3.5 Project Plan

Since the design for Run IIb stacktail cooling requires only moving the stacktail pickup tanks a few millimeters from their present position, with the additional changes to gain slope accomplished by adjusting relative gain and delay of the electronics, the plan is simple to implement. The pickup position changes could be done during a one-day shutdown of the Accumulator. Some additional beam study time will be required to measure and adjust the system settings. From the point of view of resource availability,

the stacktail upgrade is ready to go now. However, since the present operation of the Accumulator requires the accumulation of large stacks, implementation of the stacktail upgrade should be delayed until larger fluxes are available. Operation of the upgraded stacktail system would seriously compromise the performance of the Accumulator core cooling systems with large stacks ($\geq$40 mA).

	Total	M&S	Labor	Phys.	Eng.	Draft	Tech	CP
FY02	100	0	100	0.8	0.2	0	0	0
FY03	400	100	300	1	1	0	1	0
FY04	0	0	0	0	0	0	0	0
FY05	0	0	0	0	0	0	0	0
Project	500	100	400	1.8	1.2	0	1	0

Table 3.3.4 *Funding profile for Stacktail upgrade*

3.4 Recycler Electron Cooling

A complete description of the electron cooling project can be found in Reference [31]. Here we provide a discussion of the essential elements emphasizing the integration of the project into the overall plans for Run IIb.

3.4.1 Background

The Laboratory started in 1995 to investigate the application of electron cooling to 8.9 GeV/c antiprotons in the Recycler as a promising component of an upgrade of Tevatron luminosity beyond the Run IIa goals. The idea was not entirely new at that time; it had been proposed as an upgrade path for the Accumulator as early as 1985,[29] and there had been some experimental work as well as conceptual development.[30] The practice and principles are well established for ions with kinetic energy of less than 500 MeV/nucleon. For ions of higher energy the fundamentals are the same, but hardware development is required and the technical problems differ. Technical details about the Fermilab R&D program can be found in Ref. [31]. To date, electron cooling at relativistic energies remains an unproven technology, and thus constitutes a high-risk segment of the Run2b upgrades plan. Fermilab is currently the only laboratory pursuing the high-energy electron cooling R&D at full scale; conceptual and experimental studies for similar systems are being carried on at Budker INP (Russia), BNL (USA), DESY (Germany), and GSI (Germany).

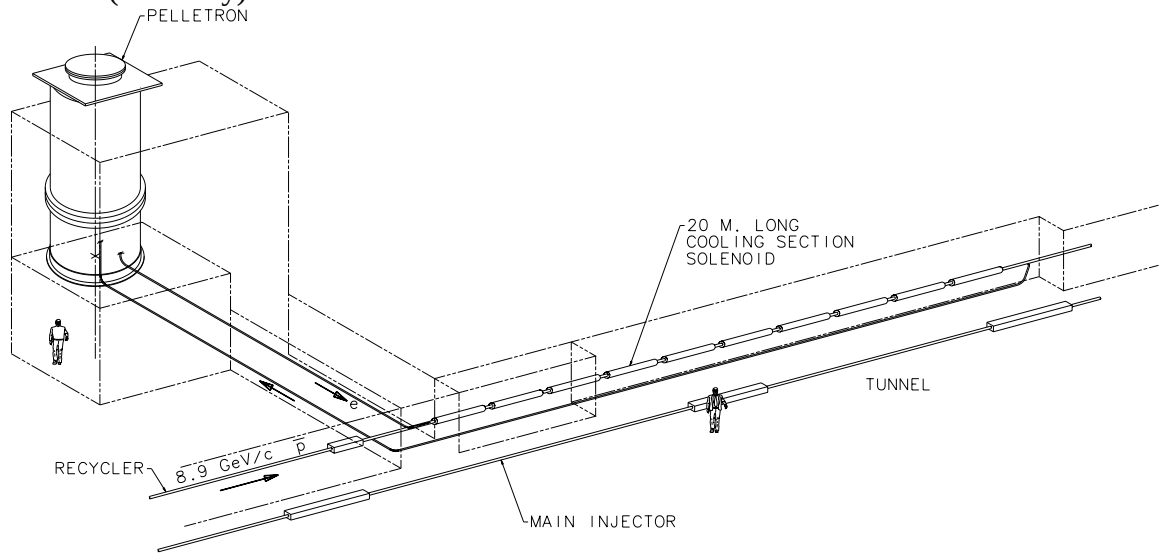

Figure 3.4.1 *Schematic layout of the Recycler electron cooling system*.

The Recycler currently employs a stochastic cooling system to collect multiple batches from the Accumulator. Electron cooling will improve cooling performance in the Recycler, permitting to have faster stacking and larger stacks, and ultimately to re-cool (recycle) antiprotons, which remain at the end of Tevatron stores. In combination with other accelerator upgrades it will permit substantially greater luminosity in the collider.

The Recycler electron cooler, discussed here, will be installed in the MI-30 section of the Recycler tunnel and it is schematically shown in Figure 3.4.1.

A charged particle (i.e. an antiproton) traveling in an electron beam undergoes Coulomb scattering with the electrons. The resulting friction and velocity diffusion tend to bring such particles into thermal equilibrium with the electrons. If the particle kinetic energy in the beam frame is high in the comparison with the electron temperature, diffusion is insignificant and the particles are cooled. The method of electron cooling was originally suggested by A. M. Budker.[32] It was developed and studied then both theoretically and experimentally. An ample list of the references can be found in Ref. [33].

3.4.2 Potential and goals

Electron cooling can reduce the spread in all three components of beam momentum simultaneously. Its primary advantage over stochastic cooling is that the cooling effect is practically independent of antiproton beam intensity up to the Recycler stack sizes of about 2×10^{13} antiprotons. Its greatest disadvantage is that the effect is very weak until the antiproton emittances are already close to the values wanted in the collider. Thus, the two processes can be seen as complementary rather than competitive. Electron cooling will prove very powerful in the Recycler as an add-on to the stochastic pre-cooling in the Antiproton Source and Recycler.

The ultimate goal is to realize a luminosity of $0.5\text{-}1.0\times10^{33}$ $cm^{-2}s^{-1}$ in the Tevatron collider by supplying a larger flux of antiprotons. The conceptual design studies[34] demonstrate that this can be accomplished by providing longitudinal emittance cooling rates in the Recycler of 200 eV·s/h or higher (in conjunction with the transverse stochastic cooling). The specific technical goal for the Recycler with the electron cooling system is to deliver 1.1×10^{13} antiprotons with a 150 eV-s longitudinal phase-space area (98%) and 10 π-mm-mrad transverse emittance (95%, norm.) in 6-7 hours.

3.4.3 Recycler beam cooling overview

The purposes of the Recycler beam cooling system (stochastic or electron) are:

1. To re-cool the recycled beam during a time period of a collider store;
2. To aid beam stacking in the Recycler during frequent transfers from the Accumulator;
3. To counteract various beam heating mechanisms, such as residual-gas and intra-beam scattering.

For Run2a, the stochastic cooling system alone is thought to be adequate. An example of simulations for the transverse cooling is shown in Figure 3.4.2. The attainable emittance cooling rate is thought to be about 15 π mm-mrad/hour (normalized, 95%) for modest stack sizes. Electron cooling and stochastic cooling are complementary in principle, and, at least during the earliest operation of the electron cooling system, that complementarity will be exploited by using the stochastic cooling for the large transverse emittance of the recycled antiprotons whereas the electron cooling will be optimized for longitudinal cooling to increase the stacking rate and maximum stack current. At the time of writing this report the Recycler stochastic cooling system has not been tested yet.

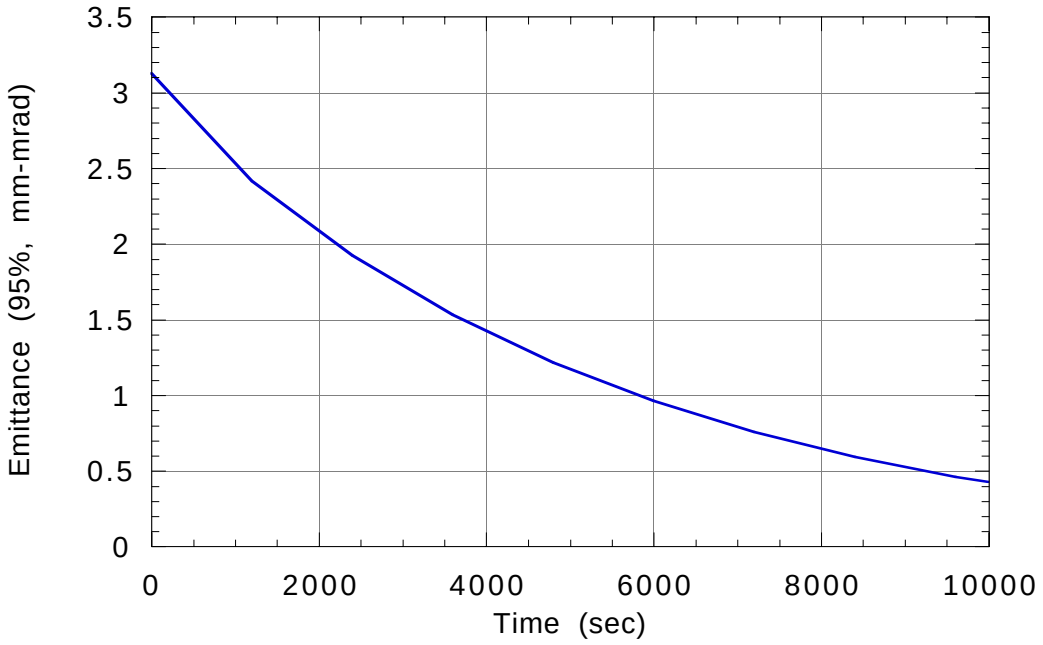

Figure 3.4.2 *Evolution of the (unnormalized) emittance of 5×10^{12} particles in the Recycler with the full momentum spread $\pm2\times10^{-3}$ during stochastic cooling with 2-4 GHz bandwidth.*

3.4.4 Cooling scenario simulations

A possible Run2b scenario for the periodic cooling-stacking process in the Recycler is as follows:

- t = 0: Up to 100 bunches of (hot) antiprotons leave the Tevatron, are decelerated in the Main Injector, and arrive at the Recycler, sharing its circumference with the already cooled antiproton beam. Then, the cold portion is transferred to the Main Injector, releasing the phase space for the hot beam with N=(2.5-10)$\times10^{12}$ antiprotons occupying A = 400 eVs of the longitudinal phase space and 30 π mm-mrad of the normalized, 95% emittance. Transverse stochastic pre-cooling begins.
- Every 15 minutes, a fresh antiproton batch arrives from the Accumulator. Its population is 10^{11} in 10 eVs and 15 π mm-mrad (normalized, 95%). It is merged longitudinally with the Recycler stack by means of a barrier-bucket technique.[35]
- t = 1-2 hours: Stochastic pre-cooling of the recycled antiprotons ends; beam emittance is now 15 π mm-mrad. Electron cooling begins.
- t = 5-8 hours: Electron cooling ends producing a beam with a 10-π emittance and 150 eVs or less longitudinal phase-space area. The cycle is then repeated.

To simulate the electron cooling process, a multi-particle computer code has been written. This code tracks the time evolution of an ensemble of cooled particles, optimizes the cooling process under various conditions and finds the tolerances for imperfections. The simulated evolution of the recycled antiprotons from the initial state is shown in

Figure 3.4.3 and Figure 3.4.4 in terms of the distribution integral as a function of the particle's betatron action and its momentum offset.

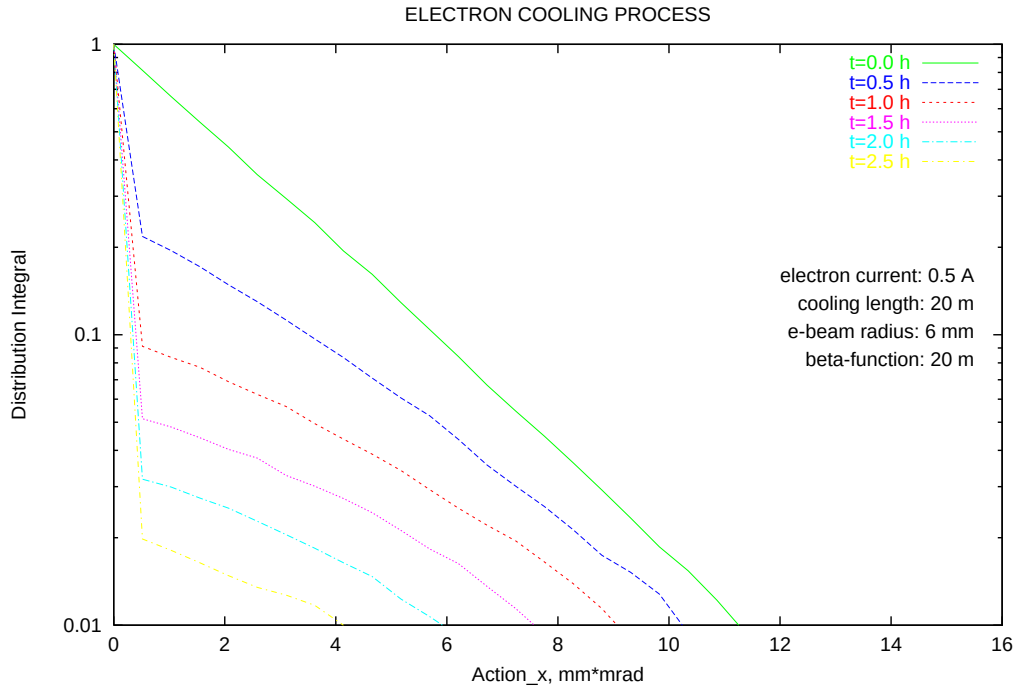

Figure 3.4.3 *Evolution of the transverse beam distribution during electron cooling. Initial distribution: gaussian with a 15 π mm-mrad (n, 95%) emittance. The initial cooling rate for a 15 π mm-mrad beam: 6 π mm-mrad/hr.*

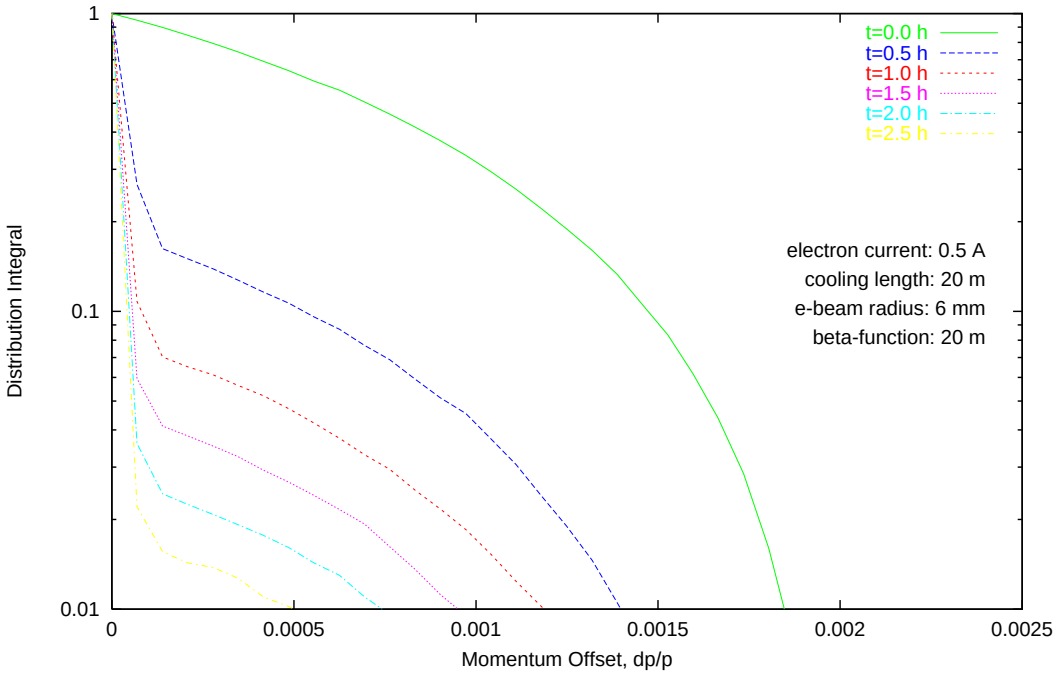

Figure 3.4.4 *Evolution of the momentum distribution. The initial distribution: parabolic.*

Electron cooling tends to shape a narrow core of super-cooled particles. The above figures show this core as a narrow peak at the origin. The actual size of this core is determined by equilibrium between cooling and the intra-beam scattering diffusion rate and is estimated elsewhere.[34]

The conclusion from the simulations is that the transverse cooling of the recycled antiprotons from ε = 15 π mm-mrad to ε = 10 π mm-mrad requires 0.9 Ampere×hour (Ah) of (electron beam current)×(cooling time), for a 20-m long cooling section. For batches from the Accumulator, this value is 0.5 Ah.

The longitudinal phase space area, A, shrinks with a rate $r_0 \approx 1.2$ $A^{-1}h^{-1}$ over the whole interesting interval 150 eVs < A < 400 eVs. This approximate rate is used in the stacking model discussed below.

The longitudinal phase-space evolution of the cooling-stacking process can be described as

$$\dot{A} = -r_0 A + f_S A_b + f_S \Delta_S A \ , \qquad (3.4.1)$$

where f_S is the stacking rate (the number of injections per hour), A_b is the Accumulator batch phase-space area, and Δ_S is the fractional phase-space area dilution because of the stacking imperfections. The solution of this equation is

$$A(t) = A(\infty) + (A(0) - A(\infty)) \times \exp(-[r_0 - f_S \Delta_S]t) , \qquad (3.4.2)$$

where $A(\infty) = A_b f_S / (r_0 - f_S \Delta_S)$ is the equilibrium steady-state phase-space area. The phase-space area evolution for zero dilution is presented in Figure 3.4.5.

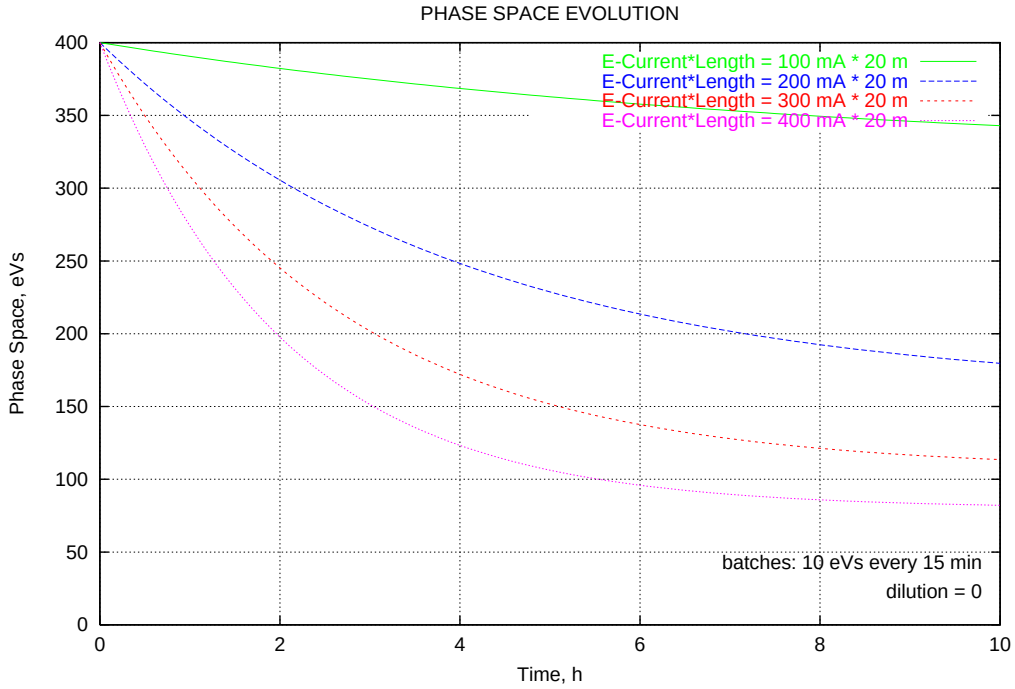

Figure 3.4.5 *Evolution of the longitudinal phase-space area in the cooling-stacking process with zero dilution.*

The sensitivity of the total cooling-stacking time to the dilution value is presented in Figure 3.4.6. The conclusion is that for the injection frequency, f_S, of 4 h^{-1} and the dilution $\Delta_S < 1\%$, the electron current of 300 mA is sufficient for the antiproton accumulation scenario as outlined at the beginning of this section. A description of the stacking process, capable of achieving such small dilutions is presented in Ref. [36]. This stacking process has not been tested yet.

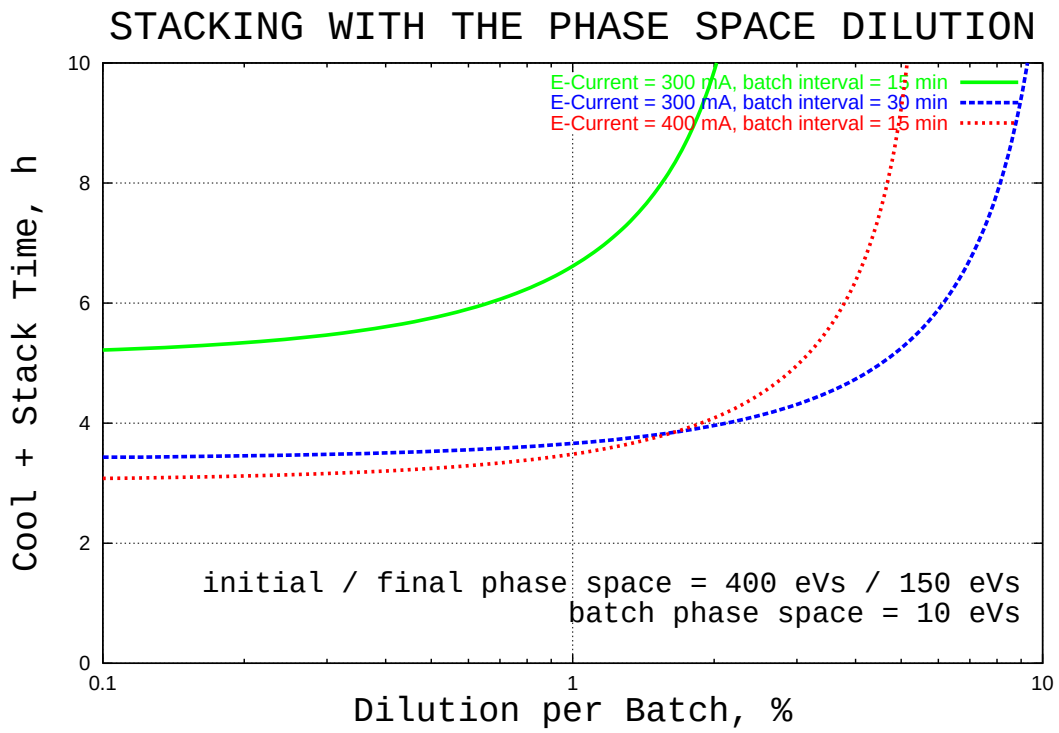

Figure 3.4.6 *Time required to reduce the longitudinal phase-space area from the initial 400 eVs to the final 150 eVs as a function of the dilution parameter, Δ_S. Various curves correspond to various electron currents and/or injection intervals.*

3.4.5 Electron cooling R&D goals

Table 3.4.1 summarizes the important parameters of the Recycler electron cooling system.

The primary technical problem is to generate a high-quality, stable, monochromatic, dc, 4.3-MeV electron beam of 300 mA or greater. The technical goal set in 1995 for an initial proof-of-principal demonstration using mostly existing equipment was to maintain a 200 mA beam for a period of one hour. The only technically feasible way to attain such high electron currents is through beam re-circulation (energy recovery).[37] This goal was achieved in 1998 by re-circulating beam currents of 200 mA for periods of up to five hours without a single breakdown.

The demonstration of the Pelletron-based electron beam re-circulation provided the necessary basis for the next step of the electron cooling R&D program, electron beam transport. Traditional low-energy electron cooling devices employ a continuous homogeneous longitudinal magnetic field in the kilogauss range for the beam transport through the cooling region. One of the main reasons is to suppress the transverse

velocities arising from the electron beam space charge. In the Recycler system, the space charge effects are much lower because of the higher beam energy. Thus, the longitudinal magnetic field value can be much smaller, allowing for a non-traditional transport scheme. Also, the choice of a standard Pelletron accelerator prohibits us from immersing the electron beam line into a continuous magnetic field. Our transport scheme assumes a homogenous longitudinal magnetic field in the gun, collector, and in the cooling section, but a lumped focusing system in between.

Parameter	**Value**	**Units**
Electrostatic Accelerator		
Terminal Voltage	4.3	MV
Electron Beam Current	0.5	A
Terminal Voltage Ripple	500	V (FWHM)
Cathode Radius	2.5	mm
Gun Solenoid Field	≤ 600	G
Cooling Section		
Length	20	m
Solenoid Field	≤ 150	G
Vacuum Pressure	0.1	nTorr
Electron Beam Radius	6	mm
Electron Beam Divergence	≤ 80	μrad

Table 3.4.1 *Electron Cooling System Parameters*

The cooling rates are extremely sensitive to the angles between the electrons and the antiproton beam. Both coherent and incoherent angles must be smaller than 10^{-4} radians to avoid cooling degradation. To provide zero angular velocity inside the solenoid, the electrons must enter the solenoid with the correct radius and divergence, determined by the Busch theorem. Diagnostics systems needed to measure the beam radius and divergence are described in Ref. [38].

Figure 3.4.1 shows the schematic layout of the Recycler electron cooling system. This system is now being reproduced at the PB-7 (WideBand) fix-target building for the full-scale proof-of-principle test. The principal goals for this test system are:

1. to demonstrate the re-circulation of a 4.3-MeV, 0.5-A electron beam for a period of one hour;
2. to verify that the electron beam quality in the cooling section meets the demands of the electron cooling;
3. to design the system for the final installation in the Recycler.

Even if these goals are fully accomplished, the ultimate test of the system can only be performed in the Recycler by demonstrating cooling of antiprotons.

3.4.6 Project Plan

Although electron cooling is well understood, the Recycler application represents a major step in beam energy, to 8 GeV from less about 0.5 GeV. The step is large enough that the high voltage generator, beam transport, and cooling region all require extension of the state of the art. Therefore, about 1.5 years (as of November, 2001) of research and development activity are likely to precede introduction of any electron cooling equipment into the Recycler.

The R & D phase of the project has the following plan:

1. To develop an optimized system parameter set (finished);

2. To procure and commission a reliable 4.3 MV electrostatic power supply[39];

3. To design and build an electron beam gun, collector and short (10 m) U-bend transport system[39] to sustain a re-circulating current of at least 0.5 A for 1 hour;

4. To design and implement a precise matching from discrete-element beam transport to continuous cooling region solenoid;

5. To design and implement a 20 m cooling section with uniform axial magnetic field with precision such that electron beam transverse angles are $\leq 10^{-4}$;

6. To design and implement magnetic shielding to protect the electron beam against the magnetic fields of the MI/RR tunnel;

7. To design and build beam instrumentation and control to maintain alignment and equal mean velocity of electron and p-bar beams to precision $\leq 10^{-4}$, to measure beam angular spread and position, to determine neutralization, *etc*.;

8. To assemble a full-scale (60 m) beam line, commission it and establish a recirculating beam current of at least 500 mA at 4.3 MeV, sustainable for 24 hours with a duty cycle of no less than 90%;

9. To demonstrate by measurements that the electron beam angles in the cooling section are $\leq 10^{-4}$.

The laboratory developments are now being carried out in the downstream end of the Wideband Lab experimental area at Fermilab. There is sufficient space at Wideband to carry out the development work envisioned for the Recycler cooling project. The hardware aspects of the development program are treated in detail in Ref. [31]. The goal of the development program is cooling-system hardware ready for installation into the Recycler. The remainder of the work constitutes an Accelerator Improvement Project of moderate scale.

The basic tasks are:

1. Architectural design and civil construction of an enclosure for the high voltage generator and an interconnection tunnel to the MI tunnel for the electron beam transport. The work on this task has already started by Fermilab's FESS;

2. Installation of a Recycler lattice insertion for the cooling region. This task is almost finished. The Recycler lattice suitable for the electron cooling system exists. However, some p-bar trim magnets, diagnostics, and vacuum equipment will have to be installed upstream and downstream of the cooling section at the time of the cooler installation;

3. Installation of cooling section and electron beam transport channels;

4. Commissioning of the cooling system.

3.4.7 Current status

Below is a summary of what has been accomplished as of November, 2001.

Pelletron commissioning:

- The 5 MV Pelletron has been installed and commissioned. While filled with SF6 (no vacuum tubes) at 5.5 atm the Pelletron reached more than 6 MV, thus, no HV problems on the gas side are expected;
- Because of the large amount of energy (3 kJ) stored in the HV terminal and its potential for damage, the HV conditioning of vacuum tubes is performed with the help of shorting rods, one 1-MV section at a time. Each section (out of 5) was conditioned separately to 1.2 MV. The Pelletron with tubes was then conditioned to 4.8 MV. The Pelletron design voltage of 5 MV has not been demonstrated yet. The manufacturer will replace the ceramic accelerating tubes to fix the problem;
- Overall, the Pelletron PO is still incomplete due to several outstanding items (voltage, controls, cooling, documentation) that do not meet the performance criteria. The last 10% invoice has not been paid yet.

Re-circulation test (short beam line):

- Successfully bridged a commercial control system, supplied with the Pelletron, with Fermilab's Acnet. The machine is now 100% Acnet compatible and transparent.
- All Pelletron electronics has been protected against sparks (April-July, 2001)
- Replaced mechanical hardware, damaged by sparks, with more robust components.
- Installed several levels of protection against beam-related full-tube HV breakdowns, which normally resulted in a tube de-conditioning (August, 2001).

- Established a procedure for HV conditioning. Established a procedure for steering the beam into collector. Any operator can now reach 100 mA in about one hour from scratch.
- At 3.5 MV, attained the maximum beam current of 350 mA; the stable current of 120 mA.

Beam line elements:

- All beam line elements are ordered and are to be delivered to Fermilab in Jan.-Feb., 2002.
- Vacuum system is being designed and procured.

Cooling section solenoid:

- A major portion of effort went into understanding the measurement sensor performance and making it stable and reproducible. This has now been achieved.
- The compass-based sensor can measure the solenoid transverse field with a relative accuracy of several mG. Absolute precision, determined by an angle between the magnetic axis of the compass and the mirror, is about 20 mG in a 100 G longitudinal field.
- Two prototype 2-m long solenoid modules were produced, installed and measured.
- The quality of measured solenoid prototypes is satisfactory for our purpose. Integrals of transverse fields can be made below 1 G-cm for the solenoid field of 150 G, if corrector currents are in optimum.
- Twelve new solenoid modules have been wound and epoxied by the Technical Division. Two will be ready for installation in December, 2001.
- We are planing to have a shielding coefficient of 5,000. Only two prototypes of this 3-layer design have manufactured but not tested. The remaining shields will be ordered after the shields are tested.

3.4.8 FY2002 schedule and budget

Project Milestone	**Start Date**	**Finish Date**	**Duration**
Commission U-Bend	3/01	12/01	10 months
500 mA, 1 hour (U-bend)		by 12/31/01	
MI-31 building CDR	01/01/02	04/01/02	3 months
Switch Over to Full Beamline	1/02	3/02	3 months
MI-31 bid out		by 04/01/02	
Commission Beamline	3/02	1/03	11 months
Build MI-31 Enclosure	6/02	12/02	7 months
Push-Pipe	8/02	10/02	3 months
(Shutdown MI)	9/02	10/02	1 month

M&S Budget (k$)	
MI-31 FESS (AIP)	1,266
WideBand (R&D) Cooling Section	342
WideBand (R&D) Supply and return lines	546

General	291
Total	2,445

Physicists	Engineers	Technicians	Drafters	Comp. Prof.
Nagaitsev 100%	Leibfritz 100%	Carlson 50%	MS Draft. 100%	Kramper 50%
Shemyakin 100%	Saewert 100%	Nelson 100%		
Crawford 100%	McGee 50%	Kellett 100%		
Warner 100%	RFI Engr. 50%	Frett 25%		
Burov 100%	Tupikov 100%	EE techs. 100%		
Schmidt 50%				
Kroc 50%				
Grad. student 100%				

3.4.9 FY2003 schedule and budget

Project Milestone	Start Date	Finish Date	Duration
500 mA, 1 hour, beam properties		by 01/31/03	
Disassemble @ Wideband	2/03	4/03	3 months
Install Pelletron @ MI-31	3/03	6/03	4 months
Shutdown MI	8/03	11/03	4 months
Install RR Components	8/03	10/03	3 months
Install Transfer line	9/03	11/03	3 months
Commission E-Cool	12/03		

M&S Budget (k$)	
MI-31 FESS (AIP)	1,800
WideBand Clean-up (R&D)	100
MI-31 installation (AIP)	200
General	200
Total	2,300

Physicists	Engineers	Technicians	Drafters	Comp. Prof.
Nagaitsev 100%	Leibfritz 100%	Carlson 50%	MS Draft. 100%	Kramper 50%
Shemyakin 100%	Saewert 100%	Nelson 100%		
Crawford 100%	McGee 50%	Kellett 100%		
Warner 100%	RFI Engr. 50%	Frett 25%		
Burov 100%	Tupikov 100%	EE techs. 100%		
Schmidt 50%				
Kroc 50%				
Grad. student 100%				

	Total	M&S	Labor	Phys.	Eng.	Draft	Tech	CP
FY02	4070	2445	1625	7	4	1	3.75	0.5
FY03	2605	1500	1105	4.75	2.75	0.75	2.5	0.3
FY04	1320	800	520	2.25	1.25	0.25	1.25	0.2
FY05	0	0	0	0	0	0	0	0
Project	7995	4745	3250	14	8	2	7.5	1

Table 3.4.2 *Funding profile for electron cooling project*

3.5 Rapid Antiproton Transfers

In Run IIb, antiprotons will be frequently transferred from the Accumulator to the Recycler. The Recycler will have responsibility for accumulating and cooling antiprotons for eventual transfer to the Tevatron. The antiproton source will be configured for maximum stacking rate and will no longer be capable of maintaining an acceptable stacking rate with larger stacks. Transfers of antiprotons from the Accumulator for collider operation in Run IIa occur at approximately 16 hour intervals. The interruption in stacking for the transfers is on the order of 100 minutes. With Accumulator to Recycler transfers in Run IIb expected to occur every 15 minutes or so, the length of the transfer process has to be drastically reduced. To provide enough antiprotons to support Run IIb luminosity goals, transfers would need to be accomplished with only about a 1 minute interruption in stacking.

There are multiple problems with the current antiproton transfers from the Accumulator to the Main Injector. The most serious problems are: the long setup time for beam transfers, beam emittance growth and beam losses related to dipole and quadrupole mismatches and lack of reproducibility of the beamlines. There are a few primary sources for these problems. First, the optics design of the beamlines is inadequate. The beamline lattice has unacceptably large values for the β-functions and a poor dispersion match, which results in increased sensitivity to errors and emittance growth. Second, an incomplete knowledge of the quadrupole fields causes a beam envelope mismatch. Third, the absence of a reliable hysteresis protocol causes irreproducible beam optics and steering errors that lead to additional emittance growth. The lack of reproducibility is aggravated by the fact that the same line is used for both the transport of 120 GeV protons and 8 GeV antiprotons.

Presently one of the largest complications in the process of switching modes from antiproton stacking to transfers is the dual role of the transfer lines. During transfers, 8 GeV antiprotons are transported from the Accumulator to the Main Injector through the combination of the AP3-AP1-P2-P1 transfer lines. However, during antiproton stacking, the P1-P2-AP1 transfer lines are used for sending 120 GeV protons to the antiproton production target. Therefore, the P1-P2-AP1 transfer lines operate at two very different momenta. This large difference in the beam momenta significantly complicates antiproton transfers and requires that the design, measurement and correction of the beamline optics be carefully performed. Alternatively, a new beamline could be installed that would separate 8 GeV and 120 GeV operation.

3.5.1 Beamlines

Initially, the prospect of building a new dedicated beamline to connect the Accumulator to the Recycler was very appealing. The new beamline would be designed specifically for 8 GeV antiproton transfers while the existing P1-P2-AP1 lines would be used for delivering 120 GeV protons to the production target. The new line, usually referred to as the AP5 line, would bring an end to the dual-energy nature of the P1-P2-AP1 lines.

After beginning to examine the implications of constructing the AP5 line, it became less attractive. Assuming that funding could have been found to cover the costs

of a project of this magnitude, the impact of civil construction would be very undesirable. Most AP5 scenarios involved new tunnel enclosures to house a relatively direct path from the AP3 line to the Main Injector enclosure. The design and construction of these enclosures would be very time consuming, delaying the benefits of the new line. The tie-in of the AP5 line into the AP3 line and Recycler would cause a lengthy interruption to the collider program. An alternative design for the AP5 line that would share the existing tunnels with the P1-P2-AP1 lines had its own share of logistical problems. This version of the new beamline would also cause a major interruption to collider operation.

The perceived problems with building the AP5 line have shifted the focus to improving the existing beamlines and to adopt them for operation in Run IIb. It is believed that the only practical beamline option within the time constraints of Run II is to use existing tunnels and service buildings to house the magnets and power supplies. Changes in quadrupole strength and location as well as aperture improvements could be carried out with a relatively minor interruption in collider operation.

3.5.1.1 Experience from Runs I and IIa

In collider Run I, beamline tuning prior to antiproton transfers went through a number of changes. Protons from the Main Injector were "reverse injected" into the P1-P2-AP1-AP3 transport lines and injected into the Accumulator. By utilizing protons in the tune-up process, adjustments could be made to orbit trajectory and closure without using the stored antiprotons. Initially, Main Ring positions at the extraction point were adjusted to a reference orbit. Then, Secondary Emission Monitors (SEM's) were used to tune beam positions in the AP1 and AP3 lines to a reference (P1 and P2 did not exist prior to the construction of the Main Injector). SEM displays were compared to a paper copy of a reference orbit and dipoles were adjusted until the tuner subjectively determined that they were "close enough". Beam Position Monitors (BPM's) were not used routinely. The transfer efficiency was also used as a figure of merit, normally 100% transfers could be achieved after tuning was completed. Turn-by-turn (TBT) oscillations were minimized using an applications program to calculate and implement corrections. It was found empirically that offsets had to be made to kickers in the Accumulator and Main Ring as well as several AP1 trims to achieve better agreement between the proton and antiproton orbits. TBT oscillations on the antiprotons in the Main Ring were minimized with an applications program during the six transfers.

Over the course of Run I, the beamline tuning became more streamlined to save time. Most notably, beamline steering was no longer done routinely. After positions in the Main Ring were adjusted, overall transmission was checked to ensure it was above a threshold of 80%. In most cases this was the case, and the next step was to minimize TBT oscillations in the Accumulator. The reproducibility of the Main Ring, AP1 and AP3 lines were good enough so that orbits only changed a few millimeters from day to day and did not adversely affect transmission. Trim changes required for TBT corrections were recorded and long term drift was compensated for by occasional changes to the initial magnet settings. The total antiproton source portion of the transfer setup in Run I eventually took less than an hour to execute.

When the Main Injector was built to replace the Main Ring, the beamline configuration became more complicated. The addition of the P1 and P2 lines (P2 mostly consists of the old Main Ring between F0 and F17) nearly doubled the length of the

beamline connected to the Accumulator. P2 is a dual mode line, running at 8 GeV and 120 GeV, P1 operates at these energies plus 150 GeV to transport beam to the Tevatron. The P1 and P2 optics were designed to match the old Main Ring lattice conditions at F17, which should have resulted in similar conditions to those in Run I. This philosophy maintained the high dispersion found in the old Main Ring near F17 plus the design of the P1 line caused the vertical dispersion to not be matched between the Main Injector and Accumulator.

Initial operational experience in Run IIa indicates that the beamlines have a restricted dynamic aperture, particularly in AP1. Since the magnets in P2, AP1 and AP3 are the same as in Run I, some combination of lattice and survey errors seems to be the most likely cause. Failure to adequately cool the core and carefully steer the antiprotons through the beamline results in poor efficiency and large transverse emittances. At present, even small deviations from the reference orbit results in decreased transfer efficiency. Although new software has been implemented so that BPM's can be used to more accurately steer to a reference orbit, the steering appears to be required on a shot by shot basis.

Future transfers between the Accumulator and the Recycler will not require some of the steps used for transfers to the Tevatron. However, the transfer process will need to be greatly simplified to achieve an antiproton transfer to the Recycler that limits the interruption in stacking to only a minute or two. In addition, there will not be time available to cool the antiprotons prior to transfer to the Recycler. The beamlines will need to have a larger dynamic aperture in order to efficiently transfer the antiprotons.

3.5.1.2 Beam Optics

Recently we started making detailed optics measurements of the Antiproton Source transfer lines. Optics measurements were performed using a differential orbits technique. One complete measurement consists of 5 differential orbits excited by 2 horizontal correctors, 2 vertical correctors and an energy change. With the appropriate betatron phase advance between correctors, such a measurement completely characterizes a linear optics transport line. In this case, the *x*-*y* coupling is sufficiently small so that only six differential orbits are required. They include, two horizontal responses from two horizontal correctors, two vertical responses from two vertical correctors, and horizontal and vertical displacements related to the energy change (dispersion measurement). To illustrate such measurements, the differential orbits from two correctors (one horizontal and one vertical) are shown in Figure 3.5.1 for the current beamline optics (March-October 2001). On the top plot, the curves are built using results from quadrupole magnetic measurements, while on the bottom plot, the curves are built from the fitted quadrupole strength using all six differential orbits (only two are shown in the figure). As one can see, there are discrepancies for both the betatron amplitude and the betatron phase if the focusing strength of the quadrupoles is not adjusted. To fit the data, several of the quadrupole fields require adjustment. For this particular measurement, the most significant discrepancies are for quadrupoles PQ2 (powered by M:Q202) (-9%) and EQ13 (powered by D:Q913) (+8%). The first discrepancy is related to the fact that the 120 GeV and 8 GeV power supplies for PQ2 have opposite polarities, which have not been correctly taken into account in the optics model.

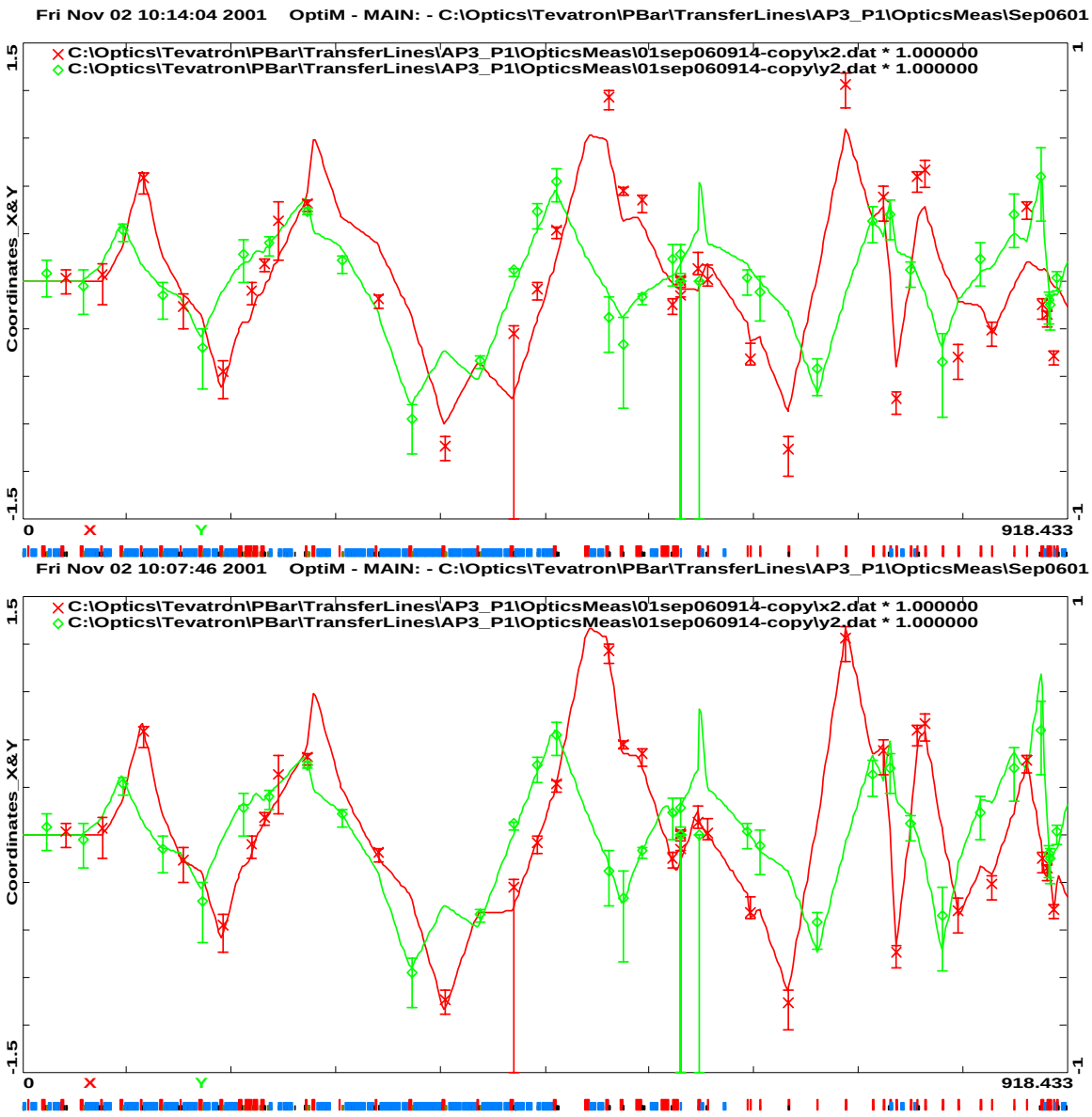

Figure 3.5.1 *Fitting of the optics model to beamline measurements: top – curves are built with design model; bottom – curves are built using updated model, where focusing for a number of quadrupoles was adjusted to get agreement with measurements. Measurements were performed with reverse protons so that the line begins at the Main Injector extraction point and ends at Accumulator injection. Only two of six differential orbits are presented in the figure.*

Currently, we do not understand the cause of the second discrepancy. In addition to the obvious disagreement between the model and the data, the current optics have a number of other problems such as large beam sizes at regions with small apertures, large β functions and unmatched dispersion. The most severe problem is related to the large beam size at regions with small apertures. Currently, it causes about a 15-25% loss in antiprotons during transfers to the Main Injector. Large β functions cause an undesired

increase in the sensitivity of optics due to the quadrupole gradient errors. Even in cases where the acceptance of the beamline is adequate, the large β functions should be avoided if possible. Therefore, the β functions should be minimized through the entire transport line. Although the dispersion mismatch does not cause significant emittance growth because of the small energy spread of the antiproton beam, it would also be desirable to match both the vertical and horizontal dispersion. Thus, to improve the Accumulator to Main Injector antiproton beam transport, both well-designed optics and careful corrections based on beam measurements are required.

There are a few practical limitations imposed on the redesign of the optics. The first is related to the fact that many quadrupoles in the AP3 line are combined into groups so that they are powered from a single power supply. Taking into account that reconfiguring power supply connections with magnets can be an involved process, it is desirable to avoid or, at least, minimize it. The second limitation is caused by the fact that different power supplies are used in AP1 for 8 GeV and 120 GeV operation. Presently, both power supplies have the same polarity and using them with different polarities requires significant hardware modifications. Therefore, changing polarity of the AP1 quadrupoles at 8 GeV implies a simultaneous polarity change for the 120 GeV mode. Generally speaking, the goal is to find a solution that would result in reliable transport line operation quickly and with minimum expense.

Two optics solutions have been proposed as possible upgrades. The optics of the first solution is matched for both β functions and dispersion, but to implement requires significant changes to connections of quadrupoles to power supplies. In contrast, the second solution has unmatched vertical dispersion but does not require any power supply reconfiguration. It still requires a change in polarity for seven AP1 quadrupoles, but is a relatively quick and uncomplicated procedure. Figure 3.5.2 presents the dispersion and β functions for both choices and how they compare to the current optics. Efforts to implement the second optics solution have already begun. Final tuning of the new optics is expected to be completed in the first quarter of 2002.

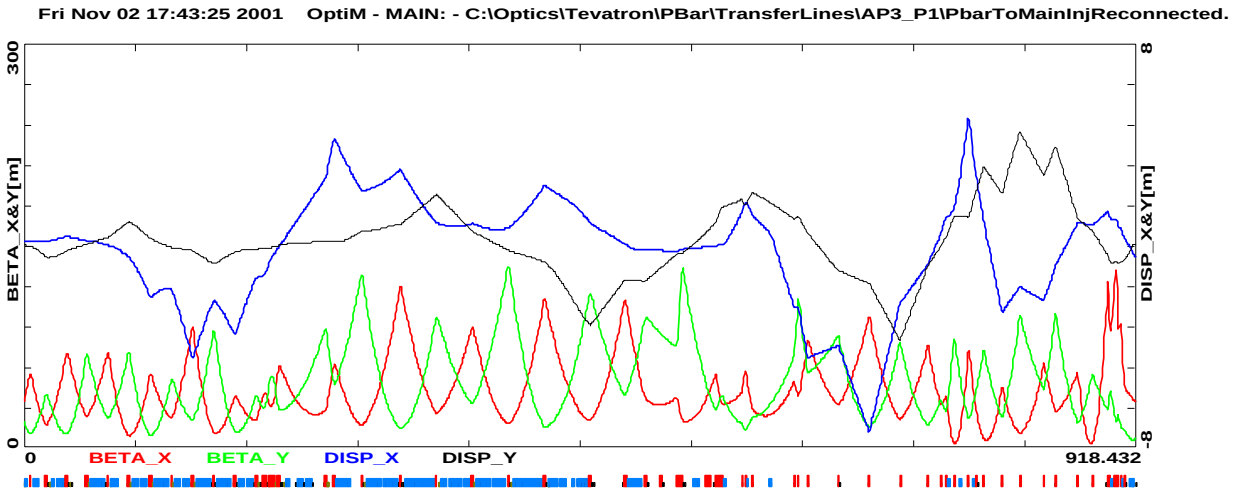

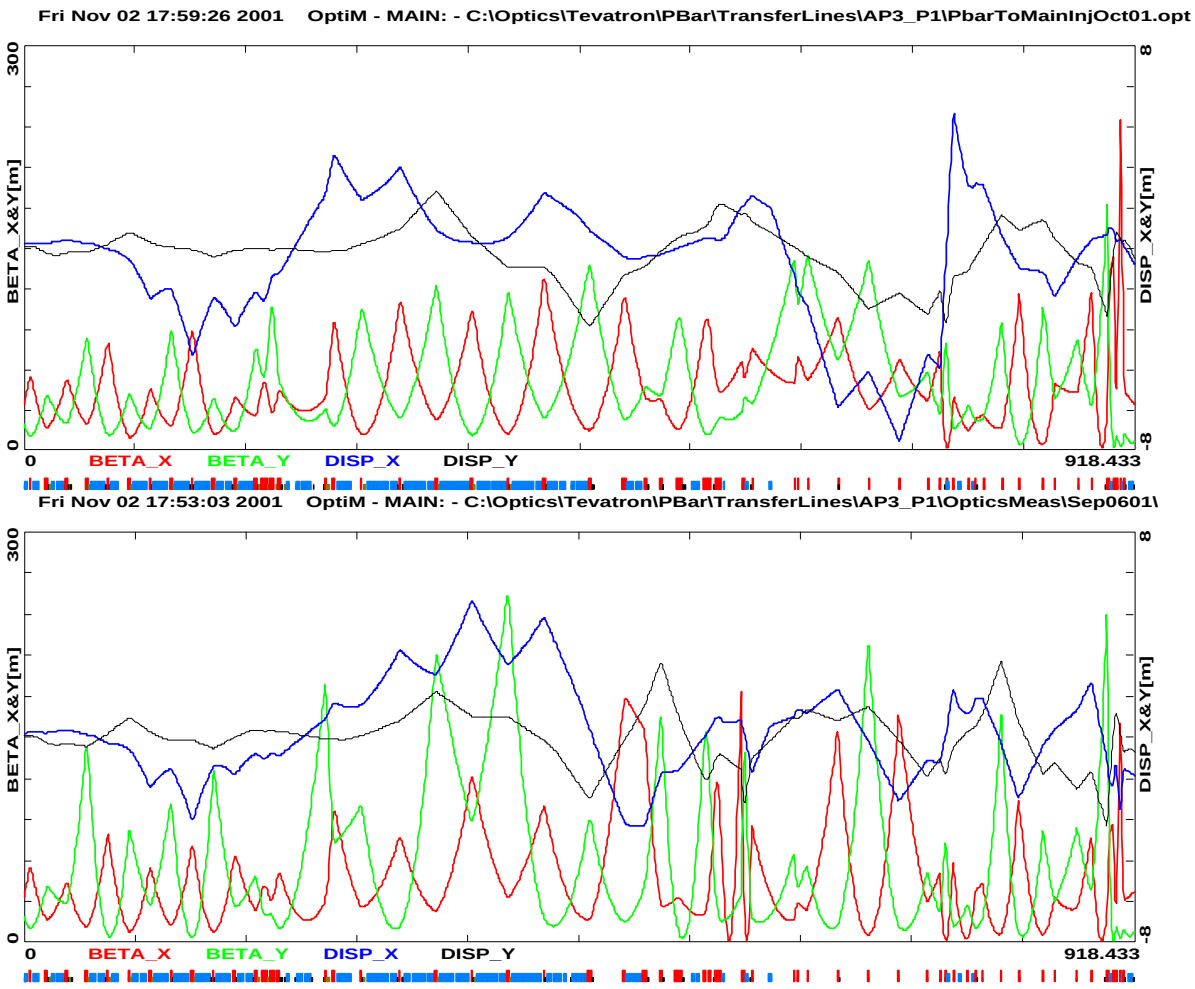

Figure 3.5.2 *β functions and dispersion for various optics options for transport from the Main Injector to the Accumulator: top – completely matched optics, middle – optics with no changes to the quadrupole power supply configuration (vertical dispersion is not matched), bottom present optics as it follows from reconstructed measurements.*

3.5.1.3 Reproducibility

Reproducibility of the beam optics is another serious issue. In order to limit the emittance growth due to an optics mismatch to a few percent, the reproducibility of the integrated quadrupole strengths should be about 10-20 G. This corresponds to $(3\text{-}5)\cdot 10^{-4}$ relative to the total gradient. For comparison, note that for 3Q120 quadrupoles (located in the P1 and AP1 lines), the integral strength resulting from the residual field is approximately 2000 G and is about hundred times greater than the necessary accuracy. Thus, reliable transfers require both good regulation in the quadrupole power supplies and reliable hysteresis cycling of the magnets. A comparison of differential orbit measurements performed on different days has been used to measure long term transfer line reproducibility. Figure 3.5.3 presents such results from measurements performed on September 6 and 16, 2001. The top picture shows differential orbits corresponding to the excitation of the I:HT702 corrector in the P1 line. The orbits exhibit a significantly larger difference than orbits corresponding to the other three correctors. In the presented data,

the beam displacement is normalized to the square root of the β function, $x\sqrt{\beta_0/\beta}$ (β_0 =10 m), and the betatron phase advance is used as a longitudinal coordinate. In the variables, the beam motion exhibits a sinusoidal character. One can see that the measurements are approximately the same, but show some discrepancy between the two measurements and between the measurements and theory. The bottom picture shows the difference of differential measurements. One can see that at the beginning of the line the difference is nearly zero, then grows and exhibits a sinusoidal behavior in the second half of the line. The appearance of such a discrepancy is related to differing focusing strength for one or more quadrupoles. Detailed analysis has shown that for this particular case, the irreproducibility is mainly related to the PQ7A&B quadrupoles (powered by M:Q207), which experienced a field change of approximately 300 G. That corresponds to approximately 7% of its integral strength compared to the residual field and to 0.5% of its total focusing strength at 8 GeV. We need about an order of magnitude improvement in the reproducibility of the quadrupoles. The belief is that the improvement can be achieved by introducing hysteresis cycling for all magnets immediately before transfers.

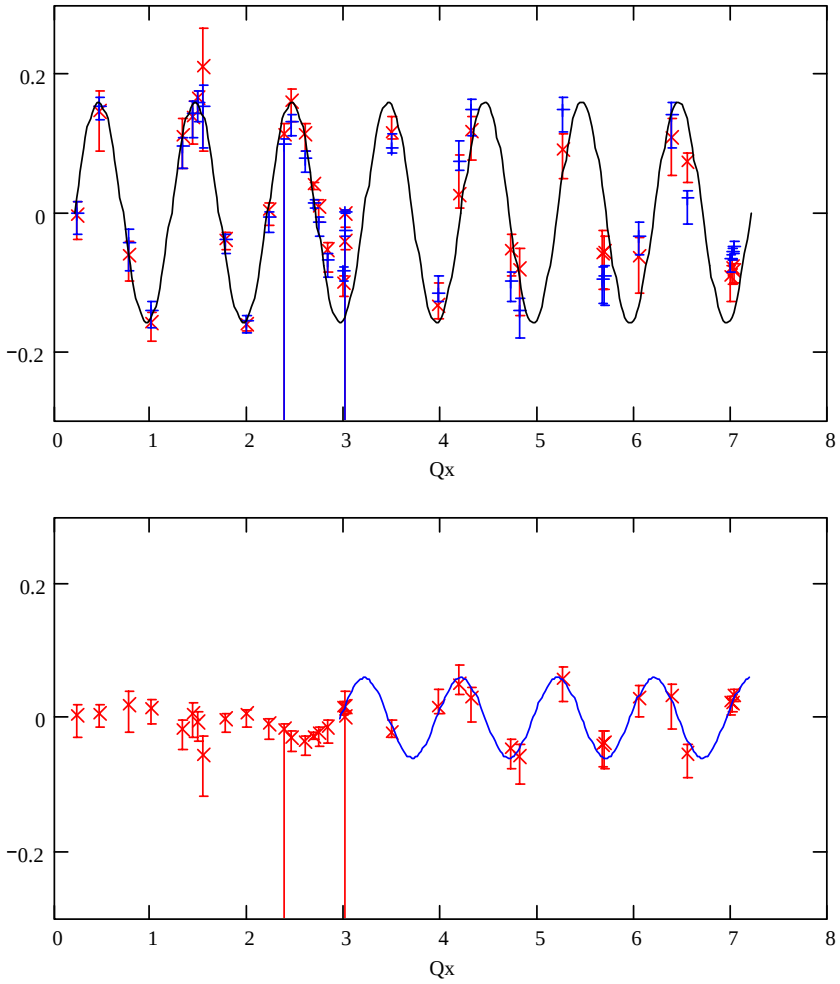

Figure 3.5.3 *Comparison of differential orbit measurements performed on September 6 and 16, 2001; top – differential orbits, bottom – difference of differential orbits. Data are presented in normalized coordinates*

Lack of reproducibility of the beam orbit (steering) is easier to control and correct. Figure 3.5.4 presents the difference between beam orbits for measurements performed on September 6 and 16, 2001. Solid curves represent the beam orbit for the beam injected with an initial beam offset and angle coming from the Main Injector and with no beam deflection by correctors. This is justified by the fact that the correctors, with the exception of the last two horizontal correctors, were the same for both measurements. One can see that the total difference between the orbits is as much as 5 mm. Most of the error is caused by a trajectory change originating from the Main Injector. Discrepancies related to the transfer line are less than 2 mm. The emittance growth related to the dipole mismatches can be estimated by the following formula:

$$\frac{\Delta\varepsilon}{\varepsilon} = \sqrt{1+\frac{x_0^{\,2}}{\varepsilon\beta}} - 1 \approx \frac{x_0^{\,2}}{2\varepsilon\beta} \qquad (3.5.1)$$

where x_0 is the maximum beam displacement related to the β function β, and ε is the rms beam emittance

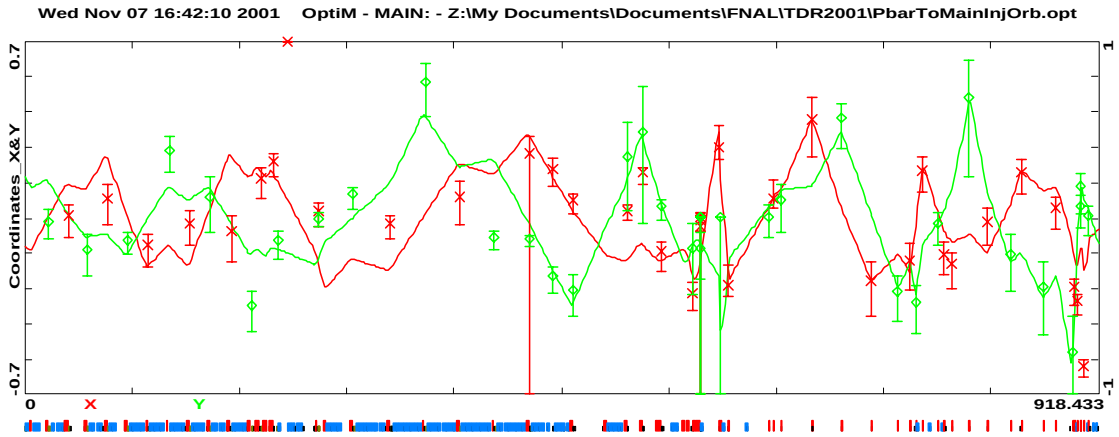

Figure 3.5.4 *Difference of horizontal and vertical beam positions for differential orbit measurements performed on September 6 and 16 of 2001*

To meet the requirement that emittance growth due to dipole mismatches is below 1%, the maximum beam orbit deviations should not exceed 0.6 mm (ε = 0.33 mm mrad, β =50 m), which is significantly smaller than the observed long term orbit stability. The requirements for beam transport with no losses are less strict. An orbit within 5 mm of the ideal would still allow transfer efficiencies near 100%. A beam damper could be used to greatly reduce TBT oscillations, it is realistic to expect that the P1-P2-AP1-AP3 beamlines will have adequate reproducibility to efficiently transfer antiprotons.

While differential orbit measurements are well suited for measuring optics properties of a beamline, they are not able to measure the actual beam envelope match for beam transfers. Therefore, it's necessary to use an additional diagnostic for correcting the beam envelope match. A quadrupole pickup is well suited for this role. As with most other optics tuning procedures, the measurements will be performed with reverse protons injected into the Accumulator. The presence of quadrupole oscillations in the beam will indicate an envelope mismatch. Four "orthogonal" quadrupoles in the transport line will

be used for the final tuning of the envelope match. It would be desirable to resolve the beam envelope oscillations corresponding to about a 1% growth in emittance. That implies that for a standard pickup with signals coming from two electrodes subtracted from each other, we need to resolve oscillations with an amplitude of 10^{-4} relative to the total plate signal. Knowing that the oscillations occur at double the betatron frequency significantly simplifies the problem. For the case of 10^{10} protons injected into the Accumulator, there should be no problem resolving quadrupole signal from electronics noise. However, there is a challenging problem of rejecting the common mode signal. A quadrupole pickup already exists in the Accumulator. It was used in collider Run I with limited success and has not been used since that time. The plan is to revive it and try to make it a useful diagnostic. If it is found to not be possible to achieve the required common mode rejection for this pickup, a new quadrupole pickup similar to a CERN design could be used. The CERN design does not have a problem with common mode rejection.

3.5.1.4 Suitability of present beamlines

After analyzing the optics and aperture data for the P1-P2-AP1-AP3 lines, all indications are that the present beamlines can be modified for use in Run IIb. At the present time, it is believed that the physical apertures will be adequate for efficient antiproton transport with the anticipated beam emittances. Presently the beamline lattice is not adequate and the transfer efficiency is less than 100%. The lattice will need to be modified to minimize the transverse beam size at locations with small physical apertures and also provide a lattice match. Some AP-1 magnets may still need to be replaced to provide larger aperture if losses remain. Magnets in AP1 will need to be ramped in order to achieve rapid transfers as described in the next section. The existing power supplies will need to have improved regulation in order to operate at both 8 GeV and 120 GeV. Ramp cards will also be installed to provide the appropriate reference for the supplies.

The option of upgrading the existing beamlines is much more manageable in scope to the alternative of building the AP5 line. Most of the upgrades can take place during relatively short periods of machine downtime. Besides the large improvement in program interruption, the cost of implementing the plan is far less. Changes to the lattice will take place over the next year and will provide an immediate benefit to the collider program, both in improved transfer efficiency and emittance preservation.

3.5.2 Frequent, rapid transfers

3.5.2.1 Run IIa sequence

Presently, the process of preparing to transfer antiprotons from the Accumulator to the Tevatron (via the Main Injector) is a lengthy process. The tune-up and preparation for transfers usually takes between 1 and 2 hours. Listed below are the major steps that are undertaken in the setup process. Also listed is the approximate time required for each step (including intermediate or related steps) and an explanation of how the step will be modified or eliminated when making transfers to the Recycler.

(1) Antiprotons in the Accumulator core are stochastically cooled to reduce the momentum spread and transverse emittances. The core cooling takes place in parallel with the following steps, but takes at least 30 minutes. Some of the following steps are synchronized with transfer preparations in the Tevatron. [30 minutes in parallel with steps below] *No additional time is spent cooling the core, emittance needs to be controlled during stacking. Also, there will be no need to synchronize with activities in the Tevatron.*

(2) Stacking is halted, beam in the stacktail is swept far enough towards the core so that the core momentum systems can capture the beam. [10 minutes] *Beam left in the stacktail is not swept into the core. Beam in the stacktail is not lost during the extraction process and is swept over when stacking resumes.*

(3) Main Injector injection energy and last turn positions at the extraction Lambertson magnet are checked and corrected. [10 minutes] *There is no check, with reverse protons, of Main Injector positions. If needed, low field stacking orbits could be correlated to orbits on antiproton transfers allowing corrections between transfers.*

(4) AP-1 power supplies are switched from 120 GeV to 8 GeV operation. Timers and other devices related to the transfer process are set to nominal. [10 minutes] *Beamlines are ramped, ramps are triggered to play when the transfer is initiated. No changeover is required for AP-1 and timers are already set for antiproton transfers.*

(5) The beamline orbit is checked with reverse protons between the Main Injector and Accumulator. A steering program is used to make corrections to less than 1 mm from the reference orbit. [15 minutes] *There will be no steering corrections with reverse protons. The beamline will be able to tolerate orbit drift anticipated to be a few millimeters.*

(6) Turn by turn oscillations in the Accumulator are minimized to ensure the first turn matches the closed orbit to within 0.5 mm. [10 minutes] *There will be no turn by turn corrections with reverse protons. Antiproton oscillations in the Main Injector will be reduced by injection dampers. Additionally, oscillations will be minimized with adjustments based on measurements and made between transfers.*

(7) RF systems and timing are set up for antiproton transfers. [5 minutes] RF systems will already be on and configured for transfers, awaiting the appropriate trigger.

(8) The antiproton longitudinal distribution is "squared" so that the nine transfers have approximately the same intensity and to maximize the total flux. [10 minutes] *There will be no need to square the core, the entire core will be removed in single transfers to the Recycler.*

(9) Antiprotons are transferred in nine separate transfers at approximately 60 seconds apart. Details of the transfer process are listed below. [10 minutes] *Only a single antiproton transfer will be made. Beam is bunched at 2.5 MHz and moved to the extraction orbit in about 10 seconds.*

   (a) Adiabatic bunching and acceleration from the core to the extraction orbit of about 10% of the original antiproton stack with an h=4 2.5 MHz RF system.

(b) Bunching with an h=84 53 MHz RF system for synchronous transfer to the Main Injector

(c) Transfer from the Accumulator to the Main Injector down the AP3, AP1, P2 and P1 lines.

(d) Acceleration to 150 GeV in the Main Injector and coalescing the antiprotons into four bunches.

(e) Transfer from the Main Injector to the Tevatron down the A1 line.

(f) Injection into the Tevatron with beam cogged to the proper longitudinal location.

(10) The antiproton source is reconfigured for stacking. [15 minutes] *Stacking resumes immediately after the transfer when the appropriate timing events return.*

3.5.2.2 Mechanics of transfers to the Recycler

In the future the transfers from the accumulator to the Recycler will consist of the following steps:

(1) Stacking is halted and appropriate transfer events are loaded. A small number of devices are switched from stacking to transfer configuration. (10 seconds)

(2) The stack is adiabatically bunched at 2.5 MHz and accelerated to the extraction orbit. [10 seconds]

(3) The transport lines will undergo two hysteresis cycles prior to the transfers. P1, P2 and AP1 will ramp, AP3 will be cycled prior to the interruption in stacking. [10 seconds]

(4) Extraction from the Accumulator and transport to the Main Injector through the AP3, AP1, P2 and P1 lines. [0 seconds]

(5) Injection into the main injector and synchronous capture into Main Injector RF buckets. [0 seconds]

(6) Fast damping of the betatron oscillations created by injection errors. [0 seconds]

(7) The beam energy and frequency are matched to the Recycler. [5 seconds]

(8) The beam is transferred from the Main Injector to the Recycler. [0 seconds]

(9) Beam is debunched adiabatically in the Recycler. [10 seconds, but takes place after transfers have been completed]

(10) Main Injector stacking events return and stacking resumes. [10 seconds]

Intermediate steps will add a small amount of additional time, but the transfer process is expected to take about one minute. To achieve this ambitious goal, the following are prerequisites:

(1) P1, P2 and AP1 all need to be ramped (P1 and P2 are already ramped). Ramps should be designed so that virtually no time will be needed to switch between stacking transfers. EB6, which is located where AP3 joins the AP-3 line, will also need to be ramped. AP3 power supplies will continue to run DC, but will need to follow a hysteresis protocol prior to each transfer.

(2) Orbit reproducibility in the transport line has to be better than 5 mm. P1-P2-AP1-AP3 optics and dynamic aperture need to be improved to the point that 5 mm oscillations do not cause beam loss.

(3) Lack of quadrupole reproducibility should not cause emittance growth.
(4) Injection oscillations in the Main Injector and Recycler will be minimized by a combination of trim magnet adjustments between transfers and injection dampers in both machines.
(5) Injection dampers need to suppress injection errors in about 100 turns.
(6) Reverse proton tune-up will only be used for troubleshooting failures, poor transfers or for operation after longer periods of downtime.
(7) Settings changes to devices need to be kept at a minimum for the transfer process to be acceptably short. The transfers need to be highly automated, but mostly driven by hardware awaiting appropriate triggers.

It is important to note that the beamline BPM's will not be able to detect the antiproton positions because of the 2.5 MHz RF structure. The BPM's are designed for a 53 MHz RF structure, so SEM's and multiwires will be the only diagnostic available to determine antiproton positions. It is assumed that orbit corrections will be infrequent and will either be based on SEM and multiwire data or BPM data taken with reverse protons.

3.5.3 Reducing injection oscillations

3.5.3.1 Orbit correction and closure

In collider runs I and IIa, reverse protons are used to tune up the P1-P2-AP1-AP3 lines prior to antiproton transfers. Antiprotons have traditionally not been used for beamline tune-up due to their limited supply. Besides being wasteful, typical antiproton transfers do not have enough intensity to provide reliable BPM data. Secondary Emission Monitors (SEM's) can be used to identify gross steering errors, but would not be appropriate for fine adjustments with a steering program. BPM's in the Accumulator are used with the reverse protons to close the injected beam to the closed orbit. In principal, the antiprotons transferred into the Main Injector would follow an identical orbit to the reverse protons and there would be no injection oscillations. In practice, the orbits are only approximately the same and significant TBT oscillations are observed.

Beamline tune-up with reverse protons will not be routinely performed for antiproton transfers to the Recycler. Although this mode of operation is still available for identifying failures and infrequent orbit adjustments, the beamline orbit will generally not be adjusted. Antiproton TBT oscillations in the Main Injector will be reduced using BPM data and a closure program. Closure of the antiprotons into the Main Injector is already performed routinely during collider operation and was also used in Run I. The BPM's are designed for a 53 MHz beam structure so new detectors designed for a 2.5 MHz RF structure will need to be built and installed. A similar system will need to be created for the Recycler, although their BPM system is already designed for 2.5 MHz.

Even with closure tuning between antiproton transfers, residual injection oscillations will still remain. Transverse dampers will be used to minimize the remaining oscillations and preserve transverse emittances. The dampers are a key component of the fast transfer scenario and are needed to ensure small emittance dilution and efficient transfers.

3.5.3.2 Injection dampers

Maintaining orbit stability within 5 mm of the ideal orbit on antiproton transfers should result in transfer efficiencies near 100%. However, to prevent emittance growth in the Main Injector, the plan is to use an injection damper to minimize oscillations. The damper will need to suppress initial betatron oscillations with amplitude of up to 5 mm within 100 turns.

	Horizontal	Vertical
Momentum [GeV/c]	8.9	
Kicker length [m]	1.0	
Kicker gap [cm]	9.5	9.5
Amplifier power [kW]	1.6	
Power amplifier bandwidth [MHz]	10-80	
Maximum kick [μrad]	1.8	1.8
Range [±mm]	5	5
Beta function [m]	60	60
Damping time [turns]	90	90

Table 3.5.1 Main Injector damper parameters

Instead of designing and installing a new damper system, the plan is to enhance the capabilities of the existing Main Injector injection damper. The damper currently is used to damp proton injection oscillations, but is unable to damp an antiproton beam because of the direction of travel. The plan is to add low-level electronics to the existing damper system for the antiproton direction and to use the existing power amplifier and kicker. This not only has the benefit of reducing the cost, but also more importantly will reduce the downtime needed to implement the system. A simplified diagram of the system is presented in Figure 3.5.5 and damper parameters are listed in Table 3.5.1. To achieve $\pi/2$ betatron phase advance between the BPM and kicker, the signals from two BPMs are combined. While the power amplifier has a sufficiently wide bandwidth, the existing system is built to damp only the lowest betatron sideband. This significantly alleviates the sensitivity to noise on the pickup. As will be illustrated below, the existing amplifier has adequate power to prevent emittance growth due to injection errors on the protons and would be suitable for the antiprotons. The system has to be able to damp betatron oscillations of up to 5 mm and to suppress the emittance growth by about 100 times as compared to undamped betatron oscillations.

In the case of strong damping, $g >> \sqrt{\overline{\Delta\nu^2}}$, the emittance growth due to injection errors is determined by the following expression:

$$\frac{\Delta\varepsilon}{\varepsilon} \approx 2\pi^2 \frac{\overline{\Delta\nu^2}}{g^2} \frac{{x_0}^2}{2\varepsilon\beta} \qquad (3.5.2)$$

where g is the dimensionless damping decrement, and $\sqrt{\overline{\Delta\nu^2}}$ is the rms betatron tune spread related to the beam decoherence time $\tau_{decoh} \approx 1 \Big/ \left(f_0 \sqrt{\pi^2 \overline{\Delta\nu^2}} \right)$. As one can see

from Table 3.5.1, the damping time is about 90 turns for a 5 mm beam displacement. Then, Eq. (3.5.1) yields that the betatron tune spread has to be below $2.4 \cdot 10^{-4}$, which corresponds to about a 1500 turn decoherence time. The decoherence time of the Main Injector is mainly determined by the lattice chromaticity and is usually in the range of a few hundred to a few thousand turns. Figure 3.5.6 shows a turn-by-turn BPM measurement made with protons showing the damper response time after the beam is "pinged" with a kicker. The diagram illustrates that a beam with 5 mm oscillations can be damped with the existing system. It also shows that the machine can be tuned so that the decoherence time is long enough so that damped injection oscillations will cause only small emittance dilution.

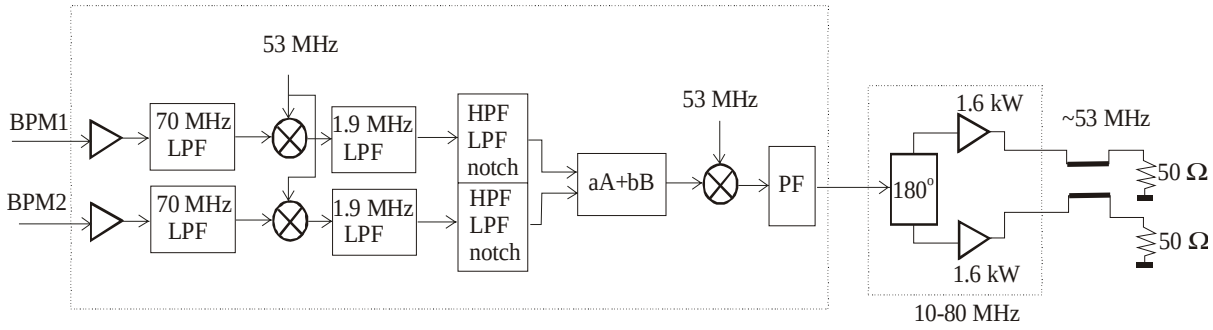

Figure 3.5.5 *Simplified schematic of the narrow band feedback system*

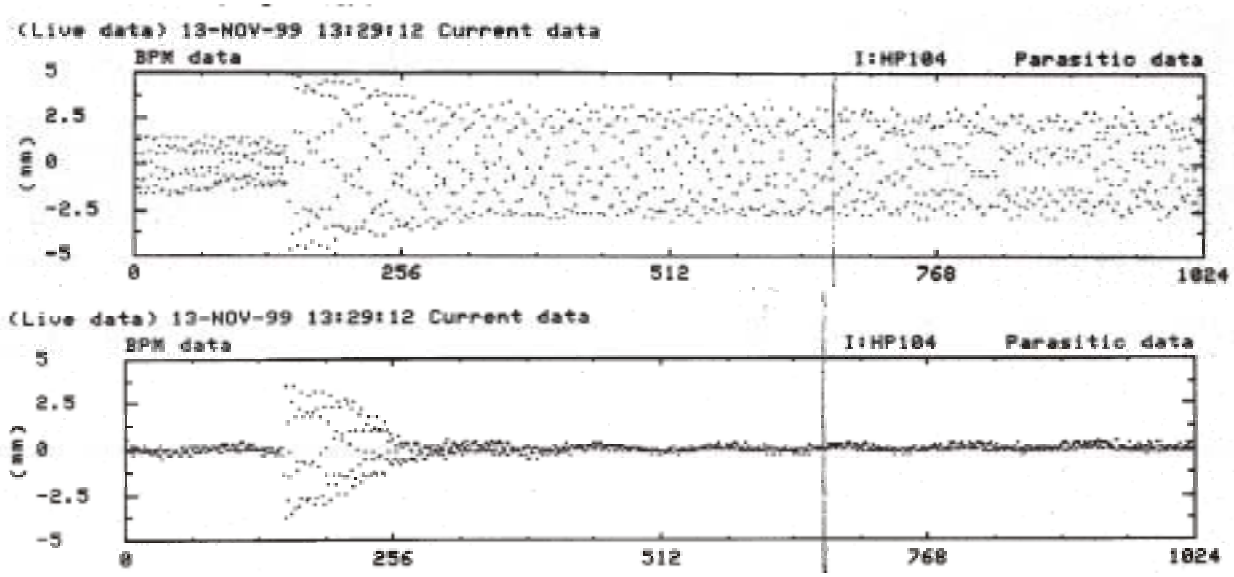

Figure 3.5.6 *BPM turn by turn of an undamped proton beam (top) and damped proton beam (bottom)*

The orbit length of the accumulator is 1/7 of the orbit length of the Main Injector. This allows the use of a narrow band system, which damps only the lowest betatron side band. The bandwidth of the system has to be narrower than the revolution frequency and wider than the damping decrement. In this case, the betatron oscillations of the injected

batch are damped by a low frequency sinusoidal waveform. If the system is appropriately phased, the residual betatron oscillations are below $(\pi/14)^2/2 \sim 0.025$ of the initial betatron oscillations. The corresponding emittance growth is the square of this number and is negligible in comparison with other effects.

3.5.4 Plan and status

The primary goals of the project are to avoid any beam loss during antiproton transfers to the Recycler and to minimize or eliminate emittance growth. In addition, transfers need to be made in a short period of time, much shorter than the time required presently for transfers to the Tevatron. To address these problems, the plan is as follows:

(1) Redesign and correct the lattice in the Accumulator to Main Injector transport lines (P1-P2-AP1-AP3).
(2) Introduce a consistent hysteresis cycling protocol for all quadrupoles, dipoles and trims in the transfer lines into the transfer process.
(3) Make final lattice adjustments with a diagnostic quadrupole pickup, either the existing device in the Accumulator or a newly designed pickup.
(4) Modify electronics for AP-1 120 GeV power supplies so that regulation is good enough for 8 GeV operation.
(5) Add electronics to the Main Injector injection damper for the suppression of dipole injection errors on the antiproton transfers.
(6) Improve the efficiency of beam steering and optics analysis.

Expenditures related to this project can be grouped into five categories.

(1) The lattice upgrade for the transport lines will eventually involve some reconfiguration of power supplies and magnet shunts. M&S requirements for installing cables and shunts will be \$40k for FY '02. Labor requirements in this time frame will be 0.2 FTE of technician time for installation and 0.4 FTE of physicist time to commission the new lattice.
(2) The Main Injector injection damper will be modified for use with antiproton transfers. In FY '02, \$20k of M&S will be spent for upgrades to the low level electronics and instrumentation. Labor requirements will be an engineer at 0.3 FTE and a technician at 0.2 FTE for the design and installation of the electronics. 0.2 FTE of physicist time will also be needed to commission the system with beam.
(3) Power supplies for the AP1 line will need to be upgraded to have adequate regulation during 8 GeV operation. To support rapid transfers, the AP1 line will need to operate at both energies with a single power supply. The upgrade is expected to take place in FY '03, so there will be no expenditures in FY '02. M&S requirements for FY '03 will be \$300k for the electronics modifications to the supplies. To support the modifications, 1 FTE of engineering and 1.5 FTE of technician time will be required. 0.5 FTE of physicist labor and 1.0 FTE of computer professional labor is included for software related to implementing the rapid antiproton transfers.
(4) On-line modeling of the transfer lines will be upgraded to improve orbit correction and lattice measurements. No outlay of M&S is expected in FY '02.

Labor will be 0.5 FTE of physicists time and 0.5 FTE of computer professional time.

(5) The diagnostic quadrupole pickup in the Accumulator will be recomissioned and used for lattice corrections. If this device proves inadequate, a new pickup will be required that will require more resources than those estimated here. M&S requirements for FY '02 will be $20k which will cover electronics upgrades to the existing detector. Labor requirements for the next year will be 0.25 FTE of engineering time and 0.2 FTE of technician time for the design and installation of the electronics and 0.2 FTE of physicist time for commissioning the system.

	Total	M&S	Labor	Phys.	Eng.	Draft	Tech	CP
FY02	380	90	290	1.3	0.5	0.6	0	0.5
FY03	700	300	400	0.5	1	0	1.5	1
FY04	0	0	0	0	0	0	0	0
FY05	0	0	0	0	0	0	0	0
Project	1080	390	690	1.8	1.5	0.6	1.5	1.5

Table 3.5.2 *Funding profile for rapid antiproton transfer project*

3.5.5 Conclusion

Rapid transfers from the Accumulator to the Recycler can be achieved in Run IIb, but will require a significant change in philosophy from transfers made in the past. Routine beamline orbit corrections with reverse protons will be eliminated, greatly reducing setup time. To be successful in this mode of operation, several changes and improvements will need to be made. The beamlines will need to be far more reproducible than has been experienced in the past. A combination of lattice improvements, ramped power supplies and a consistent hysteresis protocol will be used to make the magnetic fields more reproducible and the beamline more tolerant to errors. The existing beamlines will be utilized for the transfers, avoiding the cost and program interruption that would accompany the construction of a new beamline. To achieve a short interruption to stacking for the transfers, device setting changes will need to be kept to a bare minimum. The transfer process will need to be highly automated, requiring minimal interaction from the Operators.

There are a number of advantages to taking this approach for rapid transfers. Lattice measurements and improvements will take place in the near future and the benefits will improve transfer quality prior to the start of Run IIb. The cost and program interruption associated with the beamline upgrade will be modest compared to what a new beamline will require. Ramped AP-1 power supplies can be tested and implemented prior to Recycler operation. Similarly, pbar injection dampers would improve collider luminosity as soon as they are commissioned. In general, the upgrades and improvements anticipated to support rapid antiproton transfers to the Recycler are incremental. Potentially, they will provide operational improvements to the collider program as they are implemented.

3.6 Antiproton Tuneshift in the TEVATRON

In the Tevatron, the antiproton bunches suffer a tuneshift due to their interactions with the more intense proton bunches. In multibunch operation, the tuneshifts vary from antiproton bunch to antiproton bunch, leading to an effective spread in tune. An electron lens, consisting of a short, low energy, electron beam propagating along the axis of a solenoidal field, can induce a tuneshift on the antiproton bunches, which has the opposite sign to that, which they experience, from the protons. With appropriate choice of parameters two such lenses could provide effective beam-beam tuneshift compensation. An R&D program has resulted in the construction and, recently, the successful testing of a single such device. If results continue to be positive the use of such devices could lead to a longer luminosity lifetime in the Tevatron and hence to a large integrated luminosity. Further luminosity improvement could come from compensation of the nonlinear beam-beam tune spread using shaped electron beams.

3.6.1 Goal and Potential of Beam-Beam Compensation

3.6.1.1 Luminosity of the Tevatron and Beam-Beam Effects in Run II

3.6.1.1.1 Luminosity

As already discussed in Section 2 the luminosity of the Tevatron collider may be written as

$$L = \frac{3\gamma_r f_0}{\beta^*}\left(BN_{\bar{p}}\right)\left(\frac{N_p}{\varepsilon_p}\right)\frac{F\left(\beta^*,\theta_x,\theta_y,\varepsilon_p,\varepsilon_{\bar{p}},\sigma_z\right)}{\left(1+\varepsilon_{\bar{p}}/\varepsilon_p\right)} \qquad (3.6.1)$$

where $\gamma_r=E/mc^2$ is the relativistic energy factor, f_0 is the revolution frequency, and β^* is the β function at s=0 (where it is assumed to attain the same minimum in each plane). The proton (antiproton) beam transverse emittance $\varepsilon_p\,(\varepsilon_{\bar{p}})$ is defined to be $\varepsilon = 6\pi\gamma_r\sigma^2/\beta$ for a bunch with a gaussian distribution and assumed to be the same in both transverse planes, B is the number of bunches, $N_p\,(N_{\bar{p}})$ is the number of protons (antiprotons) per bunch, θ_y and θ_y are the crossing half-angles, σ_z is obtained from the rms proton and antiproton bunch lengths $\sigma_z^2 = \left(\sigma_{zp}^2 + \sigma_{z\bar{p}}^2\right)/2$ and $F\leq 1$ is a form-factor that accounts for the depth of focus (hourglass) and crossing angle effects on the luminosity caused by non-zero bunch lengths. The bunch lengths depend on the longitudinal emittance and the RF voltage, but the luminosity depends only on the bunch lengths. In Run IIa, the form-factor is dominated by the hourglass effect (the design crossing-angle is 0). For Gaussian beams the hourglass effect may be written as:

$$\mathrm{F} = \frac{\sqrt{\pi}\beta}{\sigma_z}\mathrm{e}^{\frac{\beta^2}{\sigma_z^2}}\mathrm{erfc}\left[\frac{\beta}{\sigma_z}\right] \qquad (3.6.2)$$

where the complementary error function is related to the error function by $\mathrm{erfc}(z) = 1 - \mathrm{erf}(z)$. For Run IIb the crossing angle effect is large and the luminosity comes mainly from the z=0 region where the hourglass effect is small. In this case the form-factor F may be written as

$$F = \frac{1}{\sqrt{1 + \sigma_z^2\left(\theta_x^2/\sigma_x^2 + \theta_y^2/\sigma_y^2\right)}} \qquad (3.6.3)$$

where $\sigma_x^2 = \left(\sigma_{xp}^2 + \sigma_{x\bar{p}}^2\right)/2$ and similarly for y.

The luminosity formula (1) is written to emphasize the major issues in achieving high luminosity. The first quantity in parentheses is the total number of antiprotons. Under current and probably future operating conditions, the most important factor contributing to the achievable luminosity is the total number of antiprotons in the ring, $BN_{\bar{p}}$. The second most important factor is the proton phase space density, N_p/ε_p, which is constrained by the need to limit the beam-beam tune shift. The form-factor (F) and the emittance ratio factor $\varepsilon_p/\left(\varepsilon_p + \varepsilon_{\bar{p}}\right)$ are important, but they cannot exceed unity and the amount of luminosity that can be gained using these factors is limited.

3.6.1.1.2 Beam-Beam Effects

The formula for the (linear) antiproton beam-beam tune shift (and equal non-linear tune spread) with no crossing angle is:

$$\Delta\nu = 6\frac{r_p}{4\pi} n_c \frac{N_p}{\varepsilon_p} = 0.0073\,(\pi \text{ mm - mrad}/10^{10}) n_c \frac{N_p}{\varepsilon_p} \qquad (3.6.4)$$

where r_p is the classical proton radius (1.535×10^{-18} m) and n_c is the number of interaction points. Note that the Tevatron functions with antiproton and proton bunches executing helical orbits such that at all points except the interaction points, the counter rotating bunches are transversely separated. Operating experience in the Tevatron Run I suggests that the maximum tolerable beam-beam tune shift lies in the range 0.020 to 0.025. When the beam-beam tune shift is caused primarily by head-on interactions at zero crossing-angle, the beam-beam tune shift determines the maximum value of the factor N_p/ε_p, which appears in Eq (3.6.1)

The biggest change from Run I is the increase from 6 to 36 and later, in Run IIb, to hundreds of bunches bunches per beam[40]. 36 bunches per beam correspond to a minimum bunch spacing of 396 nsec. In Run IIb, the minimum bunch spacing will be 132 ns. The peak luminosity achieved during Run Ib was 2.8×10^{31} cm^{-2} sec^{-1}. For 6x6 operation, this corresponds to about 4.9 inelastic interactions per bunch crossing. Multiple interactions per crossing (IC) make the triggering, the event reconstruction, and physics analysis more difficult. Generally, CDF and D0 detectors would prefer no more than 5 IC. The limit on the number of ICs, combined with the desire for more luminosity, pushes the collider to more bunches.

The main beam-beam concern for multi-bunch operation is that, because bunches are not evenly spaced around the ring, different bunches within a train encounter the

bunches in the opposing beam at different places around the ring. (Proton and antiproton beams share the same vacuum pipe and, in addition to the two main interaction points at B0 and D0, there are many near misses.) This causes differences between bunches in the train. Because of much higher intensity in the proton beam, the antiprotons suffer most from the beam-beam effects.

Figure 3.6.1 shows the tune spreads for all pbar bunches under Run IIa and IIb conditions[41]. The tuneshifts for pbars with zero betatron amplitudes are shown as open circles. Gaussian distributions for the horizontal and vertical displacements and angles of pbars are assumed. From these we calculated their horizontal and vertical betatron amplitudes, and then interpolated between previously calculated tuneshifts with amplitudes for each pbar. The darker the spot in Figure 3.6.1, the more antiprotons have those tunes. As seen from Figure 3.6.1, the bunch-to-bunch (linear) tune shift and intrabunch (non-linear) tune spread are:

$\Delta\nu_{BB}$	$\approx$ 0.007	$\Delta\nu_{NL}$	$\approx$ 0.025	for Run IIa
$\Delta\nu_{BB}$	$\approx$ 0.004	$\Delta\nu_{NL}$	$\approx$ 0.008	for Run IIb

During Run IIa, the tune footprints for most bunches are almost identical. However, pbar bunches 1 and 12, 13 and 24, 25 and 36 are shifted from the others because they do not see protons at the first crossing point upstream or downstream of the IPs, respectively. (The filling pattern has 3 fold symmetry, the 2 bunches at a given location in the 3 trains should all behave identically). As a result, the pbars take up more space in the tune plane. This may make it more difficult to find operating conditions that are acceptable for all the pbar bunches. If this becomes an intractable problem, we are considering the possibility of not using (not filling) pbar bunches 1,12,13,24,24, 36. This would give us stores of 36 proton bunches on 30 pbar bunches. There are other problems with this approach, but it is a possibility. An alternative solution is *linear beam-beam compensation* (see below).

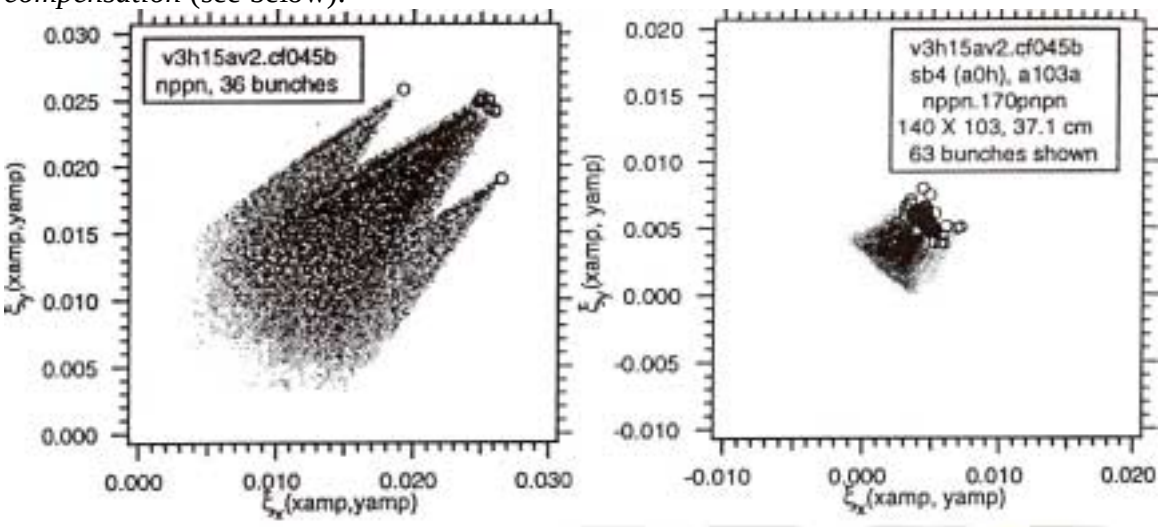

Figure 3.6.1 *Gray scale plots showing the tune footprints for all pbar bunches under Run IIa (left) and Run IIb (right) conditions. The darker the point, the more pbars have those tunes. No synchrotron motion for the pbars. The open circles show the tunes for pbars with zero beatron amplitudes.*

During Run IIb 140 proton bunches collide with 103 pbar bunches. Because we don't have any symmetry in the 132 ns filling pattern, no two pbar bunches encounter the protons at exactly the same set of crossing points and generally every pbar bunch has a slightly different footprint. The spread between bunches is smaller than for 36x36. That is mainly because the crossing angles have improved the separation at the first few crossing points on either side of the IPs. The footprint in Figure 3.6.1 (right) is "folded". Pbars with horizontal and vertical betatron amplitudes of about ($4\sigma_x$,$4\sigma_y$) have about the same tunes as those with betatron amplitudes (0,0). For small amplitude particles, the tunes decrease with increasing amplitude due to the main IPs and the tune changes due to the first few near misses are small. For larger amplitude particles, the tunes increase with increasing amplitude due to the first few near misses and the tune changes due to the main IPs are small. Taken together, the competition between these effects leads to the fold in the footprint. On the good side, these folds mean that the beam occupies less area in the tune plane and if the resonances have not become stronger and wider, one may have more room in the tune plane between resonances. On the bad side, the folds mean that a particle can have a larger amplitude range for a given range of its tunes. Certain amplitude particles will not detune off the resonances as quickly and so a resonance that aligns with the fold will cause a greater amplitude change than it could without the fold. In summary, the folds are bad signs and indicators of strong nonlinearities.

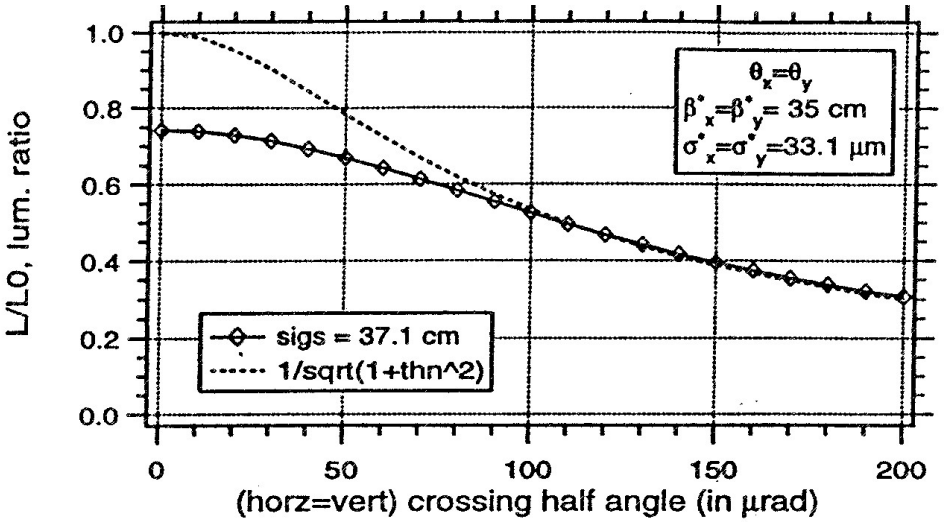

Figure 3.6.2 *The luminosity form-factor as a function of angle. The angle is the half-angle in either plane: it is assumed to be the same horizontally and vertically.*

For Run IIb, the tuneshift formula Eq. (3.6.4) does not apply. The beams cross at an angle to avoid unwanted beam-beam interactions near the interaction region. At a bunch spacing of 132 ns, the first crossing points on either side of the main Interaction Points are before the electrostatic separators. The second crossing points are just beyond the separators, but without a crossing angle, the separation at these points is only about 0.7σ. Without a crossing angle, for each IP, we would have 3 head on collisions and two crossings with separation of about 0.7σ. This is unacceptable and so for this bunch spacing, we require a crossing angle. Because the bunches are very long (~37 cm with the present Tevatron rf system) with very small transverse beam sizes at the interaction point

(about 30. microns), the crossing angles we are contemplating are not small. They have significant effects on the overlap of the beams and hence on the luminosity and beam-beam tune shifts. Figure 3.6.2 shows the form-factor in the luminosity equation as a function of crossing angle.

The dramatic loss in peak luminosity is a strong incentive to keep the crossing angles as small as possible. However, the crossing angle essentially determines the separation at the first 2 crossing points on either side of the IPs (this is the total of 8 crossing points). With both these considerations in mind, we presently plan for half crossing angles of +- 136 μrad. in both the horizontal and the vertical plane. This gives a total angle between the beams of $2^{3/2}$ x136 μrad=385 μrad and corresponds to about 4σ at the first crossing points.

There are several implications of these large crossing angles: a) loss of peak luminosity; b) integrated luminosity concerns; c) change in size and shape of the tune footprints from the main IP; d) synchro-betatron resonances driven by the beam; e) strong effects from the first few crossing points as the tune spreads from these points are not small, moreover, since the beams are separated, the beam-beam interaction can drive both even and odd resonances; f) large displacements in low-beta quads which may reduce dynamic aperture.

Besides the footprints, beam-beam dipole kicks are of concern. Each time a bunch encounters a bunch from opposing beam, they both receive kicks. Of the beams are separated, then the average kick received by the bunch will be non-zero. The average kicks received by both beams will change their orbits and hence their separation. The change in separation in turn changes the average kicks, which bunches give each other. For 36x36, the separations at the IPs are about 1.5 μm (the beam size at the IPs is 33μm), and the total crossing angles are less than 11 μrad (with rms angle spread at the IPs of 100 μrad). For 140x103, these beam beam dipole kicks result in 7μm maximum separation at the IP, and the rms separation 1.6μm.

3.6.1.1.3 Integrated Luminosity

Figure 3.6.2 shows that we expect to lose about a factor of 2 in peak luminosity with 136 μrad crossing angle. But this does not directly translate into a loss of integrated luminosity. Estimates of the sustainable luminosity depend on many factors related to how well the entire accelerator complex is working. The most important factors affecting the performance are the pbar stacking rate and the pbar recycling efficiency. There are a number of strategies, which have been proposed to reduce the instantaneous luminosity while mitigating the corresponding reduction in integrated luminosity. This has is advantageous both for the experiments and for the luminosity lifetime, which aids the mitigation strategies. We do not explore fully the several luminosity leveling schemes but use the following as an example. Figure 3.6.3 shows the dependence of the weekly integrated luminosity on pbar stacking rate into the Accumulator for different Run II operation regimes[42]: 36x36 with the Accumulator only (without pbar stacking in the Recycle Ring); 36x36 with Recycler used for stacking but without pbar recycling; 36x36 with intensity dependent recycling efficiency between 60% and 80% and luminosity leveling to keep the number of ICs at 5; 140x103 with crossing angle; 140x103 without crossing angle.

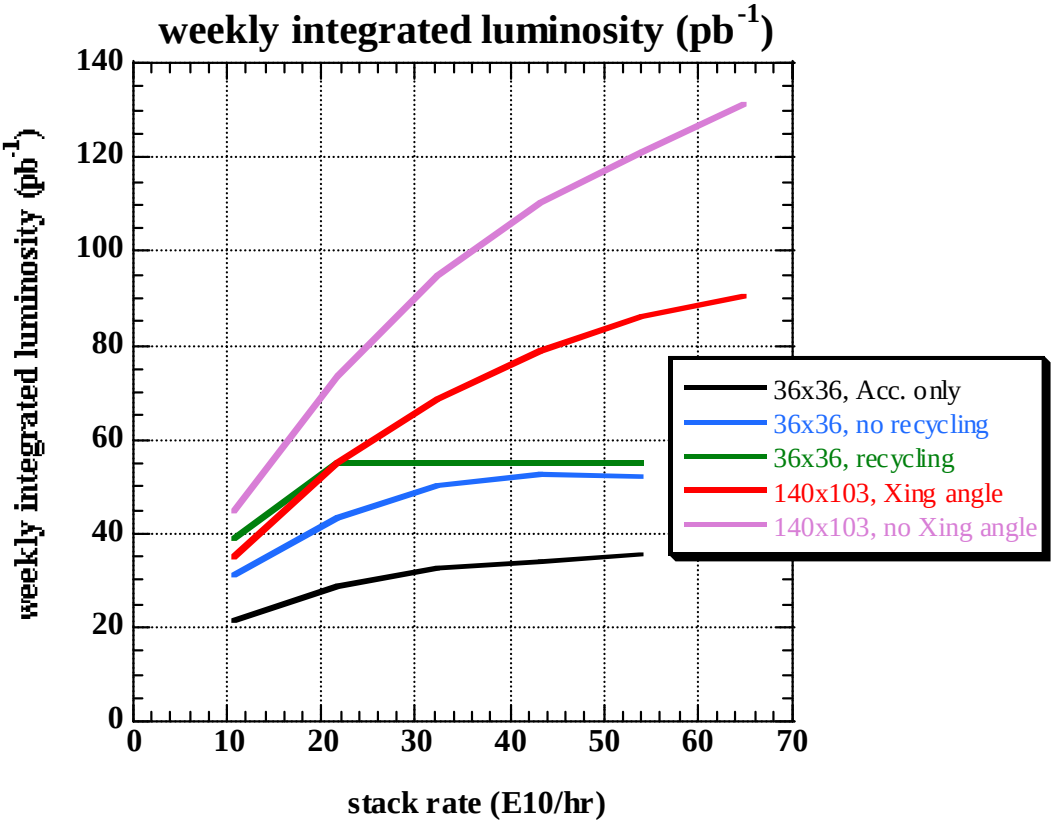

Figure 3.6.3 *Tevatron weekly integrated luminosity vs pbar stacking rate into the Accumulator. The following assumptions have gone into this plot:*

- *Accumulator maximum stack size is 250x 10^{10}, the stack rate is intensity dependent.*
- *No Recycler maximum stack size; stack rate is not intensity dependent.*
- *8% loss in Accumulator to Recycler transfers.*
- *Intensity dependent Recycler to Tevatron transfer efficiencies.*
- *Run II emittances and proton intensities; intrabeam scattering only for growth rates.*
- *Luminosity counted only within ±35cm from IR, matching to the silicon detector acceptances*
- *70 mb cross section for luminosity*
- *3ev-sec, 20π-mm-mrad pbars are recycled*
- *IR crossinging angle is ±136 μrad*
- *Luminosity levelled to ≤5 interactions/crossing (@48mb cross section)*
- *20% weekly downtime; 1 hour shot-setup time*

We conclude that the effect of the crossing angle on the integrated luminosity might be mitigated such that the loss is approximately 30%. While reduced, this is nevertheless substantial. If the Tevatron Lens could reduce this by permitting the use of a smaller crossing angle, the margin would be very welcome.

3.6.1.2 Compensation of Beam-Beam Effects with Electron Beams

We have seen above how the beam-beam interaction in the Tevatron collider sets limits on bunch intensity and luminosity. It has been proposed to compensate these effects with use of a counter-traveling low-energy high current electron beams.[43]

Two electron beam setups for compensation of the beam-beam effects in the Tevatron (TEL- Tevatron Electron Lens) are planned to be installed away from the interaction points at B0 and D0. They provide the electron beams which collide with the antiproton beam. The electron beam is created on an electron gun cathode, transported through the interaction region in a strong solenoidal magnetic field, and absorbed in the collector. Since the electron charge is opposite to the proton charge, the electromagnetic force on antiprotons, due to the proton beam, can be compensated by the electron beam. The proton beam has to be separated from the electron and antiproton beams in the device.

There are two implementations of the proposal:

1) an ‘‘electron lens” with modulated current to provide different linear defocusing forces for different antiproton bunches in order to equalize their betatron frequencies (further referred as *linear compensation*)
2) an ‘‘electron compressor”, that is a nonlinear DC electron lens which compensates (on average) the nonlinear focusing due to the proton beam – *nonlinear compensation*. The latter has a potential for *crossing angle elimination.*

Initial estimates of the maximum increase in the collider luminosity due to the BBC are based on a simplistic relation between the peak luminosity, the maximum tune area available for operation $\Delta\nu_{max}$, and the tune spreads, both bunch-to-bunch and intrabunch. That is to say, we can write $\boldsymbol{L/L_0} \approx \Delta\nu_{max}/(\Delta\nu_{BB}+\Delta\nu_{NL})$. In addition we take the maximum footprints permitted, without tune compensation, to be those indicated in Fig. Figure 3.6.1. Assuming that a fully working beam beam compensation scheme can eliminate the bunch to bunch (linear) variation and that the tune spread within each bunch can be reduced by a factor of 2, we can deduce that:

- the *linear* BBC may potentially lead to some 16%-30% increase in <u>peak</u> luminosity with 36x36 bunches in Run IIa and some 50% in Run IIb
- in addition to that, the *nonlinear* BBC has a potential of a 60-100% increase of peak luminosity in Run IIa and Run IIb,
- if the nonlinear BBC will make it possible to eliminate the *crossing angle* by compensating 2 or 4 additional collision points around each IP, that would allow a 2-fold increase in the peak luminosity in Run IIb.

The potential increase in the <u>integrated</u> luminosity is more modest:

- the *linear* BBC may potentially lead to some 8% increase in integrated luminosity in Run IIa with pbar stack rate 40e10/hr and some 12% with 20e10/hr (see Figure 3.6.3) and some 30% in Run IIb
- in addition to that, the *nonlinear* BBC has a potential of a 40% increase of peak luminosity in Run IIa and Run IIb,

- if the nonlinear BBC will make it possible to eliminate the *crossing angle* by compensating 2 or 4 additional collision points around each IP, that would allow to increase peak luminosity by 41% in Run IIb.

It is assumed that $\Delta\nu_{max}$ remains the same and that the required increase, up to a factor 2, in the proton beam intensity is possible. We do not have an idea yet how the BBC will affect the maximum allowable tune area for operation. But the higher proton beam intensity in the Tevatron is definitely of concern.

3.6.1.3 Concerns of Higher Proton Intensities in the Tevatron

With this increase in current in the Tevatron, one of the things, which we will have to do, is to maintain the longitudinal stability of the bunches. Even now, at the start of Run IIa, we have already observed bunch oscillations, which persist for a very long time. Although we have not observed that these oscillations grow in time, they do dilute our longitudinal emittance unnecessarily. Therefore, it is important that we solve this problem in Run IIa before proceeding with any upgrade plans with the Beam-Beam Compensation or /and for Run IIb.

Another concern is antiproton lifetime at injection. At present, the Tevatron is having greater difficulties due to reduced antiproton lifetime at 150 GeV. The proton intensity is currently only half of the design value. This may be due to the fact that we have very large antiproton emittances(especially longitudinal) at 150 GeV. In Run I, the 150 GeV antiproton lifetime was also a problem at high proton intensities.

3.6.2 Machine Physics

Since 2000, significant progress has been made in analytical studies and computer simulation of the beam-beam compensation in the Tevatron and in experimental studies of impact of the 1st Tevatron Electron Lens (TEL) on the 980 GeV proton beam.

3.6.2.1 Analytical studies and numerical tracking simulations of the Beam-Beam Compensation with electron beams in the Tevatron collider

Due to a number of reasons, a larger number of protons per bunch, a smaller proton emittance, a factor of seven larger number of the parasitic long-range interactions (see Table 3.6.1), the beam-beam driven resonances (the synchro-betatron ones in particular) can present, in the Tevatron Run IIa configuration, a greater risk of instability of antiprotons than previously.

Another complication associated with the parasitic interactions is the so-called PACMAN effect: dependence of the tuneshifts on the bunch position in a train as illustrated by Figure 3.6.4a which shows the distribution of antiprotons in the tune diagram with the standard Tevatron choice of bare lattice tunes, $\nu_{x0} = 20.585$, $\nu_{y0} = 20.575$. Each of the 12 bunches in a train is represented by 3000 particles, tunes were calculated analytically following Ref.[43].

	Run Ib	Run IIa	Run IIb
N_p /bunch, 10^{11}	2.32	2.7	2.7
ε_p (95% norm.), π·μm·rad	23	20	20
ξ /nominal IP	0.0074	0.01	0.01
N parasitic Ips	10	70	278
ξ, total	~ 0.015	~ 0.025	~ 0.025
ε_{pbar} (95% norm), π·μm·rad	13	15	15

Table 3.6.1

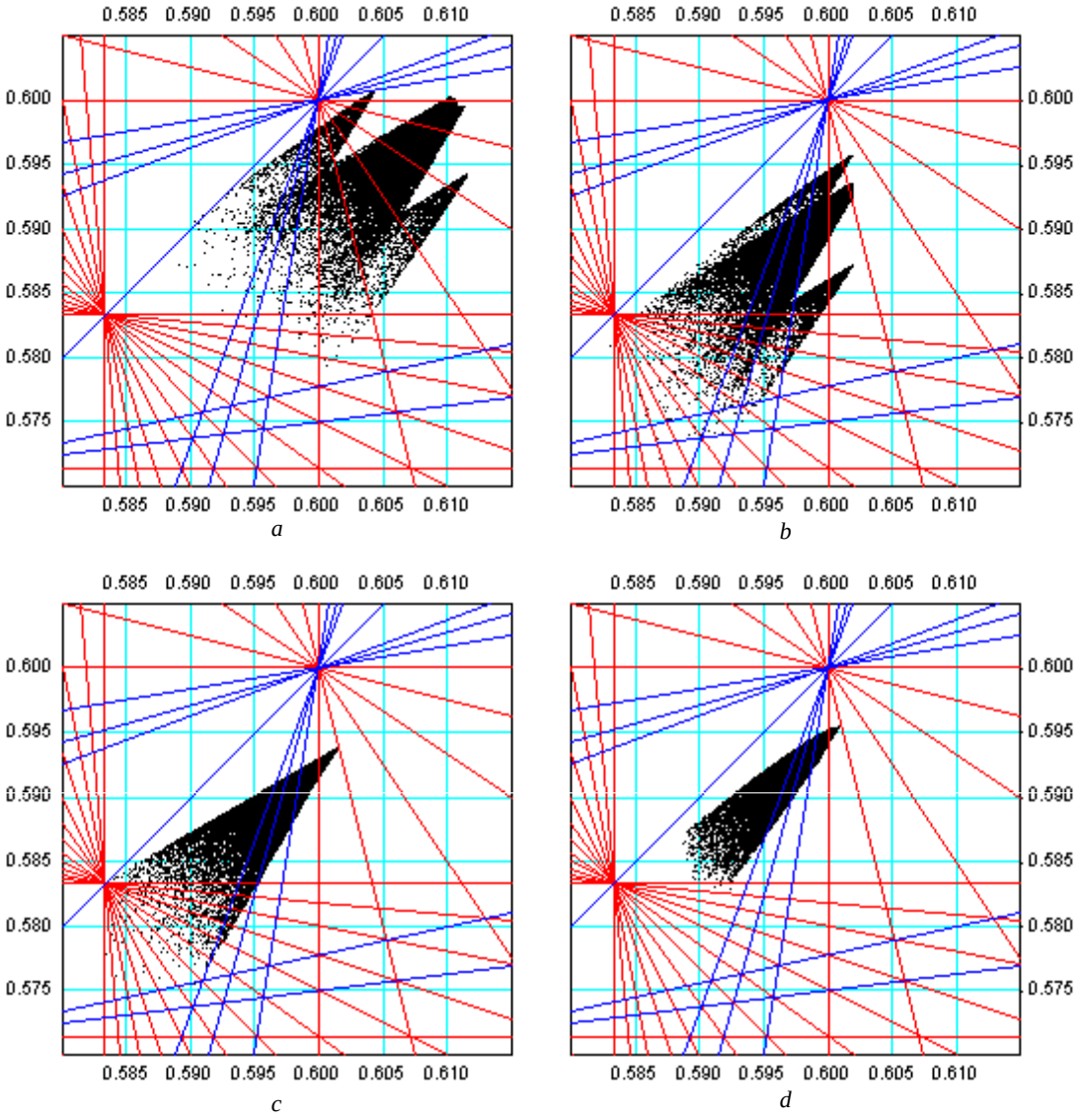

Figure 3.6.4 *a) Antiproton beam footprint in the betatron tunes plane with: a – no BBC, b – linear BBC with 1 Tevatron electron lens (TEL), c – linear BBC with 2 TELs, d – nonlinear BBC with 2 TELs*

As can be seen from Figure 3.6.4a it is impossible to accommodate all particles in the area free of the resonances of order lower than 13, which are shown as red and blue lines, for the sum and difference resonances respectively.

The beam-beam tuneshift can be compensated with the help of electron lenses [43]. Two linear lenses created by electron beams of constant charge density can completely eliminate the bunch-to-bunch tunespread (linear beam-beam compensation), by choosing a bell-like shape it is possible to reduce the intrabunch nonlinear tunespread as well (nonlinear compensation). However, the question remains as to whether this will really improve the stability of antiprotons, since the electron beams themselves may contribute to excitation of high order resonances remaining within the residual tunespread.

3.6.2.1.1 Linear Beam-Beam Compensation

Round electron beam of *constant* charge density acts as a *linear lens* on the antiprotons with amplitudes smaller than its radius a_e producing negative tuneshift in both transverse planes in proportion to the corresponding betatron function:

$$\Delta\nu_{x,y} = -\frac{1+\beta_e}{\beta_e}\cdot\frac{I_e\ L_e\ r_p}{2\pi\gamma_{\bar{p}}\ e\ c\ a_e^2}\beta_{x,y} \qquad (3.6.5)$$

,where I_e, L_e, a_e and $\beta_e = v_e/c$ are respectively the electron beam current, length, radius and relativisitic velocity.

Current modulation in the electron lens (TEL1) placed at a location where $\beta_x >> \beta_y$ allows us to equalize the horizontal tuneshift in all bunches without affecting vertical tunespread. Circles with violet fill in Figure 3.6.5 show what electron current should be applied to each of 12 antiproton bunches under Run IIa conditions in order to equalize the horizontal tuneshifts for small amplitude particles in the case of electron beam with a_e = 1.8 mm, β_e = 0.2, L_e = 2 m at location where β_x = 98.7 m, β_y = 28.4 m. The resultant tune distribution is shown in Figure 3.6.4b.

Adding the second electron lens (TEL2) at a location where $\beta_x << \beta_y$ permits us to equalize both horizontal and vertical tuneshifts. The electron currents which are needed in this case are shown in Figure 3.6.5 by circles with blue and red fill. The radius of the second beam is a_e = 2.35 mm, at its location β_x = 56.7 m, β_y = 172 m. The resultant tunespread is shown in Figure 3.6.4c.

Though the electron beam radii were chosen sufficiently large (more than $3\sigma_{p\text{bar}}$) the stability of particles in the tails of the beams, which see the sharp edges of the electron beams, is not guaranteed. The effect of the electron beam size and profile was a subject of extensive numerical simulations with the LIFETRAC code[44]. One example of simulation results is presented in Figure 3.6.6, where the contour plots of p-bar distributions in A_x, A_y plane are shown. The distance between successive contour lines is $\sqrt{e}$. Each step corresponds to 300,000 turns (6 seconds of real time in the Tevatron), 3000 particles were tracked. The data gathered are averaged over all the particles, all the turns, approximately one billion particle-turns for each step. The last column presents the effect of the TEL, which is applied at ‘‘bad” working point (0.566,0.556) and shifts tunes by 0.01 toward a ‘‘good” one. One can see the positive effect of the application of the lens in the differences between the pbar distributions at the corresponding working points

without e-lens, in columns marked as “bad” and “good”, and those with the lens operational, marked as “bad” +TEL. Several electron current density profiles considered including Gaussian and those described by the formula:

$$\rho(r) = \rho_0 \frac{1+\alpha(r/R_0)^2}{1+(r/R_0)^n} \qquad (3.6.6)$$

with ρ_0 adjusted so as to keep $\Delta\nu_{x,y}$ = - 0.01 at different values of parameters α and n. The bare lattice tunes, after some scanning, were chosen to be ν_{x0} = 20.566, ν_{y0} = 20.556. Tracking with noise showed high sensitivity to and complicated dependence on the electron beam profile. A number of other issues were addressed in the simulations with one TEL: effect of the e-beam misalignment (meanders and offsets) and noise as well as the transient effect while aligning the e-beam with the orbit of antiprotons.

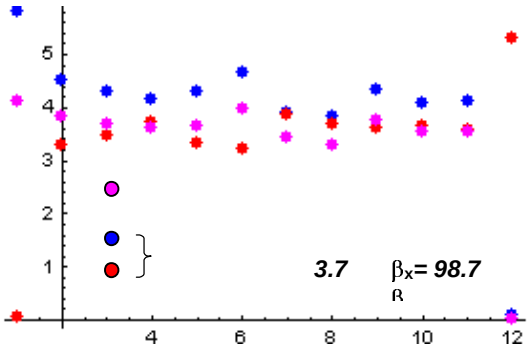

Figure 3.6.5 *Electron beam currents needed for equalization of the horizontal tuneshift with one TEL (violet) and both horizontal and vertical tuneshifts with two TELs (blue and red).*

The results can be briefly summarized as follows:

a) electron beam size has to be al least about 3 times the rms antiproton beam size $R_0 \approx 3\sigma_{pbar}$ for good beam lifetime and small emittance growth

b) Stationary offsets of up to 0.2 R_0 are tolerable

c) meandering of the electron beam around the $\bar{p}$ orbit with amplitude of 0.25 R_0 produces no harmful effect; this opens a possibility to vary the e-beam effective aspect ratio by deliberately bending the beam with correctors

d) the process of the electron beam alignment, if started from large initial offsets ($\geq R_0$), destroys the antiproton beam, therefore it has to be done in a few steps, each time with a new $\bar{p}$ bunch and/or using initially lower electron beam current

e) the $\bar{p}$-beam emittance dilution due to random turn-by-turn fluctuations in the e-beam position and current is found to be in a good agreement with the previous analytical estimates[43], for example, the relative current fluctuation of $dJ/J=2.2\cdot10^{-3}$ results in 10 hrs emittance growth time due to the noise.

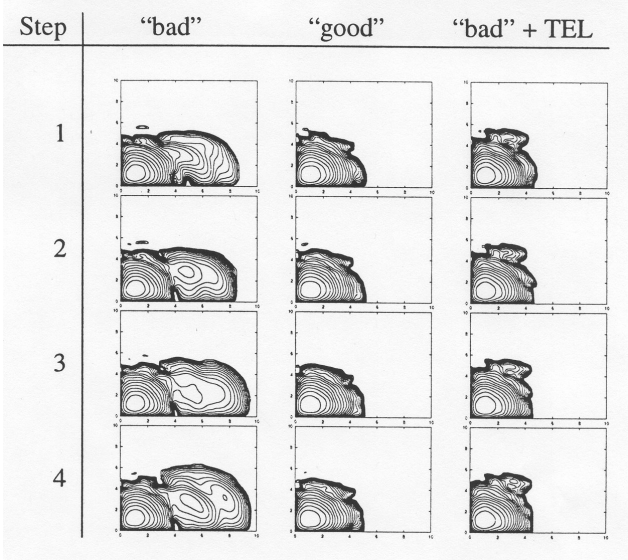

Figure 3.6.6 *Distribution of the pbar-beam in the plane of normalized betatron amplitudes after (1,2,3,4) x 300,000 turns.*

3.6.2.1.2 Compensation of Nonlinear Beam-Beam Effects

Compensation of non-linear beam-beam effects requires shaping the electron beam profile by application of negative voltage to a near-cathode Pierce-like electrode (a "profiler") or by changing geometry of anode and cathode. The beam produced will have a smaller r.m.s. size and smoother edges as shown in Figure 3.6.7, lines 2,3 and 4. As a result:, the intrabunch nonlinear tunespread is partly compensated and it is less difficult to accommodate the total footprint in a resonance free area. Compared to the linear BBC (see corresponding profile in Figure 3.6.7, line 1), there is weaker excitation of high order resonances for antiprotons with large betatron amplitudes, which see the electron beam edges. The electron beam current required for the smaller beam radius is smaller and electrostatic space charge effects in the electron beam are therefore weaker.

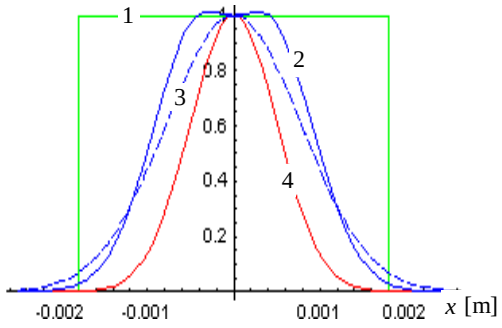

Figure 3.6.7 *Space Charge distribution: 1- linear TEL, 2- TEL with "profiler" 3- Gaussian distribution with the same current, 4- antiproton beam at TEL 1*

With the electron and antiproton beam sizes becoming comparable, there appears a strong amplitude dependence of the tuneshifts produced by a Tevatron electron lens (TEL) as shown in Figure 3.6.8. It counteracts the tuneshift of particles with significant amplitudes resulting from the head-on collisions with the proton beam thus leading to a compression of the total tunespread within a single antiproton bunch (*the nonlinear beam-beam compensation*).

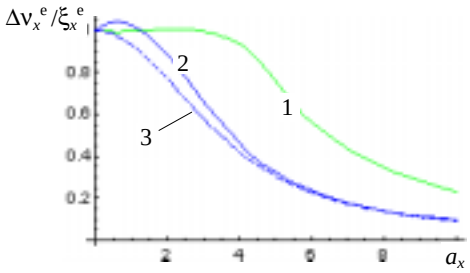

Figure 3.6.8 *Pbar normalized horizontal tuneshift due to TEL with e-beam profiles as shown in* Figure 3.6.7.

Obviously, to fully benefit from such compensation, one should eliminate the bunch-to-bunch tunespread first, so two electron lenses would be necessary: TEL1 at location with larger horizontal β-function (β_x = 98.7m, β_y = 28.4m) and TEL2 at location with larger vertical β-function (β_x = 56.7m, β_y = 172m). To begin with we have chosen the electron beam sizes (HWHM) to be r_e = 1mm in TEL1 and r_e = 1.3mm in TEL2. The electron currents, which provide a complete compensation of the bunch-to-bunch tunespread and compress the intra-bunch nonlinear tunespread by a factor of two are shown in Figure 3.6.8. Due to smaller e-beam sizes they are twice lower than needed for the linear BBC.

The effect of TELs on the nonlinear tunespread is illustrated by Figure 3.6.10, which shows the antiproton bunch #6 footprint in the tune diagram without BBC (black) and with it (teal blue). The bare lattice tunes (assumed nominally to be ν_x = 20.585, ν_y = 20.575) were slightly trimmed in the latter case. The arc lines correspond to equidistant with step 2 values of the total transverse amplitude

$$a_\perp = \sqrt{a_x^2 + a_y^2} \qquad (3.6.7)$$

where $a_{x,y}$ are taken in the pbar σ's, the radial lines correspond to constant values of a_x/a_y. The red and blue lines show respectively sum and difference resonances of orders lower than 13.

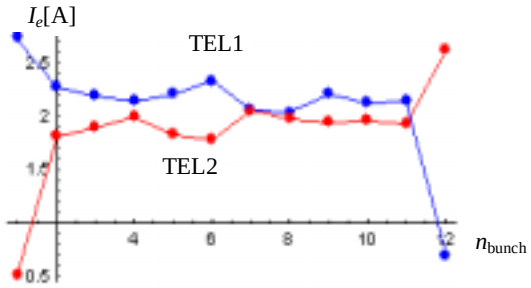

Figure 3.6.9 *Electron currents in the two TELs as seen by different antiprotons*

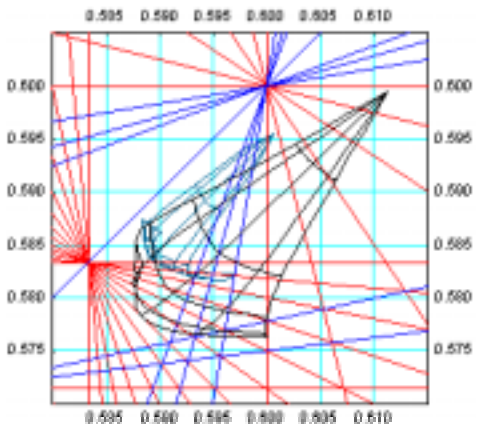

Figure 3.6.10 *Original and compressed pbar bunch #6 footprint around nominal working point.*

It can be seen that the footprint "folding", which is caused by the long-range interactions with the proton beam and without BBC happens at amplitudes ~8σ, with BBC takes place at amplitudes as low as 5σ. Since even very weak high order resonances may lead to a fast particle transport over the region of folding thus reducing the pbars lifetime, this effect sets a natural limit on the degree of the footprint compression. Another limitation comes from the requirement that the tune modulation by the synchrotron motion due to finite dispersion at the TEL locations was small: $r_e >> D_x \sigma_E \approx 1.7\text{m} \times 9 \cdot 10^{-5} \approx 0.15\text{mm}$, to avoid strong excitation of the synchrotron satellites of betatron resonances.

The electron beams of TELs can themselves contribute to excitation of resonances. Figure 3.6.11 shows beatings of the betatron amplitudes (calculated analytically in a single resonance approximation) due to resonances encountered by antiprotons of bunch #6 whose footprint with BBC was shown in Figure 3.6.10 in teal blue.

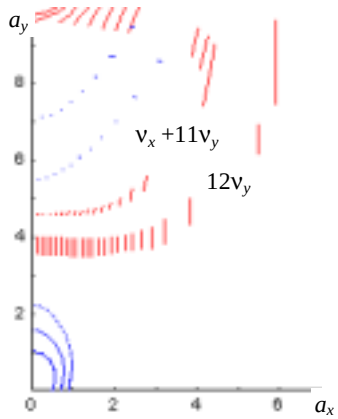

Figure 3.6.11 *Swing of the betatron amplitudes due to resonances encountered by pbars of bunch #6 at the nominal working point with BBC.*

Due to the TEL contribution the width of the $12\nu_y$ resonance is much larger than that of the $\nu_x+11\nu_y$ resonance which, in the absence of misalignments, is excited exclusively by the long-range interactions. For off-momentum particles the effective resonance width is even larger owing to the synchrotron satellites.

Choice of the working point

The footprint, when compressed by the TELs, can fit into other areas in the tune diagram which are surrounded by less dangerous resonances. One such possibility, with the tunes around ν_x=20.563, ν_y=20.557, was considered for the linear BBC. However, this area is not wide enough to avoid setting some particles on either 7^{th} or 9^{th} order resonances. Another option is the SPS working point ν_x = 20.689, ν_y = 20.682.

Effect of the electron beam profile

Excitation of the 16^{th} order resonances (and its satellites) by TELs can facilitate diffusion of antiprotons, especially in the region of amplitudes where the footprint folding occurs. As the example of $10\nu_x+6\nu_y$ resonance shows, excitation of high order resonances by TELs can be reduced by making the e-beam charge distribution more monotonous (e.g. Gaussian). One more advantage is that the footprint folding occurs at somewhat larger amplitudes with the Gaussian e-beams. Analytical calculation of the beatings of the betatron amplitudes at the SPS working point in the case of Gaussian e-beams predicts only moderate effect of the difference resonance $3\nu_x- 6\nu_y$ on the tail particles.

Effect of the number of TELs

There is an additional argument (besides compensation of the PACMAN effect) in favor of using two TELs at points with $\beta_x >> \beta_y$ and $\beta_x << \beta_y$ rather than one TEL at a location with equal β's. From the resonances excited by TELs the high-order sum resonances are the most dangerous (the WP can always be chosen so that the uni-dimensional ones were reached at too small amplitudes to be noticeable or not reached at all). Since the driving term of the $k\nu_x+l\nu_y = n$ resonance contains the factor $\beta_x^{k/2}\beta_y^{l/2}$, its excitation is significantly suppressed in the case of two TELs. In all cases TELs provided the same horizontal tuneshift $\Delta\nu_x$ = -0.014.

Effect of the finite dispersion

Owing to the finite dispersion TELs can contribute to excitation of the synchro-betatron resonances (SBRs) in two ways: via the tune modulation arising from the steep fall-off of the instantaneous tuneshift with the displacement $D_x\delta_p$, and via variation of the nonlinear component of the TEL field seen by an antiproton in the course of the synchrotron motion. According to the estimates the second effect should not be important, whereas the first one, the TEL second order chromaticity, is big: TEL tuneshift is modulated by more than 20% at a_s = 3. Both effects can be reduced, if necessary, by increasing the e-beam radius.

Numerical simulations

All the above presented results were obtained in the single resonance approximation using analytical formulae[45]. More realistic picture can be obtained by tracking simulations with the code LIFETRAC which can take into account the cooperative action all beam-beam and TEL nonlinearities and the external noise.

Figure 3.6.12 shows the evolution of the density of bunch #6 at the SPS working point with the BBC by two Gaussian TELs which provide zero-amplitude tuneshifts of $\Delta\nu_x^e \approx -0.0144$, $\Delta\nu_y^e \approx -0.0115$. With the bare lattice tunes 20.689, 20.682 the 13^{th} order resonances proved to be strong enough to affect the core particles (left column). With tunes shifted down by 0.005 (center column) the core was not affected, still some tails had developed which were not seen in the test run with linear lenses instead of TELs. Weakening the TELs nonlinearity by a 15% increase in the e-beam sizes diminishes the tails (right column). In none of these cases had luminosity or lifetime suffered.

Conclusions

- With the help of two electron lenses it is possible to completely compensate the bunch-to-bunch tunespread (PACMAN effect) and partially reduce the intrabunch nonlinear tunespread.
- The degree of nonlinear BBC is limited by the footprint "folding" due to the long-range contribution and the electron lens chromaticity due to finite dispersion.
- The possibility to eliminate the folding of the footprint by additional compensation of the long-range interactions (e.g. with pulsed wires) should be studied.
- Excitation of high order resonances by TELs can be reduced by choosing a smooth electron beam charge distribution (e.g. Gaussian) and using two TELs at points with strongly unbalanced β-functions.
- Compression of the footprint by a factor of two permits it to fit in areas free of resonances of order less than 13; the neighborhood of the SPS working point is a promising candidate.

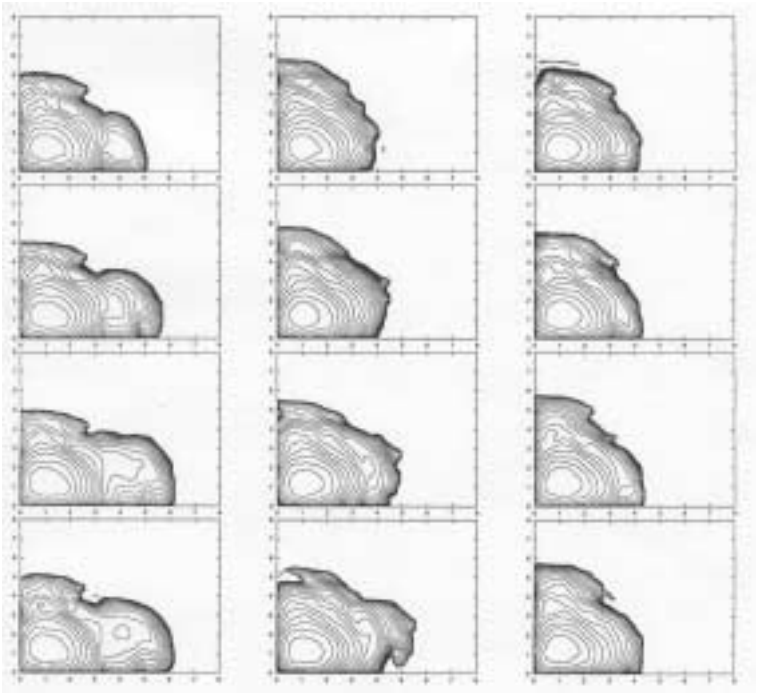

Figure 3.6.12 *Evolution of the pbar density under impact of TELs.*

3.6.2.2 Tevatron Electron Lens Studies with 980 GeV protons

In 2001 the first Tevatron electron lens (TEL) has been installed in the Tevatron, commissioned, and demonstrated the theoretically predicted shift of betatron frequencies of a high energy proton beam due to a high current low energy electron beam. After the first series of studies in March-October 2001, we achieved tuneshifts of 980 GeV protons of about dQ=+0.007 with some 3 A of the electron beam current while the proton lifetime was in the range of 10 hours (some 24 hours at the best). Future work will include diagnostics improvement, beam studies with antiprotons, and fabrication of the 2nd TEL.

3.6.2.2.1 Description of the TEL-1

Figure 3.6.13 depicts a general layout of the TEL. The magnetic system of the TEL (see details below in Section 3.6III.A) consists of a 65 kG SC main solenoid, four 8 kG and two 2 kG SC dipole correctors in the same cryostat, and 4 kG gun and collector solenoids. The TEL cryostat is part of the Tevatron magnet string cooling system. A strong Π-shaped magnetic field is needed to guide 10 kV electron beam from an electron gun thru an interaction region, where electrons collide with high energy (anti)protons, to a water cooled collector. SC dipole correctors allow precise steering in position and angle of the electron beam onto the Tevatron beams. A number of precautions have been taken during SC magnets fabrication in order to achieve very high linearity of magnetic field lines inside the main solenoid. The reason is that as the electron beam goes along magnetic field lines it should not deviate around the straight Tevatron beam trajectory, otherwise the effectiveness of the TEL would be deteriorated.

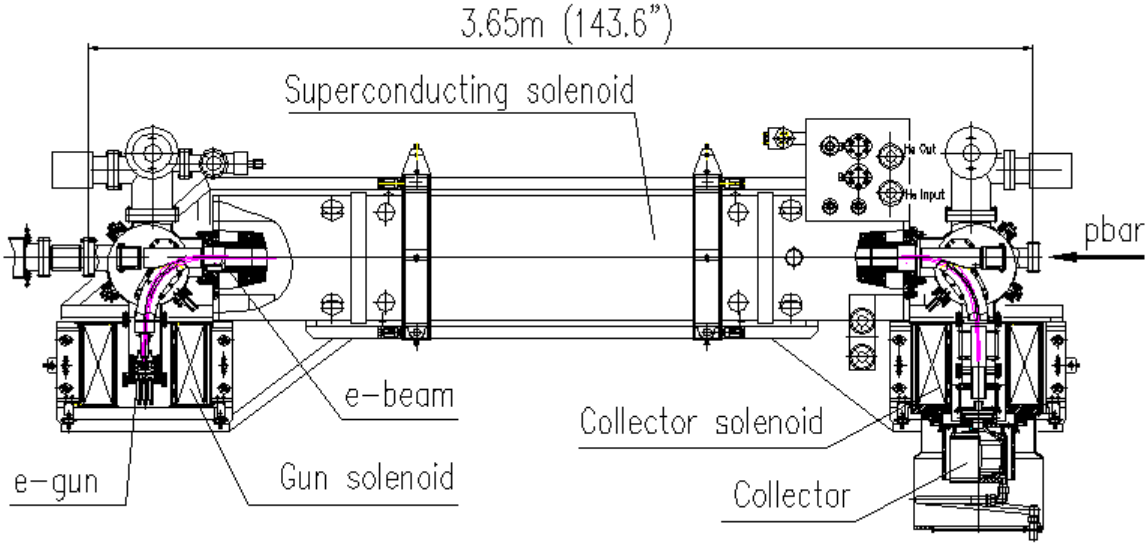

Figure 3.6.13 *General layout of the Tevatron Electron Lens.*

Measured rms deviations of the lines are 15 μm in the vertical plane and 50 μm in the horizontal plane (which is the plane of the bends). This is 10% of the Tevatron beam size in the location of the electron lens. It was found experimentally that the electron beam can be steered to pass through the main solenoid if the gun solenoid field is in the range of B_{Gun}=*1.9-4.2* kG for B_m=*35*kG (outside the range, the beam touches parts of the vacuum system).

The electron gun employs a 10 mm diameter convex thermo-cathode and can provide up to 6A of pulsed current and 3A DC of up to 15kV electrons. Perveance of the gun is 5.6 $\mu A/V^{3/2}$. Electron current profile is close to rectangular, but can be changed to a more smooth one if a negative potential (w.r.t. the cathode) is applied to a special near-cathode electrode. Water cooled collector is characterized by high-perveance of about 10 $\mu A/V^{3/2}$, high absorbing efficiency exceeding 99.5%, and dissipation up to 50 kW of electron beam power. For details of the gun and collector see Section 3.6.III.B.

In order to vary the electron current on the bunch-to-bunch basis (spacing 396ns in the Tevatron at present Run IIa), high-voltage pulses are applied to the gun anode. During the first studies an 8 kV, 800 ns FWHM modulator based on RF tube has been used to provide electron pulses synchronized with a single Tevatron bunch at the repetition frequency of 47.7 kHz. Since May 2001, we replaced the RF tube modulator by a 48kHz solid state pulser based on FID-switches with 20kV maximum amplitude in 60 ns long pulse.

The TEL is equipped with 4 BPMs: one vertical and one horizontal at the beginning and at each end of the main solenoid. The BPMs are supposed to measure transverse positions of electron, proton and antiproton beams passing through and thus, allow the electron beam to be centered on the antiproton or the proton one. 100 μm diameter tungsten wires, vertical and horizontal, can be introduced into the very middle of the interaction region for electron current profile measurements. They are remotely controlled and removed when high energy beams circulate in the machine. Electron currents leaving the cathode, into the collector and onto the collector entrance electrode are measured by 3 inductive coils. There are 10 HV electrodes around the electron beam trajectory which can be used for ion or secondary electron cleaning (though most of the time there are grounded).

The TEL vacuum under working conditions with 3 ion pumps with a total pumping speed of 300 l/s ranges from 4 to 10 e-8 Torr. Table 3.6.2 summarizes main parameters of the TEL.

electron beam energy,	U_e, kV	6-12
maximum peak electron current	J_e, A	2-3.5
magnetic field in main solenoid	B_m, kG	35
in gun solenoid	B_g, kG	3.7
e-beam radius in main solenoid	a_e, mm	1.75
cathode radius	a_c, mm	5
e-pulse width, FWHM	τ_e, mm	~800
current stability, peak-to-peak	$\Delta J_e/J_e$,%	< 0.1
effective interaction length	L_e, m	2.0
valve-to-valve length	L_{tot}, m	3.65

Table 3.6.2 *TEL operational parameters*

We observed very minimal effects of the magnetic fields of the lens on the 980 GeV proton beam. Tunes are shifted by less than 0.001 in both planes, the tune split Q_x–Q_y varies from 0.0072 to 0.0077, no coupling correctors are needed to operate the Tevatron, and the orbit distortion around the ring stays within about 1 mm. Measurements with the proton beam have shown that numerous electrodes of the TEL (BPMs, HV

electrodes) and discontinuities of the beam pipe all together generate a broadband impedance $|Z/n|< 0.1$ Ohm, that is a very small contribution to the total Tevatron impedance estimated to be some 2-8 Ohm.

In March-October 2001 there was a total of twelve 8-hour beam shifts dedicated to studies with the Tevatron Electron Lens. Most experimental results were obtained with a single coalesced proton bunch in the ring at the energy of 980 GeV. In the text below, 980 GeV should be assumed unless otherwise stated. The total proton bunch length was less then 19 ns; the bunch intensity varied from 6 to 60 $\times 10^9$. The only shift at 150 GeV on March 23 was the very first one and to our great satisfaction a decent betatron frequency shift was observed, breaking the path for application of electron lenses in high-energy accelerators.

3.6.2.2.2 Proton Tune Shift due to TEL

According to [43], a perfectly steered round electron beam with a constant current density distribution will shift the betatron tune by:

$$dQ_{x,y} = \mp \frac{\beta_{x,y}}{2\pi} \cdot \frac{1 \pm \beta_e}{\beta_e} \cdot \frac{J_e L_e r_p}{e \cdot c \cdot a_e^2 \cdot \gamma_p} \qquad (3.6.8)$$

where the sign reflects defocusing for antiprotons and focusing for protons, $\beta_e = v_e/c$ is the electron beam velocity, β_x=101 m and β_Y=28 m are the β functions at the location of the lens (the first TEL is installed in the Tevatron sector F48). a_e , J_e and L_e stand for the electron beam size, current and effective interaction length, r_p is the classical proton radius, and γ_p=1044 is the relativistic Lorentz factor for 980 GeV protons. The electron beam is assumed to be much wider than the (anti)proton beam, so that all the high-energy particles acquire the same dQ. The factor $1 \pm \beta_e$ reflects the fact that the contribution of the magnetic force is β_e times the electric force contribution and depends on the direction of the electron velocity. So far we operated with protons only (while the actual goal is to operate with antipron bunches) which move in the same direction as the TEL electrons, so the magnetic force reduces the total tuneshift.

Figure 3.6.14 shows an example of the Schottky spectra of horizontal proton beam oscillations without electron current and with 3 A electron current. One can see that the horizontal tune is shifted positively by about $dQ_x = +0.0065$ from 20.5824 to 20.5889. One should expect that the same electron beam would shift the horizontal tune of antiprotons $(1+\beta_e)/(1-\beta_e) = 1.5$ times this amount, i.e., by -0.01 given that $\beta_e \approx 0.2$. Besides a central peak corresponding to the betatron frequency (highlighted by marker line), the spectra consist of several synchro-betatron sidebands, separated by the synchrotron tune $Q_s \approx 0.0007$. The total power in the peaks depends on proton intensity and noise level exciting the beam motion. The application of the electron beam may or may not cause the spectrum shape variation seen in Figure 3.6.2. The shape also depends on the machine tuning, working point. The shape variations sometimes make precise tuneshift measurements rather difficult, and we estimate typical error to be $\delta Q \approx \pm 0.0001$.

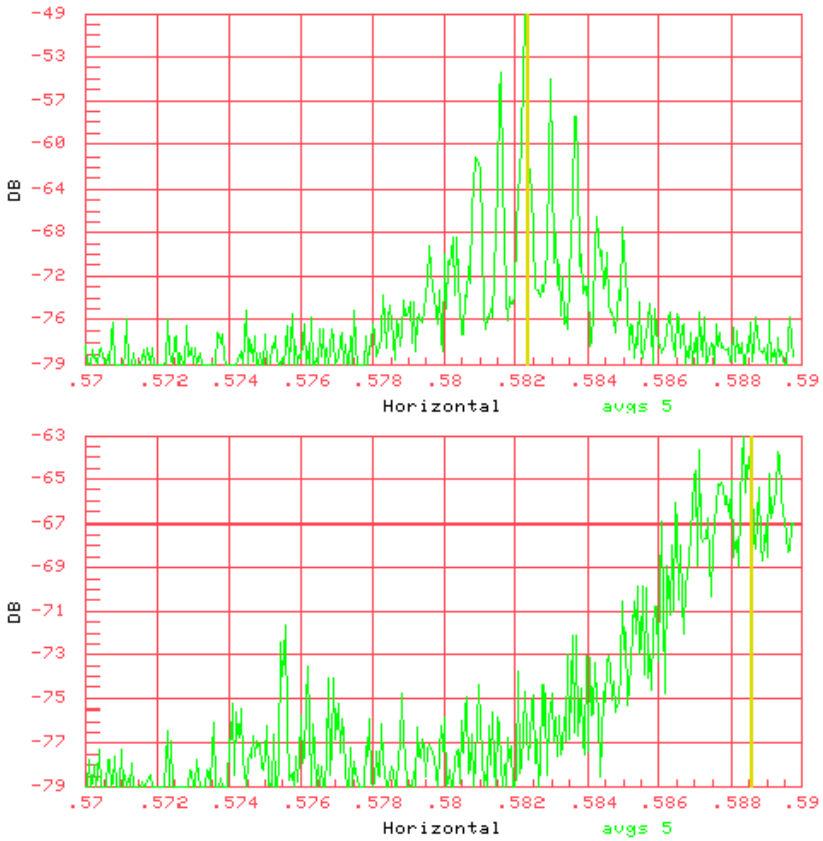

Figure 3.6.14 *Schottky spectra of horizontal motion of protons without electron current (top) and with 3A of electron current (bottom), cathode potential* $U_{c.}$ *=7.6 kV .*

Figure 3.6.15 shows how the proton tune shifts depend on the time delay between the electron pulse and the arrival of the proton bunch. One can see that a) the tune shift follows the electron pulse shape and, therefore, it's possible to shift the tune for any bunch without touching neighbors 396 ns distant, and b) the horizontal tune shift is some 4 times the vertical one. dQ_x/dQ_y = 0.0037/0.0008 = 4.6, close to the β function ratio β_x/β_y=101/28=3.6. The remaining difference can be explained by either uncertainty in β functions, which is known to be ±10% , a small ellipticity of the electron beam, or mis-steering of the electron beam, which might play role if compared with a_e.

Having the electron beam properly synchronized for maximum effect, we have studied dependence of dQ_x on the peak electron current. The results are presented in Figure 3.6.16 and compared with Eq. (3.6.8). The theoretical dependence is non-linear because the electron energy inside the vacuum pipe and, thus, β_e, goes down with the current due to electron space charge, $U_{e.}=U_{c.}-gQ_{sc}$, where g is the geometry dependent factor. As seen in Figure 3.6.4, the maximum discrepancy is about 20% at $J_{e.}$=2 A. There are systematic errors in a number of parameters used for calculations, e.g., a_e^2 is known within ±10%, effective length L_e depends on precision of the steering and may vary within ±10%, and the electron current calibration each contribute some ±5% error. In addition there might be some ±5% uncertainty in the electron velocity β_e due to formation of an ion cloud, which shields some fraction of the electron space-charge Q_{sc}. An indication is that the maximum electron current allowed to propagate through the beam

pipe at a given cathode potential of 7.5 kV goes down by 25% if the pulse repetition rate is reduced from 47.7kHz (standard regime of operation with a single proton bunch) to about 50 Hz. On the other hand, ions do not change *charge density* and thus do not contribute to *dQ* directly most probably because of larger transverse size of the cloud.

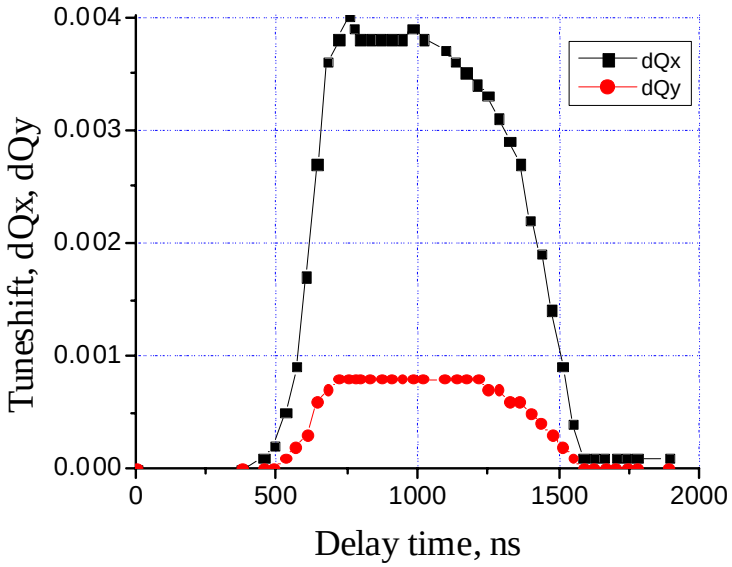

Figure 3.6.15 Shift of the horizontal (black) and vertical proton tunes vs delay between the proton bunch and 800 ns long, 1.96 A peak electron pulse, U_c =6.0 kV.

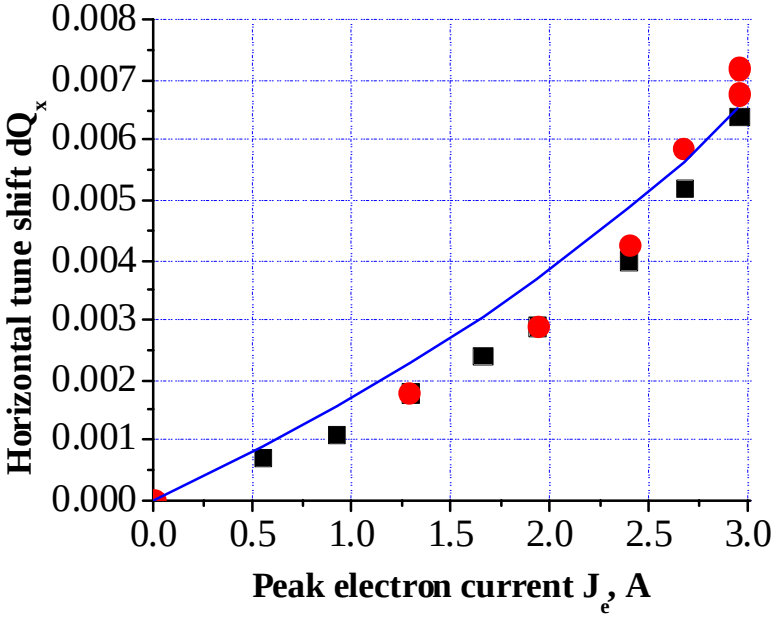

Figure 3.6.16 *Shift of the horizontal proton tune vs the electron current, U_c =7.5 kV. Circles and squares – experimental data, solid line – Eq. (3.6.8)*

It might be of interest to mention, that horizontal tune shift for protons coming just after the electron pulse (delay times from 0 to 400 ns in Figure 3.6.15) is slightly lower than dQ_x for protons arriving right before the electron beam enters the interaction region (delay times above 1600 ns). The little difference of about –0.0001 can be associated with defocusing effect due to ions freshly attracted inside the electron beam.

As long as the proton beam travels inside a wider electron beam, the proton tune shift does not depend much on the electron beam position, e.g., for the case of a 1 A electron beam $dQ_x(d_x,d_y) \approx dQ_{max}=0.0021$ if $|d_{x,y}|<2$mm – see Figure 3.6.17. But when the distance between the centers of the two beams exceeds the electron beam radius then one should expect $dQ_x(d_x,d_y=0) \approx -dQ_{max}/(d_x/a_e,)^2$, $|d_x|>>a_e$, and $dQ_x(d_x,=0,d_y) \approx +dQ_{max}/(d_y/a_e,)^2$ $|d_y|>>a_e$ (note the sign). Theoretical predictions $dQ_x(d_x,d_y)$, see smooth curves in Figure 3.6.17, are in a good agreement with experimental data. The only visible discrepancy is an asymmetry in $dQ_x(d_x,d_y=0)$. At negative horizontal displacements, $d_{x,y}<-2.5$mm, the tuneshift does not change sign as it does at $d_{x,y}>+2.5$mm. The effect is, most probably, due to the asymmetric Π-shape of the electron beam trajectory (see Figure 3.6.13), which results in additional positive contribution to dQ_x from the bending portions of the beam if the protons propagate through them. To summarize, the experimentally observed tuneshifts reasonably well agree with theory.

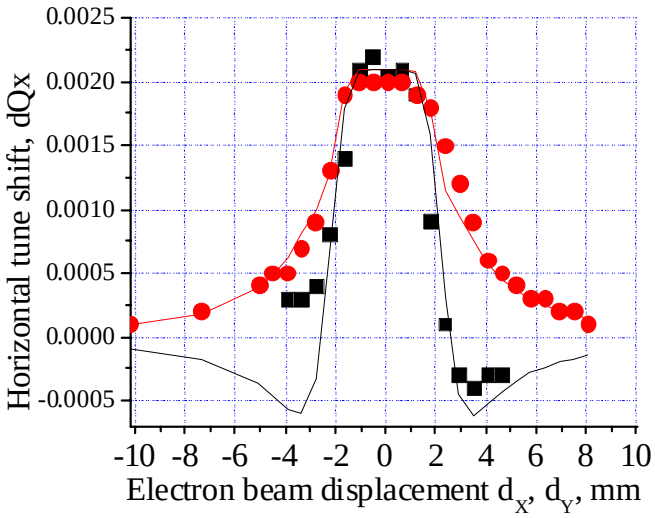

Figure 3.6.17 *Horizontal tune shift vs horizontal (squares) and vertical (circles) displacement of the electron beam, J_e =1A, U_c =6.0 kV.*

3.6.2.2.3 Proton Lifetime with TEL

There is no formula to estimate the (anti) proton beam lifetime $\tau=(dN/dt/N)^{-1}$ under impact of the TEL. Nevertheless, analytical studies and numerical tracking predict that the following phenomena affect the lifetime: 1) τ depends on non-linear resonances in the vicinity of the machine working point; 2) τ should decrease if the electron beam is mis-steered and the protons experience non-linear forces of the electron beam; but if the beam-beam separation is very large, then the electron beam should not affect the lifetime; 3) one should expect better lifetime for the same dQ if the electron beam is wider and its current density profile is a smooth, bell-like function.

We found that without collisions with the TEL beam, the Tevatron proton beam lifetime is very good over a broad range of the beam parameters and the machine working points (WP) Q_x , Q_y. Because of the limited time of the studies, we measured lifetimes based on 15 minutes records of the beam intensity. This resulted in some 50% error in $1/\tau$, when the typical lifetime was τ_0 =90 hours.

Collisions with the multi-Ampere electron beam always caused some deterioration of the τ , but the best lifetime was observed at good WPs. Figure 3.6.18 shows the set of resonances up to 12th order over the range $Q_{x,y}$=20.55-20.60 which is typical for the Tevatron collider operation. The arrows represent the tuneshift due to the TEL. The longest one reflects the result of the very first beam study shift, the very first attempt to operate the TEL with 150 GeV protons. All the others were obtained with 980 GeV protons on different shifts. The numbers near each arrow show the best lifetime achieved at that working point with the maximum electron current. Electron and proton currents and beam sizes were about the same for all these observations, although we can not guarantee that the electron beam was always steered with the same precision.

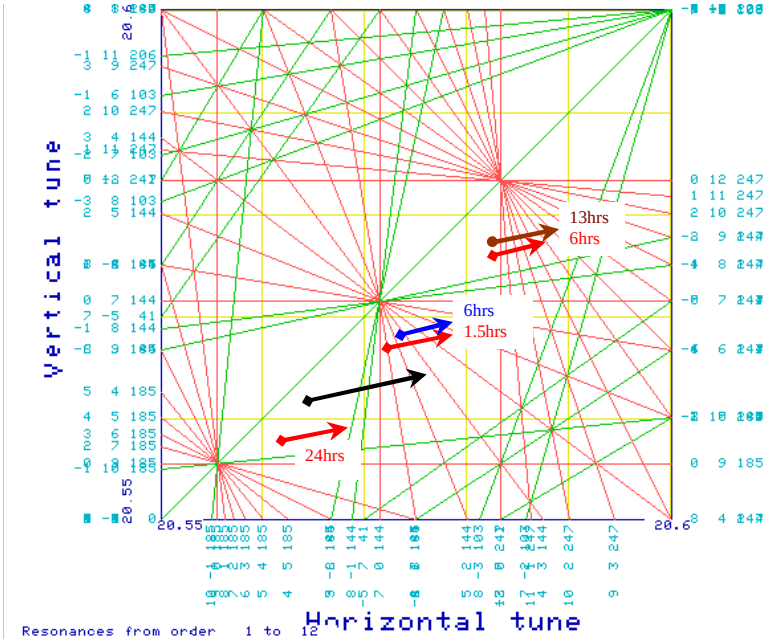

Figure 3.6.18 *Proton bunch tuneshifts due to the TEL and corresponding lifetimes.*

One can see, that the smallest lifetimes of 1.5-6 hrs were observed when the Tevatron operated at the 7th order resonances at Q_x,Q_y=0.573,0.567, better lifetimes of 6-13 hours at the 12th order resonances Q_x,Q_y=0.583,0.577, and the best lifetime of 24 hours was achieved away from resonances at Q_x,Q_y=0.564,0.555.

Our experience shows that mis-steering of the electron beam is by far the most important factor affecting the lifetime. It can affect τ even at comparatively small electron currents causing the lifetime deterioration when the proton beam crossed the electron beam edges. One may associate these phenomena with the excitation of non-linear resonances. At very large electron currents we also detected significant proton emittance blow-up, which sometime made it impossible to subsequently achieve a good lifetime.

Another factor deteriorating the lifetime is thought to be effective electron current fluctuations, which became quite large when the short pulse FID-pulser was used. For an electron pulse with about 30 ns rise and fall times and without a clean flat top, 1ns timing jitter leads to 2-3% variation of the effective electron current fluctuations at betatron frequencies; as shown above, the tolerance is under 0.1%. As a result, the best lifetime observed with the FID pulser was about 4 hours.

On the other hand, if electron and proton beams are separated by some 5 mm (about 3 times the electron beam radius a_e), than no deterioration of the proton beam intensity has been observed and the measured lifetime is about τ_0.

We did not have enough time to study the effect of the electron beam size and/or electron current density profile yet. The only indication that relative size matters is that when the proton emittance is 1.5-2 times larger than usual, e.g. 40-60π mmmrad (95%) instead of 25π mmmrad (corresponding to a rms horizontal beam size at the TEL location of 0.8-0.9 mm instead of typically 0.7 mm – compare with a_e =1.75mm), the lifetime becomes very poor.

3.6.2.2.4 Future Studies, Improvements

Topics for our further studies include: effects of the electron beam size and shape on the tuneshift and lifetime, emittance growth vs electron beam current and position stabilization, effects of ions, TEL operation with the Tevatron antiproton beam, and, finally, the TEL operation with many bunches. The ultimate goal of the studies is to achieve the same or better pbar lifetime with the TEL at dQ comparable with the Tevatron beam-beam tune shift and around typical working points.

We also look forward to having more reliable proton diagnostics for the emittance measurements (e.g., synchrotron light system instead of flying wires) and an automated tune measurement system for the multi-bunch measurements. R&D on the better electron beam for the TEL include a wider beam with smooth edges from new 10A, 30kV electron gun pulsed by solid-state HV FID-pulser, and a better stabilization of the beam current and position.

3.6.2.3 Instabilities due to Electron-Antiproton Beam-Beam Interaction

3.6.2.3.1 Electron Beam Distortions in Beam-Beam Compensation Set-Up

Collision with a round antiproton bunch in a strong magnetic field conserves axial symmetry and the radial size of the electron beam. Therefore, the electron beam space charge forces are the same for antiprotons at the head and at the tail of the antiproton bunch. This is no longer true if the electron or antiproton beam is not round. The electron beam axisymmetry can be assured by using a round cathode in the electron gun and by an appropriate choice of the magnetic field in the transport section of the set-up. The antiproton beam roundness could be achieved only in a number of Tevatron locations where vertical and horizontal β functions are the same $\beta_x = \beta_y$. The latter condition is not fulfilled for locations of TEL-1 and TEL2.

The electron beam cross section becomes a rotated ellipse as the tail of a non-round antiproton bunch passes it, whereas the head of the bunch sees the original undisturbed

round electron beam. Detailed numerical studies of the effect can be found in Ref.[46]. The electron beam distortions are of concern because:

1) the distortion of the space-charge forces which play a role in the beam-beam compensation;
2) in addition to the desired defocusing effect, electric fields of the elliptic electron beam produce x-y coupling of vertical and horizontal betatron oscillations in the antiproton beam;
3) there appears a ‘‘head-tail” interaction in the antiproton bunch via higher order wake fields propagating in the electron beam.

The electron beam density distortion due to that effect is calculated to be about [46]:

$$\frac{\Delta\rho}{\rho} \approx \frac{0.2 \cdot [N_{pbar}/6e10]}{a_e^2[mm] \cdot B[kG]} \qquad (3.6.9)$$

For example, the distortion is about 1.5% for a 1 mm radius electron beam in a B=40kG solenoid field. This value seems tolerable for operation of the electron lenses for the BBC.

3.6.2.3.2 Head-Tail Effect Due to Electron Beam

Electron space charge forces cause transverse ‘‘head-tail” coupling within the antiproton bunch which may lead to a transverse mode coupling instability (TMCI). A detailed theory, analytical studies and numerical simulations of the effect can be found in Ref.[47]. Here we present estimates of the threshold longitudinal magnetic field necessary to avoid the instability, and the dependence of the threshold on electron and antiproton beam parameters.

Low energy electrons can create significant transverse impedance comparable with the intrinsic impedance of the Tevatron ring, and this can result in a collective instability of the antiproton bunch. The electron beam is to be born on an electron gun cathode, transported through the interaction region, and absorbed in the collector. Therefore, each portion of electrons passes through the antiproton beam only once, and only short distance transverse wake fields are of interest. The phenomenon is as follow: if the centroid of the antiproton bunch head collides off the electron beam center, then the electron-antiproton repulsion causes electron motion. As the result, the electron beam has a displacement when it interacts with the tail of the bunch. Thus, the impact of the electron beam on the following antiprotons depends on the transverse coordinate of the preceding antiprotons. Such a ‘‘head-tail” interaction leads to the TMCI.

This effect is similar to the "strong head-tail" interaction via vacuum chamber impedance first observed a long time ago in electron storage rings. The TMCI in the electron rings limits the maximum single bunch current. In our case, the source of the coupling is the electron space charge which is the basic mechanism for the beam-beam compensation and, thus, can not be avoided. The way to counteract the instability is to increase the electron beam rigidity, to make its motion during the collision smaller. Naturally it can be done using a strong longitudinal magnetic field in the interaction region. It is assumed that the Tevatron ring chromaticity can be made close to zero, so that the ‘‘weak head-tail” instability is negligible.

A peculiarity of the TMCI due to TEL is that the wake field has a skew force, for example, an originally horizontal displacement results in both horizontal and vertical displacements. Both direct and skew wakes are taken into account in this numerical simulation. The simulation reveals that, although the antiproton bunch motion is essentially two-dimensional (since the wake is 2D), the instability starts in that plane where the original lattice tune is closer to half integer, e.g. in the horizontal plane for the Tevatron ring. Multi-mode analysis, analytical consideration in two-particle model and numerical simulations of the TMCI due to electron beam in the Tevatron have all derived the threshold value of the magnetic field in the e-p interaction region:

$$B^{thr} \approx 17.5[kG]\frac{[N_{pbar}/6e10]\cdot(\Delta\nu_e/0.01)}{(\sigma_{pbar}/0.7mm)^2\cdot\sqrt{\frac{\nu_s}{0.001}\cdot\frac{|\nu_x-\nu_y|}{0.01}}} \qquad (3.6.10)$$

Therefore, for nominal pbar beam parameters, the magnetic field in the interaction region should exceed 17.5 kG if the electron beam radius *a* is equal to pbar size of σ=0.7 mm. That is the case of nonlinear BBC. For the linear BBC, the electron beam size is 2-3 times larger, the wake force is weaker for the same current density, and the magnetic field needed to control the TMCI is *(a/σ)^2* times lower. The operational field in the main solenoid of the TEL is about 35 kG, therefore we expect to see no problems due to tranverse electron beam impedance.

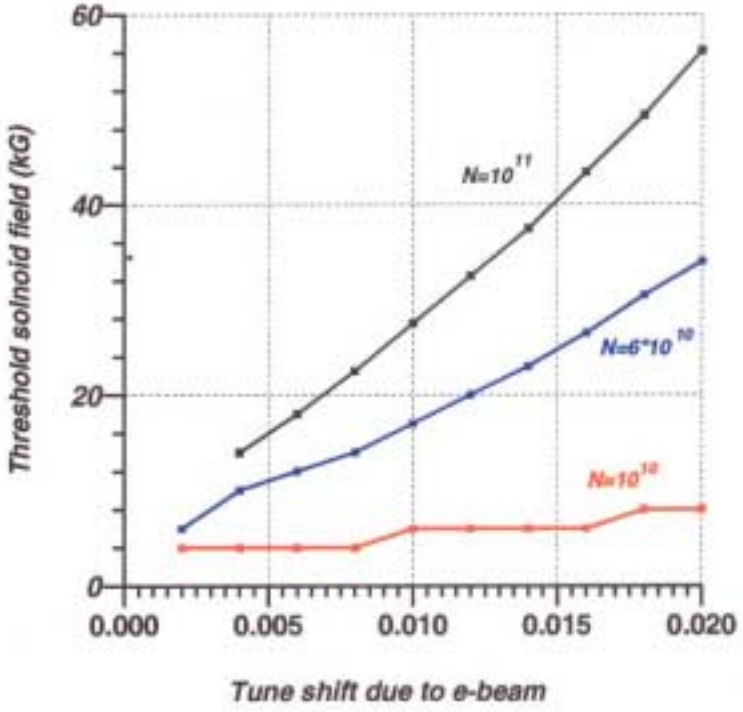

Figure 3.6.19 Threshold solenoidal field B_thr vs tuneshift due to electron beam at different pbar bunch populations N=(1,6,10) e10. Lattice tunes (0.585, 0.575), synchrotron tune 0.0012, rms pbar beam size σ=0.7 mm.

3.6.3 Technical

Here we present technical aspects of the project, including the TEL magnetic system and its possible modification, the electron beam system for linear and non-linear BBC, diagnostics, and finally the operational issues and control.

3.6.3.1 Magnetic System of the Tevatron Electron Lens

The magnetic system of the Tevatron Electron Lens (TEL) was manufactured by IHEP(Protvino) and tested at Fermilab. The system consists of seven superconducting and four conventional magnets and provides a solenoidal field to focus an electron beam. Low energy electrons follow the magnetic field lines from the cathode to the collector.

3.6.3.1.1 Magnetic System of the TEL-1

The longitudinal cross-section of the TEL magnetic system is shown in

Figure 3.6.20. The system consists of seven superconducting (SC) magnets (one large solenoid plus six steering dipoles) and two conventional solenoid magnets each equipped with corrector coils. An electron gun is placed in center of the first conventional solenoid and an electron beam collector in the second one. The electron beam is born on the electron gun cathode, transported through the interaction region in the strong solenoidal field of the SC solenoid and absorbed in the collector. The requirement of the field quality is that the magnetic field lines in the main SC solenoid are straight within 0.2 mm in both vertical and horizontal planes along the 2-m length of the long dipoles.

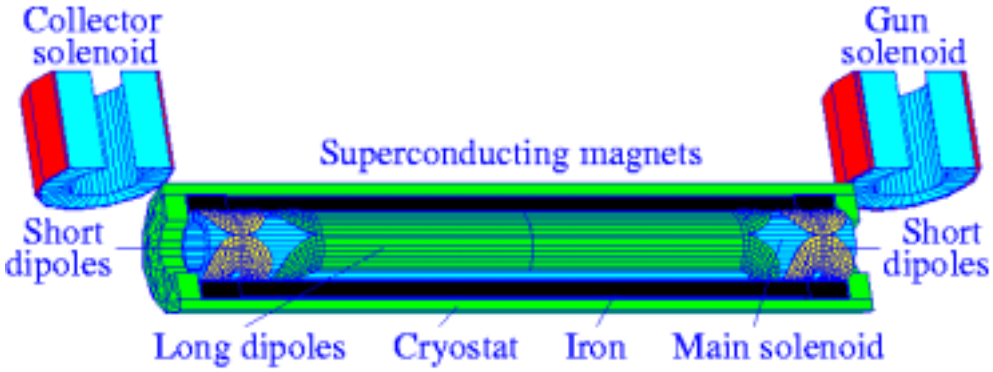

Figure 3.6.20 *Longitudinal cross-section of magnetic system.*

3.6.3.1.1.1 Superconducting Magnets

The solenoid coil is constructed of a flat transposed cable consisting of 10 SC wires (NbTi filaments in copper matrix) each 0.85-mm diameter. The wire has 550 A critical current at 4.2 K and 5 T and Cu/SC ratio of 1.38. The dimensions of the bare cable are 1.44×4.64 mm^2. Six steering dipoles are placed on the outer surface of SC solenoid coil. Four pairs of 250-mm long coils form (short) lateral vertical and horizontal dipoles at each end of the solenoid. Two pairs of 2-meter long coils are placed in the central region of the SC solenoid. All these dipoles are to correct the electron beam trajectory inside the magnetic system. The steering dipoles are wound of cable transposed from 8 wires of 0.3-mm diameter. The wire has 50 A critical current at 4.2 K and 5 T and Cu/SC ratio of 1.5. Dimensions of bare cable are 0.45×1.48 mm^2. The lateral dipole cable

is made of SC wires only. The current in central dipoles is small, and the cable has three SC wires and five Cu wires. The central dipoles have one layer; lateral dipoles consist of two layers and an inter-layer spacer of 0.2-mm thickness.

Magnetic field calculations of the magnetic system were carried out using the MULTIC code. The SC solenoid coil together with steering dipoles is enclosed in a magnetic shield made of low-carbon steel. The shield is 48.5-mm thick over the length of 270 mm and 38.5-mm thick in the central part over 1.96-m length. The yoke reduces currents in steering coils, improves homogeneity of magnetic field inside solenoid aperture, compresses magnetic field lines at the ends of the coil block, and reduces stray fields. The winding of solenoid with preliminary tension and the compression of SC coil by the wrapping of the stainless steel half-shells, allows one to reduce degradation and training of the SC coil. The main parameters of the TEL SC magnets are presented in Table 3.6.3. Computer calculations of the solenoid coil stress have been performed for all stages of winding and showed that cable tension during coil winding have to be 200 N and preload higher than 1 MPa between coil and iron.

	Solenoid	Lateral	dipoles	Central	Dipoles
Field direction	Longitudinal	Horizontal	Vertical	Horizontal	Vertical
Inner coil radius, mm	76.00	100.0	103.7	100.0	103.7
Outer coil radius, mm	98.68	103.5	107.1	103.5	107.1
Coil length, mm	2500	270	270	1960	1960
Number of layers	14	2	2	1	1
Total turn number	7289	640	664	640	664
Operating current, A	1800	200	200	100	100
Central field, T	6.5	0.79	0.82	0.20	0.20
Maximal field in coil, T	6.5	2.2	2.2	0.5	0.5
Stored energy, kJ	950	1.2	1.3	0.9	1.1
Inductance, H	0.6	0.057	0.066	0.18	0.21
Critical current (B_{max}, 4.6 K), A	3000	640	640	540	540
Critical temperature (B_{max}, I), K	5.3	7.1	7.1	8	8

Table 3.6.3

All the SC coils and the magnetic shield are enclosed in a helium vessel. There is a box in the front of the helium vessel, which contains current leads, helium pipes and pipes going to a relief valve. The cold part of the magnetic system with mass of about 1350 kg is attached to the vacuum vessel in two cross-sections with the help of two vertical suspensions and two horizontal tension members in each of the cross-sections. The cold mass is fixed axially using longitudinal titanium tension members and the anchor is fixed to the vacuum vessel.

During the change of current through the SC solenoid dynamic heat release occurs in the coil and other metal parts. Some heat is due to hysteresis in magnetization of the superconductor and the steel of the yoke. Heat is also provoked by eddy currents generated in inner stainless pipe, in the copper matrix of SC wires and in the yoke. A

current ramp rate of less than l0 A/s is taken as a guideline, in order to limit the total heat load to liquid helium at 15 W.

3.6.3.1.1.2 Quench Protection

The SC solenoid coil is not self-protected against resistive transition and fast quench detection and removal of stored energy to the external dump resistor must be provided. A simulation of quench propogation through the coil was made for the case when quench was initiated at the end of the coil inner layer at the maximum current of 1800 A. The quenching lasts about 2 s. 90 % of the stored energy (about 1 MJ at 6.5 T) dissipates in the dump resistor and 10 % inside the cryostat, and the maximum temperature at the hottest point in the coil is about 270 K.

The energy stored in the SC dipoles is much smaller, about 1.3 kJ, and, in principle, one can allow all the energy to be dissipated in the coil if the quench is detected and the current is interrupted. In that case, the hot spot temperature will not exceed 120 K. However, to lower the risk of spreading the quench to the main solenoid, the scheme of quench protection with an external dump (as for the main solenoid) is also used in this case. The hot spot temperature does not exceed 43 K for lateral, and 29 K for central, dipoles.

Quench protection circuits for each SC coil compare the voltage across the coil with *LdI/dt*. If the difference exceeds 1 V, a signal is sent to high current IGBT switches to disconnect the coil from power supply and to dump the coil current into the resistive load. Mechanical current breakers are installed in series with the solid state switches for redundancy.

3.6.3.1.1.3 Conventional Magnets

The gun and collector solenoids have almost identical design. Each is wound of 8.25×8.25 mm^2 Cu conductor with a 5.5-mm diameter water hole. The solenoid has a 0.4 T nominal magnetic field, 0.19-Ohm electrical resistance, and 18-mH inductance. The coil has 250-mm inner diameter, 474-mm outer diameter, and 300-mm length. The solenoid coil consists of 17 pancakes (total number of turns 391), which are assembled on a common pipe of a 240-mm inner diameter. Water temperature rise in the coil is 30^0 C at 0.7 MPa pressure drop and nominal current of 340 A. About 100 A of operating current are needed, in the short steering superconducting dipole, in order for the electron beam to be transported along the center of the warm solenoid.

Electron beam shape and position correctors are set inside each of the conventional solenoids. The corrector consists of four coils, which can be commutated either as a quadrupole or as two dipoles (vertical and horizontal). Each coil layer is shaped with 0.74° inner and 40.04° outer angles, 112.5-mm inner radius and 8.6-mm thickness. The length of coil is equal to 298 mm. The dipole field is equal to 19 G/A; the quadrupole field is equal to 6 G/A/cm.

3.6.3.1.1.4 Results of Magnetic Measurements

Magnetic fields in the TEL were measured by using 3D Hall probe and magnetic arrow set-ups. The latter was used only inside the main SC solenoid and operates with a

small trolley that holds a freely rotating magnetic rod. This trolley is moved inside the solenoid by means of a long track. A mirror is glued to the rod and, therefore, also rotates as the rod aligns itself with the local magnetic field. Beyond one end of the solenoid is a small laser aligned along the axis of the trolley's motion. The output beam hits the mirror and reflects back onto a position-sensitive device (PSD). Everything is adjusted so that, at the center of the solenoid, the laser beam is centered on the PSD. As the trolley is moved along the length of the solenoid, small deviations in the magnetic field appear as changes in the location of the reflected laser beam, which are detected by the PSD. The PSD produces signals that are easily converted back to horizontal and vertical displacement of the beam. Through geometry, the angle of the field is deduced, which is integrated to find the transverse displacement of the field along the length of the solenoid. A LabVIEW program automates the data collection and analysis process. The estimated errors of the spatial resolution are 10 μm vertically and horizontally and 2 mm along the *z*-axis.

The ellipticity $\varepsilon = 1 - B_y / B_x$ of the magnetic field in the solenoids was measured be less than $\pm 0.2\%$, the accuracy of the measurement system. A corrector coil built into each solenoid can be configured as two dipoles (horizontal and vertical) with 19 G/A field strength of each or as a quadrupole with 6 G/cm/A strength. The corrector magnetic length,

$$L_{\mathrm{m}} = \frac{1}{B_0}\int_{-\infty}^{\infty} B(0,0,z)\,dz = \frac{1}{G_0}\int_{-\infty}^{\infty} G(0,0,z)\,dz \qquad (3.6.11)$$

was calculated to be 248 mm, making the integrated dipole field equal to 471.2 G-cm/A and the integrated quadrupole field equal to 148.8 G/A. This last value allows one to adjust the ellipticity by 10% at the maximum operating field of 0.4 T. The dipole correctors can rotate the field lines about $\pm 1.3^{\circ}$ at the maximum field, which provides ±10-mm displacement of the field lines at the edges of the solenoid. The on-axis residual field along the magnetic axis is approximately 6 G near the iron cover and decreases linearly to about 2 G near the stainless steel cover.

In the first high-current test of the superconducting solenoid, 6.6 T was reached at the current ramp rate of 3 A/s and after that the solenoid could not be quenched up to 6.7 T at 10, 20, and 30 A/s. The magnet quenches very quietly and does not consume much helium at the quench. The typical operational field during Tevatron studies was about 3.5 T. The longitudinal distribution of the normalized field $B/B_{\max}$ is shown in Figure 3.6.21 for the superconducting magnets, where $B_{\max}$ is equal to 6.5 T in the solenoid (dashed line), 0.8 T in the short dipoles, and 0.2 T in the long dipoles (solid lines). The deviations of the magnetic axis from a straight line of the superconducting solenoid are shown in Figure 3.6.22. At full power, the vertical deviations are very small (roughly spanning –25 to 25 μm of the axis), while the horizontal deviations have more spread (from –100 to 75 μm); however, these values are still less than the required 0.2 mm tolerance. The left side depicts how the field lines change from 3 T to 6 T, while the right side illustrates how five field lines, distributed horizontally, differ from each other. The deviations are small enough (about 8 μm maximum, and the horizontal displacement shows similar uniformity) that unintentional lensing effects will be minimal.

3.6.3.1.1.5 Operational experience

The TEL has been installed in the Tevatron in February 2001, and been in operation since March and there were no quenches in the TEL at the typical operational field of 35 kG in the main solenoid. The magnetic system worked very reliably providing the control of the electron beam size and trajectory that allowed the first successful demonstration of the betatron tune shift of 980 GeV protons in the Tevatron. It was found experimentally that the electron beam can be steered to pass through the main solenoid if the gun solenoid field is in the range of B_{Gun}=*1.9-4.2* kG for B_m=*35*kG (outside the range, the beam touches parts of the vacuum system in the bend sections of the TEL).

3.6.3.1.2 Modifications of the Magnetic System for the TEL-2

Currently, we study possible modifications of the bending sections which can allow clean beam passage over even wider range of magnetic field ratios B_m/B_{Gun}. As it was mentioned above, that will make possible wider variation of the electron beam size in the main solenoid magnet.

Magnetic field simulations performed in the fall 2001 have shown that it is possible to increase magnetic field in the bend from 0.8 to about 2kG and increase the range of operational magnetic fields B_m/B_{Gun} about two fold if two conventional coils are installed and the bending angle is reduced from 90 degrees to about 45 degrees – see Figure 3.6.23.

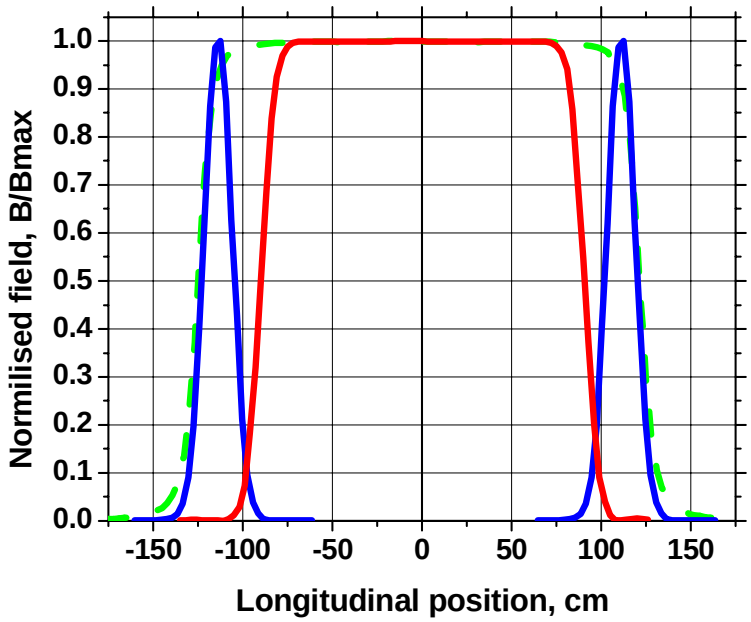

Figure 3.6.21 *Longitudinal distribution of the normalized fields of the super-conducting magnets.*

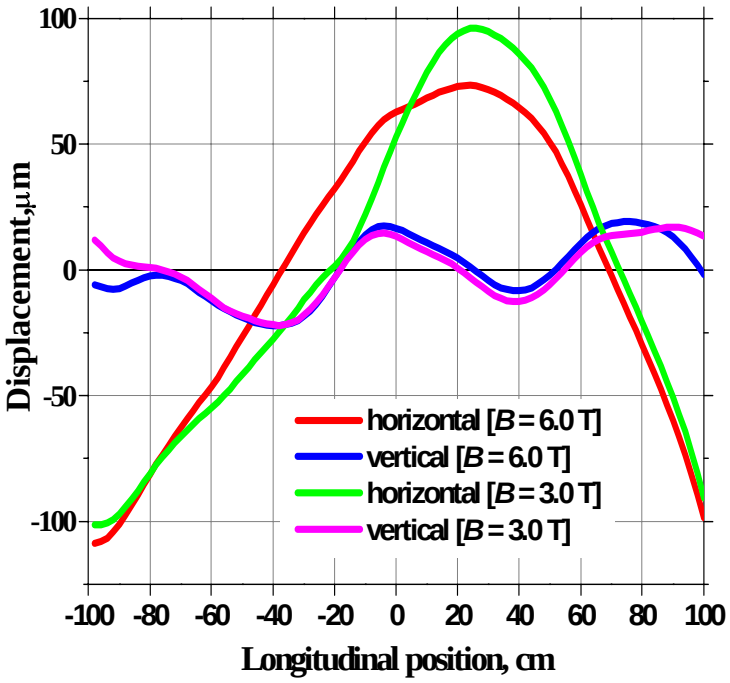

Figure 3.6.22 *Transverse displacement of various field lines along the length of the main solenoid at different field strengths.*

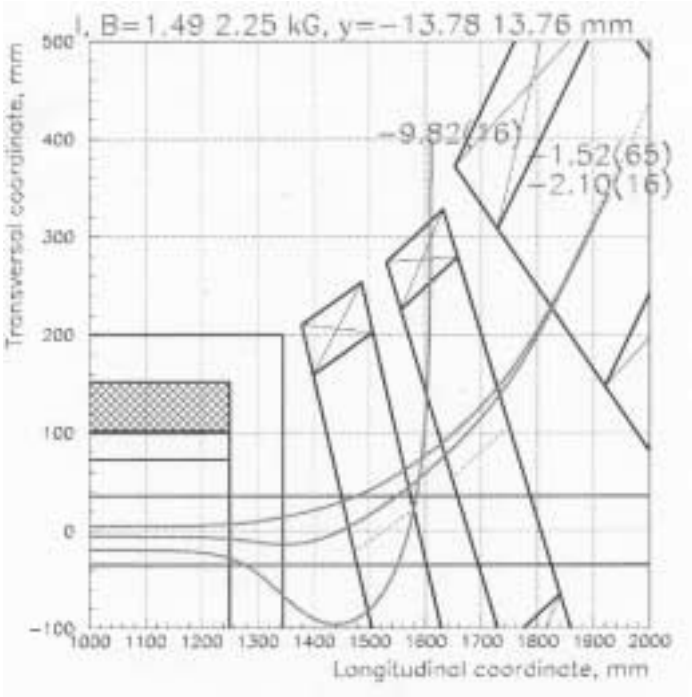

Figure 3.6.23 *Magnetic field simulations for the TEL-2.*

The new smoother bend also will also result in about 5 times smaller drift of the electron beam in the bend, and thus much weaker dependence of the vertical electron beam position on the electron beam current and energy. The 2nd TEL will be installed in A10 sector of the Tevatron ring and the closest cryo port will be some 15-30 ft away, so, corresponding modifications will need to be done in the cryogenic system design.

3.6.3.2 Electron Beam System of the TEL

The electron beam system of the TEL, which includes electron gun, collector, ion and secondary electron cleaning electrodes, high voltage modulator, vacuum system and beam diagnostics (BPMs, current monitors, scrapers, wire scanner). Results of the electron beam studies are presented.

3.6.3.2.1 General Layout

Figure 3.6.24 shows the general layout of the TEL electron beam system. The total length of the TEL (flange-to-flange) is 3.65m; the interaction length (zone inside SC solenoid, where electron and antiproton beams can overlap) is about 2m.

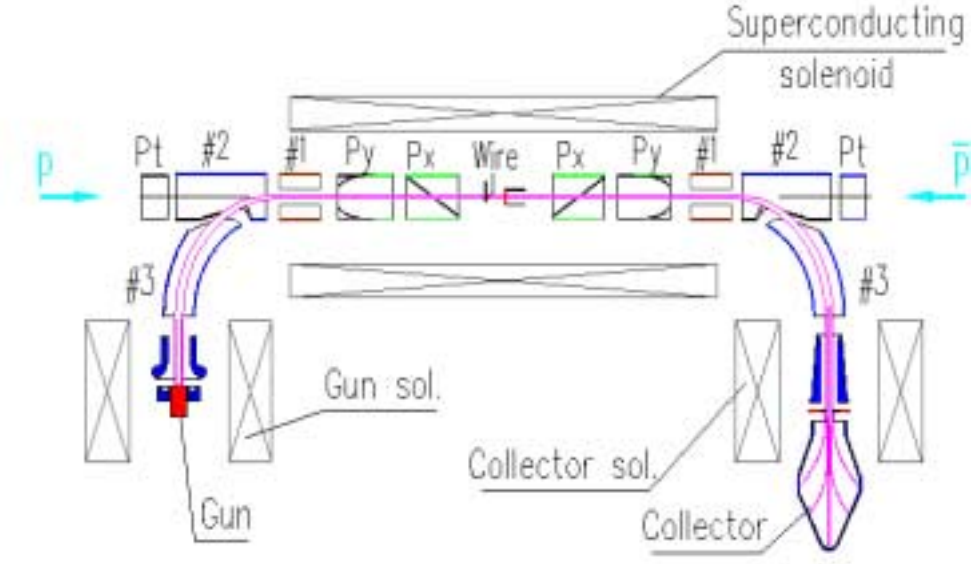

Figure 3.6.24 *Electron beam system of the TEL.*

The electron beam is born on the thermionic cathode of the gun immersed in some 4 kG magnetic field remains magnetized all the way to the to collector. Π-shaped magnetic system is formed by two conventional and one super-conducting solenoids. The electron beam follows the magnetic force lines (magenta in Figure 3.6.24). Beam diameter in the main solenoid is defined by the cathode radius a_c=5mm and the ratio of the magnetic field at the cathode B_c, and in the main solenoid B:

$$a = a_c \sqrt{B_c / B} \qquad (3.6.12)$$

The operational magnetic fields allow the electron beam size to be 3 times the antiproton rms size σ=0.5mm, while at the same time the electron beam does not touch any apertures. The typical TEL parameters are presented in Table 3.6.4.

electron beam energy,	U_e, kV	6-12
maximum peak electron current	J_e, A	2-3.5
magnetic field in main solenoid	B_m, kG	35

in gun solenoid	B_g, kG	3.7
e-beam radius in main solenoid	a_e, mm	1.75
cathode radius	a_c, mm	5
e-pulse width, FWHM	τ_e, mm	~800
repetition rate	f_{rep}, kHz	47.7
current stability, peak-to-peak	$\Delta J_e/J_e$,%	< 0.1
vacuum pressure	*e-8*, Torr	2-8

Table 3.6.4 *TEL operational parameters*

The main SC solenoid has built-in dipole correctors for electron beam position and angle steering. Additional 4 coils are built-in in the gun and collector solenoids and can be used as quadruple correctors of the beam ellipticity

The beam diagnostics consist of two pairs (P_x&P_y) of pick-ups (BPMs) 150mm long and ∅70mm each, located at the beginning and at the end of the interaction zone. Pick-ups made of diagonally cut SS cylinder for better linearity. BPMs can measure positions of electron, proton and antiproton beams. Gun and collector beam currents as well as beam losses on the scraper electrode at the collector entrance are measured by inductive coils (IC). Two wires can be remotely introduced into the center of the lens for the beam profile measurements in both (X&Y) planes.

Figure 3.6.25 shows the TEL electrical circuit. Vacuum beam pipe and pick-up electronics stay at the ground potential. Cathode and anode potentials are negative, typically -10kV to -15kV and held by low-current DC power supply (V1) to compensate beam losses to the ground. High-current power supply (V2) with potential up-to +10kV drives cathode to anode beam current. To modulate the beam current three different types of HV modulators were used. The modulating positive signal feeds the electron gun anode through a capacitor.

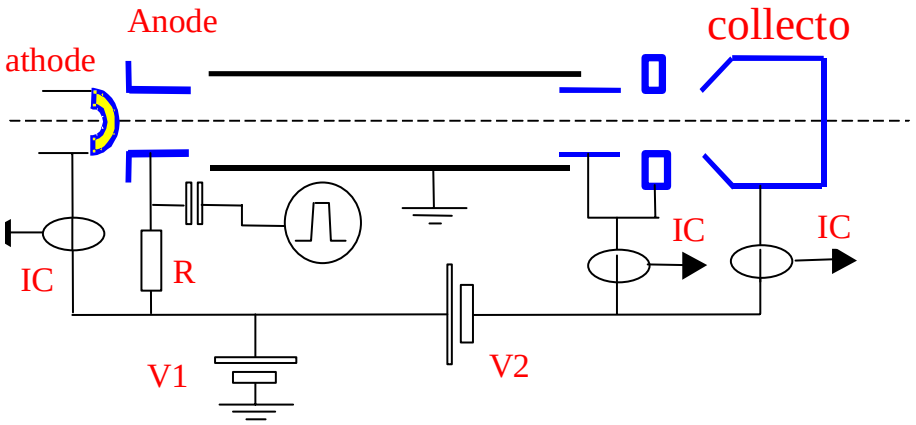

Figure 3.6.25 *Electrical circuit of TEL.*

The electron beam ionizes residual gas and if these ions and electrons are trapped and stored, their charge may change the lens performance. For cleaning the ions and electrons, several HV cleaning electrodes are installed. Two of them (#1) are installed inside the main solenoid, each consist of a tube (∅70×129mm) cut in half and these two halves are insulated by semi-conducting glass. Ions can escape if cleaning potential (±U) strongly distorts the potential well due to the electron beam space charge. Semi-

conducting glass avoid storing of the secondary electrons as well. Two elbow electrodes (#3) in the bends work the same way. The electron beam size at that place is about 15-20mm, hence ±(5kV to 8 kV) of voltage thought to be enough for the cleaning. Cylindrical electrodes (#2) provide ion cleaning in longitudinal direction by changing potential barrier. The cleaning procedure for the TEL is not studied well yet.

3.6.3.2.2 High-perveance Electron Gun

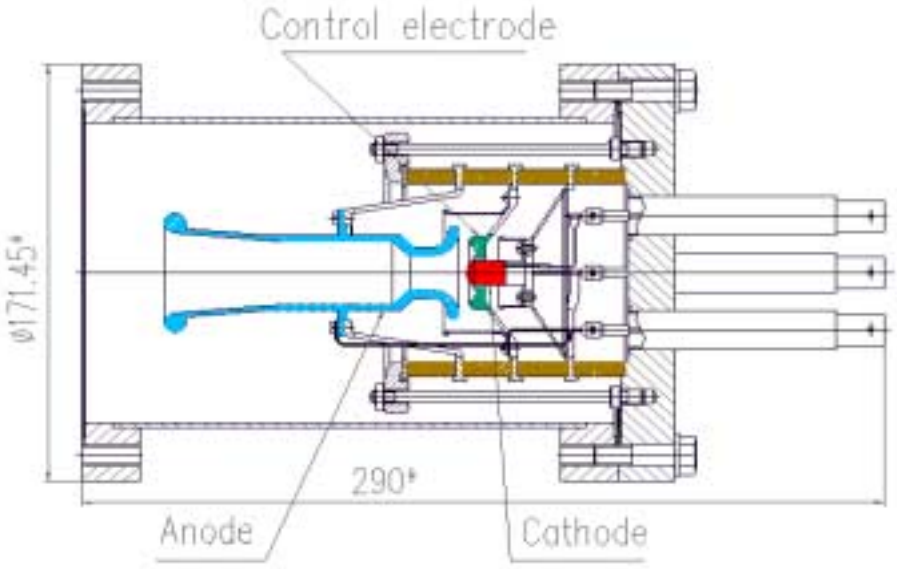

Figure 3.6.26 *Electron gun for TEL.*

The electron gun, see Figure 3.6.26, employs a 10 mm diameter convex cathode and can provide 10A of pulsed current and about 3A DC. The measured perveance of the gun is 5.6μA/V$^{3/2}$, which is close to the design value[46]. The gun is assembled on 6.75" CF flange. All the electrodes are insulated by 4 ceramic rings (ID×OD=79×85mm and 20mm wide) and are constricted by stubs. The electrode capacitances are: 40pF anode to ground, 38pF anode to control electrode, 17pF anode to cathode. Vacuum HV feed-throughs provide 20 kV DC to all electrodes. In presence of a magnetic field the maximum electric potential may fall to 15kV if the vacuum is worse than 5*10^{-7} Torr; this is due to Penning discharge. We plan to fix this problem in the improved gun design.

In the pulsed regime, the anode is driven by a pulse modulator. In the first tests a tetrode modulator with 800 ns and up to 7.5kV output pulse amplitude was used. The plot of beam current vs. anode pulse voltage for 50 Hz and 50kHz (operational regime) repetition rates is shown in Figure 3.6.27.

The difference in behavior between low and high repetition rate can be explained by the presence of stored ions in the case of 50kHz. During the 20μs between electron pulses, the ions have not enough time to escape from the TEL and partly compensate the electron space charge. In this case, the beam current follows Child's law. In absence of ions we have some restriction of electron current due to the beam pipe perveance.

For the electron beam profile measurement, two wire scanners are installed in the TEL close to the middle plane of the main solenoid. One is for horizontal plane and the other

is for vertical plane. Wires can be moved in or out of the beam pipe by remotely controlled step motor. In normal operation with the proton beam they are moved completely out of the beam orbit in order not to disturb the proton beam or/and not to burn out the wire. The geometry of the wire is shaped like a "fork". The distance between the fork claws is 15mm, from the wire to top edge 22mm, wire diameter 100μm, the tube diameter 70mm. As an ancillary benefit, the dimensions give us a good scale for calibration of steering strength of correctors for the electron beam and in turn, to calibrate the pick-up BPM systems.

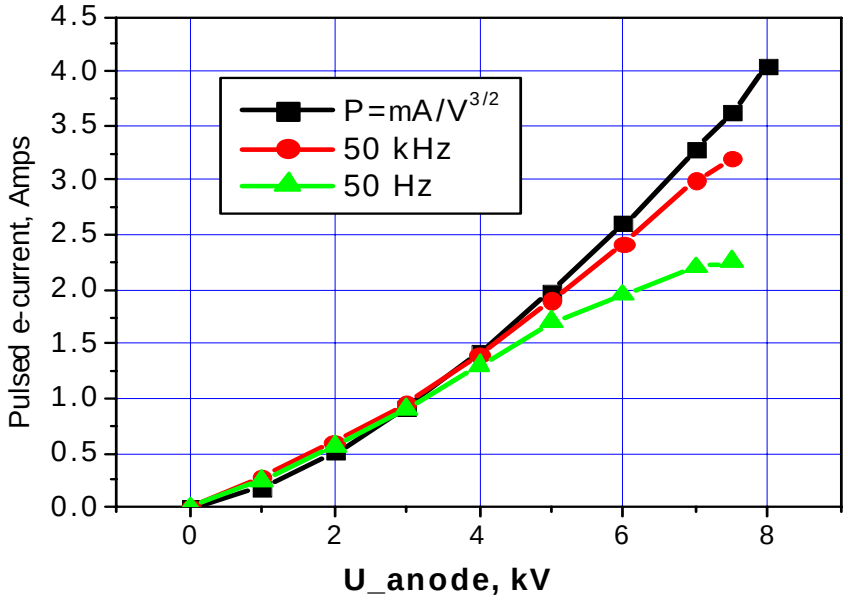

Figure 3.6.27 *Beam current vs. anode voltage at 50Hz and 50kHz*

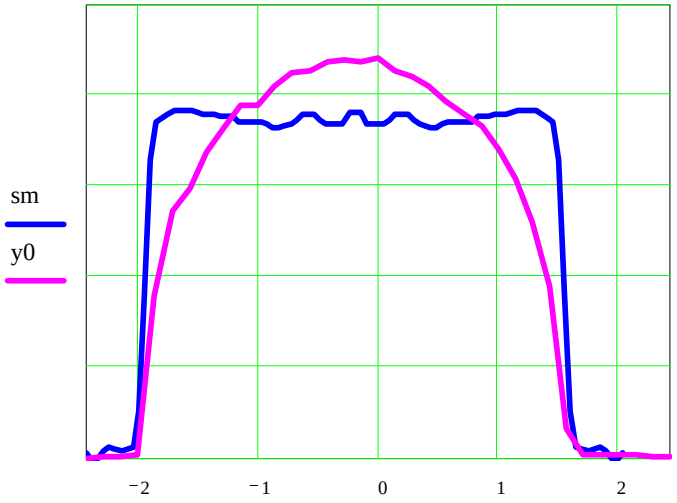

Figure 3.6.28 *Electron beam current density profile.*

Measured (X-slices) and restored beam profiles are shown on Figure 3.6.28 (top). The beam diameter is about 3.5 mm. The restored profile is in a good agreement with the

two-dimensional electron current profile (bottom), previously measured by special beam profile-meter at the TEL prototype. That profile-meter measured a small portion of the beam current, which goes through tiny hole in electron collector. By scanning the electron beam in XY plane we can measure the 2-D electron current profile. The electron current density profile is almost flat as required for the linear beam-beam compensation, but can be changed by applying negative potential to a special (control or "profiler") electrode near the cathode. In this case the beam profile becomes smoother, while it reduces the total current and the beam size decrease.

3.6.3.2.3 Electron Gun for Non-Linear BBC

An electron beam with transverse charge distribution close to the Gaussian is thought to be needed for non-linear beam-beam compensation. No studies have been done so far in that direction. Nevertheless, we currently investigate the electron gun geometry for non-flat current profiles. In particular, according to numerical tracking results (see above) a "smooth edge" distribution is anticipated to be beneficial for the linear beam-beam compensation as the high-order resonance strengths will be suppressed compared to a flat electron current density profile. Figure 3.6.29 shows electron current distributions for current electron gun geometry (black curve) and for modified geometries; all were calculated using the SuperSAM code. The corresponding shapes of the electrodes are shown in Figure 3.6.30.

3.6.3.2.4 HV Modulator for the Electron Gun

The HV modulator uses the output from the anode of a grid driven tetrode. The tube anode is connected to a +10kV dc anode supply through a 1500Ω resistor. The modulating voltage on the anode of the tetrode is then ac-coupled through two 1000pF ceramic capacitors to the electron gun anode. This modulator has the advantage that it is not susceptible to radiation damage and can be installed directly adjacent to the Tevatron beamline.

A CPI/EIMAC 4cw25000B water-cooled tetrode, with a maximum plate dissipation of 25kW, is used in this modulator. Its anode voltage is supplied by a Hipotronics 10kV,16A, dc power supply. An additional LC filter (1.5H, 20μF) was added to the output of the Hipotronics supply to reduce ripple to less that 1 part in 10,000. The anode supply is connected to the tetrode through a 1500Ω, 250kW, water cooled resistor (Altronic Research). The grid of the tetrode is driven by an Amplifier Research 500A100 amplifier which can provide 500 watts of power from 10kHz to 100MHz.

To compensate a single bunch of protons or antiprotons, the tube is typically operated with a screen voltage of 750V and a dc grid voltage of –15V. Under these conditions, the voltage on the anode is held slightly above the screen voltage at 1kV with a plate current of 6A. The tetrode grid is then pulsed with a negative voltage pulse from the broadband amplifier, reducing the current flow through the tetrode. The positive pulse appearing on the anode is then coupled, using two 1000pF ceramic capacitors in parallel, through a short (0.6m) section of 50Ω, RG213 cable to the anode electrode of the electron gun. A typical output pulse is shown in

Figure 3.6.31.

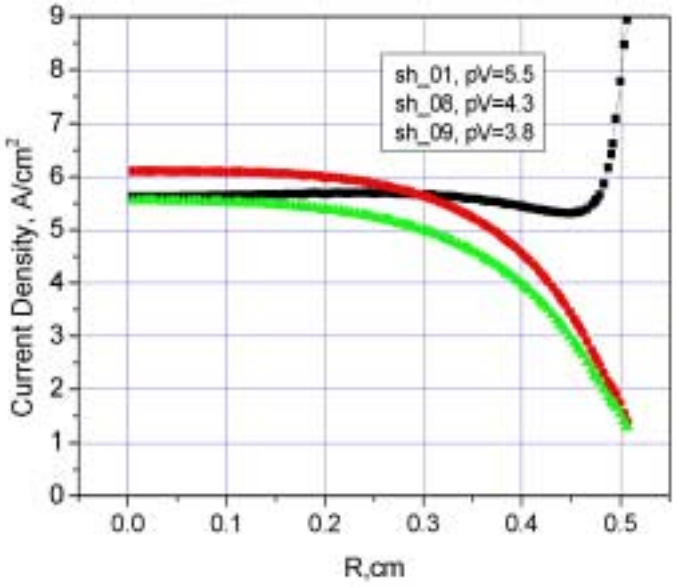

Figure 3.6.29 *Calculated distribution of electron current density vs radius with original (black) and modified geometry of the gun electrodes (green and red)*

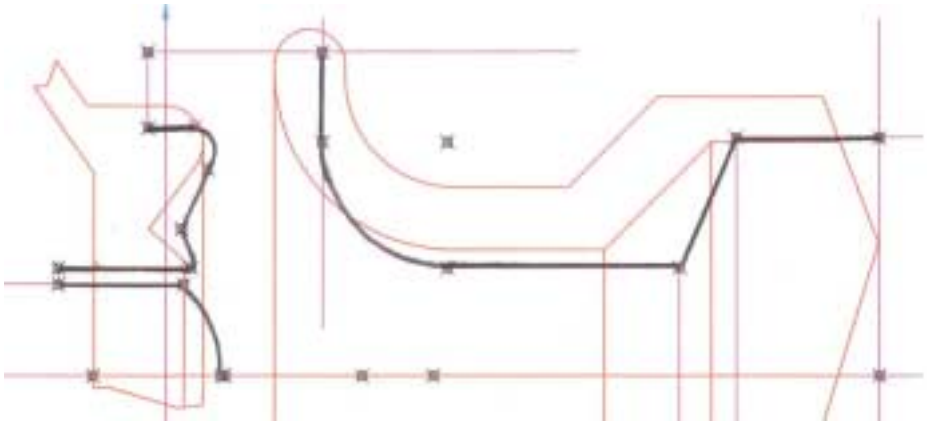

Figure 3.6.30 *Shapes of electron gun electrodes (anode, cathode and near-cathode electrode)for bell-shape profile (black) and for flat-top electron current profile (red line).*

Since the gun anode must be charged through the 1500Ω resistor, the risetime is limited by the sum of the tetrode's anode-screen capacitance (35pF), the capacitance of the cable connecting the modulator to the gun (60 pF), and the gun anode to ground capacitance (60pF). A pulse to pulse amplitude stability of 2 parts in ten thousand was achieved by applying a feedforward compensation signal to the grid of the tetrode to reduce ripple on the modulator output at power line frequencies.

There is need for a higher amplitude HV pulse (some 12-14kV) for linear BBC operation. That would require different HV DC power supply and little modification of the circuitry. Two HV modulators will be necessary for two TELs and one more spare for routine operation.

The second modulator tested was 20kV, 50ns wide pulser (model # FPG20-50S) designed and manufactured by FID Technology. The pulser uses a combination of fast

(<1ns) closing Fast Ionization Device (FID) switches and fast opening Drift Recovery Diodes (DRD) to generate the output pulses. The pulser is arranged into four identical blocks whose outputs are then combined. Each block has a single DRD shunting its output connector. The DRD is connected by coaxial cables to two LC circuits, each LC circuit having its own stack of FID switches. The pulsing sequence begins when one of the two FID stacks closes, exciting the first LC circuit and sending current through the conducting DRD. After a half cycle oscillation in the first LC circuit, the current reversed direction and the second FID stack closes, exciting the second LC circuit. During this time charge is being pumped out of the DRD. When all of the charge has been pumped out, the DRD opens, interrupting the large current flow and generating a 5kV, 50ns pulse at the output.

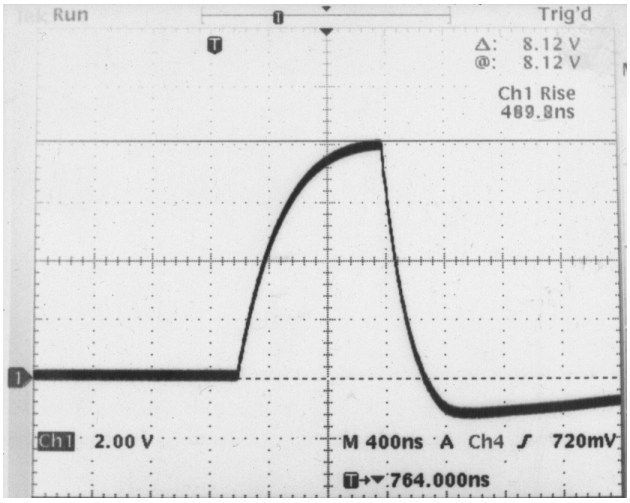

Figure 3.6.31 *Tetrode modulator output pulse (2kV/div) with a sweep time of 400ns/div*.

The four 5kV block outputs are combined, using a Blumlein type circuit consisting of four, 6m long, 100Ω coaxial cables, into a single 20kV positive pulse. The output is matched into a 480Ω resistive load. The pulse width is fixed at 50ns and the pulse height is adjustable from 0-20kV by varying the 0-300V dc input voltage. The pulse repetition rate is limited to 50kHz at the maximum voltage due to component heating.

Since the output consists of positive pulses referenced to ground and the electron gun anode is normally biased at the negative cathode potential (-13kV), the pulser output must be capacitively coupled to the gun anode through a 3300pF, 30kV, ceramic capacitor. The pulser, along with its combining network, 480Ω resistive load (water and air cooled), and output coupling capacitor is enclosed in a shielded equipment rack to eliminate electrical noise generated in the combining network from interfering with other electronics in the TEL. We have experienced several failures of the HV connectors on the cable between the modulator and the electron gun anode feedthrough due to corona discharges at voltages above 15kV.

3.6.3.3 Diagnostics and Operation

3.6.3.3.1 Introduction

The 1st TEL operation requires(in order of urgency): better electron beam steering, better proton beam diagnostics, and a better quality electron beam. To achieve more precise steering, we are currently working on the BPM hardware and electronics improvement (the existing ones gave unreliable readings of the proton bunch position).

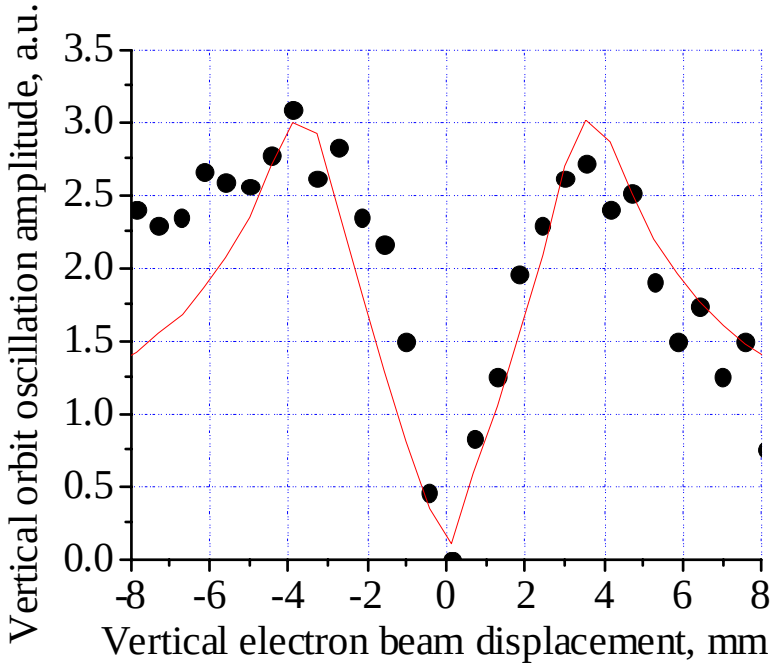

Figure 3.6.32 *Rms amplitude of vertical proton orbit variation vs vertical position of AC electron beam.*

Using "tickling" of the proton orbit with the electron beam can potentially improve the steering as well. The idea is similar to the "K-modulation" in the beam based alignment: variation of the electron current in the electron lens should cause variations in the proton beam orbit around the ring if the electron lens beam is not centered. Figure 3.6.32 shows the rms amplitude of the vertical proton orbit variation at the Tevatron BPM located at A0 sector vs vertical displacement of the electron beam at F48 which had the current modulation of J_e =1.02+ 0.18sin($2\pi t$*107Hz) A. The amplitude becomes equal to 0 if the proton beam goes through the center of the electron beam. The 7 mm distance between the two peaks reflects an effective diameter of the electron current distribution, and, thus, indicates angular misalignment of the electron beam because it exceeds the electron beam diameter of about 3.5 mm. Therefore, steering by the orbit tickling should concentrate not only on the search of the minimum orbit response, but also on having two maxima closer to each other. In the first experiments, such a tickling measurements took about 2-3 hours, and now we are looking for a faster automated system.

3.6.3.3.2 Proton and Antiproton Beam Diagnostics

Besides the BPM system of the TEL, we also use the beam diagnostics of the Tevatron to monitor proton and antiproton parameter, which include intensity, emittance, orbit, lifetime and tune. The Tevatron orbit measurement system has a resolution of 150 micrometer. The tunes are measured by the Shottky spectra analyser. A new bunch-by-bunch tune meter is under commissioning. Its resolution needs to be improved to be better than 0.001. The beam emittances are measured by the flying wire systems. We found that the flying wire system gives large errors, e.g., about 14% in horizontal proton emittance. We expect that recently installed synchrotron light monitor will perform better and will allow us to monitor the proton or antiproton emittance variations during the beam-beam compensation studies. The beam lifetime is monitored by the Fast Beam Integrator (FBI), which relies on the wall current monitor. We will also be able to monitor the luminosity and the proton losses bunch-by-bunch, which is supplied by the D0 and CDF detector via ACNet. And we also can 'tickle' the proton or antiproton beam orbit by modulating the electron beam current. That method provides us the information for precise centering of the electron beam onto the proton (or antiproton) beam.
We also look forward to having more reliable proton diagnostics for the emittance measurements (e.g., synchrotron light system instead of flying wires) and an automated tune measurement system for the multi-bunch measurements. Currently, Tevatron beam diagnostics is unable to provide reliable data on p/pbar size and tune on bunch-by-bunch basis with needed accuracy.

3.6.4 Project Plan

Table below summarizes implementation plan of the Beam-Beam Compensation project from November 2001 until March 2006. Columns "Current configuration", "Linear BBC" and "Non-linear BBC" refer to Run IIa conditions (36x36 bunches); "Nonlinear BBC→ Zero Crossing Angle" refers to Run IIb with 132 ns bunch spacing.

	Current configuration		Linear BBC (2 TELs)		Nonlinear BBC		Nonlinear→ ZeroX-angle	
	Exist	0	the 2nd set of magnets, minor changes in design, magnetic measurements, radiation protection – 11mos	330 k$	Use existing	0	Use existing (TBD – larger e-current and smaller diameter may require new magnets)	0
Power Supplies	exist, minor im-provement	0	2nd set of PSs	70k$	Use existing	0	Use existing	0
Quench protection	Exist	0	2nd set of QPS	60k$	Use existing	0	Use existing	0
Electron gun	Exist, design and R&D under way to increase current to 5-7A and voltage to 30kV	40 k$	2 more copies of the improved design gun	70k$	Optimized shape gun electrodes	25k$	3 optimized shape electrode guns with 3-5 time larger current and twice larger cathode	100 k$
Electron collector	Exist	0	two the same type	60k$	Use existing	0	3 100kW collectors	150$
HV PSs for e-system	Exist	0	one more set of PSs	40k$	Use existing	0	Higher current higher voltage	120 k$
HV pulse generator and its PSs	Exist	0	build two somewhat modified tetrode 12kV 2MHz pulsers	300 k$	Use existing	0	Two 18kV and 6MHz pulsers to be built, existing	100 k$

							20kV PSs	
Vacuum/diagnostics	Exist	0	Build the 2nd set	60k$	Use existing	0	Use existing	0
Cables/LCW/construction	Exist	0	Work at sector A10	150 k$	Use existing	0	Additional cable work	60k$
Cryo	Exist	0	He/N2 connections, bypass modification	70k$	Use existing	0	Use existing	0
Studies	14TeV shifts till May'02	0	Magn.meas.+tests in E4R (3mos), then 30 Tevatron shifts	40k$	30 Tevatron shifts, DC wires	95 k$	e-Studies in E4R with SC magnets needed (6 mos)	300 k$
Theory/calculations[1]	None		1S+1RA		1S+1RA		1S+1RA	
Cost[2], M&S	total in FY'01-02	40k$	50%-50% in FY'02-03	1500 k$	All in FY'04	150 k$	2/3 in FY'05 1/3 in FY'06	1000 k$
Time scale	now-June'02		2yrs till Oct'03		1yr - Oct'04		1½ yr till Mar'06	
Additional man-power[3]	None		2x(P,EE),1x(S,PE,ME, CS,D)		2P, 1S		2x(P,EE),1(S,ME)	

[1] in terms of people working on the project: S – Scientist or Ass.Sci., RA – postdoc

[2] 20% contingency added

[3] compared to Summer-Fall'01 work-force of 2 Physicists (P), 1 Student(S) and 1ProjectEngineer(PE); abbreviations: EE-Electrical Engineer, ME-mechanical engineer; CS – computer specialist; D- drafter; assumed that the people requested work over the time period listed in each column

3.6.4.1 Status as of November, 2001

Fermilab Beams Division BBC (Beam-Beam Compensation) Project group is currently focused on implementation of the *linear BBC*. One TEL was designed, built, tested, installed in the Tevatron Sector F48 and operated by March 1, 2001. Because of the larger horizontal beta function β_x=101m >> β_y=29m at that location, the first TEL can shift mostly horizontal tune of the Tevatron beams. It is anticipated that the second TEL to be built will be installed at the Sector A10 where β_y=172m >> β_x=56m will shift mostly the vertical betatron tune.

In the period March-October 2001, the TEL operated in a single bunch regime with 47.7 kHz electron pulse repetition rate. The maximum horizontal tuneshift achieved with 980 GeV protons (6 shift of studies) is about dQ_x=+0.0071 with 980 GeV protons, while vertical tune shift is about 4 times less, all in a good agreement with theoretical expectations. Among other achievements we note: a) a decent proton beam lifetime exceeding 20 hrs has been obtained with maximum electron current; b) it has been demonstrated that electron beam separated by 5 mm from the proton beam, the default regime for the BBC, as the electron beam will collide with pbars, does not affect the proton beam (infinite lifetime); c) it has been demonstrated that having TEL magnets on and/or electron beam but not interacting with the Tevatron beams does not affect the Tevatron beams. That is, no significant changes in orbits, tunes, coupling, chromaticity, dispersion, lifetime, or impedance are seen.

A Fermilab Beams Division Internal Review of the BBC project took place on June 4, 2001. Status of the project was appraised positively, and recommendation to continue the studies has been given. For that it was decided to allocate about 3 Tevatron study shifts a month for the BBC in order to finish studies early in 2002. This is, of course contingent on the collider meeting certain operating performance criteria.

3.6.4.2 Plans for FY 2002

Further plans of the BBC project in FY02 include beam studies and the start of construction of the second TEL, and preliminary studies of non-linear beam-beam compensation.

Tevatron beam studies with the TEL are focused on demonstration of single electron lens operation to produce tuneshift of about 0.005-0.01 on a single antiproton bunch at collision (980 GeV) without significant degradation of the luminosity lifetime.

The beam studies plan includes:

a) operation with 980 GeV antiprotons;
b) investigation of the dependence of the p(pbar) lifetime on e-beam steering, current, size and shape, magnetic field, current and position stability, p(pbar) size/emittance;
c) understanding of the ion accumulation process and relevant effects, clearing/storing of ions;
d) measurement of the p(pbar) emittance evolution under impact of the TEL;
e) attempting improvement dynamics of a single pbar bunch by the only existing TEL;
f) studies of non-linear effects under operational conditions similar to those required by the *non-linear BBC*;
g) observation of "strong head-tail" instability at reduced main solenoid magnetic field.

In parallel, we will continue hardware improvement, e.g., of the electron gun, electron and p(pbar) beam-position monitors, electron beam diagnostics, power supply stabilization, and higher power HV modulators.

Building the second TEL will require:

a) studies of the bending section magnetic field optimization and potential design changes in positioning gun and collector solenoid magnets
b) design of the magnetic structure for the 2nd TEL
c) design of crygenic system for the 2nd TEL
d) measurements of the radiation levels at A10
e) calculation/design of radiation shielding for the 2nd TEL
f) fabrication of the magnetic system and quench protection system for SC magnets
g) design and build modified 30 kV electron gun, build electron collector, electron beam diagnostics and vacuum system
h) design and fabrication of a faster HV modulator for Run IIb operation;
i) assembly and test of the TEL in E4R building
j) preparation work at A10 sector, including radiation shielding for SC magnets and cryogenics infrastructure
k) installation and commissioning of the second TEL
l) modification of the control system.

We plan to accomplish items a) to e), and part of item g) (design of 30 kV electron gun) in FY2002. Items f) to h) are to be started in FY2002 and finished in FY2003.

In parallel, we will fabricate and test the electron gun for non-linear beam-beam compensation and perform analytical studies and tracking of the Tevatron beam dynamics with non-linear BBC devices.

3.6.4.3 Plans for FY 2003

The plan for FY03 includes finishing fabrication of the second TEL, its installation and commissioning of the system of two TELs for linear BBC; design and fabrication of the electron gun for the nonlinear beam-beam compensation; non-linear BBC experiments with Tevatron beams.

To complete the system of two TELs for linear beam-beam compensation in FY03 we plan : a) fabrication of the magnetic system and quench protection system for SC magnets; b) fabrication of electron collector, electron beam diagnostics and vacuum system; c) fabrication of faster HV modulator; d) assembly and test of the 2nd TEL in E4R building; e) preparation work at A10 sector, including installation of radiation shielding for SC magnets and cryogenics infrastructure; f) installation and commissioning of the second TEL; j) modification of the control system.

In parallel, we will perform Tevatron beam studies with non-linear electron beam profiles to better understand beam dynamics issues of non-linear BBC.

3.6.4.4 Manpower

Currently, the BBC group has only enough man power to perform beam studies and make minor hardware/software improvements. More man power will be needed as soon as we start design, fabrication and test of the second electron lens, design and test of the electron beam system for non-linear BBC.

We anticipate either new hires or transfer of people to the group or temporary assignments from other BD departments. In particular, we need

(FTE in FY2002):

1 Electrical Engineer and 1 Tech to fabricate/test QPS
1 Electrical Engineer and ½ Tech to develop HV modulator
1 Electrical Engineer and ½ Tech to develop other HV PSs
1 Electrical Engineer to build beam diagnostics
1 Mech.Engineer – project engineer
1 Drafter
½ CryoEngineer
½ Computer Specialist
1 Scientist (Assoc.Sci. or higher) to carry out electron gun/collector diagnostic development/fabrication/test .
1(or 2) Scientist(s) (grad student/RA) to take part in beam studies
2 Scientists to carry out analytical and numerical studies of nonlinear BBC.

In addition to that we expect to get some help from external organizations and collaborators, including IHEP(Protvino, Russia), which will take part in design and fabrication of the magnetic system for the 2nd TEL, and Budker INP (Novosibirsk, Russia), which helps us to perform Tevatron beam dynamics simulations and computer tracking.

4 Resources, Cost, Schedule

4.1 Luminosity Schedule

The project schedule was developed to accommodate the luminosity schedule shown in Table 4.1.1. Such a schedule is illustrated in terms of initial store luminosity in Figure 4.1.1 and in terms of integrated luminosity in Figure 4.1.2. One notes that the goal of 15 fb^{-1} is indeed achievable if an initial luminosity of $4x10^{32}$ $cm^{-2}sec^{-1}$ can be achieved.

Fiscal Year	Luminosity $\mu barn^{-1}/sec$	$pbarn^{-1}$ per week	Months of Operations	Shutdowns (months)	$fbarn^{-1}$ per year	$fbarn^{-1}$ Total
FY02	75	17	10	2[i]	0.32	0.32
FY03	120	24	10	2[ii]	0.83	1.2
FY04	220	43	9	3[iii]	1.3	2.5
FY05	310	61	8	4[iv]	1.8	4.4
FY06	410	81	11	1	3.4	7.6
FY07	410	81	10	1	3.9	11.5
FY08	410	81	10	1	3.9	15.0

Table 4.1.1 *Luminosity Schedule. The values in the table are assumed to be obtained at the end of the fiscal year. The shutdowns are planned shutdowns. The effects of "unplanned" shutdowns are incorporated in estimate of the integrated luminosity per week.*

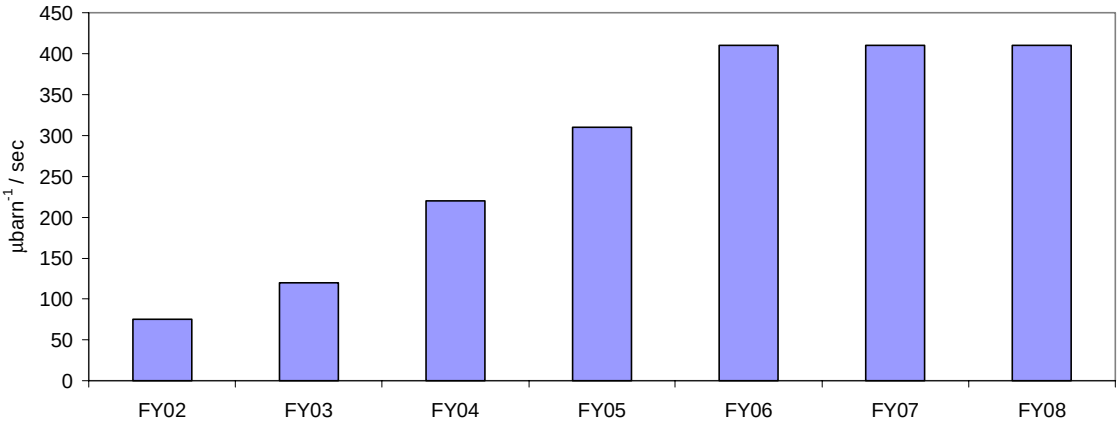

Figure 4.1.1 *Peak Luminosity Schedule*

[i] Shutdown in October for Recycler alignment. Shutdown in September to install Electron Cooling push pipe.
[ii] Assume Recycler is working. Shutdown in August to install 132 nS hardware and Electron Cooling into the Recycler
[iii] Finish installation of 132 nS and Electron Cooling. Spend 1 month commissioning 132 nS.
[iv] Shutdown for Run IIb silicon and CO I-R. Initiate NUMI with 20% impact

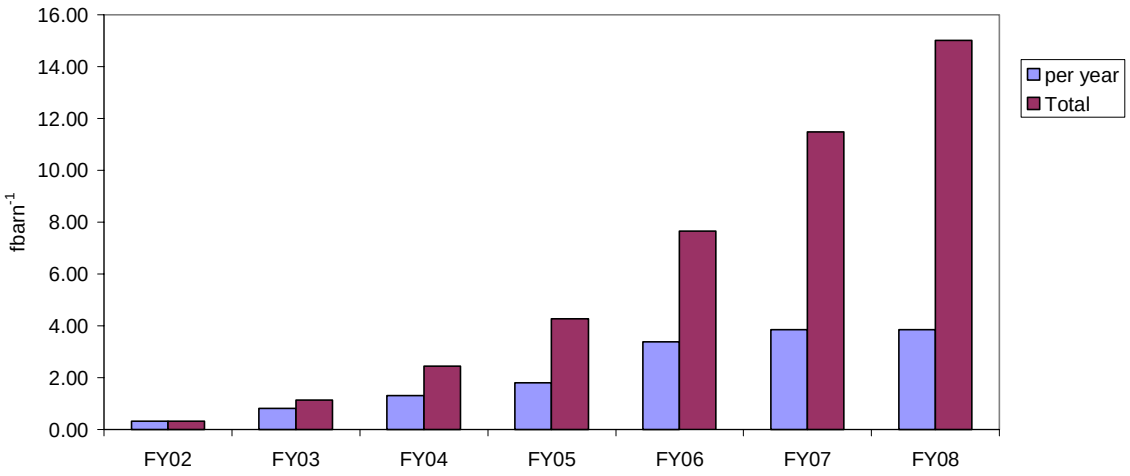

Figure 4.1.2 *Integrated Luminosity Schedule*

4.2 Costs by Fiscal Year

The following tables and charts contain a summary of the material and service costs and the labor costs for specific sub-projects.

	Project Total	FYO2 Total	FYO3 Total	FYO4 Total	FYO5 Total
Slip Stacking	1160	770	390	0	0
Antiproton Target Station	2870	820	1140	710	200
Pbar Collection Aperture	7485	1410	2955	2180	940
Stacktail Upgrade	500	100	400	0	0
Electron Cooling	7995	4070	2605	1320	0
Pbar Transport	1080	380	700	0	0
Beam-Beam Compensation	7890	2070	2070	1875	1875
Total	28980	9620	10260	6085	3015

Table 4.2.1 *Total sub-project cost by fiscal year in k$*

	Project M&S	FYO2 M&S	FYO3 M&S	FYO4 M&S	FYO5 M&S
Slip Stacking	260	170	90	0	0
Antiproton Target Station	1190	380	450	260	100
Pbar Collection Aperture	3725	550	1425	1200	550
Stacktail Upgrade	100	0	100	0	0
Electron Cooling	4745	2445	1500	800	0
Pbar Transport	390	90	300	0	0
Beam-Beam Compensation	2690	770	770	575	575
Total	13100	4405	4635	2835	1225

Table 4.2.2 *Material and service sub-project costs by fiscal year in k$*

	Project Labor	FYO2 Labor	FYO3 Labor	FYO4 Labor	FYO5 Labor
Slip Stacking	900	600	300	0	0
Antiproton Target Station	1680	440	690	450	100
Pbar Collection Aperture	3760	860	1530	980	390
Stacktail Upgrade	400	100	300	0	0
Electron Cooling	3250	1625	1105	520	0
Pbar Transport	690	290	400	0	0
Beam-Beam Compensation	5200	1300	1300	1300	1300
Total	15880	5215	5625	3250	1790

Table 4.2.3 *Labor sub-project costs by fiscal year in k$. Estimate of $100k per Full-Time-Equivalent (FTE)*

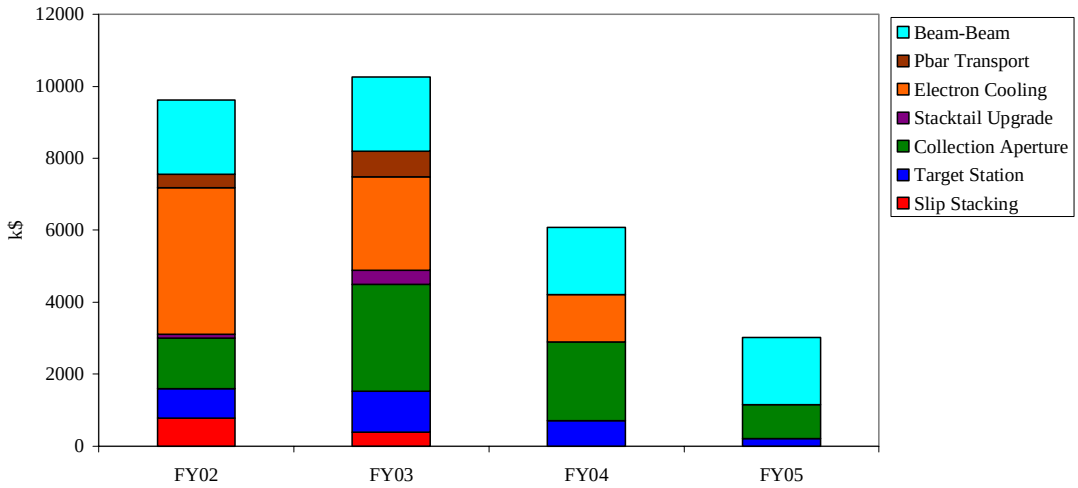

Figure 4.2.1 *Total Project Cost*

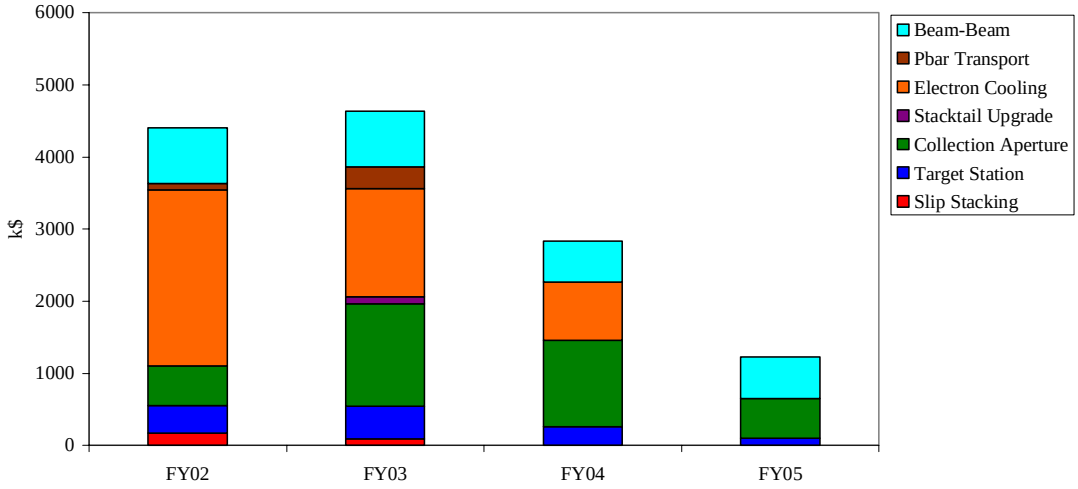

Figure 4.2.2 *Total M&S Cost*

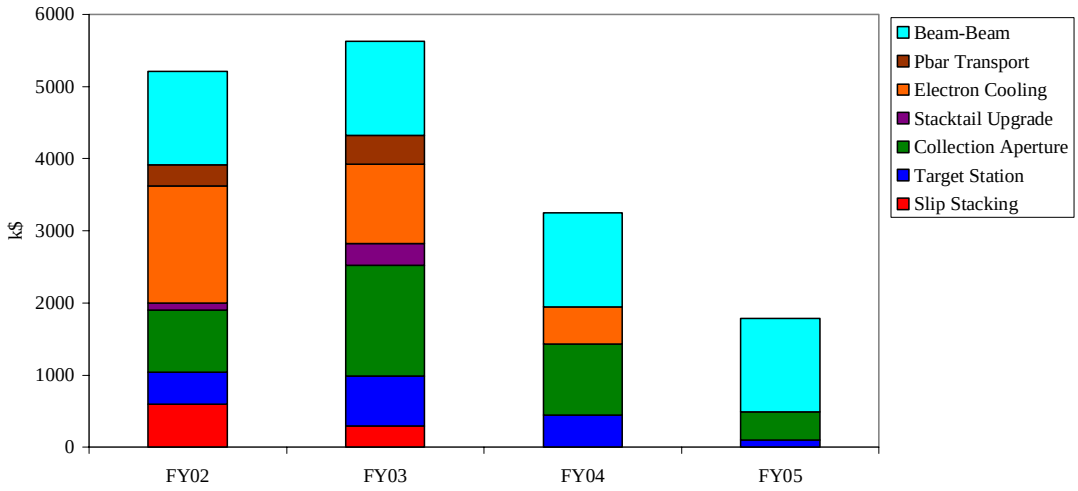

Figure 4.2.3 *Total Labor Cost assuming $100k per FTE*

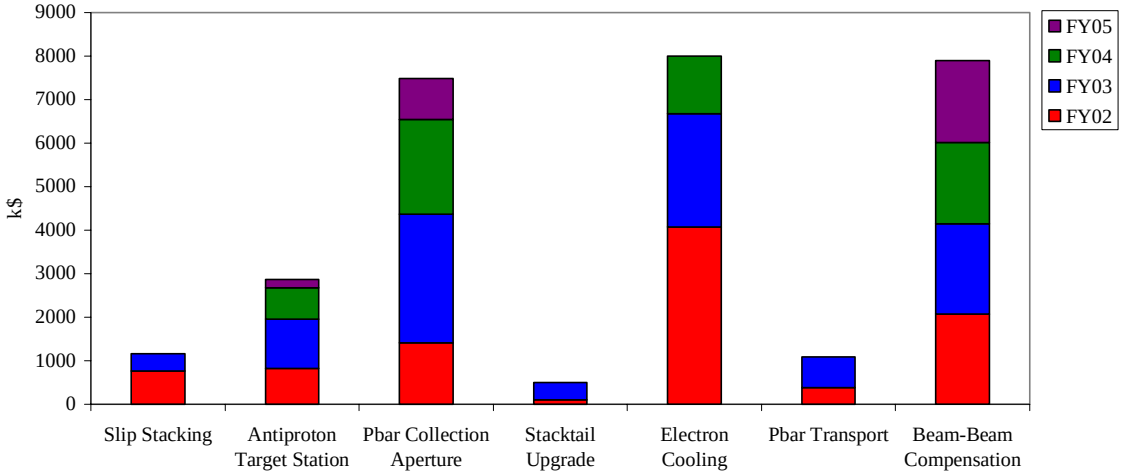

Figure 4.2.*4 Total sub-project cost*

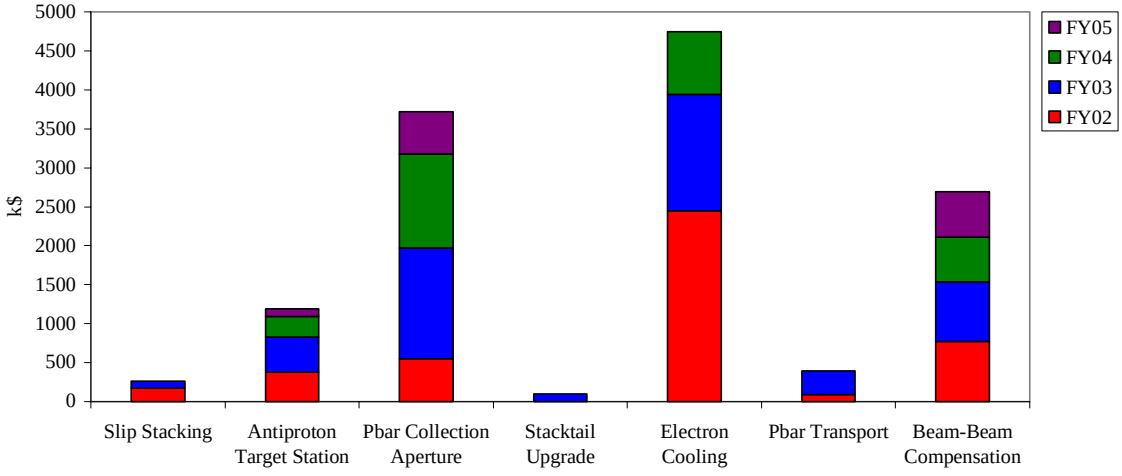

Figure 4.2.5 *Material and service sub-project costs*

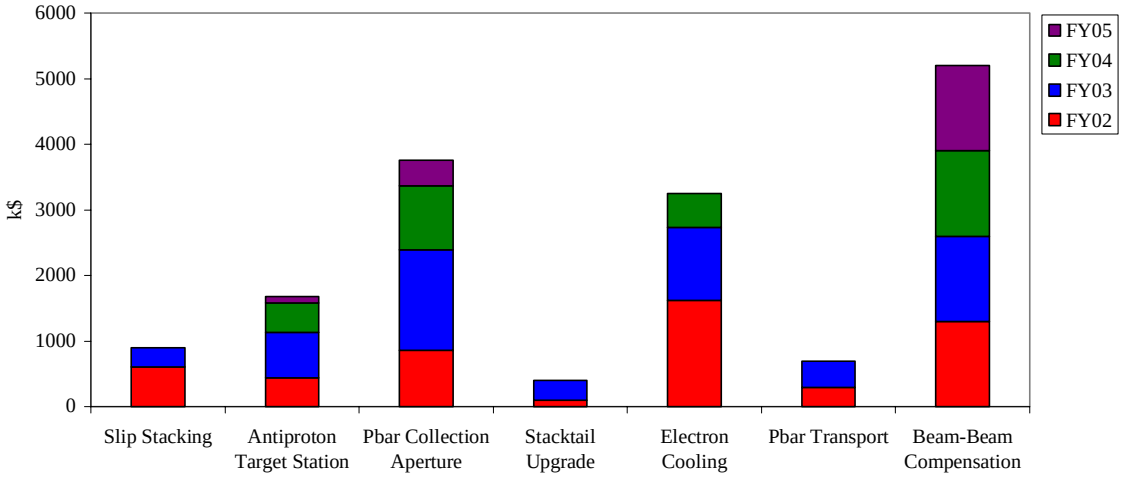

Figure 4.2.6 *Labor sub-project costs*

4.3 Sub-Project Resources

The following tables and charts contain a summary of the resources need for specific sub-projects. The estimates in costs are in units of k$. The estimates in manpower are in units of full-time-equivalents (FTEs)

	Total	M&S	Labor	Phys.	Eng.	Draft	Tech	CP
FY02	9620	4405	5215	18.2	15.4	3.8	11.95	2.8
FY03	10260	4635	5625	14.05	16.35	4.95	16.9	4
FY04	6085	2835	3250	8.55	9.35	3.45	9.75	1.4
FY05	3015	1225	1790	5.6	6.1	1.5	3.7	1
Project	28980	13100	15880	46.4	47.2	13.7	42.3	9.2

Table 4.3.1 *Total Run IIb resources*

	Total	M&S	Labor	Phys.	Eng.	Draft	Tech	CP
FY02	770	170	600	2	2	0	2	0
FY03	390	90	300	1	1	0	1	0
FY04	0	0	0	0	0	0	0	0
FY05	0	0	0	0	0	0	0	0
Project	1160	260	900	3	3	0	3	0

Table 4.3.2 *Slip Stacking*

	Total	M&S	Labor	Phys.	Eng.	Draft	Tech	CP
FY02	820	380	440	0.9	1.2	0.7	1.5	0.1
FY03	1140	450	690	0.6	2	1.2	2.6	0.5
FY04	710	260	450	0.6	1.1	0.3	2.3	0.2
FY05	200	100	100	0.4	0.2	0	0.4	0
Project	2870	1190	1680	2.5	4.5	2.2	6.8	0.8

Table 4.3.3 *Antiproton Source Target Station*

	Total	M&S	Labor	Phys.	Eng.	Draft	Tech	CP
FY02	1410	550	860	2.2	2	0.5	2.7	1.2
FY03	2955	1425	1530	2.2	3.1	2	6.3	1.7
FY04	2180	1200	980	1.7	1.5	1.9	4.2	0.5
FY05	940	550	390	1.2	0.4	0.5	1.3	0.5
Project	7485	3725	3760	7.3	7	4.9	14.5	3.9

Table 4.3.4 *Antiproton Collection Aperture*

	Total	M&S	Labor	Phys.	Eng.	Draft	Tech	CP
FY02	100	0	100	0.8	0.2	0	0	0
FY03	400	100	300	1	1	0	1	0
FY04	0	0	0	0	0	0	0	0
FY05	0	0	0	0	0	0	0	0
Project	500	100	400	1.8	1.2	0	1	0

Table 4.3.5 *Accumulator Stacktail Upgrade*

	Total	M&S	Labor	Phys.	Eng.	Draft	Tech	CP
FY02	4070	2445	1625	7	4	1	3.75	0.5
FY03	2605	1500	1105	4.75	2.75	0.75	2.5	0.3
FY04	1320	800	520	2.25	1.25	0.25	1.25	0.2
FY05	0	0	0	0	0	0	0	0
Project	7995	4745	3250	14	8	2	7.5	1

Table 4.3.6 *Recycler Electron Cooling*

	Total	M&S	Labor	Phys.	Eng.	Draft	Tech	CP
FY02	380	90	290	1.3	0.5	0.6	0	0.5
FY03	700	300	400	0.5	1	0	1.5	1
FY04	0	0	0	0	0	0	0	0
FY05	0	0	0	0	0	0	0	0
Project	1080	390	690	1.8	1.5	0.6	1.5	1.5

Table 4.3.7 *Antiproton Transport*

	Total	M&S	Labor	Phys.	Eng.	Draft	Tech	CP
FY02	2070	770	1300	4	5.5	1	2	0.5
FY03	2070	770	1300	4	5.5	1	2	0.5
FY04	1875	575	1300	4	5.5	1	2	0.5
FY05	1875	575	1300	4	5.5	1	2	0.5
Project	7890	2690	5200	16	22	4	8	2

Table 4.3.8 *Antiproton Tuneshift in the Tevatron*

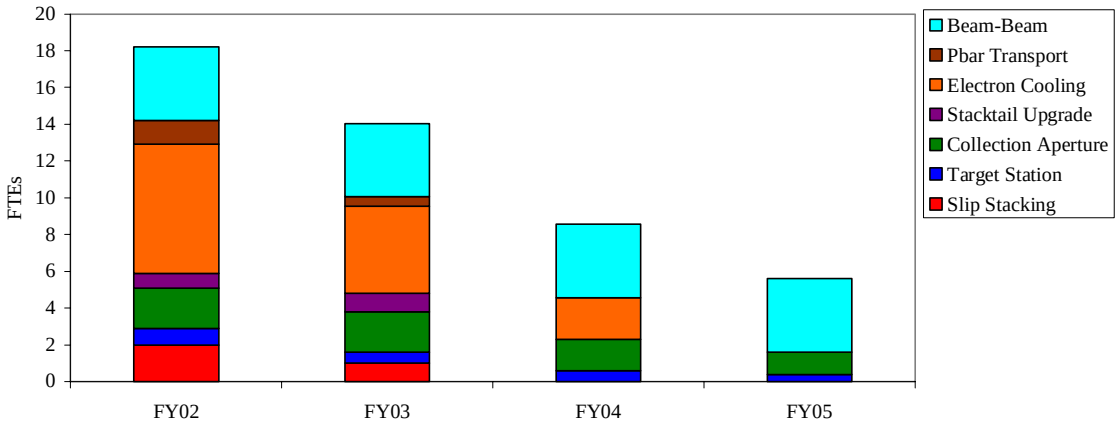

Figure 4.3.*1 Physicist Resources*

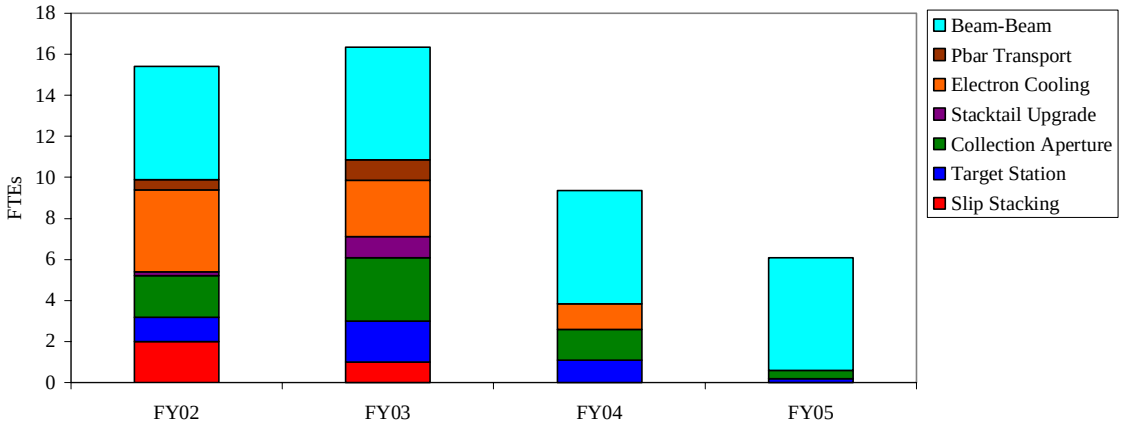

Figure 4.3.2 *Engineer Resources*

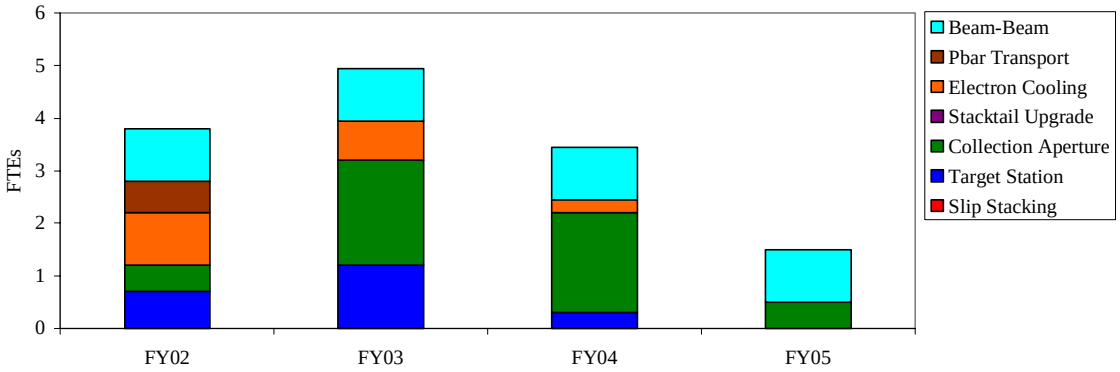

Figure 4.3.3 Drafting Resources

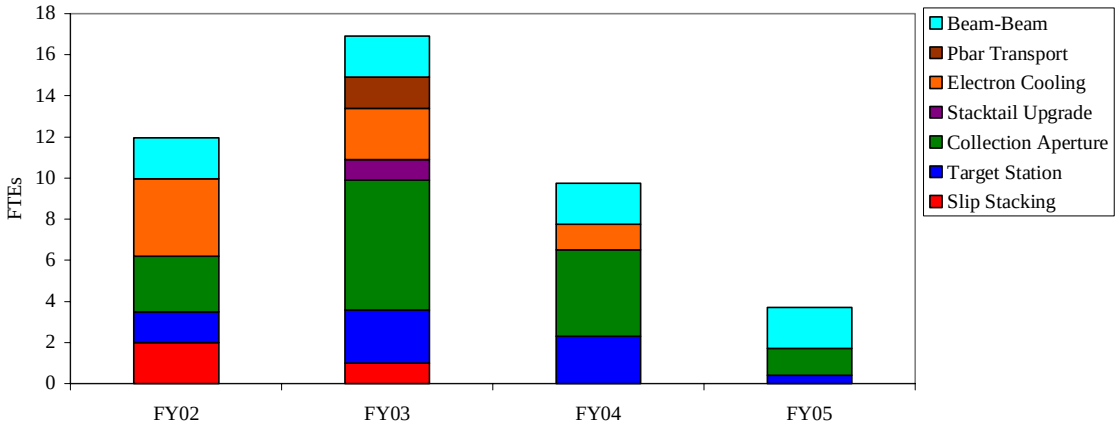

Figure 4.3.4 Technician Resources

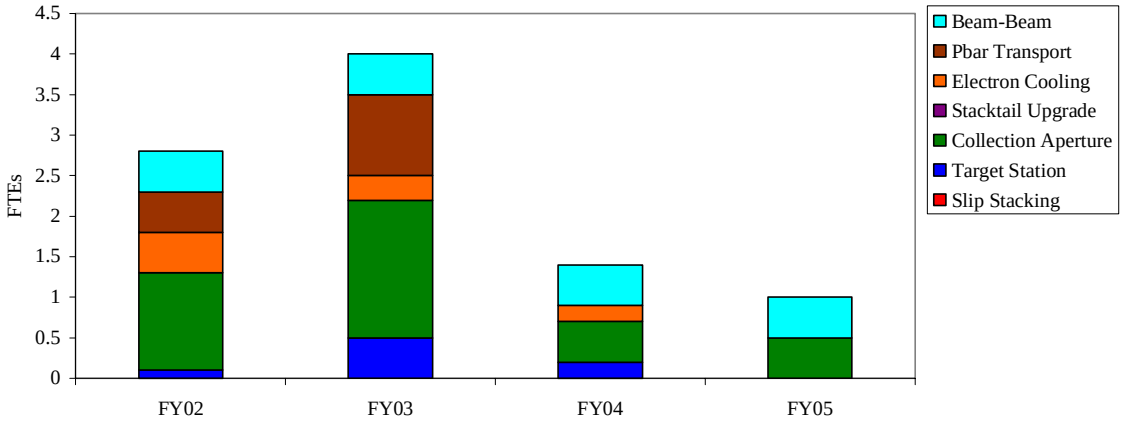

Figure 4.3.5 Computing Professional Resources

5 Summary

The goal of Run IIb is integrate 15 fb^{-1} by 2008. This document describes a plan for obtaining this goal by tripling the antiproton production rate over the anticipated Run IIa target. The increase in antiproton flux through the accelerator complex is obtained by a series of relatively modest accelerator upgrades. To reach the luminosity goal by 2008, the upgrades must be completed quickly, inexpensively, and with minimal impact on Run IIa. With these constraints in mind, the upgrades exploit many features of the Main Injector Project.

The major improvements in antiproton yield result from:

- increasing the number of protons on the antiproton production target by a factor of 1.8 by slip stacking two Booster batches in the Main Injector. (The extra Main Injector cycle time required for NUMI will reduce this factor to 1.5)
- increasing the antiproton collection efficiency by a factor of 2.0 –2.7 by:
  - increasing the gradient of the antiproton collection lens by 30%
  - increasing the effective aperture of the antiproton collection transfer line and Debuncher ring by a factor of 2.7.

The large increase in antiproton flux will require:

- an increase in the antiproton flux capability of the Accumulator Stacktail momentum stochastic cooling system
- implementation electron cooling in the Recycler Ring
- the streamlining and improvement of antiproton transfers between the Accumulator and the Recycler.

Finally we are pursuing an aggressive R&D project to build an electron lens that would compensate the beam-beam tune spread of the antiproton bunches in the Tevatron. The use of such a device could lead to a longer luminosity lifetime in the Tevatron and hence to a large integrated luminosity. Because of the R&D nature of this project, we have not explicitly assigned any luminosity gains for Run IIb from this project.

6 References

[1] The TeV33 Committee Report, February 1996.
[2] Report on Plans of the Beams Division for Tev33, 1997, unpublished.
[3] D0 Note Number: 003515,Luminosity Distribution During Collider Run II,Mike Martens, Peter Bagley
[4] G. Jackson, "The Fermilab Recycler Ring Technical Design Report", Fermilab Report No. TM-1991 (1996)
[5] Proton Driver Study, Fermilab-TM-2136, December 2000
[6] Debuncher Stochastic Cooling Upgrade for Run II and Beyond, Pbar Note 573, J. Marriner, April 1998
[7] V. Bharadwaj, et al, "Study of Space Charge Effects in the Fermilab Booster", FERMILAB-EXP-170, FNAL, (1990).
[8] J. Dey, J. Steimel, J. Reid, "Narrowband Beam Loading Compensation in the Fermilab Main Injector Accelerating Cavities," 2001 Particle Accelerator Conference, Chicago, ID# MPPH047, http://pacwebserver.fnal.gov/papers/Monday/PM_Poster/MPPH047.pdf.
[9] J. Marriner, "RF Power Considerations for Beam Loading Compensation During Slip Stacking in the Main Injector," FNAL, not published, (1997).
[10] J. A. MacLachlan, J. Ostiguy, "User's Guide to ESME v. 8.2", FNAL http://www-ap.fnal.gov/ESME/esme-manual/esme-manual.html , (1997).
[11] J. A. MacLachlan, "The Beam Dynamics of Slip Stacking," FNAL, not published, (2001).
[12] R. Garoby, "Beam Loading in RF Cavities", Joint US-CERN School, CERN/PS 91-33 (RF) (1990).
[13] R. Garoby, "Low Level RF and Feedback", Joint US-CERN School, CERN/PS 97-34 (RF) (1997).
[14] S. Shukla, et al, "Slip Stacking for the Fermilab Luminosity Upgrade," FNAL, not published, (1997).
[15] D. Boussard, "Cavity Compensation and Beam Loading Instabilities", SPS/ARF/Int. Note/DB/gs/78-16 (1978).
[16] R. Garoby, et al, "RF System for High Beam Intensity Acceleration in the CERN PS", Particle Accelerator Conference 1989, CERN/PS 89-28 (RF) (1985).
[17] F. Pedersen, "RF Cavity Feedback", Stanford Linear Accelerator, (1992).
[18] Main Injector Design Report
[19] S. O'Day, F. Bieniosek, K. Anderson, "New Target Results from the FNAL Antiproton Source", Pbar note #547
[20] N.V. Mokhov, "The MARS code system user's guide version 13(95)", Fermilab Note #628
[21] T.A.Vsevolozskaya, The optimization and efficiency of antiproton production within a fixed acceptance, NIM 190(1981) pp.479-486.
[22] J. Morgan, "FNAL target station issues", Snowmass 2001 T4 presentation, July 2001.
[23] V. Visjnic, "Fermilab Stochastic Cooling Code User's Guide", Pbar Note #498. The Fortran code was rewritten in C++ for these simulations.
[24] J. A. MacLachlan, J. Ostiguy, "*User's Guide to ESME v. 8.2*" http://www-ap.fnal.gov/ESME/esme-manual/esme-manual.html (1997).

[25] J. A. MacLachlan, "*The Beam Dynamics of Slip Stacking*" FNAL, not published, (2001).
[26] "The 4-8 GHz Stochastic Cooling Upgrade for the Fermilab Debuncher", Pbar Note 625, D. McGinnis, Nov. 1999
[27] Known as the van Der Meer method, a description can be found in D. Edwards and M. Syphers, An Introduction to the Physics of High Energy Accelerators, J. Wiley & Sons, 1993.
[28] A. Ando and K. Takayama, "RF Stacking and Tail Cooling in the Antiproton Accumulator", Fermilab-TM-1103, 1982
[29] D. B. Cline et al.,"Intermediate Energy Electron Cooling for Antiproton Sources Using a Pelletron Accelerator", IEEE Trans. Nucl. Sci., NS-30, no. 4 (1983), p2370.
[30] D. J. Larson,"Intermediate Energy Electron Cooling for Antiproton Sources", PhD dissertation, U. Wisconsin, Madison WI (1986).
[31] J. MacLachlan (editor), "Prospectus for an electron cooling system for the Recycler", Fermilab-TM-2061, http://www-lib.fnal.gov/archive/1998/tm/TM-2061.html
[32] A. M. Budker, Atomnaja Energija, 22 (5), p246 (1967).
[33] I. N. Meshkov, Phys. Part. Nucl., 25 (6), p631 (1994).
[34] A. Burov, *et al.*, "Design of Antiproton Medium Energy Electron Cooling at Fermilab", NIM A 441 (2000), 234.
[35] J. Griffin et al., IEEE Trans. Nucl. Sci NS-30 (1983), 3502.
[36] J.A. MacLachlan, "RF Stacking without Emittance Dilution", FERMILAB-Conf-00/117, June 2000.
[37] A.C. Crawford, S. Nagaitsev, A. Sharapa, and A. Shemyakin, "Successful MeV-range electron beam recirculation", in Proc. of EPAC-98 (Stockholm, Sweden, June 22-26, 1998).
[38] S. Nagaitsev et al., "Diagnostics for the 5 MeV electron cooling system", NIM A 441 (2000), p. 246.
[39] A. Burov et al., " Fermilab Electron Cooling project: Commissioning of the 5 MeV recirculation test set-up", PAC 2001, Chicago.
[40] Run II handbook http://www-bd.fnal.gov/runII/index.html
[41] P.Bagley, BNL-52601 (2000), p.23.
[42] M.Church, communication on Tevatron luminosity (Oct., 2001).
[43] V.Shiltsev et al., PRST-AB, v.2, 071001 (1999).
[44] D.Shatilov, V.Shiltsev, FERMILAB-TM-2124 (2000).
[45] Y.Alexahin, FERMILAB-TM-2148 (2001).
[46] V.Shiltsev, A.Zinchenko, PRST-AB, v.1, 064001 (1998).
[47] A.Burov, V.Danilov, V.Shiltsev, Phys.Rev. E, 59 (1999), p.3605